

This item was submitted to Loughborough University as a PhD thesis by the author and is made available in the Institutional Repository (<https://dspace.lboro.ac.uk/>) under the following Creative Commons Licence conditions.



For the full text of this licence, please go to:
<http://creativecommons.org/licenses/by-nc-nd/2.5/>

BLDSC no:- DX 77879

LOUGHBOROUGH
UNIVERSITY OF TECHNOLOGY
LIBRARY

AUTHOR/FILING TITLE

KNEESHAW, J A

ACCESSION/COPY NO.

015308/02

VOL. NO.

CLASS MARK

15 NOV 1998

4 DEC 1998

15 JAN 1999

25 FEB 1999

LoAN copy

001 5308 02



THE CORROSION BEHAVIOUR OF Fe-Cr-Ni ALLOYS
IN COMPLEX HIGH TEMPERATURE GASEOUS ATMOSPHERES
CONTAINING THE REACTANTS OXYGEN, SULPHUR
AND CARBON

by

JONATHAN ANDREW KNEESHAW, B.Sc., B.Eng.

A Doctoral Thesis submitted in partial fulfilment
of the requirements for the award of
Doctor of Philosophy
of the Loughborough University of Technology, U.K.,
based on research carried out at the
Commission of the European Communities Joint Research Centre,
Petten, Netherlands.

JUNE, 1987.

© by J. A. Kneeshaw, 1987.

Loughborough University of Technology Library	
Date	Jan 58
Class	
Acc. No.	015308/02

VOLUME 2

THE
JOURNAL
OF
THE
ROYAL
ANTHROPOLOGICAL
INSTITUTE
PART 1
1902

CONTENTS

	Page
1. INTRODUCTION	1
2. REVIEW OF THE RELEVANT LITERATURE	5
2.1 Technological Requirements	5
2.2 Corrosion Processes in Single Reactant Gaseous Environments	22
2.2.1 Oxidation	22
2.2.2 Sulphidation	59
2.2.3 Carburization	83
2.3 Corrosion Processes in Multiple Reactant Gaseous Environments	98
2.3.1 Thermodynamic Considerations	98
2.3.2 Carburization/Oxidation	114
2.3.3 Carburization/Sulphidation	126
2.3.4 Sulphidation/Oxidation	132
2.4 Research Requirements Emerging from the Literature Review	172
3. EXPERIMENTAL	174
3.1 Materials and their Preparation	174
3.2 Gases and their Thermodynamic Characterisation	178
3.3 Corrosion Autoclaves and Experimental Procedures	179
3.4 Analytical Techniques	182
4. RESULTS AND THEIR INTERPRETATION	205
4.1 Oxidation Governed Regime at 800°C	206
4.1.1 Model 25Cr-35Ni-Fe Alloy	206
a) Sulphur-free gas	206
b) 0.2% H ₂ S gas	211
Summary	223
4.1.2 HP40Nb	262
a) Sulphur-free gas	263
b) 0.2% H ₂ S gas	269
Summary	277
4.1.3 AISI314	316
a) Sulphur-free gas	317
b) 0.2% H ₂ S gas	320
Summary	325

4.1.4	HP40A1	354
	a) Sulphur-free gas	355
	b) 0.2% H ₂ S gas	358
	Summary	362
4.2	Sulphidation Governed Regime at 800°C	387
4.2.1	Model 25Cr-35Ni-Fe Alloy in the 0.6% H ₂ S gas	387
4.2.2	HP40Nb in the 0.6% H ₂ S gas	401
4.2.3	HP40A1 in the 0.6% H ₂ S gas	417
4.3	A Preliminary Investigation on Alloy 800H at 800°C	436
	a) Sulphur-free gas	436
	b) 0.2% H ₂ S gas	440
	c) 0.6% H ₂ S gas	445
	d) 2.0% H ₂ S gas	452
5.	DISCUSSION	482
5.1	Corrosion Mechanisms in the sulphur-free gas	482
5.2	Corrosion Mechanisms in the low sulphur 0.2% H ₂ S gas	496
5.3	Corrosion Mechanisms in the high sulphur 0.6% H ₂ S gas	510
5.4	Recommendations for Technological Applications	513
6.	CONCLUSIONS	517
7.	SUGGESTIONS FOR FURTHER WORK	520

4.1.3. AISI 314

To further assess the role of Si on the corrosion behaviour in the oxidation-governed regime a less detailed study was carried out on the high Si containing alloy AISI 314. This alloy is a 25Cr-20Ni-Fe alloy with additions of 2.04 % Si and 1.12 % Mn. The alloy was supplied as wrought bar with a small grain size (10 μm).

To establish any microstructural changes resulting from aging processes, examinations were carried out on the as-received material and on specimens annealed in argon at 800°C for 1 hour, 7.25 hours, 100 hours and 2000 hours.

As-received

Cross-sectional examination showed that the alloy consisted of austenite with a few carbide precipitates at grain boundaries. These were electrolytically extracted for one hour and identified by X-ray diffraction analysis as M_{23}C_6 , figure 4.58.

1 hour

Extracting the carbides for the same time (1 hour) followed by X-ray diffraction analysis showed that the relative intensity of the M_{23}C_6 carbides had increased, figure 4.58.

7.25 hours

Carbide extraction and subsequent X-ray diffraction analysis indicated that the intensity of M_{23}C_6 was approximately the same as after annealing for 1 hour, figure 4.58.

100 hours

Cross-sectional examination now revealed that the alloy contained a considerable amount of the "globular" looking σ phase at the grain boundaries in addition to the long thin M_{23}C_6 precipitates, figure 4.59a.

Extraction of these phases and subsequent X-ray diffraction analysis again confirmed that the relative intensity of $M_{23}C_6$ was increasing and that the σ phase was now present in detectable quantities, figure 4.58.

2000 hours
.....

Cross-sectional examination showed that the phase precipitates were now more pronounced and much coarser. The $M_{23}C_6$ precipitates had not changed significantly, figure 4.59b.

Thus in summary the alloy in the as-received condition consisted of austenite with a few $M_{23}C_6$ precipitates at grain boundaries. As time progressed at 800°C, aging processes led initially to the amount of $M_{23}C_6$ precipitates increasing followed by the formation of the σ phase.

a. Sulphur-free gas

Kinetic data for the electropolished (EP) and 180 grit (180) surface finishes are presented in figure 4.60. There was no difference between the surface finishes with the weight uptake being very small (0.3 mg/cm² in 5000 hours).

Replotting these data as weight-gain squared against time, figure 4.61, showed that the corrosion kinetics were parabolic, with the rate approximately equal to that of the HP40Nb alloy in the 180 grit condition. The reaction rate constants are given in table 4.12. Data for the HP40Nb and Model 25Cr-35Ni-Fe alloy in the electropolished (EP) condition are also presented for comparison purposes to illustrate the very low corrosion rates of the AISI 314 material, figure 4.61.

Structural examinations were carried out on the 180 grit specimens after 100, 2000 and 5000 hours exposure and on the electropolished (EP) specimens after 1 hour, 5 hours, 100 hours and 2000 hours exposure.

180 grit condition

100 hours
.....

Cross-sectional examination showed that a very thin ($\sim 1 \mu\text{m}$ thick) scale formed on the alloy surface, figure 4.62a. X-ray diffraction analysis

using surface reflection detected the M_3O_4 spinel and the σ phase, table 4.13. Because of the thinness of the scale the signal for the σ -phase was assumed to have come from the precipitates contained within the alloy substrate. The relatively large lattice parameter value of the oxide spinel indicated that it contained a considerable quantity of Mn, figure 4.63.

2000 hours
.....

ESCA-AUGER analysis, figure 4.64, showed that the oxide scale now consisted of three distinct layers; an outer layer containing slightly more Cr than Mn, an intermediate layer rich in Mn with some Cr and Si and most importantly an inner layer rich in Si. The definite increase in the oxygen level as the Si level increased, together with the peak position indicating that the silicon was present as Si^{4+} led to the conclusion that a complete inner SiO_2 layer had formed.

5000 hours
.....

Although not shown, cross-sectional analysis showed that the scale after this long exposure time was only 1-3 μm thick. X-ray diffraction using surface reflection now detected M_3O_4 , Cr_2O_3 , traces of SiO_2 and $M_{23}C_6$, table 4.13. Because the scale was very thin it was assumed that the $M_{23}C_6$ peaks came from precipitates within the alloy substrate. The M_3O_4 lattice parameter value was similar to that obtained after 100 hours exposure, figure 4.63. The lattice parameter value of Cr_2O_3 was slightly higher than that of pure Cr_2O_3 , figure 4.65, but because of the very low intensity perhaps not too much significance should be attached to this observation. Again the most important observation was the presence of SiO_2 . The rather low intensity of SiO_2 detected was attributed to it being present in the inner layer of the scale and the lack of sharpness of the X-ray peaks.

Thus in summary it appears that the corrosion process proceeded at the same rate and in a similar manner to the HP40Nb 180 grit material. A complete internal SiO_2 layer formed which prevented the outward diffusion of Cr and Fe into the scale and resulted in very low weight gains and scale thicknesses.

Electropolished (EP) condition

1 hour

.....

X-ray diffraction analysis using surface reflection showed that Cr_2O_3 , M_3O_4 and M_{23}C_6 formed on the alloy surface in the initial stages, table 4.14. The Cr_2O_3 lattice parameter value corresponded to that of pure Cr_2O_3 (figure 4.65) and the M_3O_4 lattice parameter value indicated that this phase was MnCr_2O_4 , figure 4.63.

5 hours

.....

X-ray diffraction analysis using surface reflection detected the same phases, table 4.14. Whereas the intensities of the M_3O_4 and Cr_2O_3 increased the intensity of M_{23}C_6 remained the same. The M_{23}C_6 lattice parameter did however increase. The lattice parameters of Cr_2O_3 and M_3O_4 were relatively unchanged, figures 4.65 and 4.63.

100 hours

.....

X-ray diffraction using surface reflection now detected only M_3O_4 spinel and Cr_2O_3 with no trace of M_{23}C_6 , table 4.14. The lattice parameter of the M_3O_4 increased indicating that the spinel was becoming richer in Mn, figure 4.63. The lattice parameter value of the Cr_2O_3 also increased, figure 4.65.

2000 hours

.....

Cross-sectional examination showed that even after 2000 hours the scale was exceptionally thin ($< 2 \mu\text{m}$), figure 4.62b. X-ray diffraction analysis using surface reflection now detected only M_3O_4 and no Cr_2O_3 , table 4.14. Again the M_3O_4 lattice parameter had increased, figure 4.63.

In summary the low weight gains and scale thicknesses led to the conclusion that the high 2.04 % Si level in the AISI 314 material was sufficient, even in the electropolished (EP) condition, to form a complete internal SiO_2 layer. Thus the corrosion process proceeded in a similar manner to that of the 180 grit condition.

b. 0.2 % H₂S gas

The corrosion kinetics for the 180 grit surface finish for exposure times up to 5000 hours and the electropolished (EP) surface finish up to 2000 hours exposure are given in figure 4.66. The weight uptake of the material in the 180 grit condition ($\sim 5 \text{ mg/cm}^2$ in 2000 hours) was higher than on the electropolished material ($\sim 3 \text{ mg/cm}^2$ in 2000 hours). Because the extent of corrosion was greater on the 180 grit material the majority of the analysis was concentrated on this surface finish. Only a limited amount of information is presented for the electropolished (EP) material.

180 grit condition

Replotting the kinetic data as weight gain squared against time showed that the corrosion process commenced at a high rate and subsequently slowed down until after approximately 1000 hours it became parabolic, figure 4.67. The corrosion rate remained parabolic until after 3000 hours a significant increase in the rate occurred, indicating the onset of breakaway corrosion. Whilst in the parabolic range the corrosion rate was very similar to the HP40Nb alloy (table 4.12), however once breakaway commenced the upturn in the rate for AISI 314 was much more pronounced, figure 4.67. The Model 25Cr-35Ni-Fe alloy is also included in the figure for comparison purposes.

To gain a clearer understanding of the corrosion process examinations were carried out after 1 hour, 5 hours, 100 hours, 500 hours, 1000 hours and 5000 hours.

1 hour
.....

X-ray diffraction analysis using surface reflection detected the M_3O_4 spinel and Cr_2O_3 on the alloy surface, table 4.15. The lattice parameter values indicated that the spinel was probably FeCr_2O_4 , figure 4.63, and that the Cr_2O_3 phase was relatively pure, figure 4.65.

5 hours
.....

X-ray diffraction analysis using surface reflection now detected M_3S_4 in addition to M_3O_4 and found no trace of Cr_2O_3 , table 4.15. The lattice parameters of the oxides were approximately the same as before.

100 hours
.....

Some spallation of the scale started to occur. SEM examination showed that the surface of the scale was very filamentary, figure 4.68a. Cross-sectional examination using the Pepperhoff technique revealed that the scale consisted of two layers : an outer filamentary looking layer (10 μm thick) and a slightly thinner uneven inner layer (5 μm thick), figure 4.69a. A few isolated metallic particles were also visible between the two layers. Although the two layers were predominantly oxide both contained a number of sulphide particles. Spherical sulphide precipitates were also present in the alloy substrate.

An EPMA line scan taken through the two layers indicated that the outer oxide layer contained predominantly chromium and oxygen with approximately 5 % Fe, 2 % Mn and 4 % S also present, figure 4.70. X-ray mapping indicated that the Fe tended to be concentrated in localized regions. The inner layer was rich in both Si and Cr and contained considerably more S (up to 10 %) than the external layer. The alloy substrate beneath the scale at this stage contained 12 % Cr. The spherical sulphide precipitates present in the Cr depleted alloy substrate were found to be rich in Mn and Cr but had no fixed composition. No carbides or σ -phase were present in the Cr-depleted zone.

500 hours
.....

Cross-sectional examination after 500 hours showed that both the outer (20 μm) and inner (14 μm) layers were thicker but otherwise the corrosion morphology was very similar to that after 100 hours, figure 4.69b. The internal spherical sulphide precipitates had however become larger but fewer in number and penetrated deeper into the alloy substrate.

1000 hours
.....

After 1000 hours surface SEM examination revealed that the outer layer had become coarser, figure 4.68b. An appreciable amount of spallation was also continuing to occur. The outer layer which was still attached to the specimen was removed, ground to a powder and examined by ESCA-AUGER analysis. This showed that it still consisted of predominantly Cr-rich oxides with small amounts of Fe, Mn and S also present, figure 4.71.

To obtain more information about the composition of the inner layer argon ion sputtering was used in conjunction with ESCA-AUGER analysis to obtain a concentration profile through the inner layer which was still attached to the specimen, figure 4.71. This revealed that at the original alloy interface the scale contained 28 % Si, 10 % Cr and small quantities of Fe, Mn and S. Deeper in the layer the level of chromium increased as the level of Si decreased. The peak positions showed that the Si and Cr were present as Si^{4+} and Cr^{3+} , indicating a mixture of SiO_2 and Cr_2O_3 . X-ray diffraction using surface reflection, however, detected no trace of SiO_2 , instead the scale was found to consist of Cr_2O_3 and M_3O_4 , table 4.15.

5000 hours
.....

Surface SEM examination showed that in general the scale had now become even coarser, figure 4.68c. At corners of the specimen, where quite often most of the spallation had occurred, large sulphide particles had formed, figure 4.68d. These were identified by X-ray diffraction using surface reflection as M_3S_4 , table 4.15. The rest of the surface was identified as M_3O_3 and Cr_2O_3 , table 4.15. The lattice parameter of the spinel indicated that it was FeCr_2O_4 , figure 4.63. The Cr_2O_3 lattice parameter however was still approximately equivalent to that of pure Cr_2O_3 , figure 4.65.

Cross-sectional examination using the Pepperhoff technique showed that in general areas away from the corners the two layered oxide scale was still present, figure 4.69d.

Both layers had thickened considerably and a large amount of localized internal oxidation had also taken place. Sulphides were often observed in these localized regions particularly at the deepest point of the attack where it appeared that sulphur was attacking the carbides and σ -phase before they were converted to oxides. Sulphides were still present in the Cr-depleted substrate.

The corrosion attack was much more severe at the corners of the specimens, figure 4.72 and 4.69c. Rather voluminous looking M_3S_4 sulphide lamellae were now present in place of the outer oxide layer. The internal oxide layer remained, but a vast amount of localized internal oxidation had taken place.

To ascertain the reasons for the upturn in the kinetic curve and the presence of the M_3S_4 sulphides at the corners, an EPMA line scan was taken through one of the general areas of the scale, where sulphide formation had not commenced, figure 4.73. This showed that the external layer consisted of a predominantly Cr_2O_3 , with isolated pockets of $(FeMn)_3O_4$ spinel. An appreciable amount of sulphur was still present throughout the scale. The internal layer as before was rich in Cr and Si and again contained appreciable quantities of sulphur. Perhaps the most significant observation however was that the alloy substrate beneath the internal layer contained only 8 % Cr.

The line scan was continued deeper into the alloy substrate, figure 4.74. This showed that the localized internal oxide was rich in Cr and Fe in the centre and Cr and Si around the edges. The internal spherical sulphides present in the Cr-depleted substrate were again identified as $(MnCr)S$. Once the Cr-level in the alloy substrate reached 14 % carbides were stable and slightly deeper into the alloy σ phase was also visible.

Thus in summary it appears that in the parabolic range (1000-3000 hours) the corrosion process proceeded at approximately the same rate and in a similar manner to the HP40Nb under the same conditions. However in the case of AISI 314 the breakaway trend which commenced after approximately 3000 hours was much more pronounced and eventually led to the formation of sulphides instead of oxides in the external scale. The reasons for

this appear to be associated with the considerable amount of spallation and the formation of the σ phase, which placed high demands on the Cr reservoir in the alloy. Eventually the alloy substrate beneath the scale became so depleted in Cr that the Cr rich oxide layer was no longer able to offer protection and sulphides started to form. The presence of 0.2 % H_2S in the gas led to some internal sulphidation which prevented the Si rich inner layer from forming a barrier to the outward diffusion of Cr and Fe.

Electropolished (EP) condition

The corrosion process proceeded in a similar manner but at a slightly lower rate than the 180 grit condition, figure 4.66.

The difference between the behaviour of the AISI 314 exposed to the sulphur-free gas and the 0.2 % H_2S gas for the same exposure time (2000 hours) is summarized in figure 4.75. In the case of the sulphur-free gas a complete SiO_2 inner layer formed which prevented the outward diffusion of Cr and Fe into the outer layers of the scale with the result that a very thin scale formed, figure 4.75a. The presence of 0.2 % H_2S in the gas led to the formation of sulphides both within the alloy substrate and oxide scale, figure 4.75b. The presence of sulphur prevented the inner Si rich layer from forming a protective barrier to the outward diffusion of Cr and Fe and inward diffusion of S and O. This resulted in the outer and inner layers growing relatively quickly, figure 4.75b. A significant amount of localized attack of the $M_{23}C_6$ and σ phase initially by S and subsequently by O occurred after longer exposure periods.

A line scan AB taken through a typical area of the scale is shown in figure 4.76. This confirmed that the scale consisted of three layers; an outermost $(MnFe)Cr_2O_4$ layer, an intermediate Cr_2O_3 layer and an inner layer rich in Si and Cr. The line scan and elemental mapping also showed that all three of these layers contained a significant amount of sulphur. After 2000 hours the alloy substrate beneath the inner layer contained only approximately 10 % Cr, figure 4.76. If the corrosion process was continued for longer exposure times this low level of Cr

would eventually become insufficient for a protective Cr-rich oxide layer to form and breakaway would take place, as demonstrated by this material in the 180 grit condition.

Summary for AISI 314

Aging processes

The alloy in the as-received condition consisted of austenite with a few $M_{23}C_6$ carbide precipitates at grain boundaries. As time progressed at 800°C aging processes led initially to the amount of $M_{23}C_6$ precipitates increasing followed by the formation of the σ phase.

S-free gas '180' grit condition

Examinations were not carried out for short term exposures (< 100 hours). However it is reasonable to assume that the corrosion process was similar to the HP40Nb material which progressed at the same rate. Thus a continuous layer of Cr_2O_3 and $MnCr_2O_4$ formed on the alloy surface in the initial stages. An inner SiO_2 layer started to form and block off the outward diffusion of Cr into the surface layer with the result that the Cr_2O_3 was converted to $MnCr_2O_4$. Mn continued to diffuse into the outer $MnCr_2O_4$ layer increasing the Mn to Cr ratio. Once the SiO_2 layer became complete no further outward diffusion of Mn occurred and the corrosion morphology consisted of a $Mn_{1+x}Cr_{2-x}O_4$ outer layer and an inner SiO_2 layer, figure 4.77a. Subsequently the inner SiO_2 layer continued to thicken very slowly, figure 4.77b. After long term exposures (5000 hours) an additional intermediate Cr_2O_3 layer was detected, figure 4.77c. This could have formed due to the growth of the σ phase and perhaps the carbides disrupting the inner SiO_2 layer and allowing the outward diffusion of Cr to recommence.

S-free gas 'electropolished EP' condition

Cr_2O_3 , $MnCr_2O_4$ and $M_{23}C_6$ formed on the alloy surface, figure 4.77d in the initial stages. These subsequently grew to form a complete surface layer figure 4.77e. An inner discontinuous SiO_2 layer started to form. Once the surface layer became complete the oxides overgrew the carbides. The carbides were then converted to oxides with the carbon released diffusing deeper into the alloy, figure 4.77f. The inner SiO_2 layer

started to cut off the outward diffusion of Cr, with the result that the Cr_2O_3 was converted to MnCr_2O_4 . The outward diffusion of Mn continued, increasing the Mn to Cr ratio in the outer layer until the inner SiO_2 layer became complete. The corrosion morphology at this point thus consisted of a outer $\text{Mn}_{1+x}\text{Cr}_{2-x}\text{O}_4$ layer and an inner SiO_2 layer, figure 4.77f. After long term exposures a slight thickening of the inner SiO_2 layer took place, figure 4.77g. Thus it can be concluded that the 2.01 % Si addition in the alloy was sufficient even without the assistance of surface working to form a complete inner SiO_2 layer which provided a very good barrier to outward cationic diffusion. Due to the complex aging process it was not possible to determine if any inward ingress of C took place.

0.2 % H_2S gas 180 grit condition

The corrosion process can be summarized in a number of stages.

- Stage 1 (1 hour)

Initially a layer consisting of Cr_2O_3 , FeCr_2O_4 and some sulphides formed on the alloy surface and a large number of Mn/Cr rich internal sulphide precipitates formed in the alloy substrate, figure 4.78a.

- Stage 2 (5 hours)

M_3S_4 sulphide filaments grew on top of the surface layer and the larger internal sulphide precipitates grew at the expense of the smaller ones, figure 4.78b.

- Stage 3 (100-500 hours)

The oxides then overgrew the sulphides to form a porous uneven external layer containing Cr_2O_3 , FeCr_2O_4 and sulphide filaments, figure 4.78c. Some of the sulphide filaments and sulphides in the former surface layer started to transform to FeCr_2O_4 and metallic particles. This layer contained the new SiO_2 phase, some of the former internal sulphide precipitates and Cr_2O_3 (formed from the transformation of some of the sulphide precipitates and carbide precipitates in the alloy). The presence of the sulphides and Cr_2O_3 in this layer prevented the SiO_2 from forming a barrier to the

outward diffusion of Cr, Mn and Fe. The internal sulphide precipitates in the alloy substrate continued to grow at the expense of the smaller ones.

- Stage 4 (3000-5000 hours)

The outer layer now consisted of predominantly Cr_2O_3 with pockets of $(\text{Fe}_2\text{Mn})\text{Cr}_2\text{O}_4$; Cr_xS_y and metallic particles, figure 4.78d. It appeared that some of the sulphides had transformed to FeCr_2O_4 and metallic particles, but an appreciable amount of sulphur remained in the form of chromium sulphides. The inner layer as before contained SiO_2 , Cr_2O_3 , $(\text{Fe,Mn})\text{Cr}_2\text{O}_4$ and some Cr/Mn rich sulphides. The alloy substrate beneath this layer now only contained $\sim 8\%$ Cr. This Cr-depletion was leading to a large amount of localized internal attack of the carbides and σ phase initially by S then by O to form FeCr_2O_4 and SiO_2 . Some Cr/Mn rich sulphide precipitates remained in this Cr depleted region of the alloy substrate. Once the Cr level reached about 14 % the carbides and σ phase were stable.

In some places, such as corners, the external scale had spalled off and the Cr level of the substrate was now insufficient to form a new Cr_2O_3 outer layer. This resulted firstly a large amount of internal attack and secondly the formation of an FeCr-rich sulphide outer layer, figure 4.78e.

0.2 % H_2S electropolished condition

The weight uptake of the electropolished material was slightly lower. Examination after 2000 hours showed that the corrosion morphology was very similar to the 180 grit condition, figure 4.78f. The main difference was that a smaller volume of internal sulphide precipitates were present and that the M_3O_4 spinel contained a higher Mn to Fe ratio than the 180 grit material. This spinel was concentrated in an outer layer on top of the Cr_2O_3 layer. Thus it was concluded that because less Mn was consumed by the internal sulphides, more was available for external oxidation.

Environment	Surface Finish	Reaction Rate Constant ($\text{mg}^2\text{cm}^{-4}\text{h}^{-1}$)
Sulphur free	EP	1.8×10^{-5}
	180	1.5×10^{-5}
0.2 % H_2S	EP	-
	180	6.4×10^{-3}

Table 4.12

Reaction rate constants for AISI 314 at 800°C ($p\text{O}_2 = 10^{-21}$ bar, $a_c = 0.3$).

Exposure time	Phases Identified (Intensity/Parameter A)					
	Austenite	Cr_2O_3	M_3O_4		M_{23}C_6	SiO_2
100 hours	214/3.589	-	6/8.467	6/8.467	-	-
5000 hours	231/3.587	3/4.973-13.506	7/8.447	-	6/10.632	traces

Table 4.13

X-ray diffraction data for AISI 314 exposed to the sulphur-free environment at 800°C ($p\text{O}_2 = 10^{-21}$ bar, $a_c = 0.3$). 180 grit condition.

Exposure time	Phases Identified (Intensity/Parameter A)					
	Austenite	Cr_2O_3	M_3O_4	M_3S_4	M_{23}C_6	SiO_2
1 hour	198/3.592	1/4.953-13.615	4/8.440	-	3/10.568	-
5 hours	158/3.578	4/4.962-13.577	8/8.440	-	3/10.625	-
100 hours	161/3.587	5/4.970-13.574	10/8.475	-	-	-
2000 hours	187/3.586	-	17/8.491	-	-	-

Table 4.14

X-ray diffraction data for AISI exposed to the sulphur-free environment at 800°C ($p\text{O}_2 = 10^{-21}$ bar, $a_c = 0.3$). Electropolished (EP) condition.

Exposure time	Phases Identified (Intensity/Parameter A)					
	Austenite	Cr_2O_3	M_3O_4	M_3S_4	M_{23}C_6	SiO_2
1 hour	137/3.582	6/4.953-13.612	14/8.408	-	-	-
5 hours	32/3.582	-	22/8.400	10/9.995	-	-
1000 hours*	127/3.582	18/4.960-13.953	8/8.441	-	-	-
5000 hours	-	5/4.956-13.587	39/8.395	2/9.953	-	-

* internal layer (external layer removed prior to examination)

Table 4.15

X-ray diffraction data for AISI 314 exposed to the 0.2 % H_2S environment at 800°C ($p\text{O}_2 = 10^{-21}$ bar, $p\text{S}_2 = 10^{-9}$ bar, $a_c = 0.3$). 180 grit condition.

Exposure time	Phases Identified (Intensity/Parameter A)					
	Austenite	Cr_2O_3	M_3O_4	M_3S_4	M_{23}C_6	SiO_2
100 hours	48/3.583	23/4.955-13.589	28/8.393	-	-	-
2000 hours	-	5/4.960-13.610	38/8.406	-	-	-

Table 4.16

X-ray diffraction data for AISI 314 exposed to the 0.2 % H_2S environment at 800°C ($p\text{O}_2 = 10^{-21}$ bar, $p\text{S}_2 = 10^{-9}$ bar, $a_c = 0.3$). Electropolished (EP) condition.

AISI 314 Phase Stability

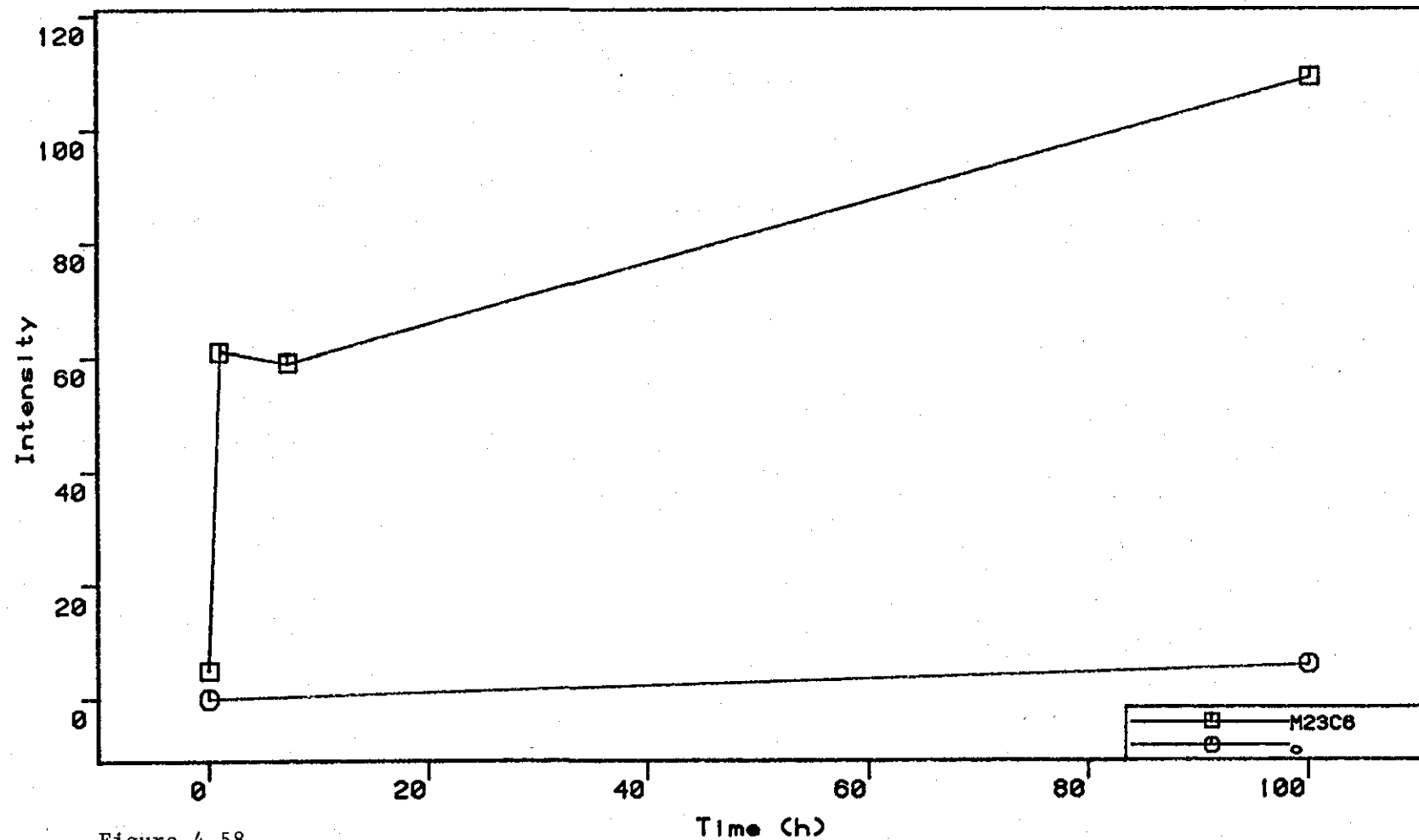


Figure 4.58

Plots of the X-ray diffraction peak intensity of the phases extracted from AISI 314 against annealing time in argon at 800°C.

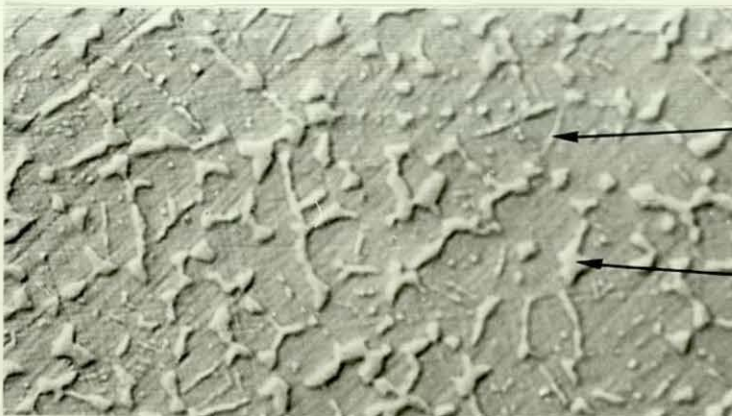
AISI 314 Aging at 800 deg. C



a)

100 hours

20 μ m



b)

2000 hours

20 μ m

Figure 4.59

Cross-sectional metallographic examination using interference contrast to show changes in the microstructure of AISI 314 which result from aging processes at 800°C.

AISI314, P02=10-21, $\alpha C=0.3$, 800degC

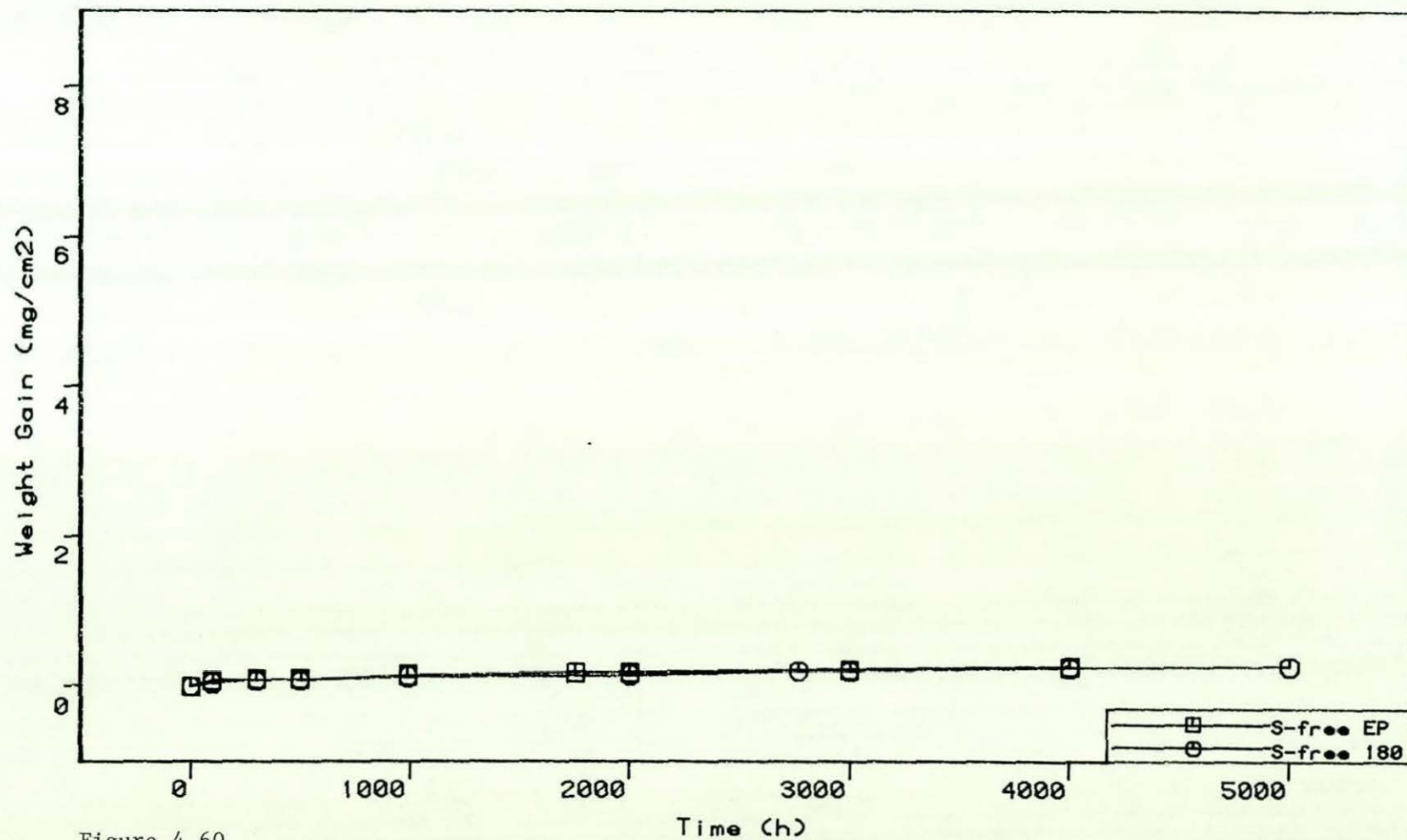


Figure 4.60

Kinetic data for AISI 314 exposed to the sulphur-free gas at 800°C.

S-free gas, $P_{O_2}=10-21\text{bar}$, $a_C=0.3$, 800°C

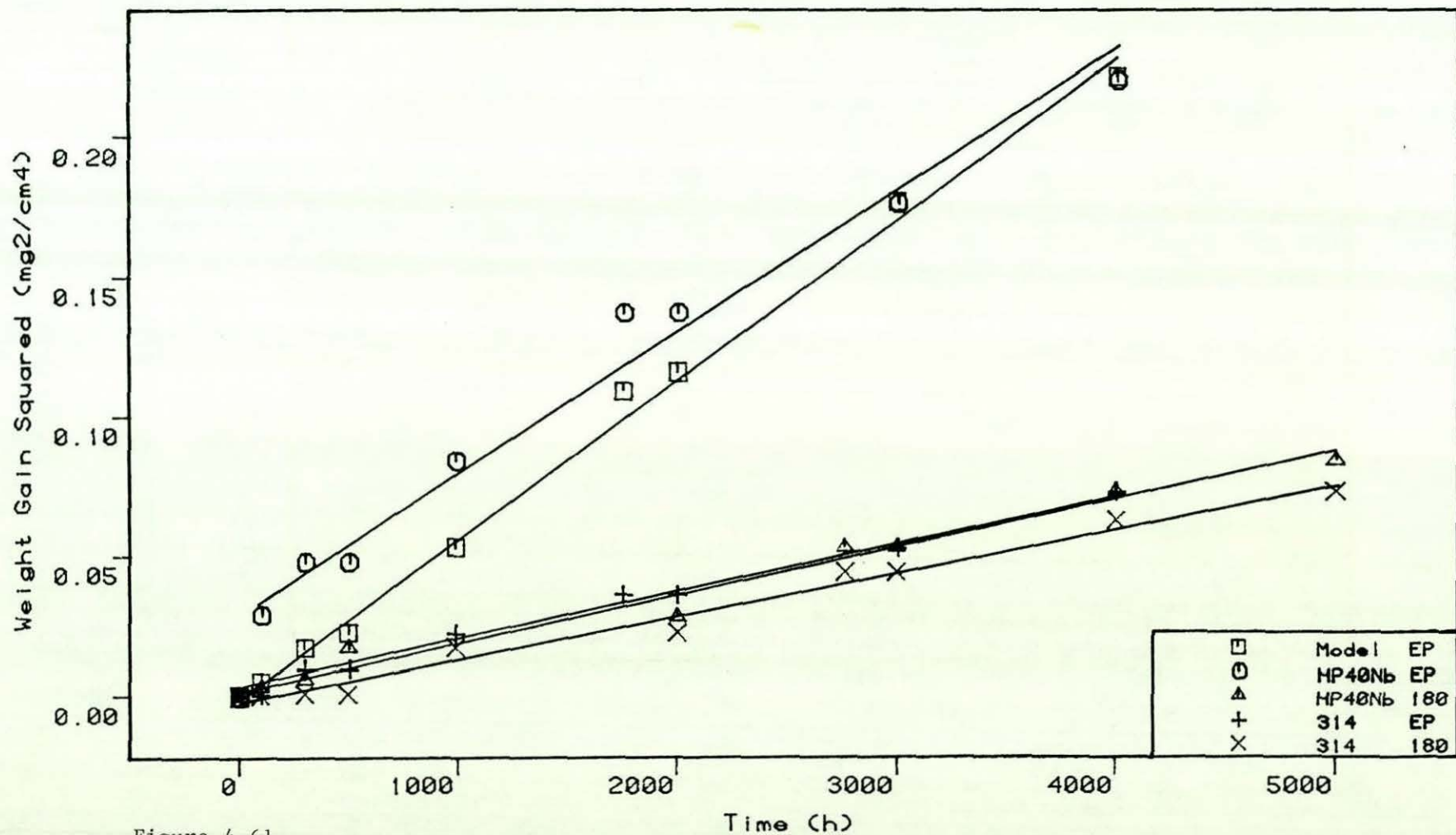


Figure 4.61

Plots of weight gain squared against time, which compare the corrosion behaviour of AISI 314 with the Model 25Cr-35Ni-Fe alloy and HP40Nb in the sulphur-free gas at 800°C .

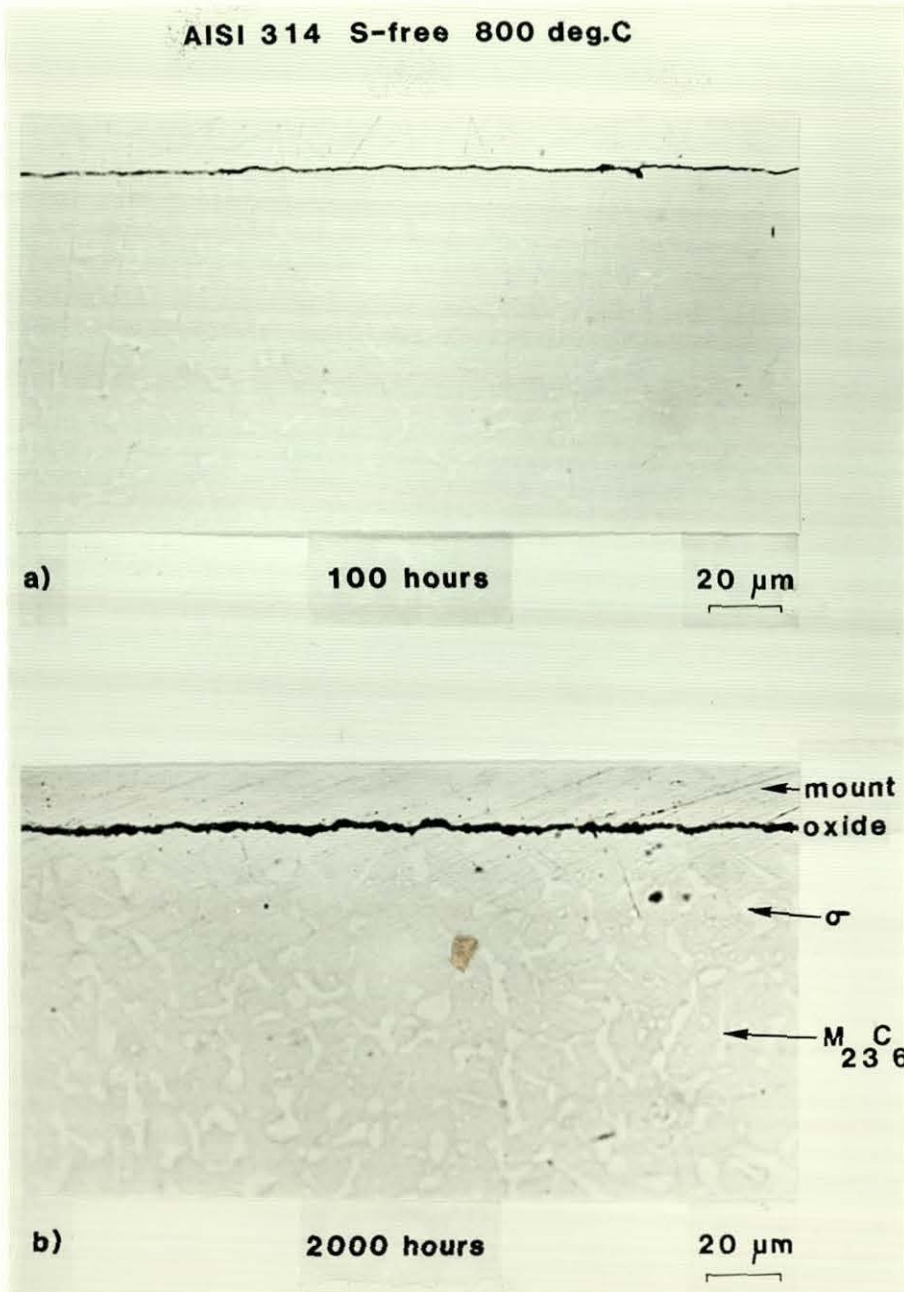


Figure 4.62

Cross-sectional metallographic examination of AISI 314 exposed to the sulphur-free gas at 800°C.

AISI 314, Oxide Spinel Lattice Parameters

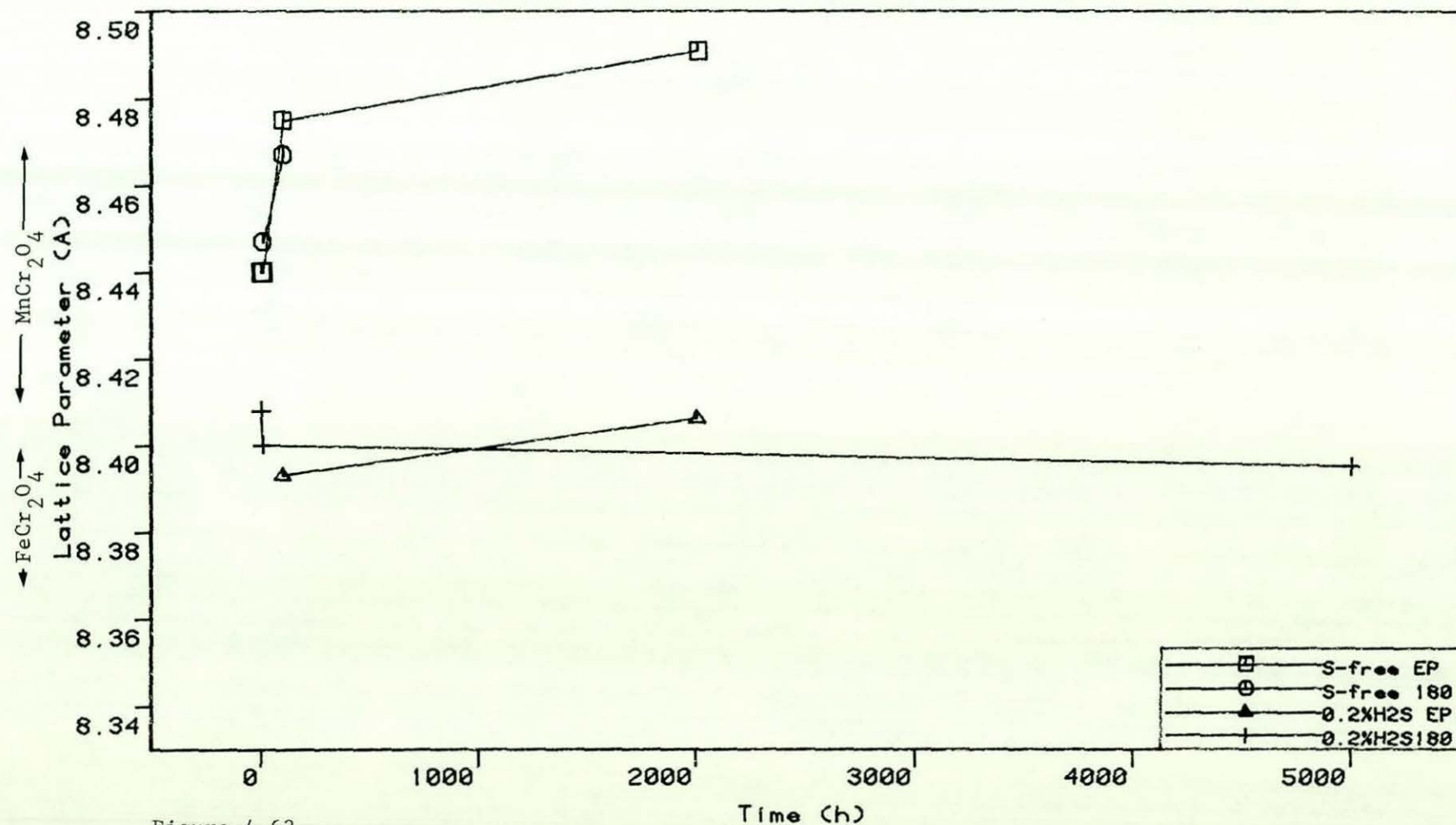


Figure 4.63

Plots of oxide spinel lattice parameter against time for the scale formed on AISI 314 exposed to the sulphur-free and 0.2% H₂S gases at 800°C.

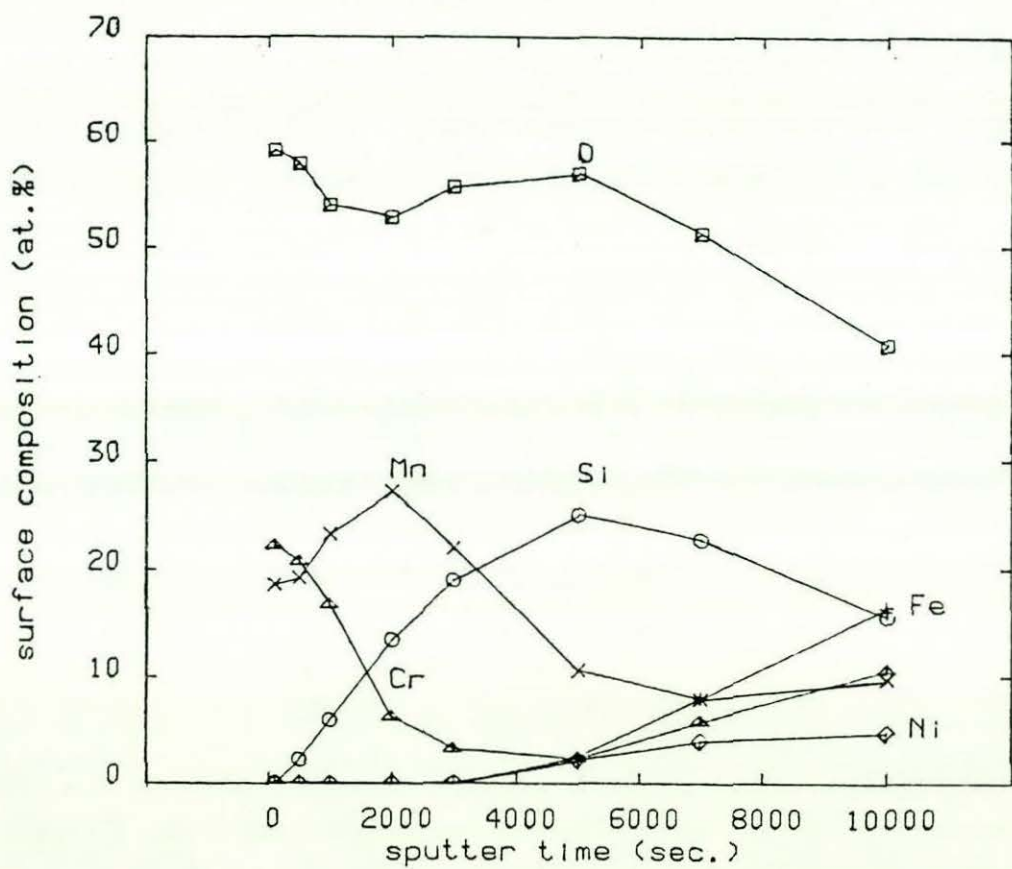


Figure 4.64

ESCA-AUGER analysis of the scale formed on AISI 314 exposed to the sulphur-free gas at 800°C for 2000 hours (surface worked '180 grit' condition).

AISI 314, Chromia Lattice Parameters

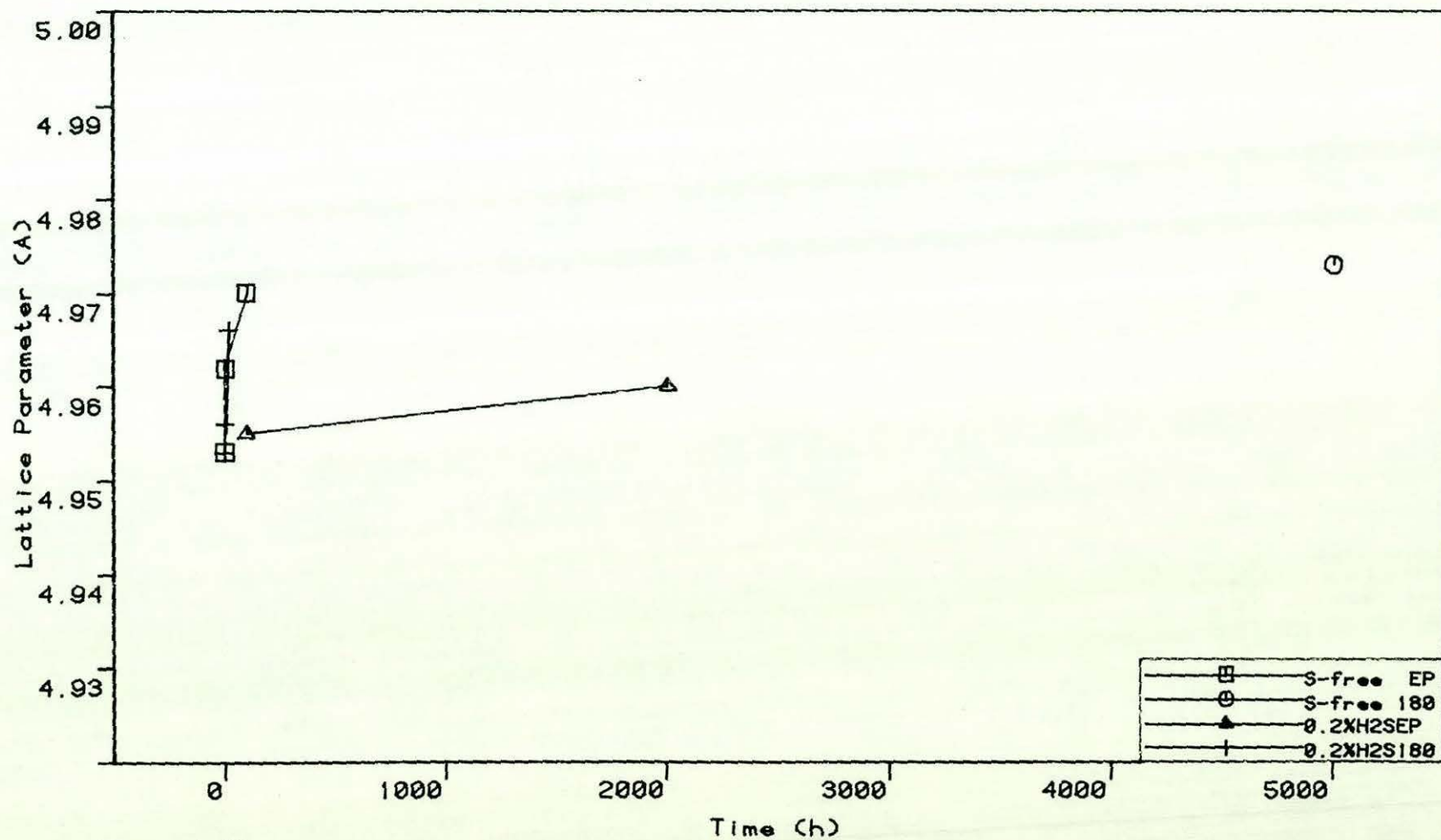


Figure 4.65

Plots of Cr_2O_3 lattice parameter against time for the scale formed on AISI 314 exposed to the sulphur-free and 0.2% H_2S gases at 800°C.

AISI314, PO2=10-21, $\alpha C=0.3$, 800degC

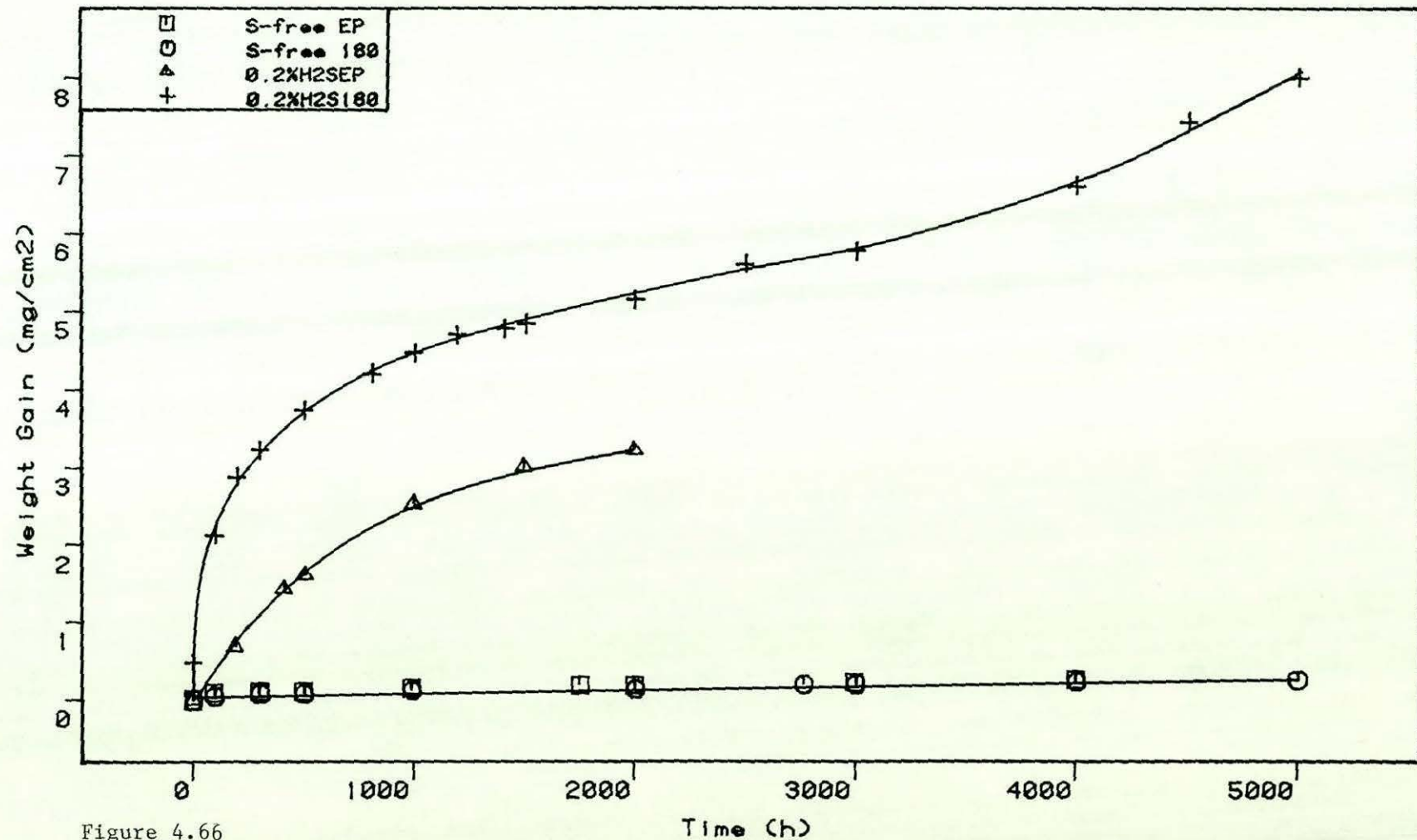


Figure 4.66

Kinetic data for AISI 314 exposed to the sulphur-free and 0.2% H₂S gases at 800°C.

0.2% H₂S, 800degC

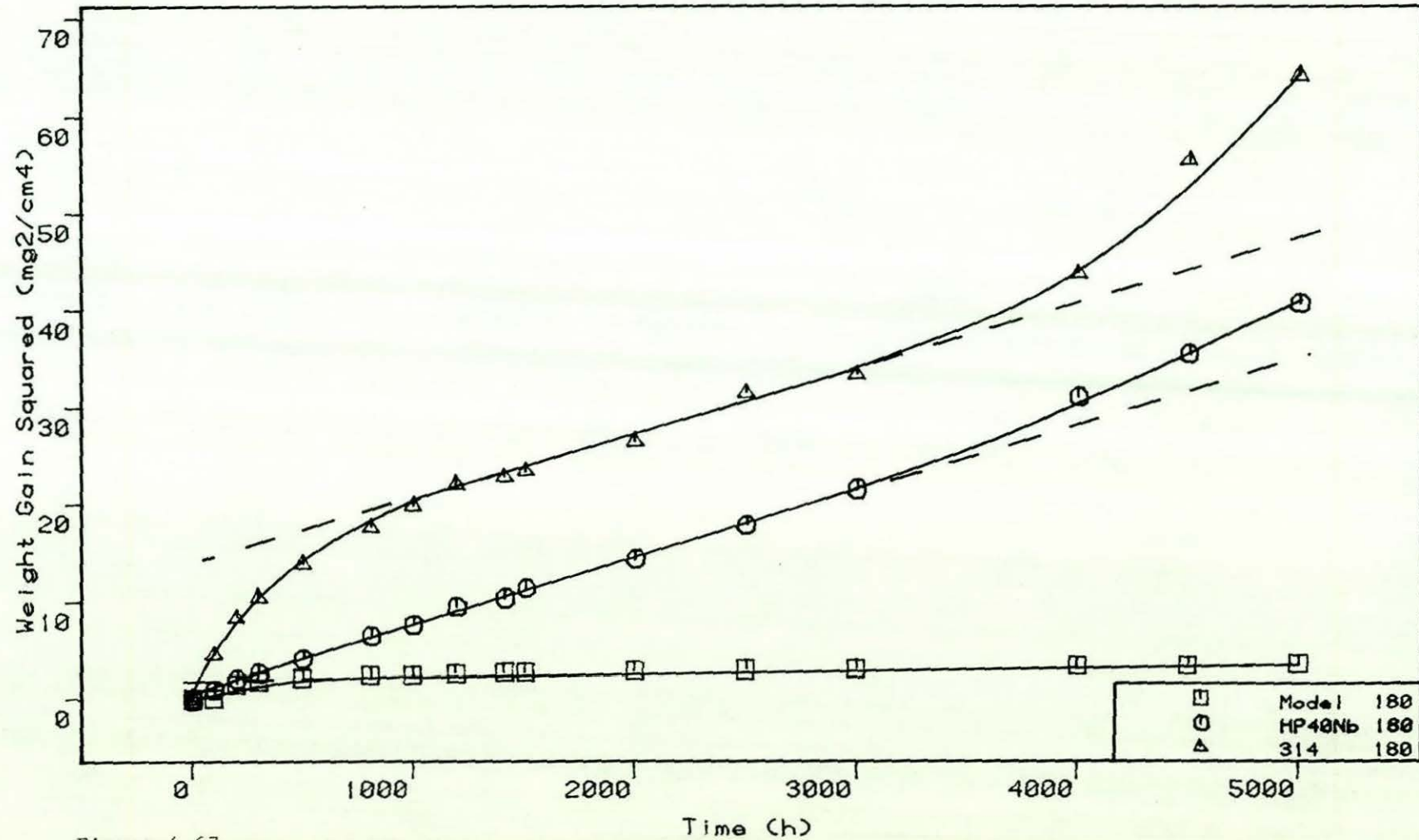


Figure 4.67

Plots of weight gain squared against time, which compare the corrosion behaviour of AISI 314 with the Model 25Cr-35Ni-Fe alloy and HP40Nb in the 0.2% H₂S gas at 800°C. (180 grit condition).

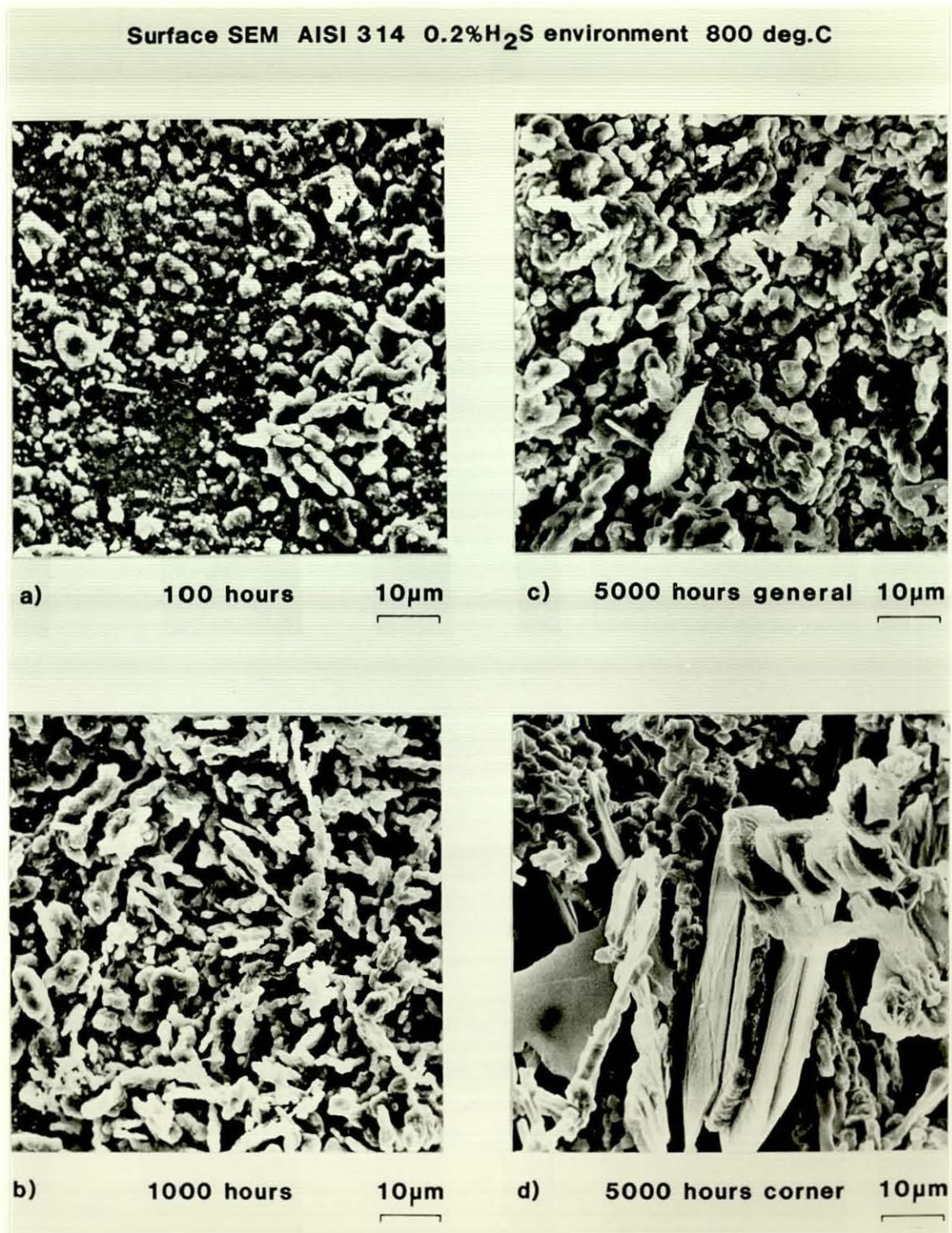


Figure 4.68

Surface SEM examination of AISI 314 exposed to the 0.2 % H_2S gas at 800°C, 180 grit condition.

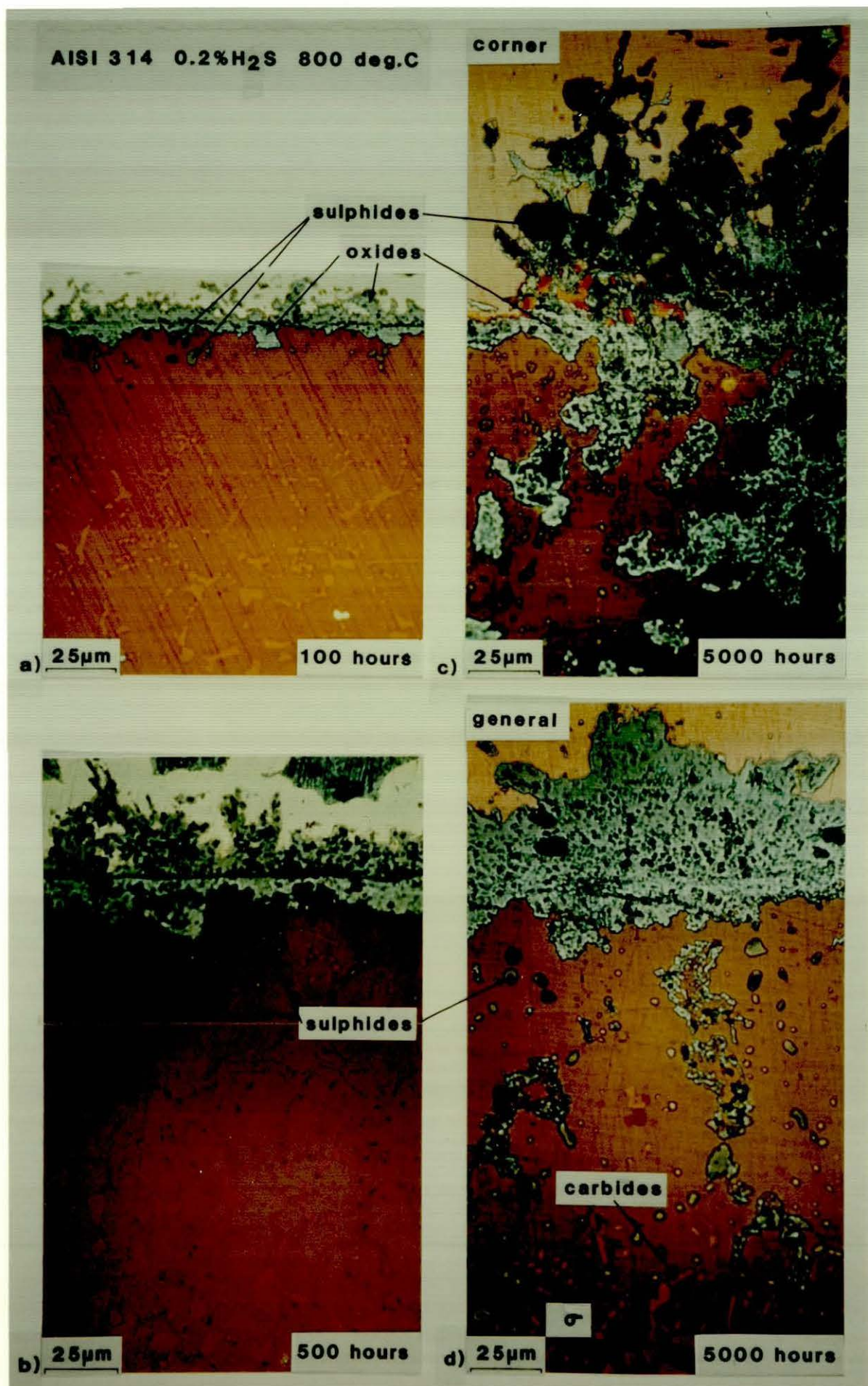


Figure 4.69
Cross-sectional examination using the Pepperhoff technique for AISI 314
exposed to the 0.2 % H_2S environment at 800°C, 180 grit condition.

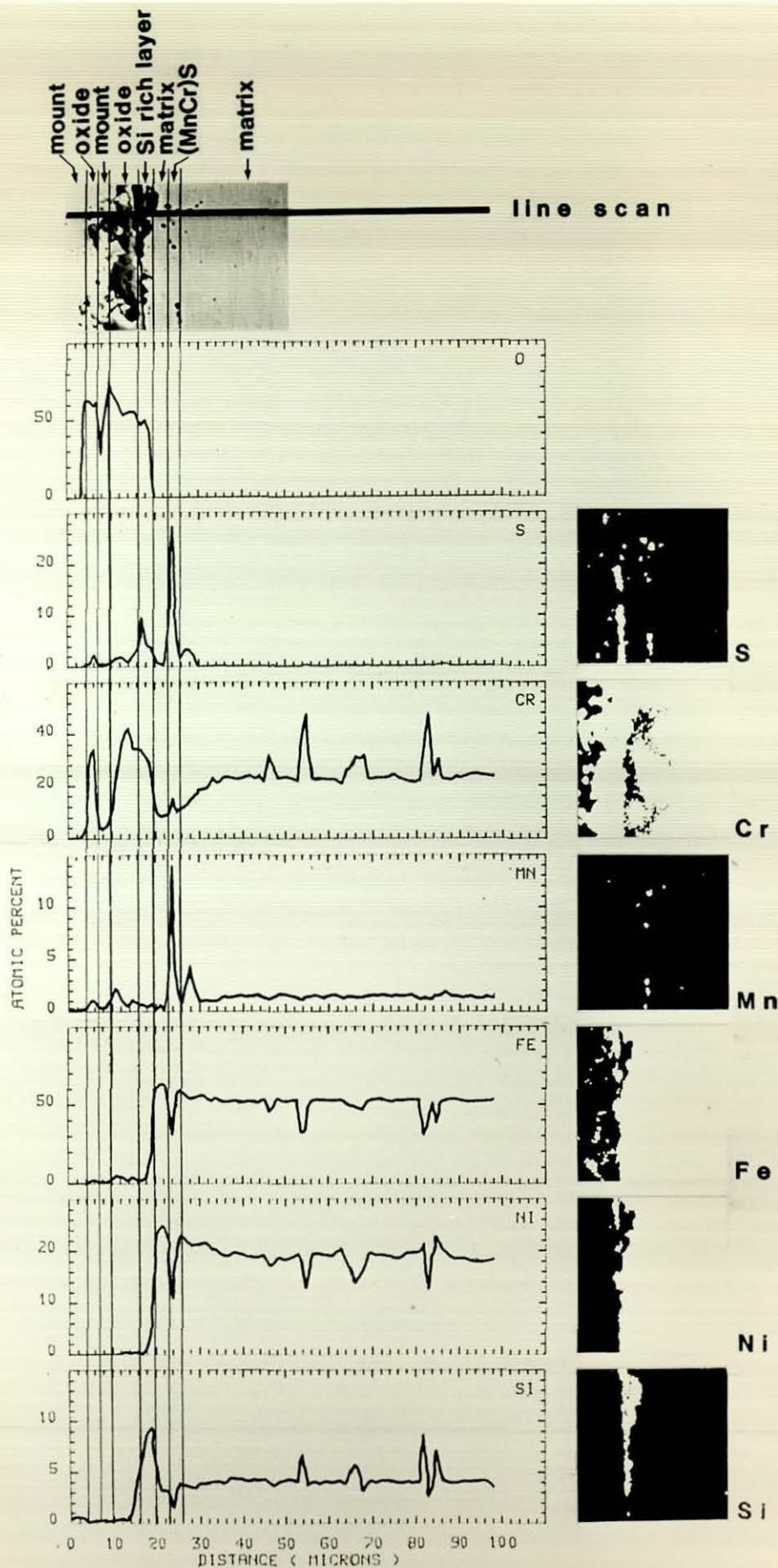


Figure 4.70

EPMA line scan and elemental concentration maps on AISI 314 exposed for 100 hours to the 0.2 % H_2S environment at 800°C, 180 grit condition.

AISI 314 180 , 0.2% H_2S , 800 deg.C 1000 hours

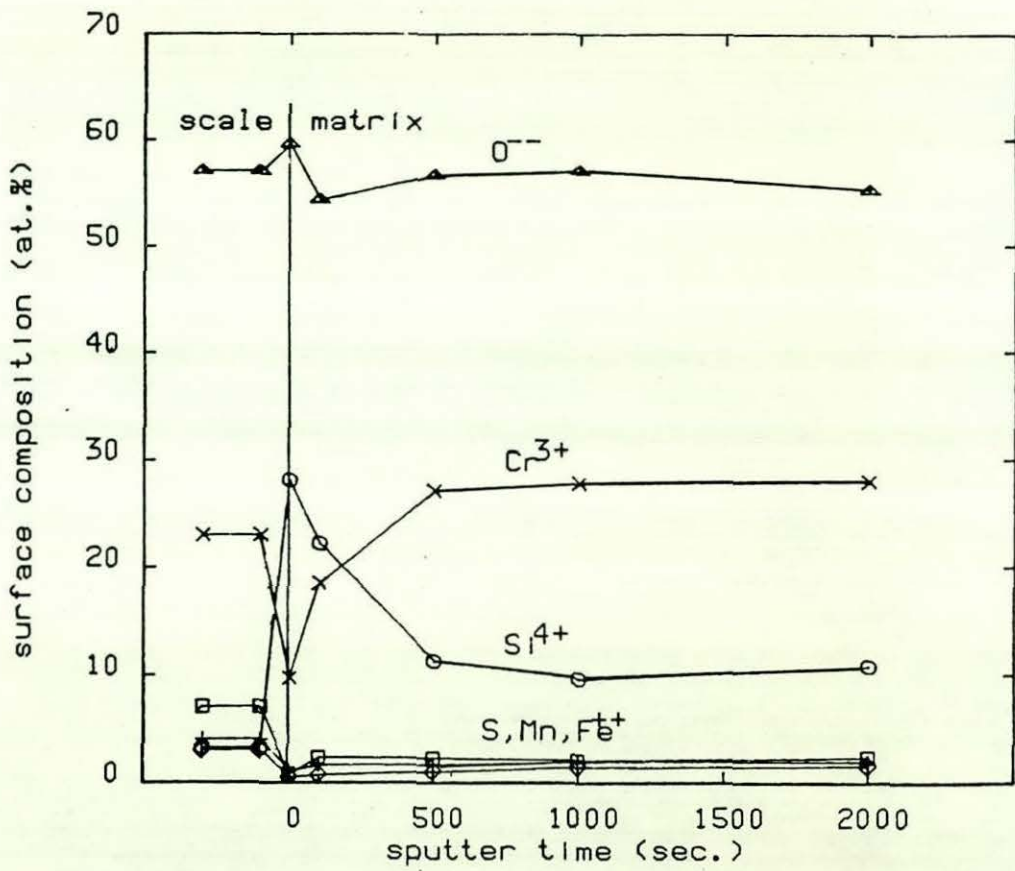


Figure 4.71

ESCA-AUGER analysis of the outer and inner layers of scale formed on AISI 314 exposed to the 0.2 % H_2S gas at 800°C for 1000 hours, 180 grit condition.

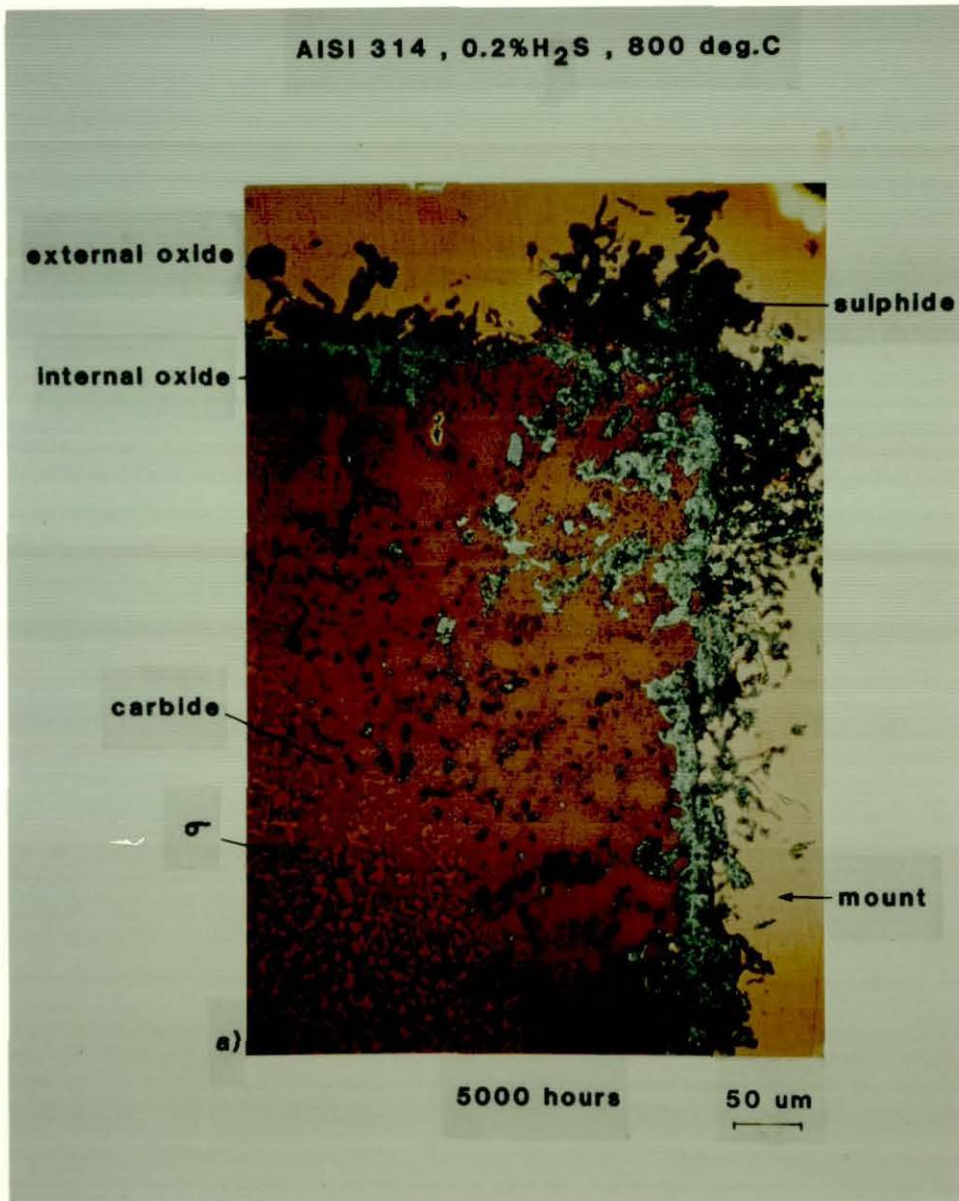


Figure 4.72

Cross-sectional examination using the Pepperhoff technique for AISI 314, exposed to the 0.2 % H_2S at 800°C for 5000 hours, 180 grit condition.

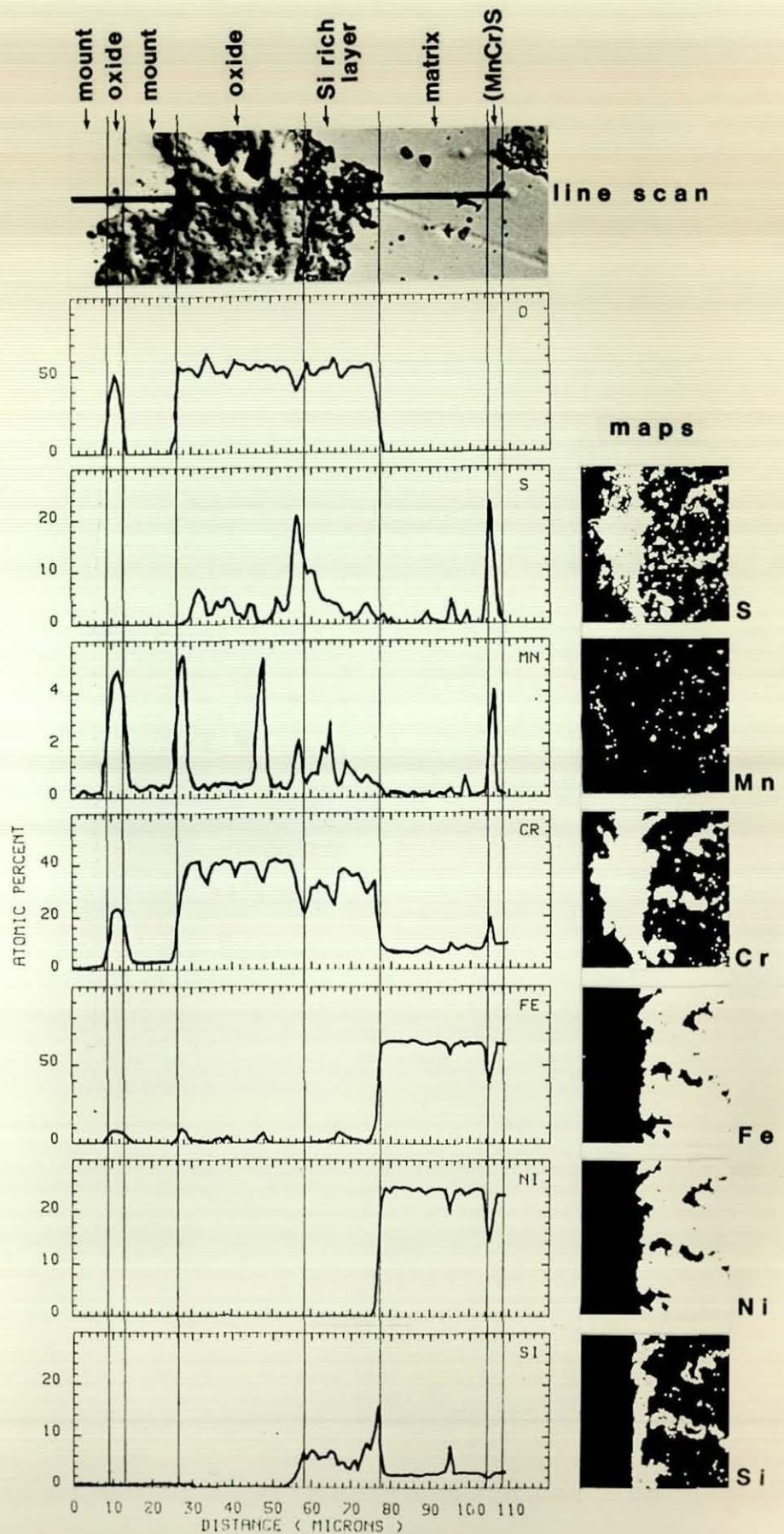


Figure 4.73

EPMA line-scan and elemental maps on AISI 314, exposed for 5000 hours to the 0.2 % H_2S environment at 800°C, 180 grit condition.

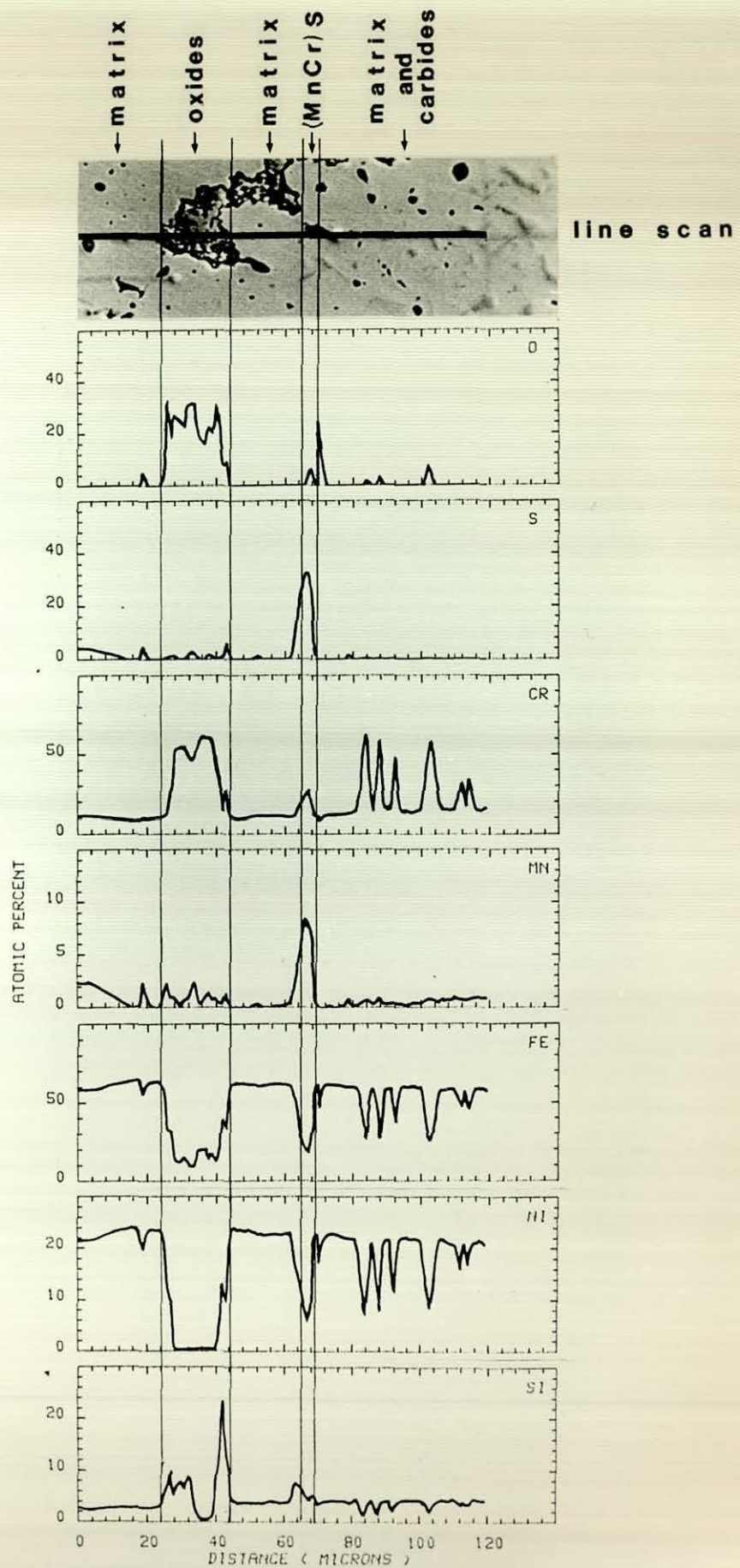
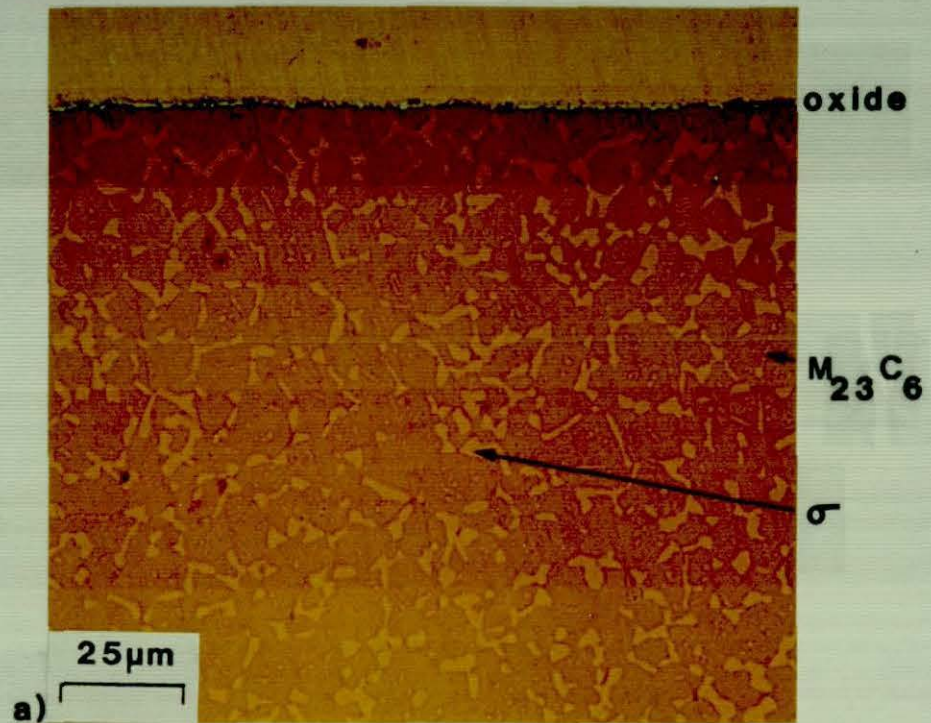
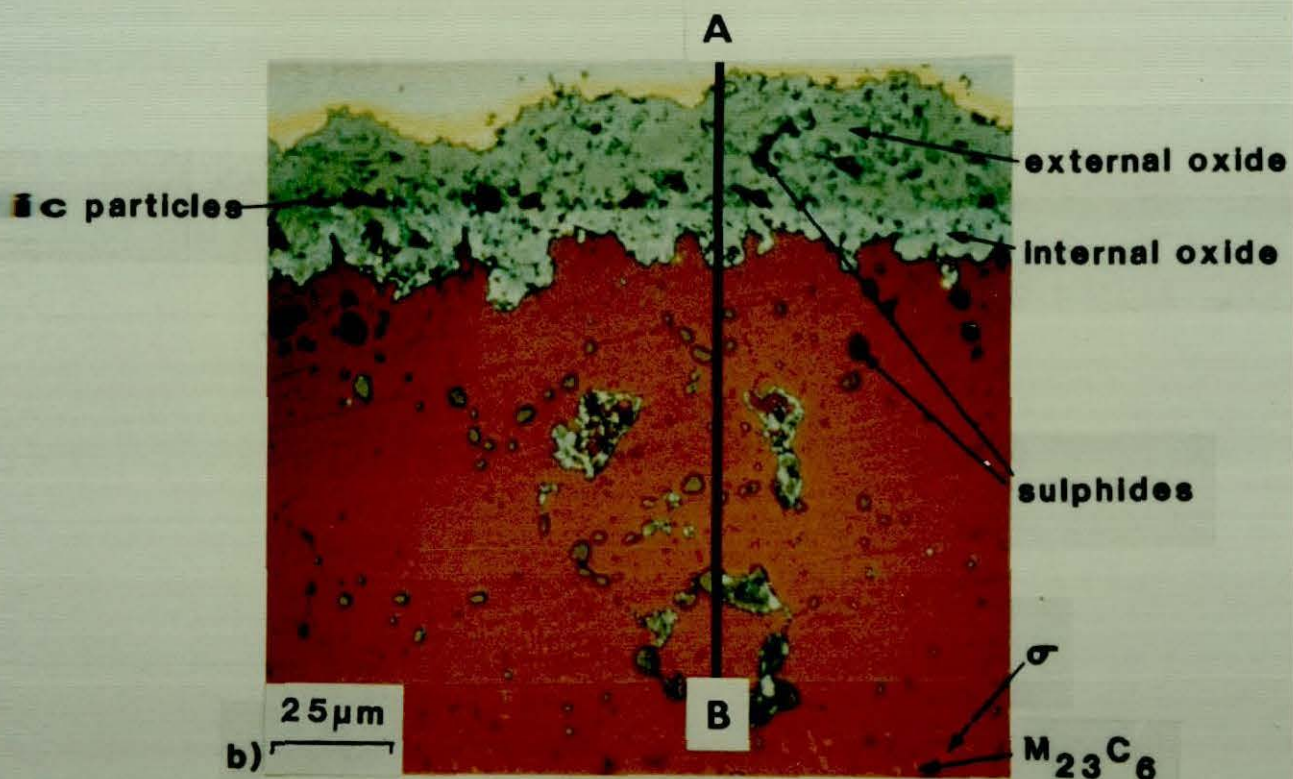


Figure 4.74
Continuation of the line scan shown in Figure 4.73.

AISI 314 800 deg.C 2000 hours



S-free



0.2% H_2S

Figure 4.75

Cross-sectional examination using the Pepperhoff technique to compare the corrosion behaviour of AISI 314 exposed in; (a) the S-free gas and (b) the 0.2 % H_2S gas, for 2000 hours at 800°C, electropolished condition.

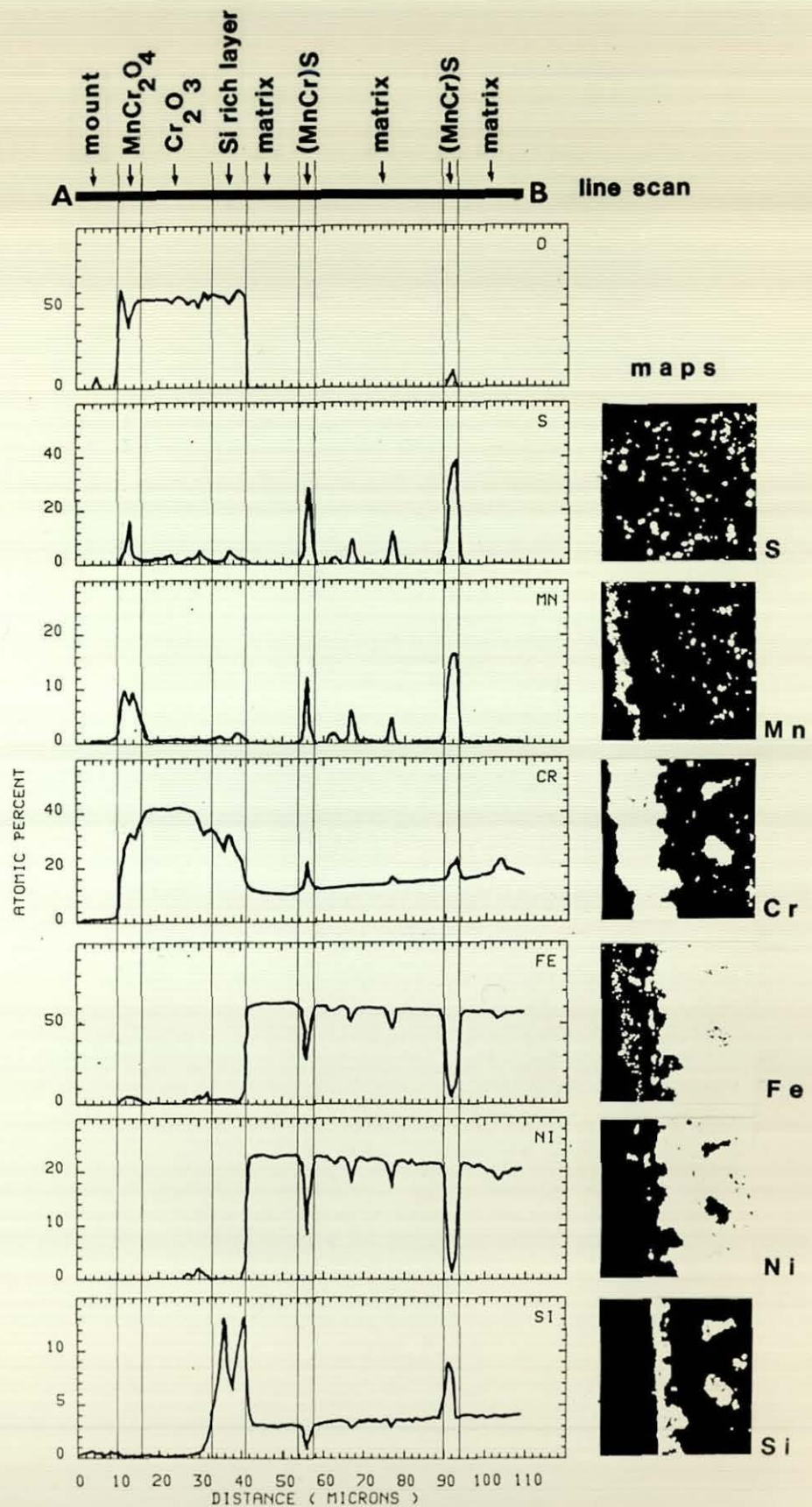
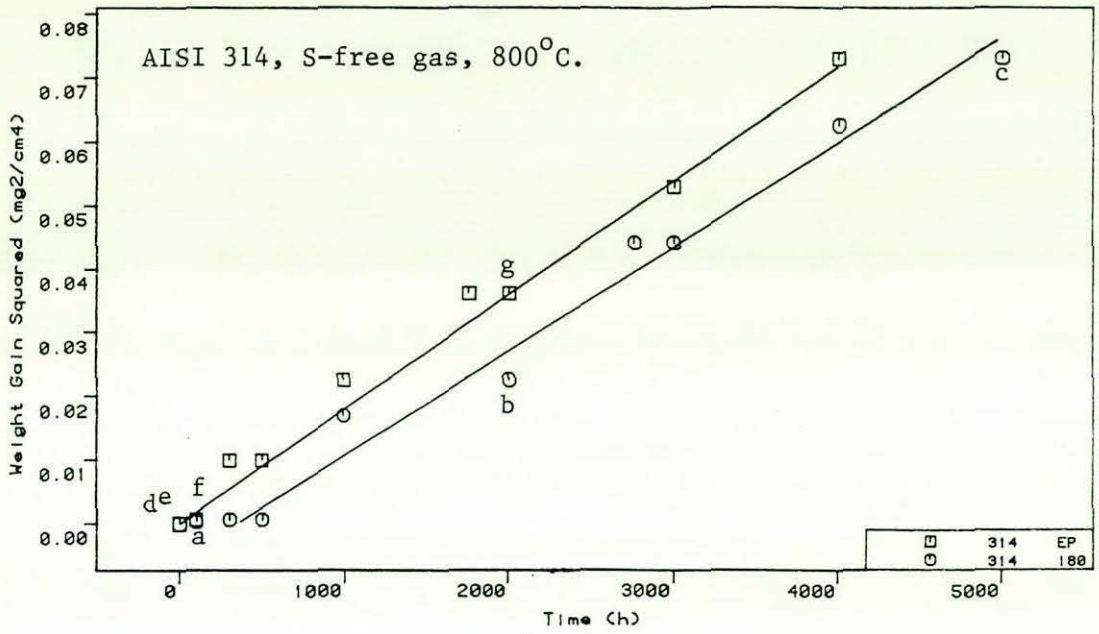


Figure 4.76

EPMA line scan, corresponding to line AB on Figure 4.75b, and elemental concentration maps on AISI 314 exposed for 2000 hours to the 0.2 % H_2S gas at 800°C, electropolished condition.



180

EP

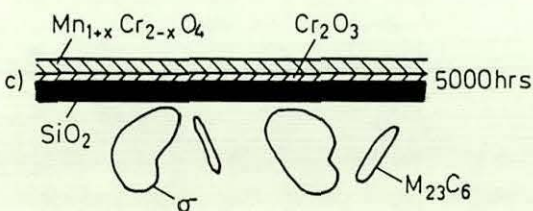
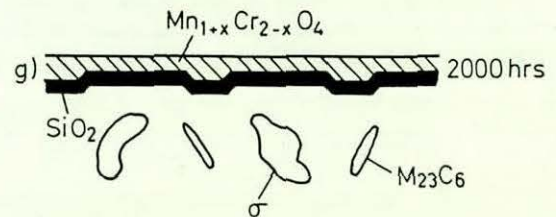
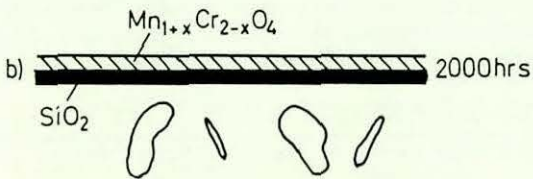
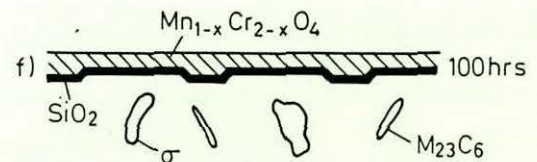
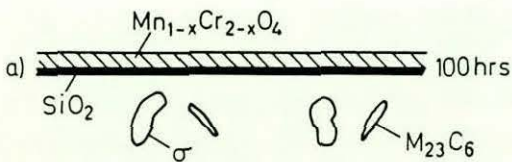
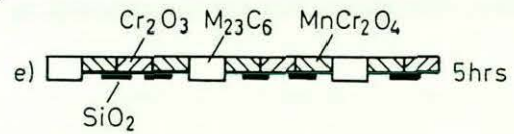
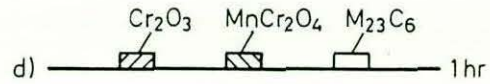


Figure 4.77

Schematic diagram summarising the corrosion behaviour of AISI 314 in the sulphur-free gas at 800°C.

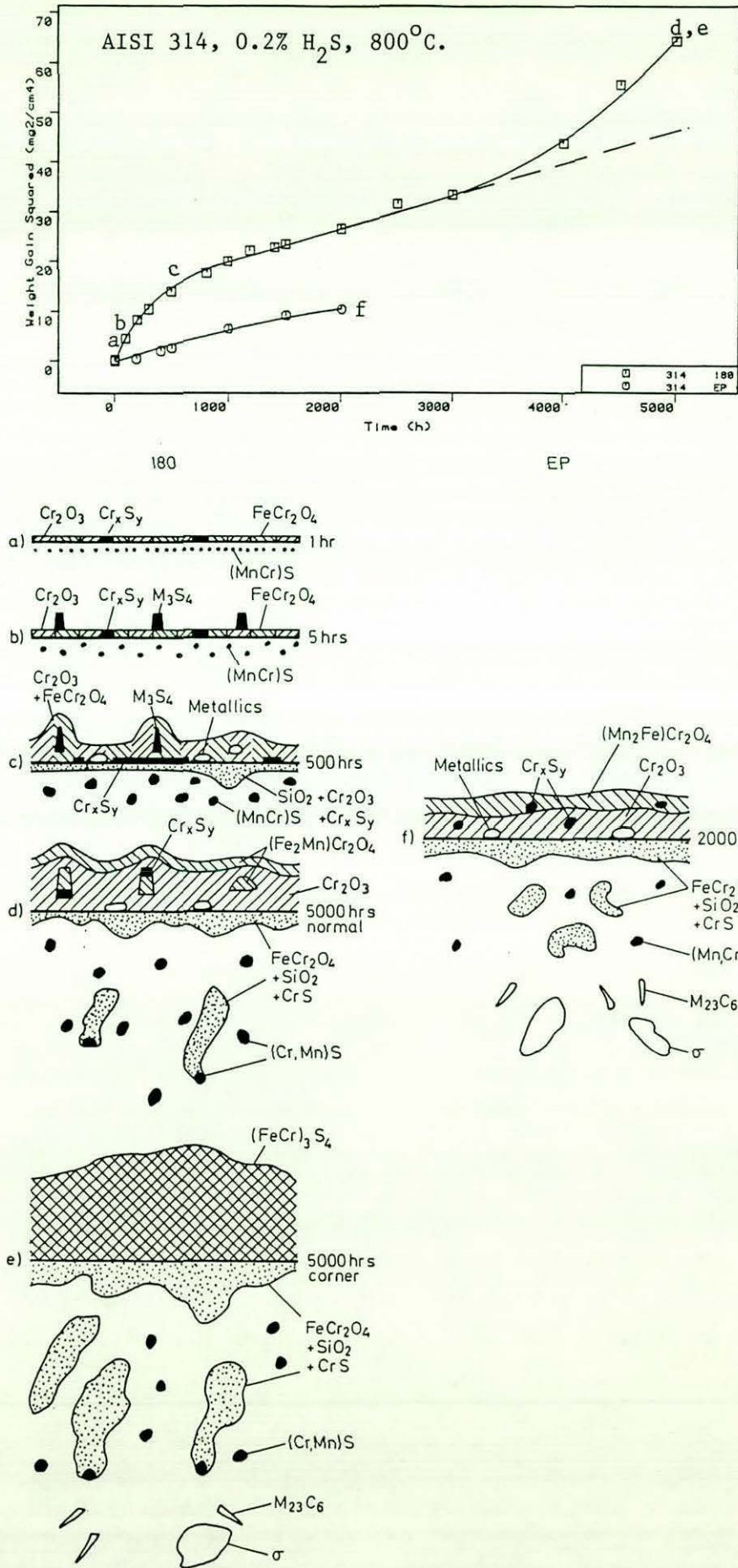


Figure 4.78

Schematic diagram summarising the corrosion behaviour of AISI 314 in the 0.2 % H₂S gas at 800°C.

4.1.4. HP40A1

This alloy is essentially the HP40Nb alloy with a 3.49 % Al addition. The alloy was supplied as centrifugally cast tube and contained a large number of indigenous carbide precipitates.

To establish any microstructural changes resulting from aging processes, examinations were carried out on the as received material and on specimens annealed in argon at 800°C for 1 hour, 7.25 hours, 100 hours, 2000 hours and 5000 hours.

As-received

Cross-sectional examination using the Pepperhoff technique showed that the alloy contained three primary carbides : M_7C_3 , MC, M_6C and an intermetallic compound NiAl, figure 4.79a. The carbides were electrolytically extracted for one hour and subsequently analysed by X-ray diffraction, which confirmed that they were M_7C_3 , MC, M_6C , figure 4.80.

1 hour

Cross-sectional examination using the Pepperhoff technique revealed that a large number of very small secondary carbide precipitates had formed in the alloy substrate, figure 4.79b. These tended to be concentrated around the primary carbides. At this stage these secondary carbides were too small to be identified by metallographic techniques. Electrolytic extraction for 1 hour followed by X-ray diffraction analysis indicated that the intensity of the primary M_7C_3 and MC precipitates had decreased, figure 4.80.

7.25 hours

Carbide extraction and subsequent X-ray diffraction analysis indicated that the intensity of both the $M_{23}C_6$ and M_6C carbides had increased significantly. This appeared to coincide with a drop in the intensity of M_7C_3 . The intensity of the MC carbides now remained relatively unchanged, figure 4.80.

100 hours
.....

Cross-sectional examination using the Pepperhoff technique showed that the primary M_7C_3 carbides appeared to have almost totally transformed to $M_{23}C_6$ with just a few traces of M_7C_3 remaining at the centre of the precipitates, figure 4.79c. The primary MC and M_6C carbide precipitates and the intermetallic compound NiAl appeared to be unchanged. The secondary $M_{23}C_6$ and M_6C carbide precipitates had grown and were now evenly distributed throughout the alloy substrate. Electrolytic extraction of the carbides followed by X-ray diffraction analysis confirmed that the primary M_7C_3 carbides had transformed to $M_{23}C_6$ with the carbon released in the process forming secondary $M_{23}C_6$ and M_6C precipitates.

2000 hours
.....

Cross-sectional examination using the Pepperhoff technique showed that the primary carbides were unchanged, figure 4.79d. The secondary $M_{23}C_6$ and M_6C carbides had grown larger but were fewer in number.

5000 hours
.....

A similar microstructure was present after 5000 hours, figure 4.79e. The secondary $M_{23}C_6$ and M_6C precipitates had continued to coarsen.

Thus in summary, the alloy in the as-received condition contained M_7C_3 , MC and M_6C primary carbide precipitates and an NiAl intermetallic phase. As time progressed at 800°C, the primary M_7C_3 precipitates transformed to $M_{23}C_6$. The carbon released in the process led to the formation of a large number of secondary $M_{23}C_6$ and M_6C carbides in the alloy substrate. These subsequently grew and became fewer in number. The aging process, although similar to the HP40Nb alloy was much more pronounced, with dramatic changes occurring to the alloy structure in a very short time.

a) Sulphur-gas free

Kinetic data for the electropolished (EP) and 180 grit (180) surface finishes are presented in figure 4.81. The curves for both surface finishes were very similar, with the weight uptake of the 180 grit material slightly higher than the EP material.

Electropolished condition

Replotting the kinetic data as weight gain squared against time, figure 4.82, showed that the kinetics did not become parabolic until after 1000 hours exposure. The rate constant for the parabolic range (1000-5000 hours) is given in table 4.17. The corrosion rate was also considerably higher than for the Model 25Cr-35Ni alloy and HP40Nb, figure 4.82.

To obtain the reasons for this examinations were carried out after 1 hour, 5 hours, 100 hours and 2000 hours.

1 hour

X-ray diffraction analysis using surface reflection detected M_3O_4 , Cr_2O_3 and $M_{23}C_6$ on the alloy surface, table 4.17. The NiAl peaks were assumed to have originated from precipitates within the alloy substrate. The lattice parameter of the oxide spinel indicated that it was $FeCr_2O_4$, figure 4.83. The lattice parameter of Cr_2O_3 corresponded to that of pure Cr_2O_3 , figure 4.84.

5 hours

X-ray diffraction analysis using surface reflection again detected M_3O_4 , Cr_2O_3 and $M_{23}C_6$, table 4.18. The intensity of M_3O_4 had increased relative to the other phases. The lattice parameter of the M_3O_4 spinel had also increased, indicating that Mn was starting to be incorporated into the oxide scale, figure 4.83. The lattice parameter of Cr_2O_3 was similar to before, figure 4.84.

100 hours

After 100 hours X-ray diffraction analysis indicated that the oxide scale consisted of M_3O_4 and Cr_2O_3 , table 4.18. Again the spinel lattice parameter had increased indicating that it now had the composition Mn Cr_2O_4 , figure 4.83. The lattice parameter of the Cr_2O_3 phase remained the same, figure 4.84. The M_7C_3 and $M_{23}C_6$ peaks were attributed to precipitates within the alloy.

2000 hours
.....

Cross-sectional analysis using the Pepperhoff technique showed that the corrosion morphology consisted of an outer oxide layer (2-5 μm thick) and a zone of internal attack (13 μm deep), figure 4.85f.

An EPMA line scan showed that the oxide layer consisted of predominantly MnCr_2O_4 , figure 4.88. X-ray diffraction using surface reflection also confirmed that this layer was MnCr_2O_4 , with small amounts of Cr_2O_3 also detected, table 4.18. The lattice parameter of the oxide spinel indicated that it was very rich in Mn. Again the Cr_2O_3 parameter corresponded to that of pure Cr_2O_3 . Surface SEM analysis showed that some localized thickening of the oxide was occurring where the indigenous carbides were in the vicinity of the surface. In general however, the oxide layer was thicker than on the Model 25Cr-35Ni-Fe alloy and HP40Nb, which are included in figure 4.85 for comparison purposes.

The main point of interest however was the zone of internal attack. This contained a large number of discontinuous lenticular shaped particles. An EPMA line scan and X-ray mapping indicated that these particles were a mixture of Al_2O_3 and NiNbSi rich MC carbides, figure 4.87. A few NiAl intermetallic particles were also present in this region. Due to its discontinuity this zone was obviously offering little additional protection.

In summary the addition of 3.5 % Al did not result in the formation of a continuous Al_2O_3 layer. Instead a zone of internal attack formed which contained a large number of discontinuous Al_2O_3 particles, some NiNbSi rich MC carbides and some metallic NiAl particles. The development of the outer oxide layer was similar to that of the HP40Nb alloy.

180 grit condition

The kinetic data showed that the weight uptake was slightly higher than on the electropolished material, figure 4.81. Replotting the kinetic data as weight gain squared against time showed that the kinetic rate progressively slowed down but never became parabolic, figure 4.87. Examinations were carried out after 100 hours and 5000 hours.

100 hours
.....

Cross-sectional examination (although not shown) revealed that a very thin (1 μm thick) oxide scale had formed on the alloy surface. More importantly a (5 μm deep) zone of internal oxidation was visible, which contained isolated Al_2O_3 and SiO_2 particles. X-ray diffraction analysis using surface reflection indicated that the oxide scale was M_3O_4 spinel, table 4.19. The lattice parameter of this phase was very small. The M_{23}C_6 and MC peaks were assumed to have come from precipitates within the alloy.

5000 hours
.....

X-ray diffraction analysis using surface reflection now indicated that the oxide scale consisted of predominantly M_3O_4 with some Cr_2O_3 also present, table 4.19. The lattice parameter of the oxide spinel indicated that it was very rich in Mn, figure 4.83. The Cr_2O_3 lattice parameter corresponded to that of pure Cr_2O_3 , figure 4.84.

In summary the limited amount of analysis carried out, indicated that the corrosion process was very similar to the electropolished material. A zone of internal oxidation containing isolated particles rich in Al offered no addition protection.

b. 0.2 % H_2S gas

Kinetic data for the HP40Al alloy in both surface finishes is presented in figure 4.88. The weight uptake of the electropolished material was slightly higher than the 180 grit material.

Electropolished (EP) material

The kinetic data are replotted as weight gain squared against time in figure 4.89. This shows that after the initial high weight uptake the corrosion rate progressively slowed down until becoming parabolic after approximately 1000 hours. The rate remained parabolic upto approximately 3000 hours exposure where a significant upturn in the corrosion curve took place. The rate constant for the parabolic region (1000-3000 hours) is given in table 4.17.

To understand the reasons for this examinations were carried out after 5 mins, 2000 hours and 5000 hours.

5 mins
.....

X-ray diffraction using surface reflection detected only M_3O_4 spinel and $M_{23}C_6$ on the alloy surface, table 4.20. The lattice parameter indicated that the spinel was $FeCr_2O_4$, figure 4.83. The NiAl signal was assumed to have come from particles of this phase within the alloy.

2000 hours
.....

Cross-sectional examination using the Pepperhoff technique showed that the corrosion morphology consisted of an uneven oxide scale and a zone of internal attack, figure 4.90.

An EPMA line scan EF showed that the oxide scale consisted of two layers, figure 4.91. The outer layer (20 μm thick) was rich in Mn and Cr and the inner layer rich in Cr. Both layers of the scale contained a significant amount of sulphur.

The zone of internal attack (70 μm deep) consisted of discontinuous islands of oxide particles which appeared to contain small quantities of sulphides, figure 4.90b. The position of the oxide islands appeared to have been determined by the indigenous primary carbides precipitates in the alloy. These carbide precipitates had behaved in different ways. The $M_{23}C_6$ precipitates had transformed to predominantly oxides, although some sulphides were present particularly at the deepest point of the corrosion attack. Sulphides had nucleated on the MC carbides, but these carbides had suffered little attack. The M_6C carbides had converted primarily to sulphides. The intermetallic NiAl particles had not been attacked. Sulphide precipitates were also present in the depleted alloy substrate. No secondary carbide precipitates were visible in this region.

The EPMA line scan EF indicated that the islands of oxide in the zone of internal attack were rich in Al and Si and Cr, figure 4.91. The alloy substrate between the oxide islands contained very low levels of Cr (5-10 %).

5000 hours
.....

Cross-sectional examination using the Pepperhoff technique showed that the corrosion morphology still consisted of an oxide scale and a zone of internal attack, figure 4.90c.

An EPMA line scan CD showed that the oxide scale (20-30 μm thick) consisted of the outer MnCr_2O_4 spinel layer (which also contained small amounts of Fe) and the inner Cr_2O_3 layer, figure 4.92. X-ray diffraction analysis using surface reflection confirmed the presence of both M_3O_4 and Cr_2O_3 , table 4.20, with the lattice parameter of the spinel indicating that it contained Cr, Mn and Fe. The Cr_2O_3 lattice parameter corresponded to that of pure Cr_2O_3 . Both cross-sectional analysis using the Pepperhoff technique and X-ray mapping showed that both these layers contained a few small sulphide particles.

The depth of the zone of internal oxidation attack had increased dramatically (170 μm). As before this zone contained discontinuous islands of oxide which contained some sulphides, figure 4.90c. Again the M_{23}C_6 carbides transformed to oxides with some sulphides at the deepest point of attack. The MC carbides although not attacked acted as nucleation points for sulphides, the M_6C carbides transformed to sulphides and the intermetallic NiAl phase was unattacked. The depleted alloy substrate around the transformed carbides again contained a few spherical sulphide precipitates. The EPMA line scan CD and X-ray mapping indicated that the oxide islands near the surface were rich in Al, Si and Cr, but the oxide islands deeper in the alloy contained only Al_2O_3 , figure 4.92. The depleted matrix beneath the zone of internal attack contained approximately 8 % Cr.

Thus in summary it appears that the addition of 3.49 % Al to the alloy resulted in the formation of a discontinuous zone of internal oxidation which contained islands of oxide rich in Al, Si and Cr. The various carbides within the alloy behaved differently. The M_{23}C_6 were initially attacked by sulphur before transforming to oxide. The MC carbides although not attacked acted as nucleation points for internal sulphide precipitates and the M_6C carbides were transformed to sulphides. The alloy substrate surrounding the transformed carbides became very

depleted in Cr which eventually led to the alloy being unable to maintain a protective oxide scale and thus breakaway corrosion commenced.

180 grit condition

The kinetic data indicated that although the weight uptake was slightly lower than the electropolished material the corrosion process appeared to proceed in a similar manner. Examinations were carried out after 5 mins, 1 hour, 5 hours, 100 hours and 2000 hours.

5 minutes

X-ray diffraction using surface reflection showed that Cr_2O_3 , M_3O_4 and M_{23}C_6 formed on the alloy surface, table 4.21. The lattice parameter value indicated that the spinel was FeCr_2O_4 , figure 4.83. The lattice parameter of the Cr_2O_3 phase corresponded to that of pure Cr_2O_3 , figure 4.84.

1 hour

X-ray diffraction using surface reflection now detected only Cr_2O_3 and M_3O_4 , table 4.21. The lattice parameter of the spinel had increased indicating that Mn was now being incorporated. The Cr_2O_3 lattice parameter was unchanged.

5 hours

X-ray diffraction using surface reflection indicated that the scale now contained M_3O_4 , Cr_2O_3 and M_3S_4 , table 4.21. The intensity of the M_3O_4 spinel indicated that this phase was starting to concentrate on the outer surface of the scale.

The lattice parameter of the M_3O_4 had again increased indicating that it was continuing to become richer in Mn, figure 4.83. The Cr_2O_3 lattice parameter was unchanged.

100 hours
.....

Cross-sectional examination using the Pepperhoff technique showed that the corrosion morphology consisted of an oxide scale and a zone of internal attack, figure 4.90.

An EPMA line scan AB showed that the oxide scale (7 μm thick) consisted of an outer MnCr_2O_4 layer and an inner Cr_2O_3 layer, figure 4.93. Both layers contained some sulphide particles.

The zone of internal attack was upto 40 μm deep. This zone contained islands of oxides formed as a result of the transformation of the M_{23}C_6 carbides. Some sulphide particles were present in these oxide regions. Sulphides had started to nucleate on the M_6C and MC carbides. A number of small spherical sulphides were also present in the Cr-depleted alloy substrate. The EPMA line scan AB and maps indicated that the oxide islands near the alloy surface were rich in Al, Si and Cr, but deeper in the alloy only Al_2O_3 was present. The Cr level in the depleted substrate beneath the zone of internal attack was approximately 15 %.

2000 hours
.....

X-ray diffraction using surface reflection indicated that the oxide scale still consisted of M_3O_4 and Cr_2O_3 , table 4.21. Again the lattice parameter of the spinel had increased, figure 4.83. The Cr_2O_3 lattice parameter had also increased, figure 4.84.

Thus in summary it appears that the corrosion process of the 180 grit material was very similar to the electropolished material.

Summary for HP40A1

Aging Processes

The alloy in the as-received condition contained M_7C_3 and M_6C primary carbide precipitates and an NiAl intermetallic phase. As time progressed at 800°C the primary M_7C_3 precipitates transformed to M_{23}C_6 . The carbon released in the process led to the formation of a large number of

secondary $M_{23}C_6$ and M_6C carbides in the alloy substrate. These subsequently grew and became fewer in number. The aging process, although similar to the HP40Nb alloy was much more pronounced, with dramatic changes occurring to the alloy structure in a very short time.

Sulphur-free gas

The corrosion behaviour of HP40Al in the sulphur-free gas is summarised in figure 4.94. In the case of the electropolished material Cr_2O_3 , $FeCr_2O_4$ and $M_{23}C_6$ nucleated on the alloy surface in the initial stages, figure 4.94b. The primary carbides intersecting the surface enlarged slightly. Subsequently the oxides overgrew the carbides and Mn diffused into the oxide scale. Eventually this scale separated into an outer $(Mn,Fe)Cr_2O_4$ layer and an inner Cr_2O_3 layer, figure 4.94c. The most significant observation was however, the formation of a zone of internal attack which contained isolated Al_2O_3 , NiNbSi rich MC carbides and NiAl particles. This zone offered no additional protection. The corrosion process was similar for the 180 grit material, figure 4.49d.

0.2 % H_2S gas

The corrosion behaviour of HP40Al in the 0.2 % H_2S gas is summarised in figure 4.95. There was no significant difference between the two surface finishes. The corrosion process can be separated into a number of stages.

- Stage 1 (5 mins)

Initially $FeCr_2O_4$, Cr_2O_3 and $M_{23}C_6$ formed on the alloy surface, figure 4.95a.

- Stage 2 (1-5 hours)

The surface layer became complete and contained a mixture of $(Mn,Fe)Cr_2O_4$, Cr_2O_3 and M_3S_4 , figure 4.95b.

- Stage 3 (100 hours)

An additional zone of internal attack started to form. This mainly consisted of transformed former carbides. The $M_{23}C_6$ were initially attacked by sulphur before transforming to oxide. The MC carbides

although not attacked acted as nucleation points for internal sulphide precipitates and the M_6C carbides transformed to sulphides. The intermetallic NiAl phase was not attacked, figure 4.95c.

- Stage 4 (2000 hours)

The corrosion process continued in a similar manner with the alloy substrate becoming very depleted in Cr, figure 4.95d.

- Stage 5 (3000-5000 hours)

Eventually the substantial Cr-depletion of the alloy substrate led to a dramatic increase in the extent of the internal attack and the onset of breakaway corrosion, figure 4.95e.

It was therefore concluded that the 3.49 % Al addition to the HP40Nb alloy offered no additional protection.

Environment	Surface Finish	Reaction Rate Constant ($\text{mg}^2\text{cm}^{-4}\text{h}^{-1}$)	
Sulphur free	EP	3.2×10^{-4}	
	180	9.5×10^{-4}	$-2.7 \times 10^{-4} *$
0.2 % H_2S	EP	3.3×10^{-3}	
	180	-	

* not parabolic

Table 4.17 :

Reaction rate constants for HP40A1 at 800°C ($p\text{O}_2 = 10^{-21}$ bar, $a_c = 0.3$).

Exposure time	Phases Identified (Intensity/Parameter A)					
	Austenite	Cr ₂ O ₃	M ₃ O ₄	M ₂₃ C ₆	M ₆ C	NiAl
1 hour	-	3/4.954-13.584	2/8.373	10/10.594	-	17/2.870
5 hours	-	2/4.945-13.614	6/8.415	14/10.581	-	7/2.862
100 hours	80/3.585	7/4.954-13.595	15/8.449	(M ₇ C ₃) 5/13.998-4.511	3/11.242	-
2000 hours	52/3.589	8/4.950-13.631	43/8.468	-	-	-

Table 4.18 :

X-ray diffraction data for HP40Al exposed to the sulphur-free environment at 800°C ($pO_2 = 10^{-21}$ bar, $a_c = 0.3$). Electropolished condition.

Exposure time	Phases Identified (Intensity/Parameter A)					
	Austenite	Cr_2O_3	M_3O_4	M_{23}C_6	MC	NiAl
100 hours	159/3.583	-	3/8.255	17/10.632	3/4.397	-
5000 hours	41/3.587	4/4.961-13.563	45/8.463	-	-	-

Table 4.19 :

X-ray diffraction data for HP40Al exposed to the sulphur-free environment at 800°C ($p_{\text{O}_2} = 10^{-21}$ bar, $a_c \approx 0.3$). 180 grit condition.

Exposure time	Phases Identified (Intensity/Parameter A)					
	Austenite	Cr_2O_3	M_3O_4	M_3S_4	M_{23}C_6	NiAl
5 mins	999/-	-	3/8.359	-	24/10.580	24/2.874
5000 hours	-	13/4.960-13.599	29/8.415	-	-	-

Table 4.20 :

X-ray diffraction data for HP40Al exposed to the 0.2 % H_2S environment at 800°C ($p\text{O}_2 = 10^{-21}$ bar, $a_c = 0.3$). Electropolished condition.

Exposure time	Phases Identified (Intensity/Parameter A)					
	Austenite	Cr_2O_3	M_3O_4	M_3S_4	M_{23}C_6	NiAl
5 mins	175/3.588	3/4.954-13.584	4/8.394	-	7/10.451	-
1 hour	121/3.584	7/4.949-13.588	9/8.422	-	-	-
5 hours	30/3.577	3/4.950-13.591	21/8.393	6/9.947	-	-
2000 hours	17/3.582	12/4.971-13.622	48/8.466	-	-	-

Table 4.21 :

X-ray diffraction data for HP40Al exposed to the 0.2 % H_2S environment at 800°C ($p\text{O}_2 = 10^{-21}$ bar, $a_c = 0.3$). 180 grit condition.

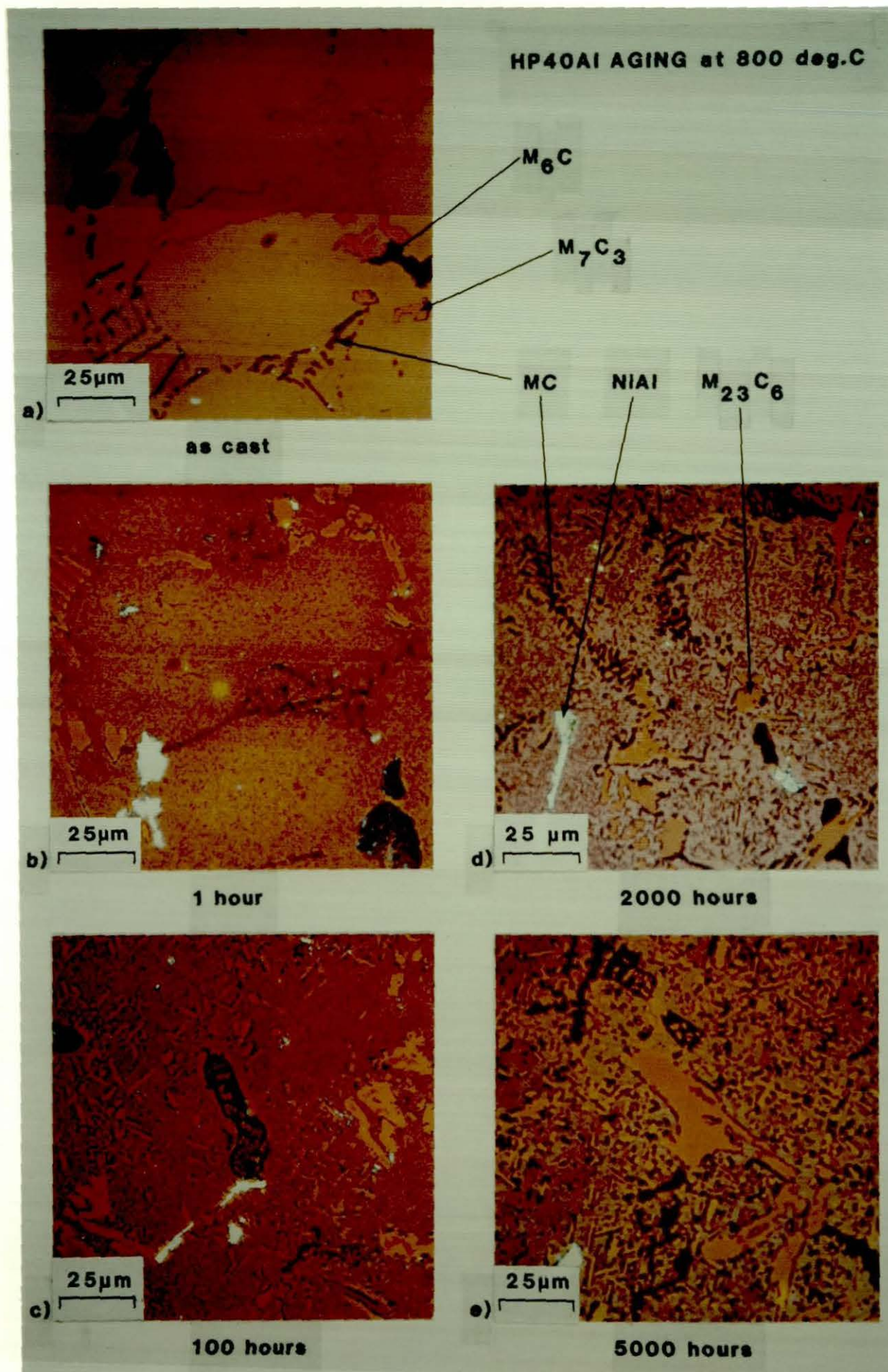


Figure 4.79

Cross-sectional metallographic examination using the Pepperhoff technique to show changes in the microstructure of HP40Al which result from aging processes at 800°C.

HP40Al, Carbide Stability.

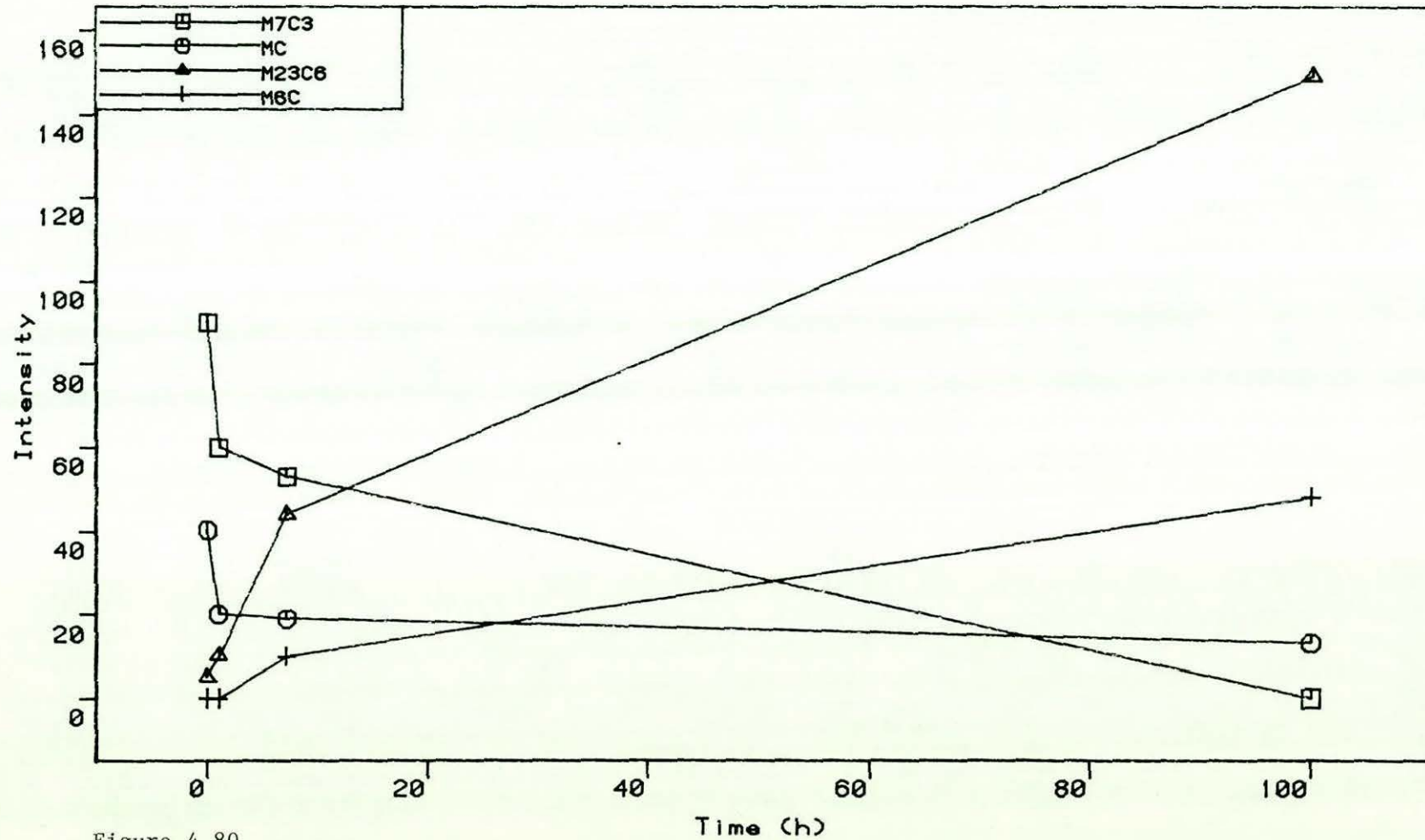


Figure 4.80

Plots of the X-ray diffraction peak intensity of the phases extracted from HP40Al against annealing time in argon at 800°C.

HP40Al, PO₂=10⁻²¹, aC=0.3, 800degC

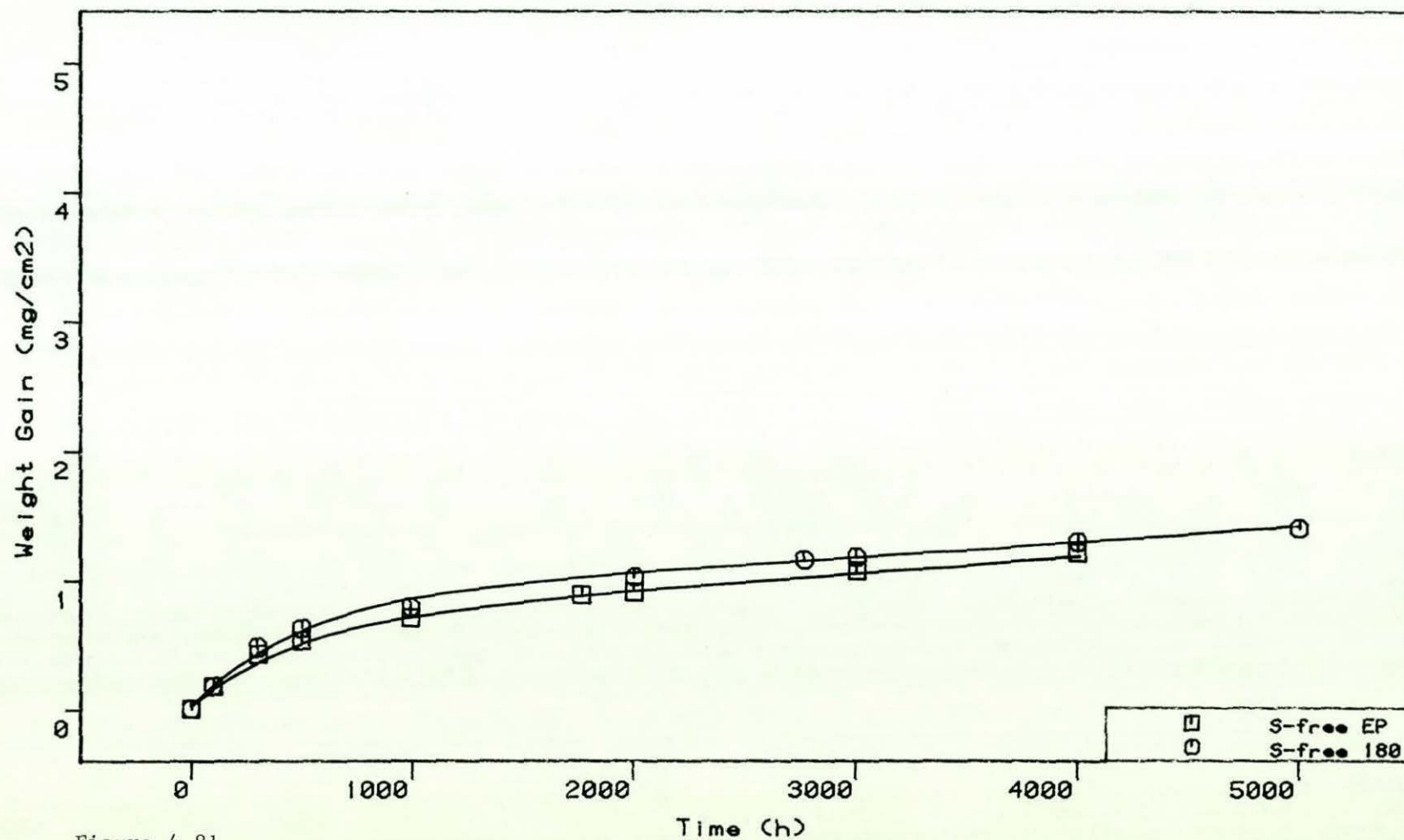


Figure 4.81

Kinetic data for HP40Al exposed to the sulphur-free gas at 800°C.

S-free gas, $P_{O_2}=10^{-21}$ bar, $a_C=0.3$, 800°C

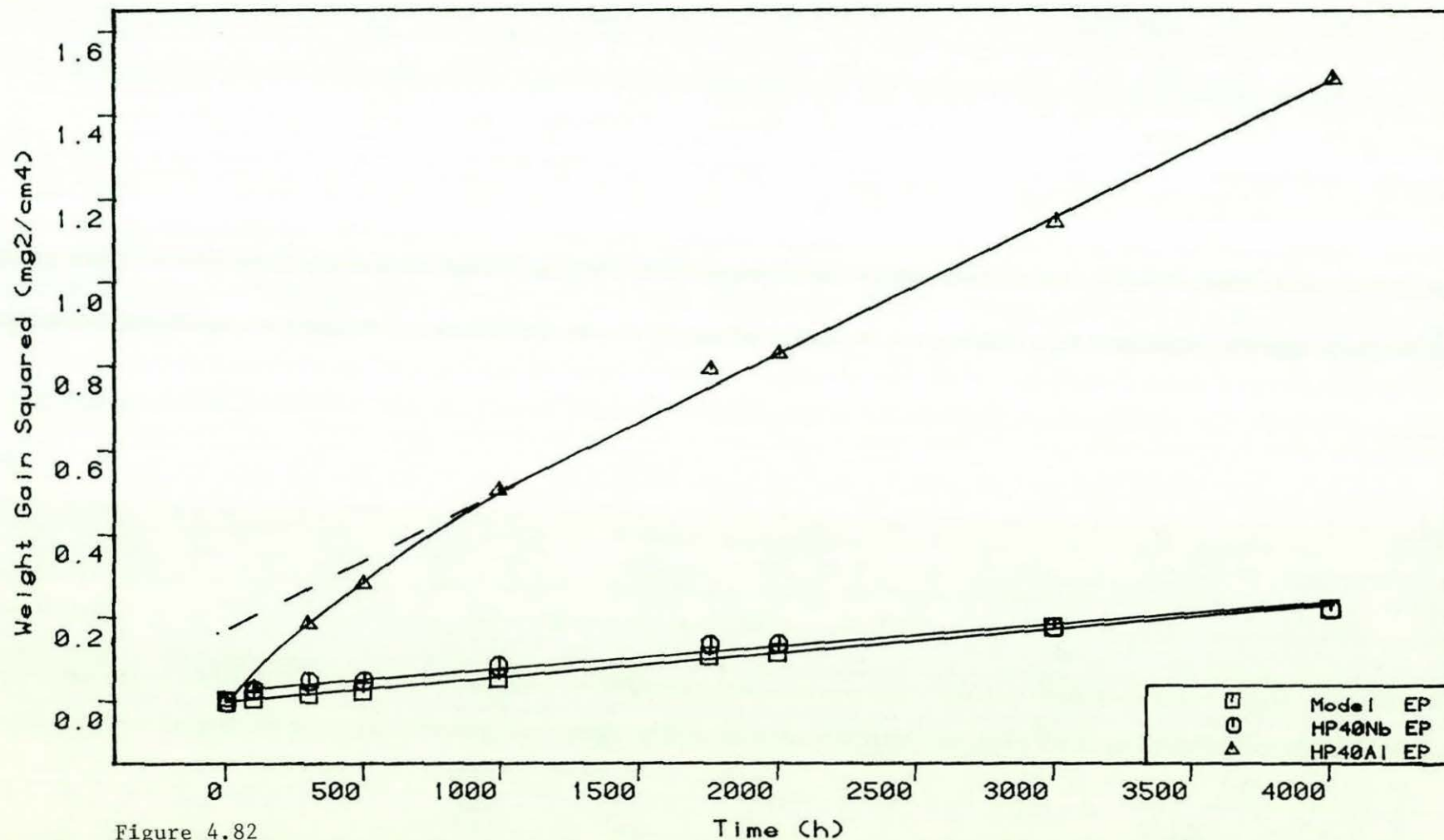


Figure 4.82

Plots of weight gain squared against time, which compare the corrosion behaviour of HP40Al with the Model 25Cr-35Ni-Fe alloy and HP40Nb in the sulphur-free gas at 800°C .

HP40Al, Oxide Spinel Lattice Parameters

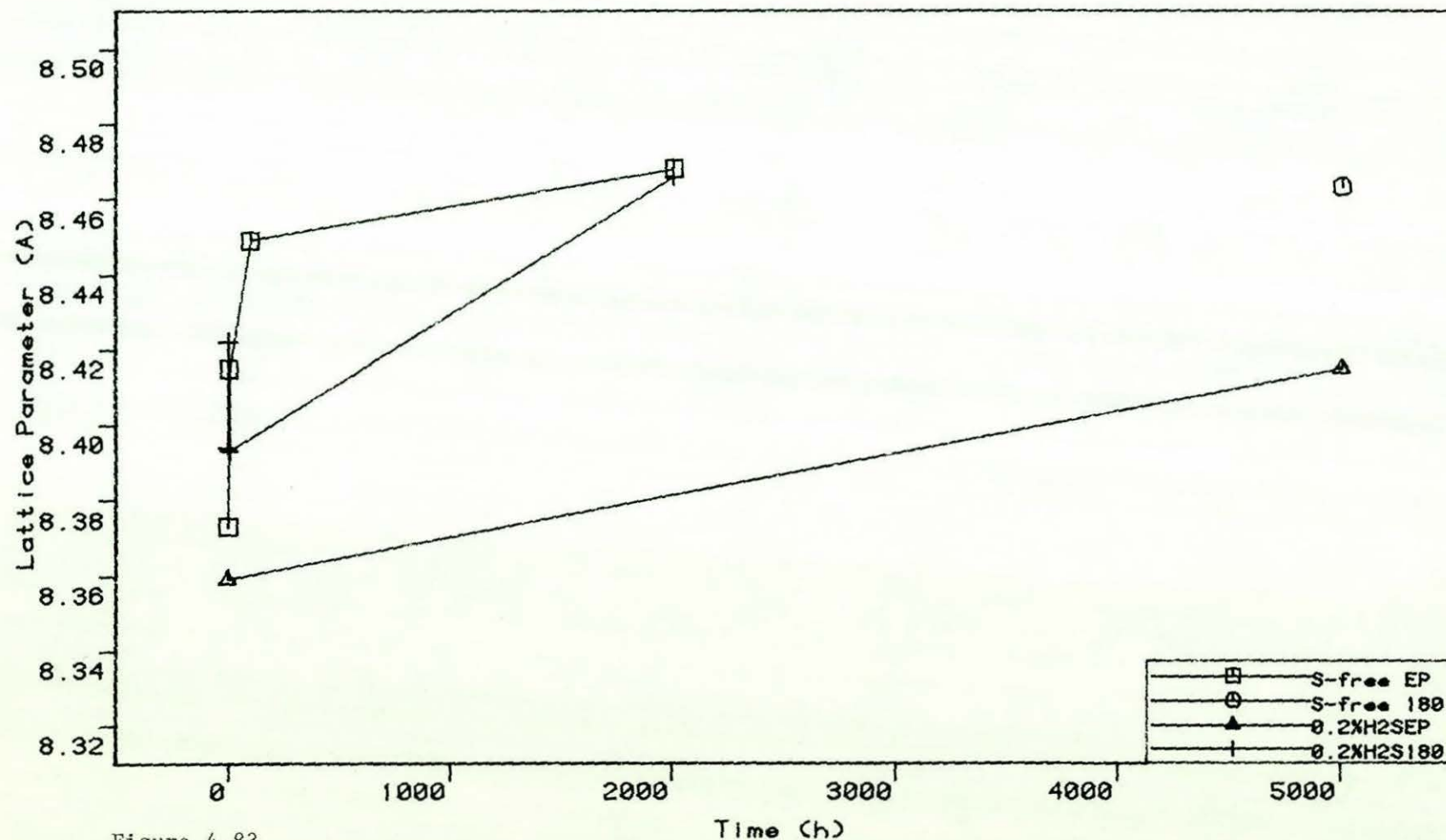


Figure 4.83

Plots of oxide spinel lattice parameter against time for the scale formed on HP40Al exposed to the sulphur-free and 0.2% H_2S gases at $800^{\circ}C$.

HP40Al, Chromia Lattice Parameters

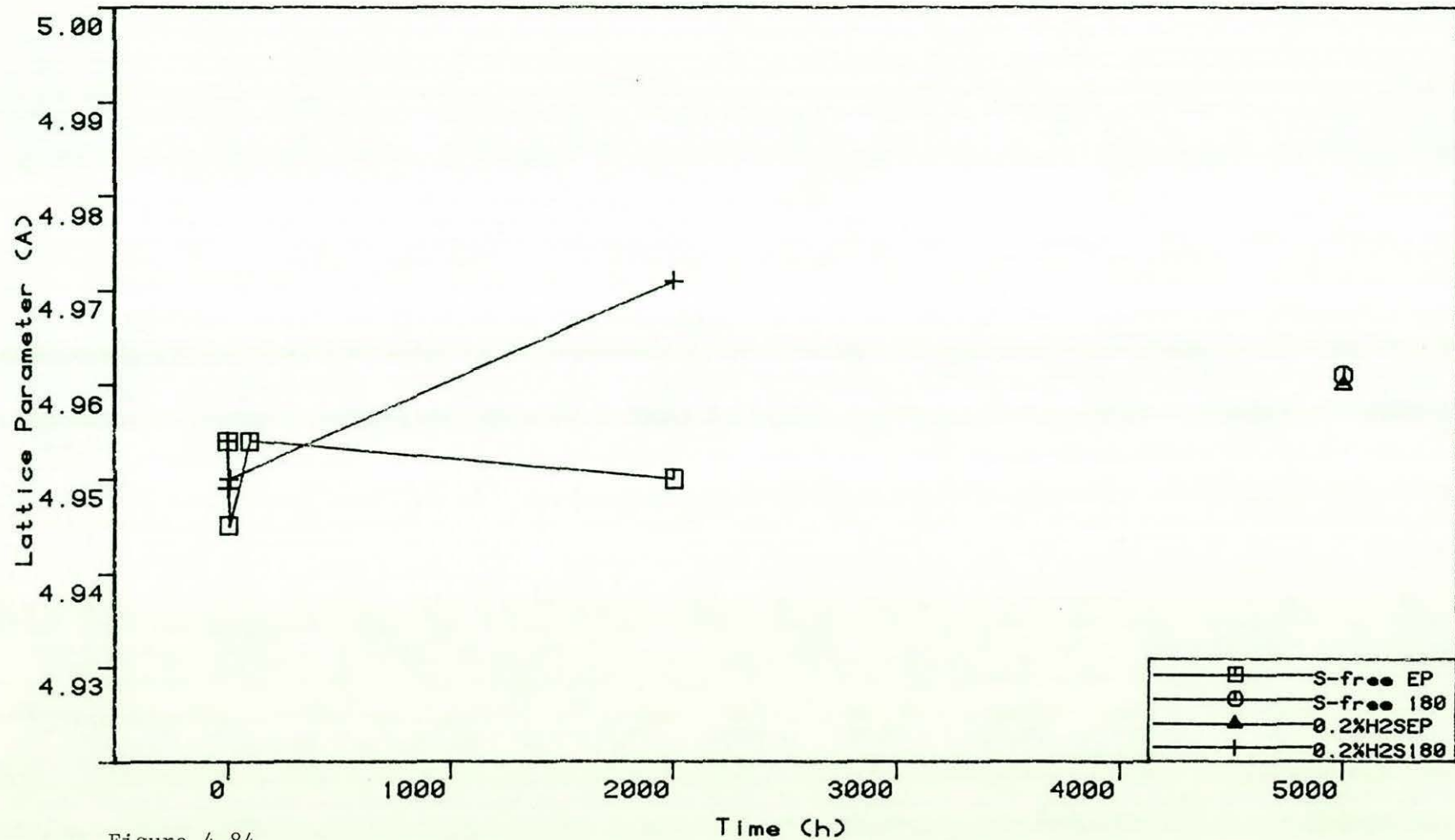


Figure 4.84

Plots of Cr_2O_3 lattice parameter against time for the scale formed on HP40Al exposed to the sulphur-free and 0.2% H_2S gases at 800°C .

H₂S-Free (O/C)

(base-line data)

"Model"

2000h.

HP40Nb

HP40Al

0 0.25 0.5 0.75 1.0
Wt. Gain (mg./cm²)

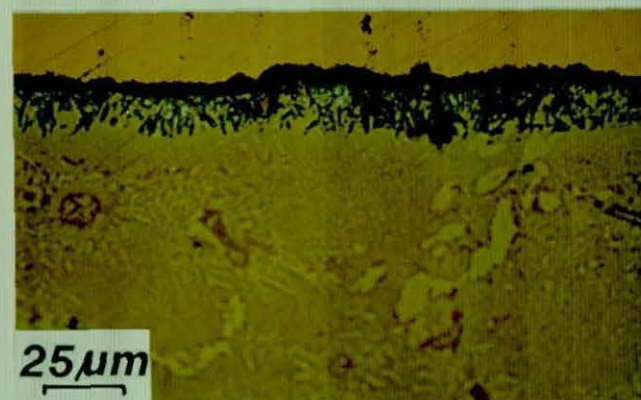
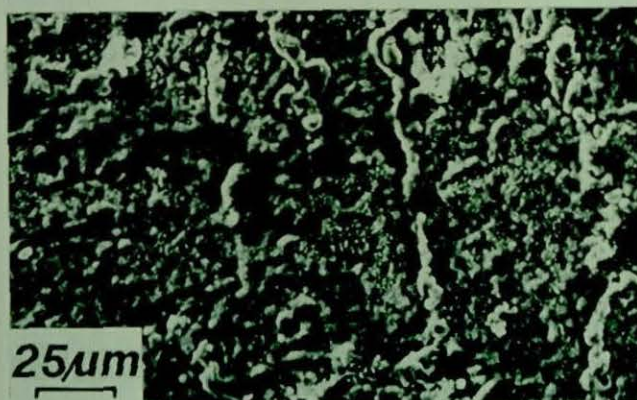
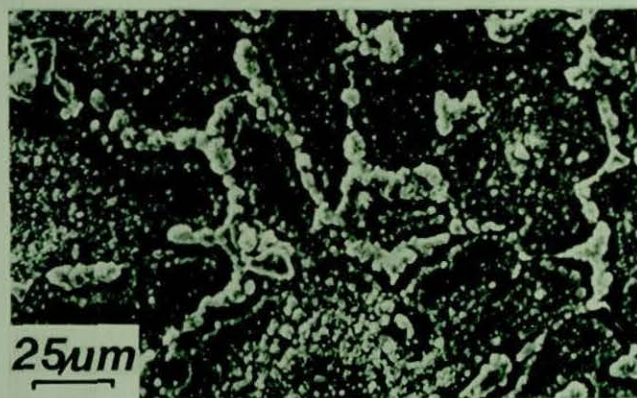
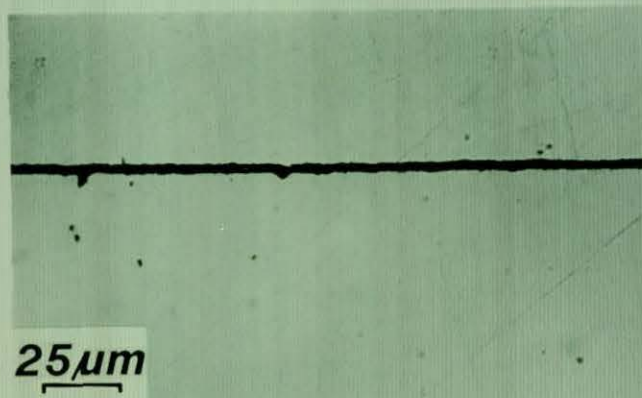
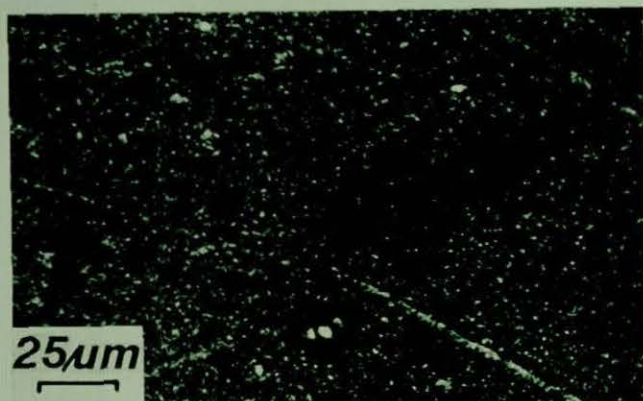


Figure 4.85

Surface SEM and cross-sectional examination using the Pepperhoff technique comparing the corrosion products formed on the Model 25Cr-35Ni-Fe alloy, HP40Nb and HP40Al alloys after exposure to the sulphur-free gas at 800°C for 2000 hours. Electropolished condition.

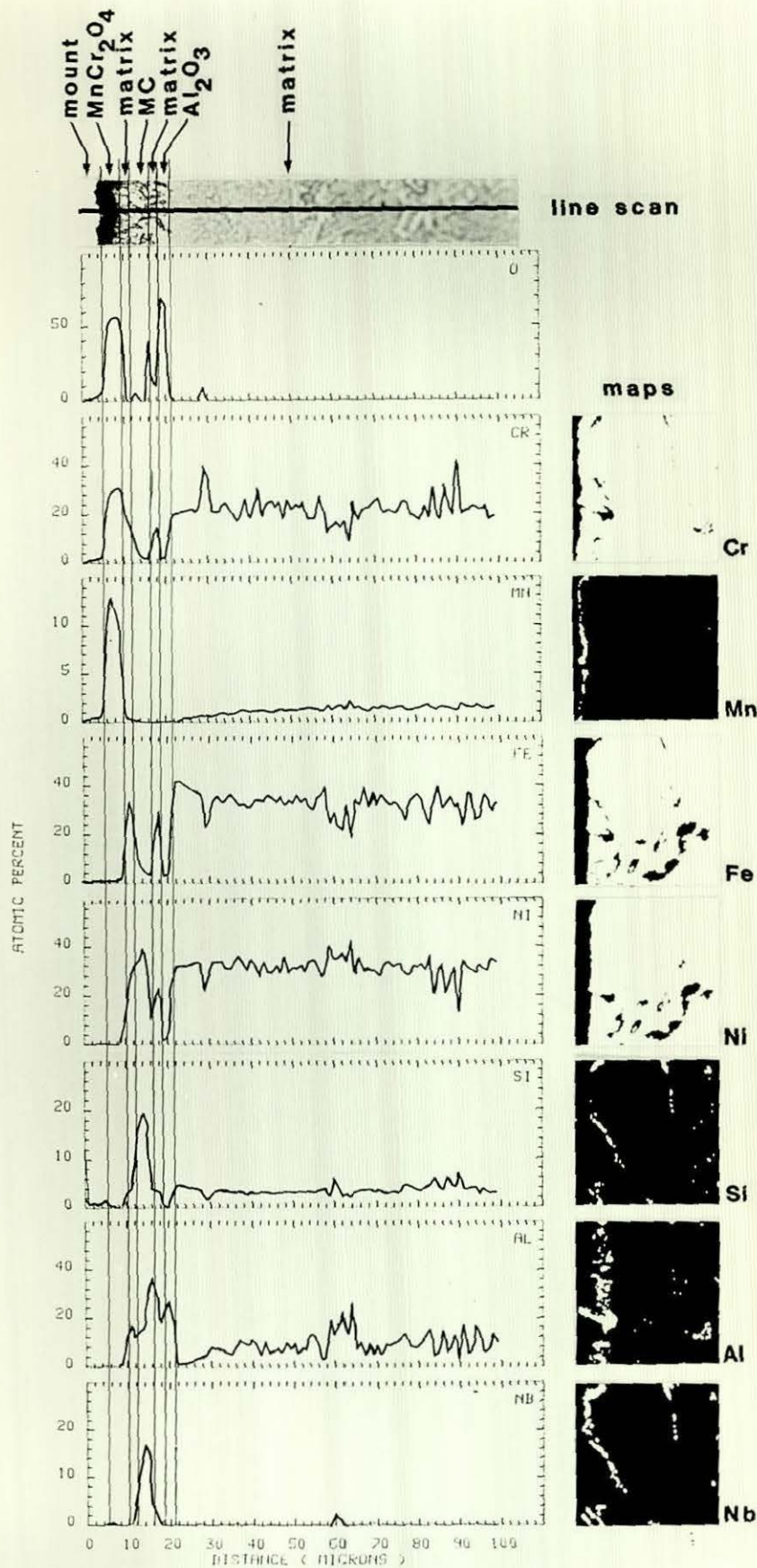


Figure 4.86

EPMA line scan and elemental concentration maps on HP40Al exposed for 2000 hours in the sulphur-free gas at 800°C (electropolished condition).

S-free gas, $P_{O_2}=10E-21$ bar, $a_c=0.3$, 800 deg.C

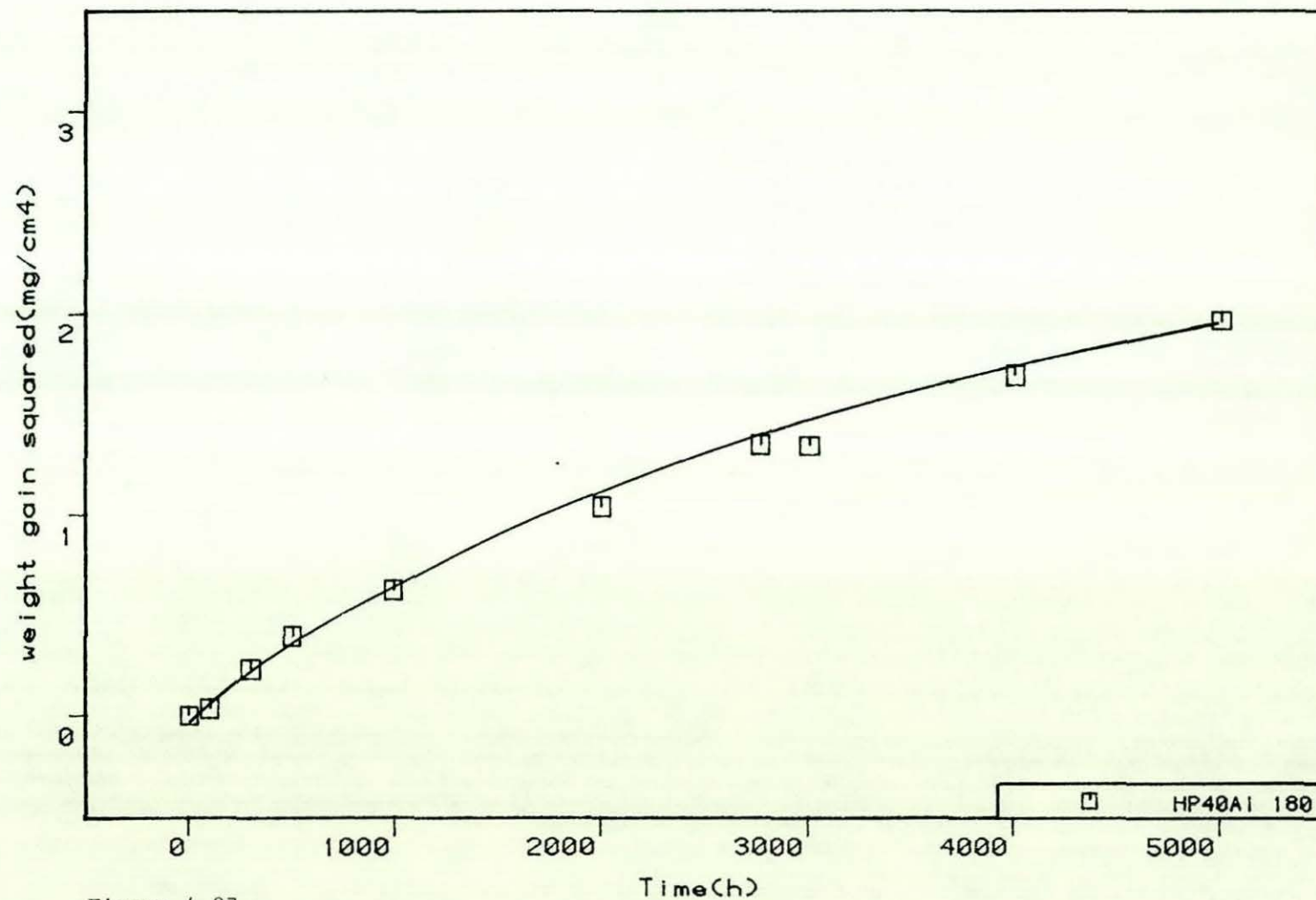


Figure 4.87

Plot of weight gain squared against time for HP40Al exposed to the sulphur-free gas at 800°C, 180 grit condition.

HP40Al, PO2=10-21, $\alpha C=0.3$, 800degC

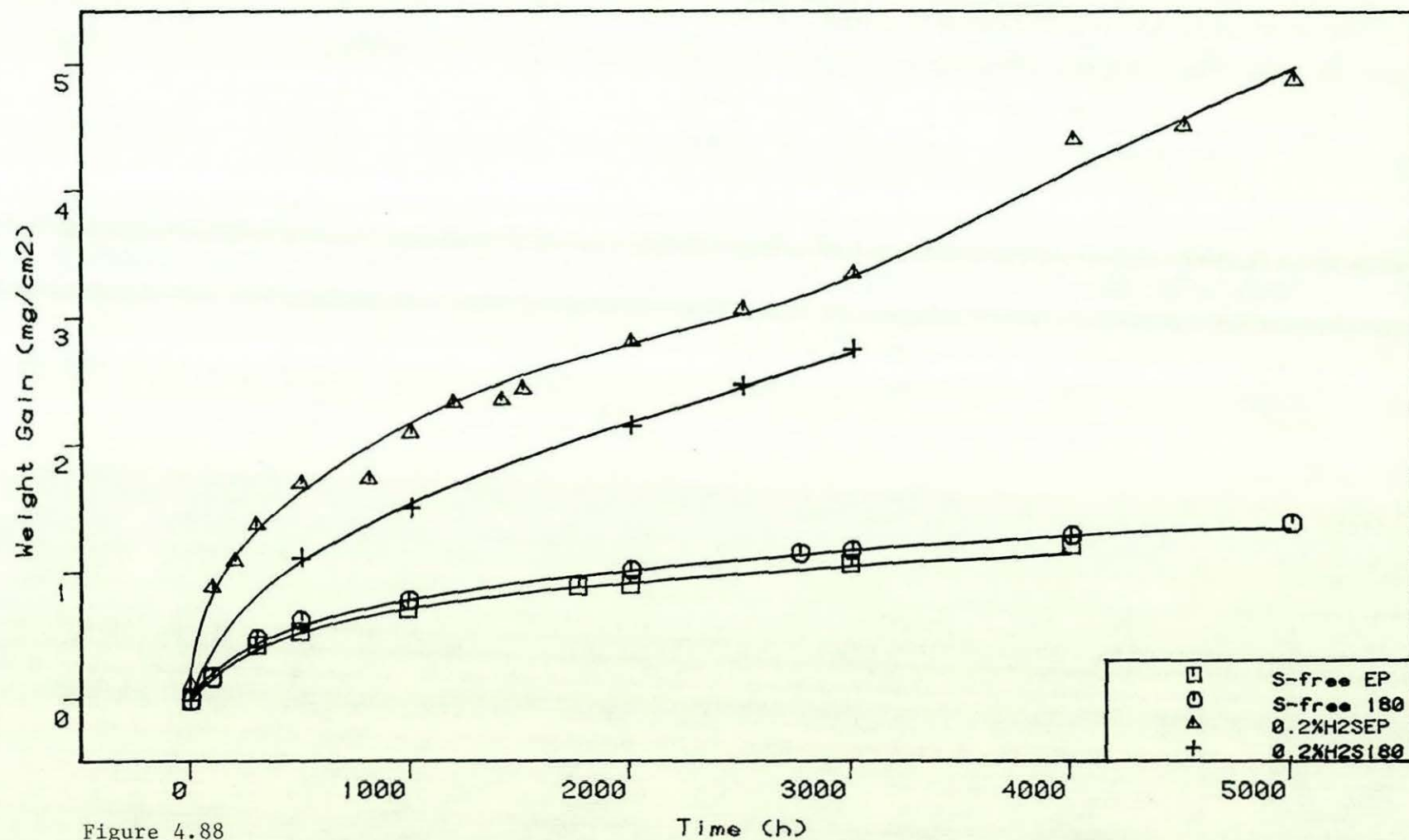


Figure 4.88

Kinetic data for HP40Al exposed to the sulphur-free and 0.2% H₂S gases at 800°C.

0.2% H₂S, 800 deg C

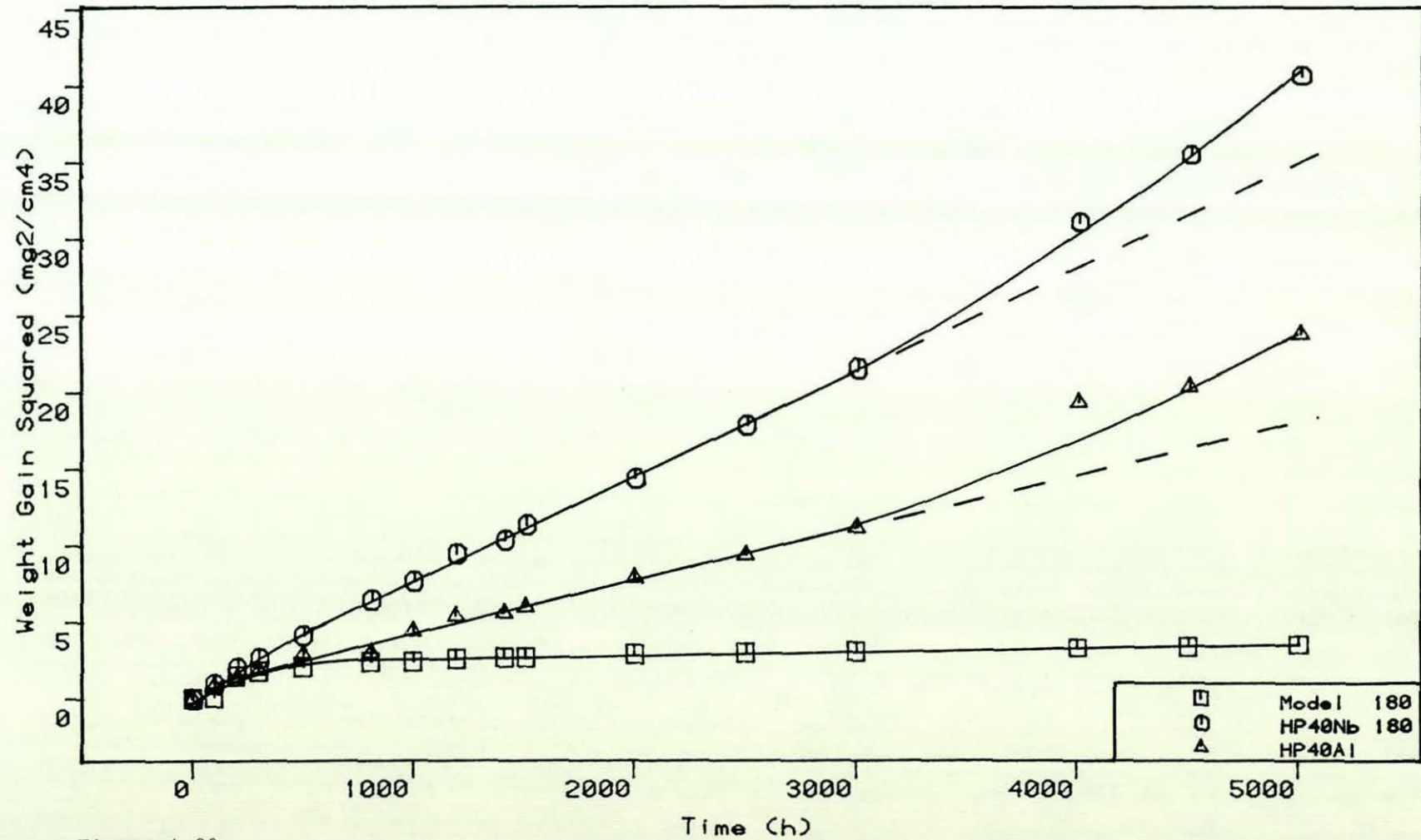


Figure 4.89

Plots of weight gain squared against time which compare the corrosion behaviour of HP40Al with the Model 25Cr-35Ni-Fe alloy and HP40Nb in the 0.2% H₂S gas at 800°C.

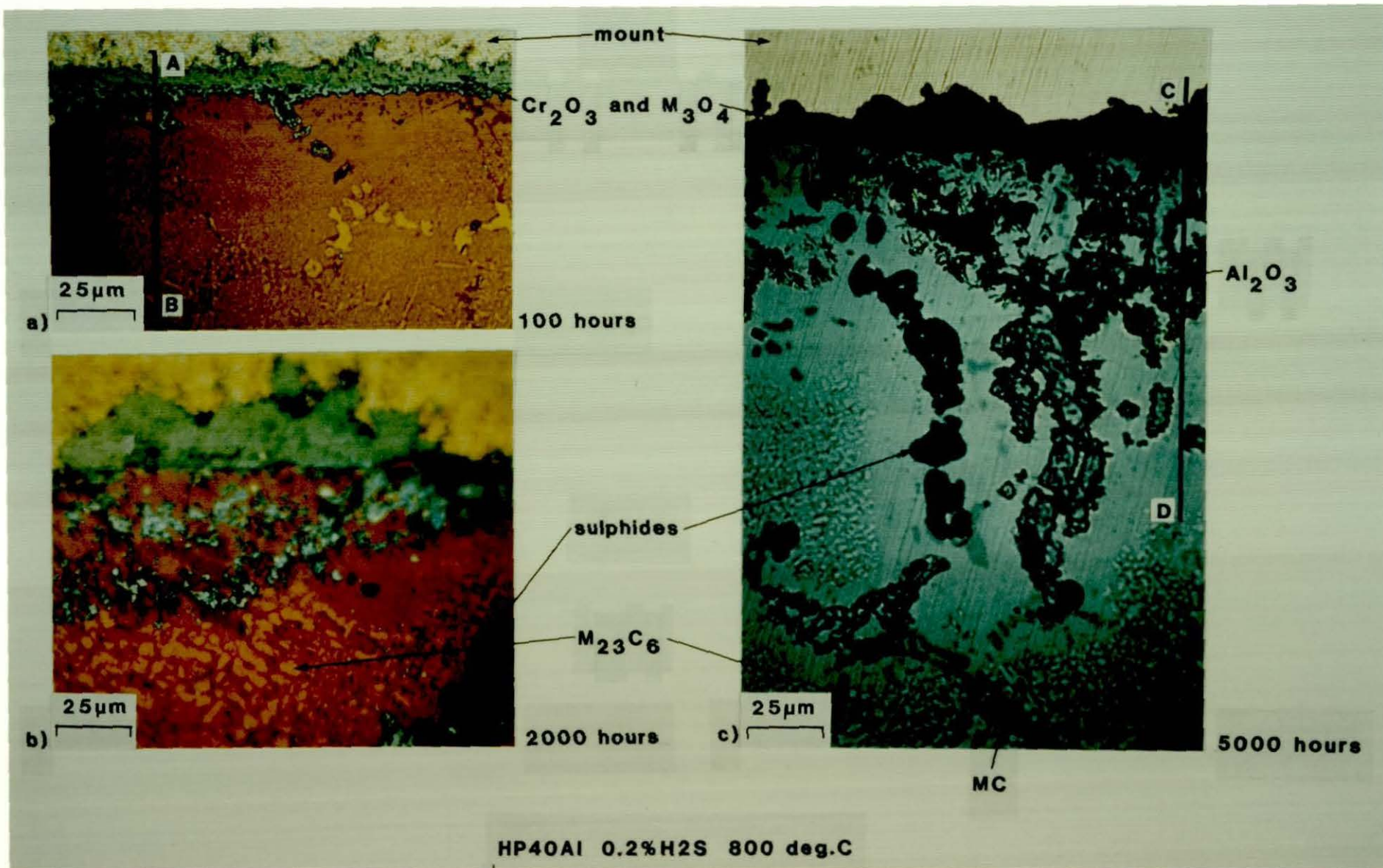


Figure 4.90
Cross-sectional examination using the Pepperhoff technique for HP40Al exposed to the 0.2% H_2S gas at 800°C.

0.2% H₂S (S/O/C)

(pS₂ : 10⁻⁹ bar)

"Model"

2000h.

HP40Nb

HP40Al

Wt. Gain (mg./cm²)

Elemental line scans

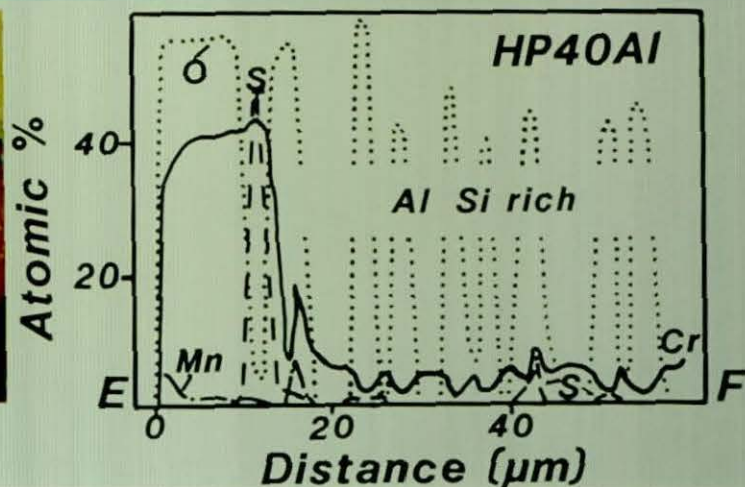
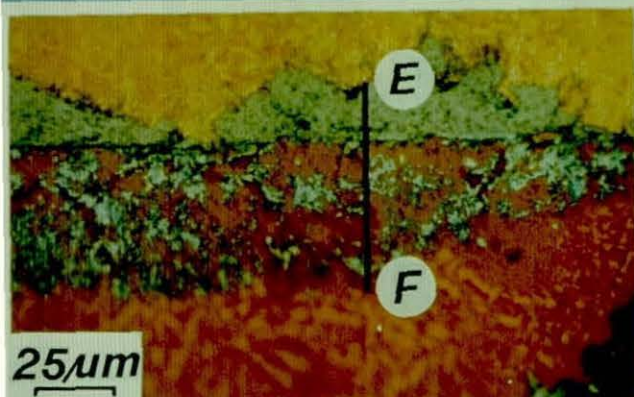
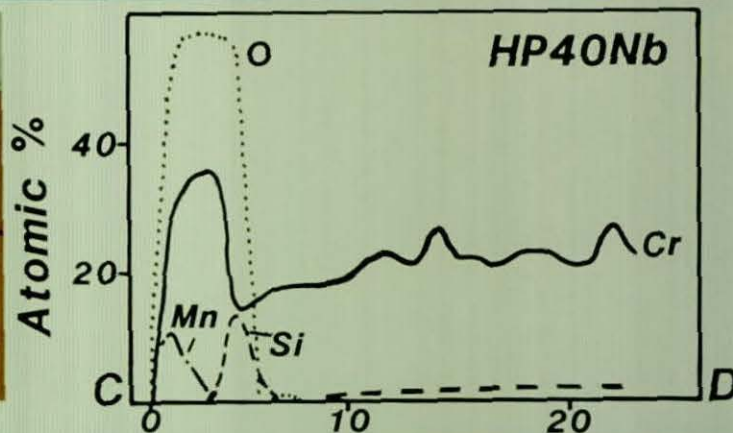
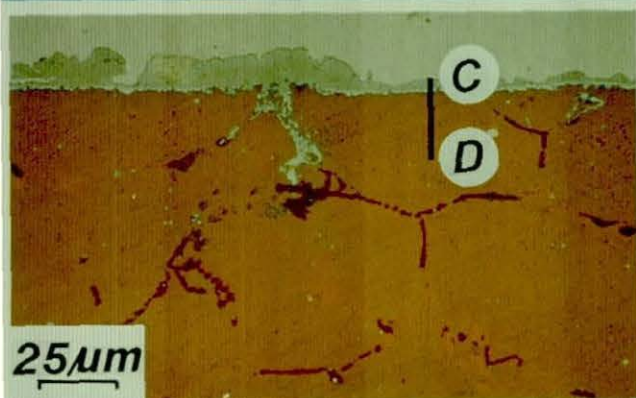
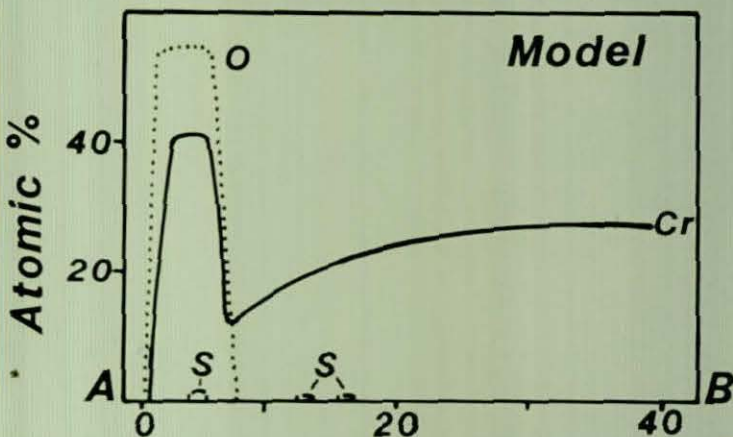
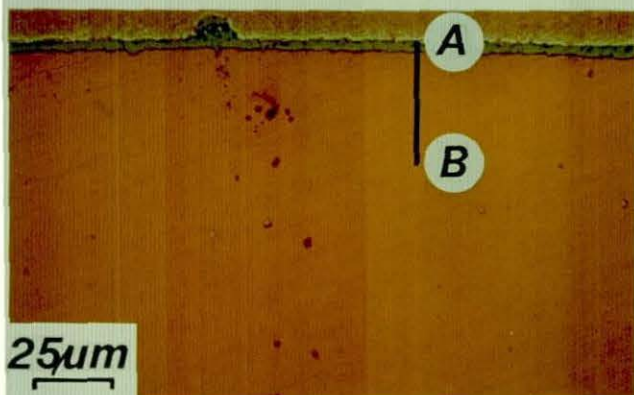


Figure 4.91

Cross-sectional examination using the Pepperhoff technique and EPMA analysis for the Model 25Cr-35Ni-Fe alloy, HP40Nb and HP40Al alloys after exposure to the 0.2 % H₂S gas at 800°C for 2000 hours. Electropolished condition.

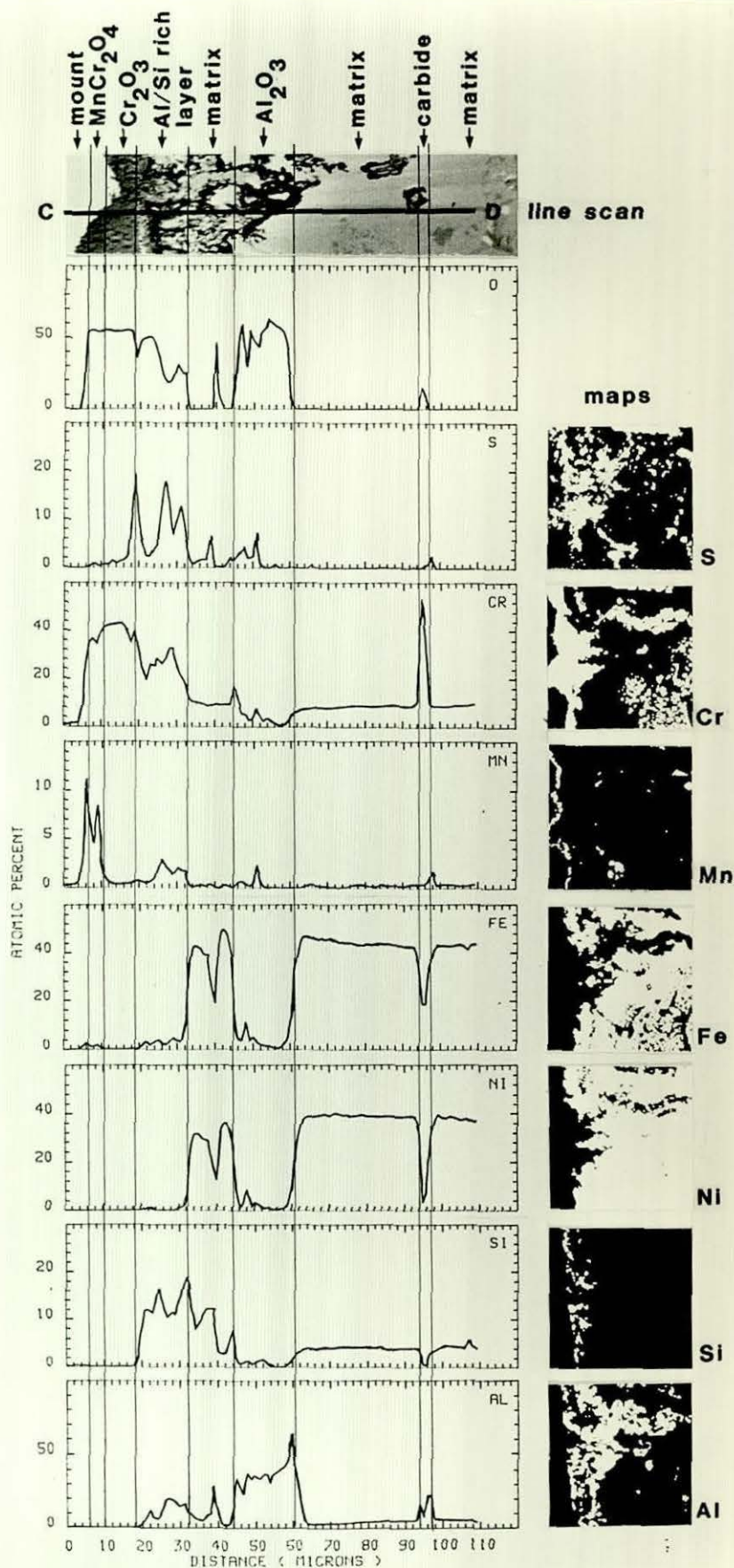


Figure 4.92

EPMA line scan and elemental concentration maps on HP40Al exposed for 5000 hours in the 0.2 % H_2S gas at 800°C. Electropolished condition.

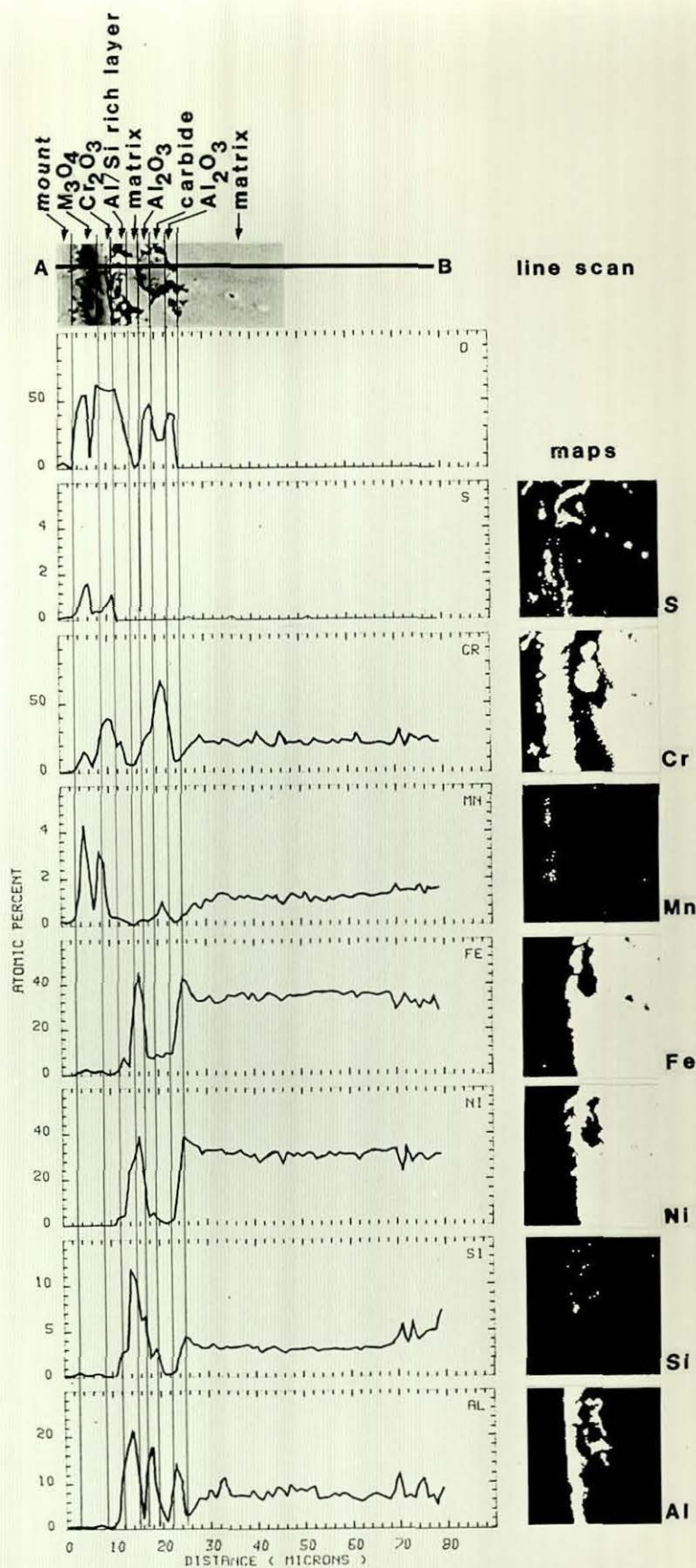
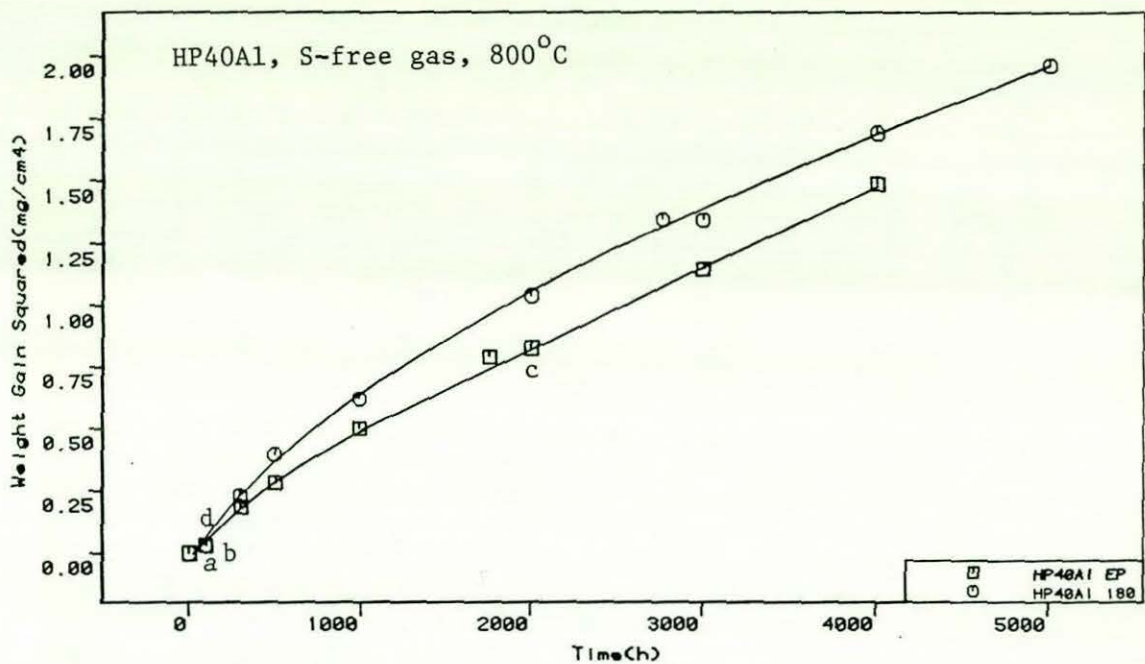


Figure 4.93

EPMA line scan and elemental concentration maps on HP40Al exposed for 100 hours in the 0.2 % H₂S gas at 800°C, 180 grit condition.



EP

180

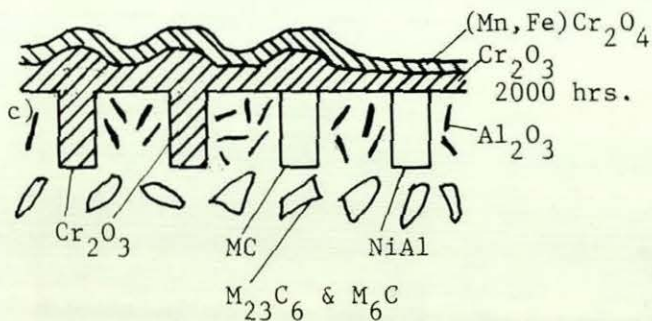
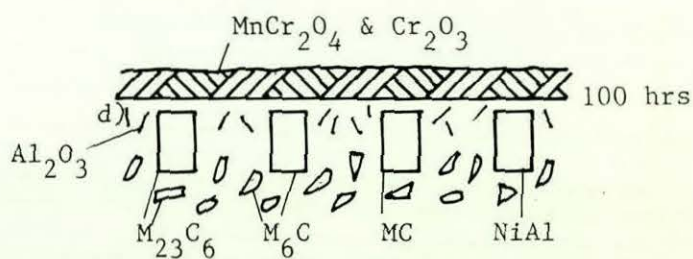
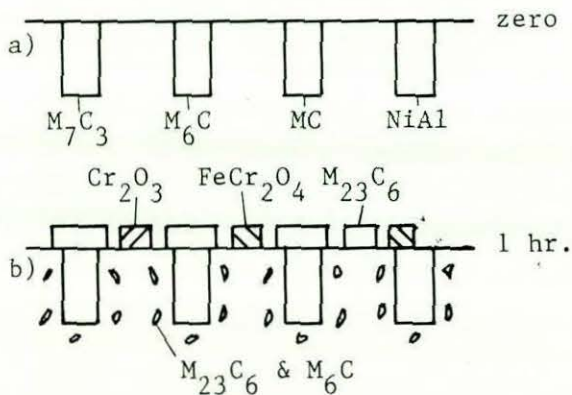


Figure 4.94

Schematic diagram summarising the corrosion behaviour of HP40Al in the sulphur-free gas at 800°C.

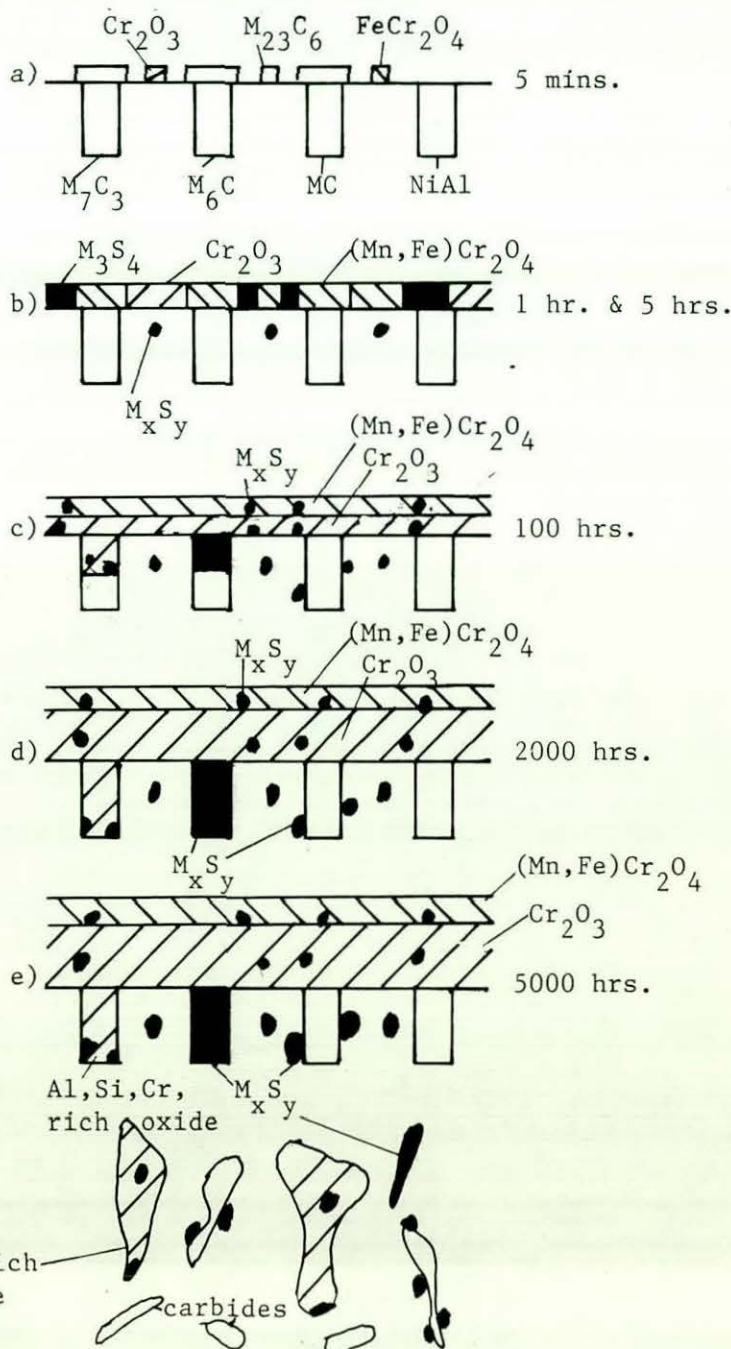
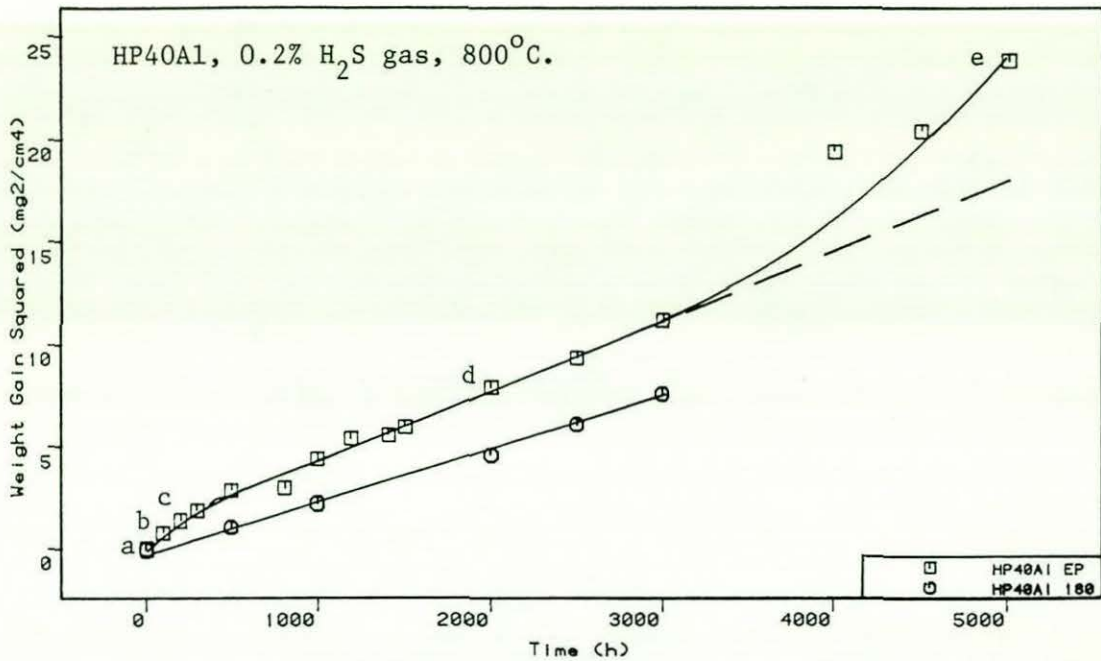


Figure 4.95

Schematic diagram summarizing the corrosion behaviour of HP40Al in the 0.2 % H₂S gas at 800°C.

4.2. SULPHIDATION GOVERNED REGIME AT 800°C

4.2.1. Model 25Cr-35Ni-Fe Alloy in the 0.6 % H₂S gas

The corrosion kinetics are presented in figure 4.96. This figure shows that the weight gains were very high (500 mg/cm² in 1000 hours) and that there was no significant difference between the electropolished and 180 grit specimens.

Examinations were carried out after 5 mins, 1 hour, 5 hours, 25 hours, 200 hours, 500 hours and 1000 hours.

5 mins.
.....

Cross-sectional examination using the Pepperhoff technique revealed that the corrosion morphology consisted of 2 regions : an oxide scale and a zone of internal sulphide precipitates, figure 4.97a.

The (blue coloured) oxide scale (4-5 µm thick) also contained a number of (brown coloured) sulphide particles. X-ray diffraction analysis using surface reflection confirmed that the scale was however predominantly Cr₂O₃, table 4.22.

The zone of (brown coloured) internal sulphide precipitates in the (yellow coloured) alloy substrate was approximately 2-3 µm deep. There was no sign of any carburization at this stage.

1 hour
.....

Cross-sectional examination using the Pepperhoff technique revealed that the corrosion morphology now consisted of 3 regions : an additional discontinuous external sulphide layer at the scale/gas interface, the original predominantly oxide layer and the zone of internal sulphide precipitates in the alloy substrate, figure 4.97b.

The discontinuous sulphide layer (up to 7 μm thick) contained two types of lamellae. EPMA point analyses identified the lighter coloured (brown) lamellae as FeCr_2S_4 and the darker coloured (purple) lamellae as the more iron rich phase $(\text{Fe}_x\text{Cr}_y)_7\text{S}_8$. A few Ni_2Fe particles were also visible on the outer surface of the thicker areas of this layer. X-ray diffraction using surface reflection confirmed the presence of M_3S_4 .

EPMA point analysis confirmed that the (blue coloured) oxide layer was Cr rich and that the (brown coloured) sulphides particles contained within this layer were chromium sulphides. X-ray diffraction using surface reflection indicated that the oxide was still Cr_2O_3 .

The (brown coloured) internal sulphide precipitates had grown and penetrated deeper (6 μm) into the (yellow coloured) alloy substrate. EPMA point analyses confirmed that these precipitates were chromium sulphides. Again there was no sign of any carburization.

5 hours
.....

Cross-sectional examination using the Pepperhoff technique showed that the corrosion morphology now consisted of 3 regions : an external sulphide layer I (65 μm thick), the remains of the former predominantly oxide layer, and a zone of internal sulphide precipitates (34 μm deep), figure 4.97c.

The former discontinuous external sulphide layer had now coalesced together to form the continuous external sulphide layer I, which contained a large number of cracks and pores. This layer contained the light (brown coloured) FeCr_2S_4 lamellae, the darker (purple coloured) more iron rich $(\text{Fe}_x\text{Cr}_y)_7\text{S}_8$ lamellae and the (yellow) metallic Ni_2Fe phase. This Ni_2Fe phase tended to be concentrated either on the outer surface or in pores in the scale. X-ray diffraction using surface reflection confirmed the presence of M_3S_4 , M_7S_8 and Ni_2Fe , table 4.22.

The former oxide layer, situated beneath the sulphide layer, now appeared to have broken up and consisted of a mixture of (blue) oxide and (brown) sulphide particles. X-ray diffraction using surface reflection again confirmed the presence of Cr_2O_3 , table 4.22.

The (brown) internal sulphide precipitates had grown and penetrated deeper into the (yellow) alloy substrate (maximum depth 34 μm). These sulphides were quite large (5 μm diameter) near the original alloy surface but smaller (2 μm diameter) deeper in the alloy substrate.

A small amount of carburization of the grain boundaries had taken place beneath the zone of internal sulphide precipitates. This was attributed to aging processes.

25 hours
.....

Cross-sectional examination using the Pepperhoff technique now showed that the corrosion morphology consisted of 4 regions : the external sulphide layer I, the broken up original oxide layer, an additional discontinuous internal sulphide layer and the zone of internal sulphide precipitates, figure 4.97d.

The external sulphide layer I was now much thicker (150 μm) than before (figure 87). This layer still consisted of the two types of sulphide lamellae and the metallic particles. EPMA point analysis confirmed the compositions of the lighter (brown) lamellae as FeCr_2S_4 , the darker (purple) lamellae as the more iron rich phase $(\text{Fe}_x\text{Cr}_y)_7\text{S}_8$ and the (yellow) metallic phase as Ni_2Fe . X-ray diffraction using surface reflection confirmed the presence of M_3S_4 and Ni_2Fe , table 4.22. The former M_7S_8 phase now had the composition MS.

As before the Ni_2Fe metallic phase tended to be situated on the external surface of the scale or in pores in the sulphide layer I. This observation and presence of the sulphide lamellae led to the suspicion that some structural changes occurred during cooling from the test temperature. To investigate this, pieces of outer sulphide layer I were heated to 800°C in the hot stage microscope and in the D.T.A. equipment. Both these techniques detected no phase changes in either heating or cooling. Thus it was tentatively concluded that the metallic phase and FeCr_2S_4 and $(\text{Fe}_x\text{Cr}_y)_7\text{S}_8$ lamellae could have formed during cooling from the original test exposure but not taken back into solution when scale was reheated to the test temperature.

The (blue) oxide particles present in what remained of the original oxide layer were confirmed as Cr_2O_3 by EPMA point analysis and X-ray diffraction using surface reflection, table 4.22.

The discontinuous internal sulphide layer (up to 25 μm thick), situated just beneath the original alloy surface, appeared to have formed from the large internal sulphide precipitates coalescing together. Most of this layer consisted of the light (brown) FeCr_2S_4 phase with smaller quantities of the darker (purple) more iron rich $(\text{Fe}_x\text{Cr}_y)\text{S}$ phase also present. The compositions of these phases were confirmed by EPMA point analysis.

The zone of internal sulphide precipitates had increased to $\sim 100 \mu\text{m}$ deep, figure 4.98. As before the precipitates deep in the alloy were much smaller than those nearer the surface. EPMA point analysis confirmed that the precipitates in this zone were chromium sulphides.

A few carbide precipitates were present beneath the zone of internal sulphide precipitates. These were often situated near the grain boundaries.

100 hours
.....

Cross-sectional examination using the Pepperhoff technique now showed that the corrosion morphology consisted of 5 regions: the external sulphide layer I, the broken up original oxide layer, an internal sulphide layer, and a zone of internal sulphide precipitates, figure 4.97e.

The external sulphide layer I although thicker (260 μm), figure 4.98, still contained the two types of lamellae and the metallic Ni_2Fe phase. EPMA point analysis showed that the darker (purple coloured) lamellae now contained a significant amount of Ni in addition to Fe and Cr. The composition of the lighter (brown coloured) lamellae (FeCr_2S_4) and the metallic phase Ni_2Fe were the same as before. X-ray diffraction using surface reflection again confirmed the presence of M_3S_4 , MS , Ni_2Fe and also detected traces of M_9S_8 .

The remains of the broken up oxide layer were identified by EPMA point analysis as Cr_2O_3 . The presence of Cr_2O_3 was also confirmed by X-ray diffraction.

The internal discontinuous sulphide layer had also thickened (30 μm thick), figure 4.98, and was now starting to exhibit a similar structure to the external sulphide layer I. EPMA point analysis confirmed that the lighter (brown coloured) phase present in smaller amounts was the more iron rich $(\text{Fe}_x\text{Cr}_y)\text{S}$.

The zone of internal sulphide precipitates had again advanced further into the alloy substrate (depth 105 μm). As before these sulphides were quite large nearer the original alloy surface, but much smaller deeper in the alloy substrate. EPMA point analysis again confirmed these precipitates as chromium sulphides.

A zone (460 μm deep) containing M_{23}C_6 carbides was now clearly visible beneath the zone containing the sulphide precipitates, figure 4.98. Although this zone was quite large the volume of carbides was relatively small.

200 hours
.....

Cross-sectional examination using the Pepperhoff technique showed that a dramatic change in the corrosion process had taken place between 100 and 200 hours. The corrosion morphology now consisted of 6 regions : a new outer sulphide layer II, the former external sulphide layer I, the remains of the oxide layer at the original alloy surface, an internal sulphide layer, a zone of sulphide precipitates and a zone of carbide precipitates, figure 4.97f.

The thickness and relative position of each of these layers and zones is given in figure 4.98. Considering each layer in turn.

The new outer sulphide layer II (upto 500 μm thick) consisted of a (dark purple) sulphide phase $\text{Fe}_{4,5}\text{Ni}_{4,5}\text{S}_8$ and (yellow) Ni_2Fe particles.

The former external sulphide layer I was only slightly thicker (300 μm) than after 100 hours. This layer still contained the lighter (brown) lamellae, the darker (light purple) lamellae and the yellow metallic Ni_2Fe particles.

X-ray powder diffraction on a mixture of outer sulphide layer II and external sulphide layer I confirmed the presence of M_9S_8 , M_3S_4 and Ni_2Fe and also detected M_7S_8 instead of MS. Only traces of the oxide layer remained at the original alloy surface.

The internal sulphide layer had now advanced a long way into the alloy (750 μm). This layer contained the light (brown) FeCr_2S_4 lamellae the darker (light purple) more iron rich phase $(\text{Fe}_x\text{Cr}_y)\text{S}$ and some metallic Ni_2Fe particles.

A zone of internal sulphide precipitates (30 μm thick) was again situated beneath the internal sulphide layer with the zone containing the M_{23}C_6 precipitates below this.

In some isolated places blisters had formed on top of the new outer sulphide layer II. Cross-sectional examination using the Pepperhoff technique showed that these blisters contained the (pink) Ni_3S_2 phase, (dark purple) $\text{Fe}_{4,5}\text{Ni}_{4,5}\text{S}_8$ and (yellow) Ni_2Fe . X-ray powder diffraction on a mixture of a blister, outer sulphide layer II and outer sulphide layer I confirmed the additional presence of Ni_3S_2 in the blister, table 4.22.

500 hours
.....

Cross-sectional examination using the Pepperhoff technique showed that corrosion morphology now contained 7 regions : a new outer sulphide layer III (which corresponded to the former blisters), outer sulphide layer II, external sulphide layer I, the remains of the oxide layer at the original alloy surface, an internal sulphide layer, a zone of sulphide precipitates and a zone of carbide precipitates. The thickness of each of these layers and zones is summarized in figure 4.98. The severity of the corrosion made it physically impossible to present cross-sectional pictures for this exposure time. However the various layers can be described as follows.

The new outer sulphide layer III (800 μm thick) consisted of Ni_3S_2 , $\text{Fe}_{4,5}\text{Ni}_{4,5}\text{S}_8$ and Ni_2Fe metallic particles and appeared to have been molten at the test temperature. The composition of these phases was confirmed by EPMA point analysis.

The outer sulphide layer II had become much thicker (1400 μm). EPMA point analysis confirmed that this layer still consisted of $\text{Fe}_{4,5}\text{Ni}_{4,5}\text{S}_8$ and Ni_2Fe metallic particles.

Outer sulphide layer I had not become much thicker (350 μm). EPMA analysis however showed that although the lamellar structure was still present both the (brown) coloured lamellar and darker (purple) coloured lamellar contained significant quantities of Ni in addition to Cr and Fe. The Ni_2Fe particles were still present.

The internal sulphide scale had again advanced much further into the alloy (1550 μm). EPMA analysis again confirmed that this contained the FeCr_2S_4 and $(\text{Fe}_x\text{Cr}_y)\text{S}$ phases and some metallic Ni_2Fe particles.

Again the zone of internal chromium sulphide precipitates was present beneath the internal sulphide layer. Although this zone was situated much deeper in the alloy its overall thickness (30 μm) had not increased.

Finally the zone of containing the M_{23}C_6 precipitates was situated beneath the zone of chromium sulphide precipitates. The amount of carburization had increased slightly.

1000 hours
.....

Cross-sectional examination showed that the same 7 regions were present, but that only a very small amount of the alloy remained unattacked. It was concluded that this specimen did not give a true picture of the corrosion process and that the examination after 500 hours was representative of the final microstructure in the sequence.

The corrosion behaviour of the Model 25Cr-35Ni-Fe alloy in the 0.6 % H_2S gas can be summarised as a number of stages, figure 4.99.

- Stage 1 (5 mins)

Initially a Cr_2O_3 scale containing a number of sulphide particles formed on the alloy surface. Simultaneously a number of small sulphides precipitates formed in the alloy substrate, figure 4.99a.

- Stage 2 (1 hour)

A discontinuous external sulphide layer I containing $FeCr_2S_4$ and more iron rich $(Fe_xCr_y)_7S_8$ lamellae formed on top of the original predominantly oxide layer. The internal chromium sulphide precipitates grew and penetrated deeper into the alloy substrate, figure 4.99b.

- Stage 3 (5 hours)

The external sulphide layer I became continuous. This layer consisted of $FeCr_2S_4$ and $(Fe_xCr_y)_7S_8$ lamellae and a number of metallic Ni_2Fe particles on the outer surface and in the pores in the scale. The former oxide layer started to break up. The internal sulphide precipitates advanced deeper into the alloy and became much larger just beneath the original alloy surface, figure 4.99c.

- Stage 4 (25 hours)

The internal chromium sulphides just below the original alloy surface started to coalesce together and take in iron to form an internal sulphide layer. The outer sulphide layer I continued to thicken and the internal sulphide precipitates advanced deeper into the alloy. The original oxide layer was now completely broken up. A few carbide precipitates started to form beneath the zone containing the internal sulphide precipitates, figure 4.99c.

- Stage 5 (100 hours)

The former $(Fe_xCr_y)_7S_8$ lamellar present in the outer sulphide layer I started to contain a significant amount of Ni. The outer sulphide layer I and the internal sulphide layer continued to thicken. The internal chromium sulphide precipitates continued to advance deeper into the alloy substrate and a zone of $M_{23}C_6$ carbides became visible beneath the internal sulphides, figure 4.99d.

- Stage 6 (200 hours)

A new outer sulphide layer II containing $\text{Fe}_{4,5}\text{Ni}_{4,5}\text{S}_8$ and Ni_2Fe metallic particles formed. The former outer sulphide layer I remained relatively unchanged. The internal (FeCr) rich sulphide layer advanced deep into the alloy. The zones of internal chromium sulphides and M_{23}C_6 carbides were still present beneath the internal sulphide scale, figure 4.99e.

- Stage 7 (500 hours)

Another outer sulphide layer III formed. This layer contained Ni_3S_2 , $\text{Fe}_{4,5}\text{Ni}_{4,5}\text{S}_8$ and Ni_2Fe and appeared to have been molten at the test temperature. The outer sulphide layer II still contained $\text{Fe}_{4,5}\text{Ni}_{4,5}\text{S}_8$ and Ni_2Fe . Outer sulphide layer I contained the two types of lamellae (both were now rich in Fe, Cr and Ni) and the Ni_2Fe metallic phase. A few traces of oxide were present at the original alloy surface. The internal Fe,Cr rich sulphide layer had penetrated deeper into the alloy. The zone of internal sulphides and zone of internal M_{23}C_6 precipitates were still present beneath the internal sulphide scale, figure 4.99f.

Exposure Time	Phase Identified (Intensity/Parameter Å)								
	Austenite	Ni ₂ Fe	Cr ₂ O ₃	M ₃ O ₄	M ₇ S ₈	MS	M ₃ S ₄	M ₉ S ₈	Ni ₃ S ₂
5 mins	154/3.58	-	11/4.95-13.59	-	-	-	-	-	-
1 hr	149/3.58	-	7/4.95-13.58	-	-	-	4/ 9.97	-	-
5 hrs	-	41/3.56	5/4.95-13.58	-	11/3.44-5.76	-	15/ 9.99	-	-
25 hrs	-	46/3.56	8/4.96-13.59	-	-	traces	18/10.00	-	-
100 hrs	-	16/3.56	10/4.96-13.59	-	-	20/?	36/ 9.99	16/10.184	-
200 hrs (normal)	-	22/3.56	-	-	15/3.45-5.76	-	90/10.00	10/10.25	-
200 hrs (blister)	-	10/3.56	5/-	-	13/3.46-5.76	-	26/10.00	100/10.12	10/5.73-7.13
1000 hrs	-	39/3.55	27/4.96-13.58	-	-	-	7/ 9.95	77/10.119	15/5.73-7.13

Table 4.22

X-ray diffraction analysis of the model 25Cr-35Ni-Fe alloy exposed to the 0.6 % H₂S gas at 800°C.

$PS_2=10^{-8}$ bar, $PO_2=10^{-21}$ bar, $aC=0.3$, 800°C

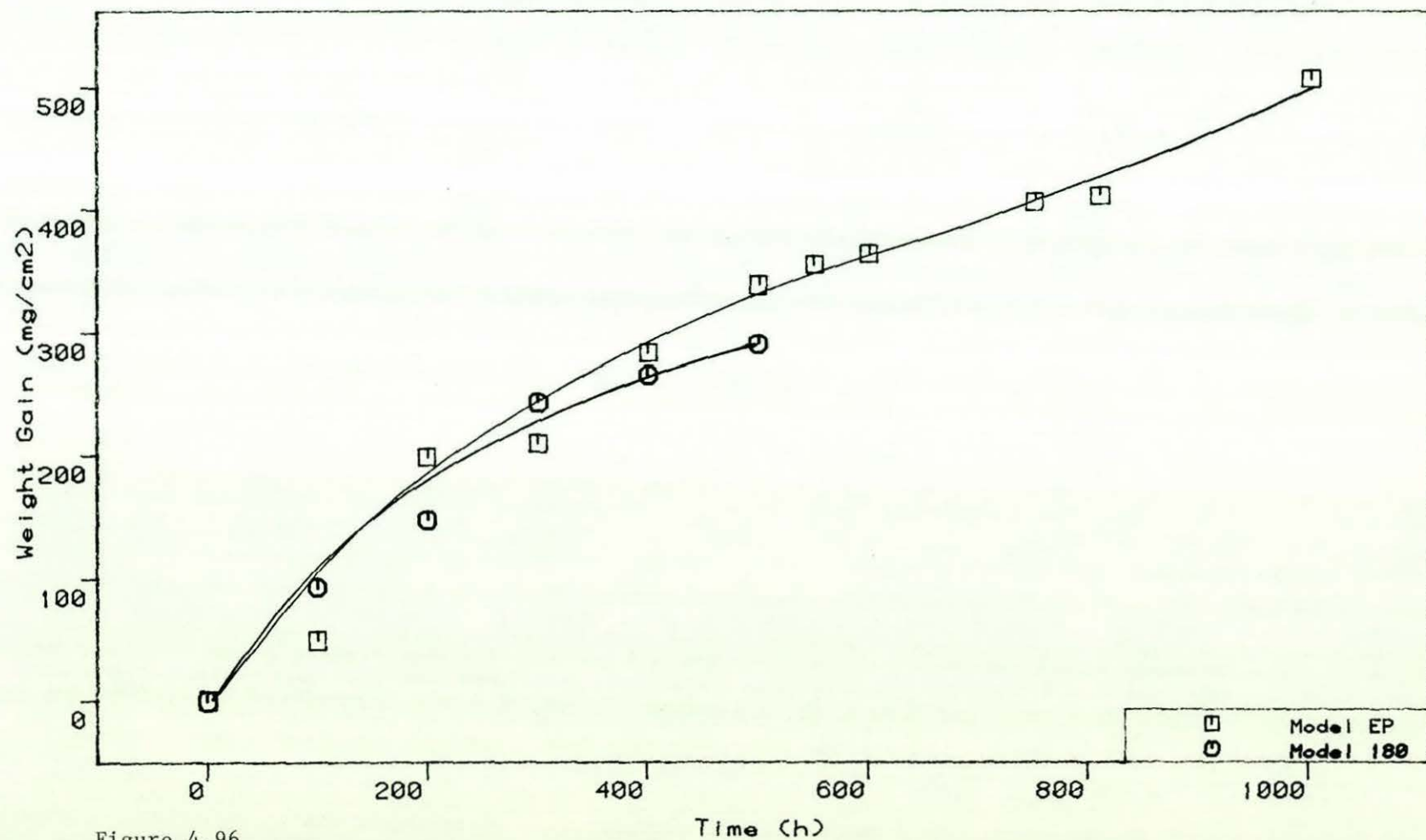
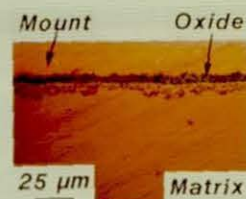


Figure 4.96

Corrosion kinetics for the Model 25Cr-35Ni-Fe alloy in the 0.6% H_2S gas at 800°C .

Figure 4.97

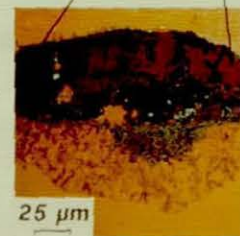
Cross-sectional examination using the Pepperhoff technique for the Model 25Cr-35Ni-Fe alloy exposed to the 0.6% H₂S gas at 800^oC.



a) 5 minutes



b) 1 hour



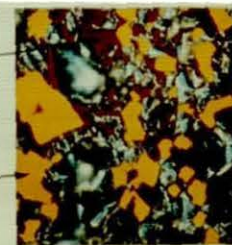
c) 5 hours



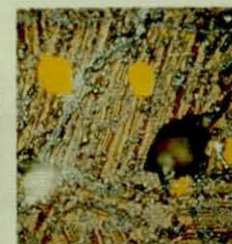
d) 25 hours



e) 100 hours



Sulphide Layer II



Sulphide Layer I



Internal Sulphide Layer



Sulphides
Carbides

Model 25Cr-35Ni-Fe 0.6% H₂S 800°C

Fe_{4,5} Ni_{4,5} S₈

Ni₂ Fe

(Fe,Cr)S

FeCr₂S₄

Sulphides

M₂₃C₆

Internal Attack — O — External Scale

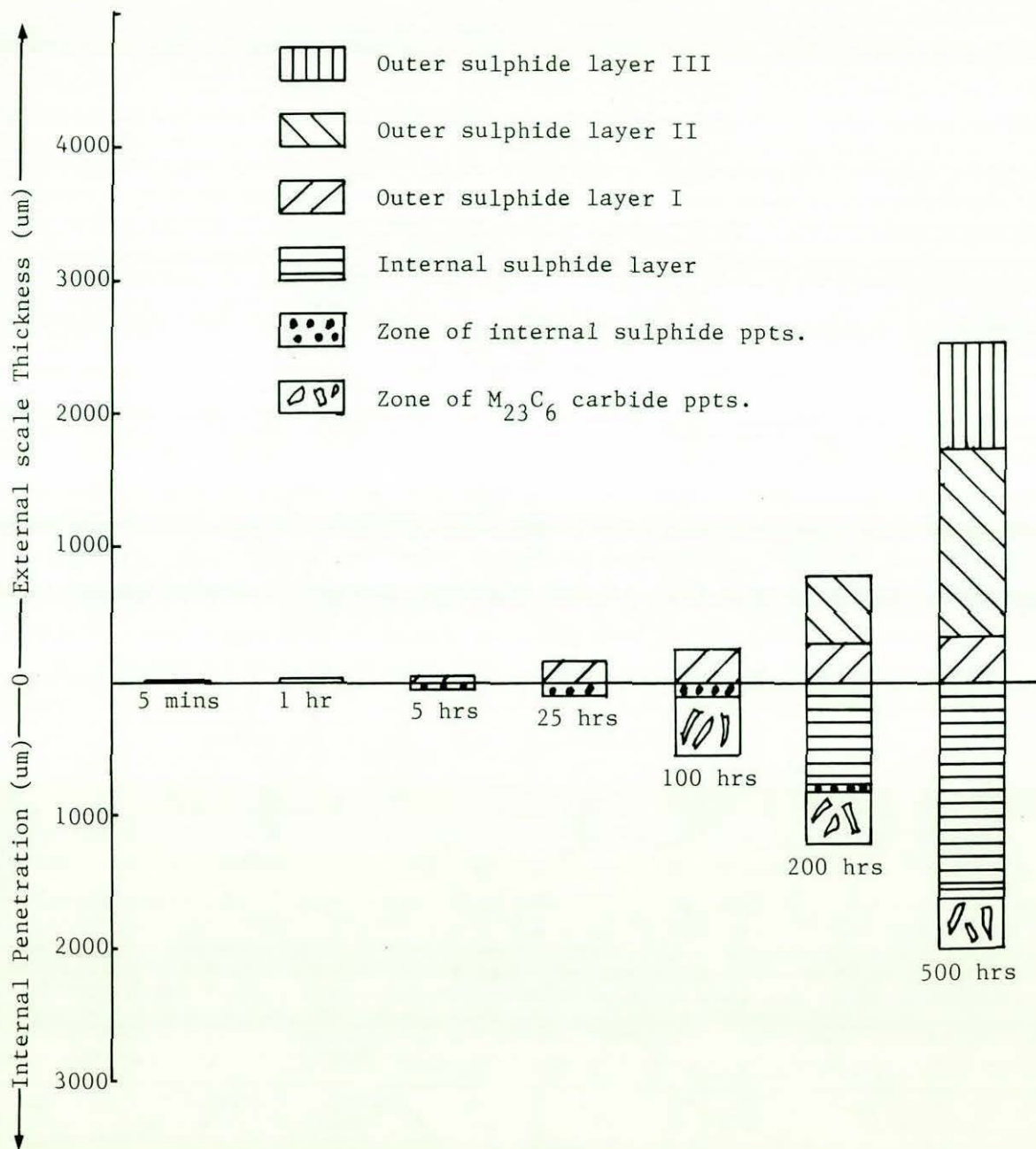


Figure 4.98

Diagram depicting the thickness of the various corrosion layers formed on the Model 25Cr-35Ni-Fe alloy during exposure to the 0.6 % H_2S gas at 800°C.

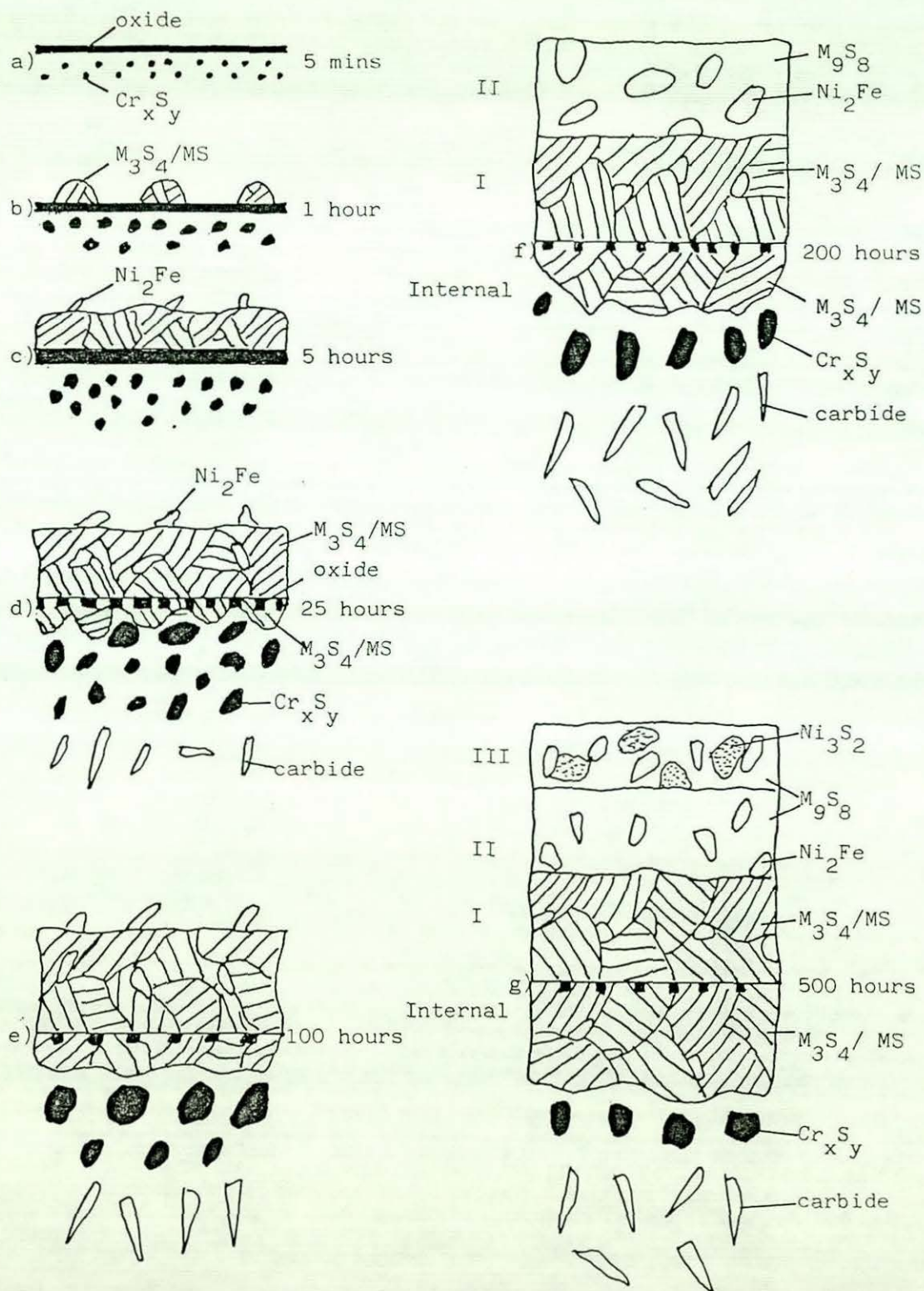


Figure 4.99

Summary figure showing the corrosion morphology of the model alloy in the 0.6% H_2S gas.

4.2.2. HP40Nb in the 0.6 % H₂S gas

The corrosion kinetics are presented in figure 4.100. This figure shows that the weight gains were very high (400 mg/cm² in 1000 hours) and that there was no significant difference between the electropolished and 180 grit specimens.

Examinations were carried out after 5 mins, 1 hour, 5 hours, 25 hours, 100 hours, 500 hours and 1000 hours.

5 mins.
.....

Cross-sectional examination using the Pepperhoff technique revealed that the corrosion morphology consisted of 3 regions : an oxide scale, a zone of internal sulphide precipitates and some localised attack of the primary carbides, figure 4.101a.

The (blue) rather porous looking oxide scale (5 µm thick) contained a number of sulphide particles. These sulphide particles tended to be concentrated in the outer regions of the scale. X-ray diffraction analysis using surface reflection confirmed that the scale contained M₃O₄, Cr₂O₃ and M₃S₄, table 4.23. The lattice parameter value indicated that the oxide spinel was FeCr₂O₄.

The zone of internal sulphide precipitates in the alloy substrate was approximately 2-3 µm deep. The different blue and brown colours of the precipitates indicated that they were a mixture of Mn and Cr sulphides.

Some localized attack of the primary M₇C₃/M₂₃C₆ carbides had taken place. This mainly consisted of oxidation although some sulphide particles were visible in the transformed carbides. The MC carbides at this stage had not been attacked and there was no sign of any carburisation due to carbon injection from the gas.

1 hour
.....

Cross-sectional examination using the Pepperhoff technique showed that the corrosion morphology consisted of 4 regions : A new discontinuous sulphide layer I on the outer surface of the scale, the former

predominantly oxide layer, a zone of internal sulphide precipitates and some localized attack of the primary carbides, figure 4.101b.

The discontinuous sulphide layer I (upto 7 μm thick) contained two types of lamellae, the lighter (brown) coloured FeCr_2S_4 and the darker coloured (purple) $(\text{Fe}_x\text{Cr}_y)_7\text{S}_8$. A few Ni_2Fe particles were also visible on the outer surface of the thicker areas of this layer. X-ray diffraction using surface reflection confirmed the presence of M_3S_4 and M_7S_8 , table 4.23.

The porous oxide layer (5 μm thick) was similar to before and still contained a number of sulphide particles. X-ray diffraction using surface reflection again confirmed the composition of the oxide phases in the layer as FeCr_2O_4 and Cr_2O_3 , table 4.23.

The internal sulphide precipitates were larger (2-3 μm diameter) and had advanced deeper (10 μm) into the alloy substrate.

As before a significant amount of localized attack of the $\text{M}_{23}\text{C}_6/\text{M}_7\text{C}_3$ carbides had taken place beneath the zone of internal sulphides. This mainly consisted of oxidation although some sulphide particles were visible in the transformed carbides. The MC carbides had not been attacked, although a few sulphide particles were nucleating around these carbides. There was no sign of any carburization due to carbon injection from the gas. The large number of secondary M_{23}C_6 carbide precipitates in the alloy substrate near the primary carbides, were attributed to aging processes.

5 hours
.....

Cross-section examination using the Pepperhoff technique now showed that the corrosion morphology consisted of 5 regions : an external sulphide layer I, the former predominantly oxide layer, a discontinuous mixed oxide/sulphide internal layer, a zone of internal sulphide precipitates and some localized attack of the primary carbides, figure 4.101c.

The former discontinuous external sulphide layer had now coalesced together to form the continuous external layer I (22 μm thick), which contained a large number of cracks and pores. This layer consisted of the light (brown coloured) more iron rich $(\text{Fe}_x\text{Cr}_y)_7\text{S}_8$ lamellae and the (yellow) metallic Ni_2Fe phase. This Ni_2Fe phase tended to be concentrated either on the outer surface or in the pores in the scale. X-ray diffraction using surface reflection confirmed the presence of M_3S_4 , M_7S_8 and Ni_2Fe .

The oxide layer (5 μm thick) at the original alloy interface was still relatively intact and contained a number of sulphide particles.

The new internal discontinuous layer (4-12 μm thick) consisted of a mixture of sulphides, oxides and metallic particles. This layer had a very fine structure making it difficult to analyse; however it appeared that the sulphides were the enlarged internal sulphides formally present in the zone of internal sulphide precipitates, the oxides were the remains of the transformed $\text{M}_{23}\text{C}_6/\text{M}_7\text{C}_3$ carbides and the metallic particles the remains of the depleted alloy substrate.

The zone of internal sulphide precipitates was still about the same thickness (10 μm) but was now situated deeper in the alloy beneath the discontinuous internal layer.

Deeper in the alloy some localized attack of the M_{23}C_6 carbides had continued to take place. The carbides appeared to have transformed predominantly to oxides with some sulphide particles often present at the deepest point of the attack (55 μm). Again the MC carbides appeared to be inert. There was no sign of any carburization due to in carbon injection from the gas. The secondary M_{23}C_6 carbide precipitates formed due to aging processes had grown and were starting to be more evenly distributed throughout the alloy.

25 hours
.....

Cross-section examination using the Pepperhoff technique showed that the corrosion morphology still consisted of 6 regions : an external sulphide layer I, the former predominantly oxide layer, a now continuous mixed

oxide/sulphide internal layer, a zone of internal sulphide precipitates, some localized attack of the primary carbides and a zone of carburization, figure 4.10ld.

The external sulphide layer I was now much thicker (160 μm) than before, figure 4.102. This layer still consisted of the two types of lamellae and the metallic Ni_2Fe particles. X-ray diffraction using surface reflection now indicated that the darker coloured lamellae were $(\text{Fe}_x\text{Cr}_y)\text{S}$ instead of $(\text{Fe}_x\text{Cr}_y)_7\text{S}_8$; the FeCr_2S_4 and Ni_2Fe were unchanged, table 4.23. These metallic Ni_2Fe particles tended to be concentrated either on the external surface or in pores in the scale.

The oxide layer was still present at the original alloy surface. This layer contained a considerable number of sulphide particles.

The internal fine grained mixed oxide/sulphide layer had now become complete, but was very uneven (5-80 μm thick). X-ray powder diffraction indicated that the layer was a mixture of FeCr_2O_4 and M_3S_4 , table 4.24. A considerable quantity of depleted alloy was still present in this layer. The zone of internal sulphide precipitates situated beneath the internal mixed oxide/sulphide layer was 35 μm thick and mirrored the outline of this layer.

Again a substantial amount of localised attack of the M_{23}C_6 carbides had occurred. In these areas most of the carbides had transformed to oxide, but some sulphide particles were visible particularly in the deepest regions of the attack (190 μm from the original alloy surface). A few small sulphide precipitates were now visible in the alloy substrate adjacent to the transformed carbides. It appeared that these had formed by transforming the secondary M_{23}C_6 carbides to sulphides. No carbides were visible in the depleted alloy substrate. Deeper in the alloy a zone containing a high proportion of carbides was now visible. It was however impossible to determine whether these had formed exclusively as the result of the release of carbon from the transformed carbides or also due to some carbon injection from the gas. The secondary M_{23}C_6 carbides formed due to aging processes had continued to coarsen and were now more evenly distributed throughout the alloy.

100 hours
.....

Cross-sectional examination using the Pepperhoff technique revealed that the corrosion morphology now consisted of 7 regions : an additional discontinuous outer sulphide layer II, the former external sulphide layer I, the remains of the oxide layer at the original alloy interface, the internal mixed oxide/sulphide layer, a zone of internal sulphide precipitates, some localised attack of the primary carbides and a zone of internal carburization, figure 4.101e.

The new discontinuous outer sulphide layer II (80 μm thick) consisted of a dark purple coloured sulphide and yellow metallic particles, figure 4.102. X-ray diffraction analysis using surface reflection confirmed that the sulphide as $\text{Fe}_{4,5}\text{Ni}_{4,5}\text{S}_8$ and the metallic particles as Ni_2Fe , table 4.23.

External sulphide layer I which was now 285 μm thick and still consisted of the two types of sulphide lamellae and the Ni_2Fe metallic phase. This metallic phase again tended to be concentrated in pores in the scale. X-ray diffraction analysis using surface reflection confirmed the presence of M_3S_4 , MS and Ni_2Fe , table 4.23.

The oxide layer was still visible at the original alloy interface. As before this oxide contained a larger number of sulphide particles.

The internal mixed oxide/sulphide layer again was rather uneven (average thickness 190 μm) and contained a mixture of sulphides, oxides and depleted alloy substrate. The oxides often had the morphology of the transformed carbide precipitates. X-ray powder diffraction confirmed that this layer was now a mixture of M_3S_4 , M_7S_8 and M_3O_4 , table 4.24.

The zone of internal sulphide precipitates (35 μm thick) was similar to before.

Again a significant amount of localised attack of the M_{23}C_6 carbides had occurred (upto 250 μm deep) with the carbides transforming predominantly to oxides. The MC carbides had remained inert. A considerable number of

sulphide precipitates were present in the depleted alloy substrate around the transformed $M_{23}C_6$ and the MC carbides. These appeared to be attacking the secondary $M_{23}C_6$ precipitates.

A very pronounced zone of carburization was now present deeper in the alloy. However it was again impossible to determine whether this was due exclusively carbon release from the transformed carbides or to some carbon injection from the gas.

500 hours
.....

Cross-section examination using the Pepperhoff technique now showed that the corrosion morphology consisted of 8 regions, figure 4.103. A new outer sulphide layer III, the now continuous outer sulphide layer II, the external sulphide layer I, the remains of oxide layer at the original alloy interface, the internal mixed oxide/sulphide layer, a zone of internal sulphide precipitates, some localised attack of the primary carbides and a zone of internal carburisation.

The new outer sulphide layer III contained the (pink) Ni_3S_2 phase, (dark purple) $Fe_{4,5}Ni_{4,5}S_8$ and (yellow) Ni_2Fe metallic particles, figure 4.102.

The external sulphide layer (500 μm thick) still consisted of the two types of sulphide lamellae, now both containing Fe and Ni in addition to Fe and Cr, and the metallic Ni_2Fe particles.

The oxide scale at the original alloy interface had become rather broken up and still contained a large number of sulphides.

The internal mixed oxide/sulphide layer was now considerably thicker (700 μm), but still contained a mixture of fine grained oxide and sulphide particles in addition to a considerable proportion of depleted alloy substrate. This layer also contained a large number of cracks. X-ray powder diffraction confirmed the presence of M_3O_4 , M_3S_4 and M_7S_8 , table 4.24.

The zone of internal sulphidation (35 μm thick) and localised attack of the M_{23}C_6 carbides were situated deeper in the alloy (800 μm from the original alloy surface), but were otherwise the same as before.

Finally the amount of carbides in the carburised zone (125 μm thick) had increased significantly, probably due to release of carbon from the transformed carbides.

Summary

The corrosion behaviour of the HP40Nb alloy in the 0.6 % H_2S gas can be summarised as a number of stages, figure 4.104

- Stage 1 (5 mins)

Initially a mixed Cr_2O_3 and FeCr_2O_4 oxide scale, which also contained a number of sulphide particles, formed on the alloy surface. Simultaneously a number of small sulphide precipitates formed in the alloy substrate and some localised attack of the primary M_{23}C_6 carbides took place. These carbides transformed predominantly to oxides with some sulphides also present at the deepest point of attack, figure 4.104a.

- Stage 2 (1 hour)

A discontinuous outer sulphide layer I containing FeCr_2S_4 and more iron-rich $(\text{Fe}_x\text{Cr}_y)_7\text{S}_8$ lamellae formed on top of the original predominantly oxide layer. The zone of internal Cr/Mn sulphide precipitates and localised attack of the carbides advanced deeper into the alloy, figure 4.104b.

- State 3 (5 hours)

The outer sulphide layer I became continuous. This layer consisted of the FeCr_2S_4 and $(\text{Fe}_x\text{Cr}_y)_7\text{S}_8$ lamellae and a number of metallic particles on the outer surface and in the pores in the scale. A new discontinuous internal layer formed which consisted of a mixture of sulphides, oxides and metallic particles. It appeared that the sulphides were the enlarged internal sulphides formally present in the zone of internal sulphide precipitates, the oxides were the

remains of the transformed $M_{23}C_6/M_7C_3$ carbides and the metallic particles the remains of the depleted alloy substrate. The zone of internal sulphide precipitates and localised attack of the carbides situated beneath discontinuous internal scale advanced deeper into the alloy, figure 4.104c.

- Stage 4 (25 hours)

The outer sulphide layer I continued to thicken and the internal mixed oxide/sulphide layer became continuous and advanced deeper into the alloy substrate. The zone of internal sulphide precipitates and localised attack of the primary $M_{23}C_6$ carbides continued to advance ahead of the internal mixed oxide/sulphide layer. The attack of these carbides led to the release of carbon which diffused deeper into the alloy substrate to form a zone of carbide precipitates. It was impossible to determine if some of these additional carbide precipitates were also due to carbon injection from the gas, figure 4.104d.

- Stage 5 (100 hours)

A new outer sulphide layer II containing $Fe_{4,5}Ni_{4,5}S_8$ and Ni_2Fe metallic particles formed. The other corrosion layers continued to advance as before, figure 4.104e.

- Stage 6 (500 hours)

Another outer sulphide layer III formed. This layer contained Ni_3S_2 , $Fe_{4,5}Ni_{4,5}S_8$ and Ni_2Fe . The outer sulphide layer II still contained $Fe_{4,5}Ni_{4,5}S_8$ and Ni_2Fe . Outer sulphide layer I contained the two types of lamellae, (both now rich in Fe, Cr and Ni) and the Ni_2Fe metallic phase. Some of the oxide layer was still visible at the original alloy surface. The mixed oxide/sulphide layer advanced deeper into the alloy substrate. This layer still contained a large amount of depleted alloy substrate. The zones of internal sulphide precipitates, localised internal attack of the carbides and internal carburisation were still present beneath the mixed oxide/sulphide layer, figure 4.107f.

In summary the sequence of events was essentially the same as for the Model 25Cr-35Ni-Fe alloy. The only difference was that in the case of HP40Nb a considerable amount of internal oxidation took place. This was due to the $M_{23}C_6$ carbides transforming to oxides and the stabilizing effect of Si on these oxides. The presence of the oxides tended to slow down the rate of the corrosion process but the amount of attack was still extremely severe.

Exposure Time	Phase Identified (Intensity/Parameter Å)								
	Austenite	Ni ₂ Fe	Cr ₂ O ₃	M ₃ O ₄	M ₇ S ₈	MS	M ₃ S ₄	M ₉ S ₈	Ni ₃ S ₂
5 mins	87/3.583	-	4/4.956-13.542	14/8.405	-	-	7/9.960	-	-
1 hr	75/3.571	-	2/4.96 -13.63	9/8.407	I = 10	-	5/9.980	-	-
5 hrs	-	32/5.568	-	-	32/3.48-5.78	-	27/10.005	-	-
25 hrs	-	40/3.562	-	-	-	traces	20/10.003	-	-
100 hrs	-	15/3.561	-	-	-	I = 20	35/10.008	16/10.176	-
1000 hrs	-	17/3.557	-	-	15/3.44-5.77	-	24/10.005	16/10.171	-

Table 4.23

X-ray diffraction analysis of HP40Nb exposed to the 0.6 % H₂S gas at 800°C.

Exposure Time	Phase Identified (Intensity/Parameter)								
	Austenite	Ni ₂ Fe	Cr ₂ O ₃	M ₃ O ₄	M ₇ S ₈	MS	M ₃ S ₄	M ₉ S ₈	Ni ₃ S ₂
25 hrs	-	-	1/-	-	10/-	-	60/10.000	-	-
100 hrs	-	-	-	54/8.398	34/3.45-5.766	-	70/ 9.999	-	-
500 hrs	-	-	-	60/8.390	1/-	-	60/ 9.989	-	-

Table 4.24

X-ray powder diffraction data for the internal mixed oxide/sulphide layer formed on HP40Nb during exposure to the 0.6 % 0.6 % H₂S gas at 800°C.

PS2=10-8 bar, PO2=10-21 bar, aC=0.3, 800degC

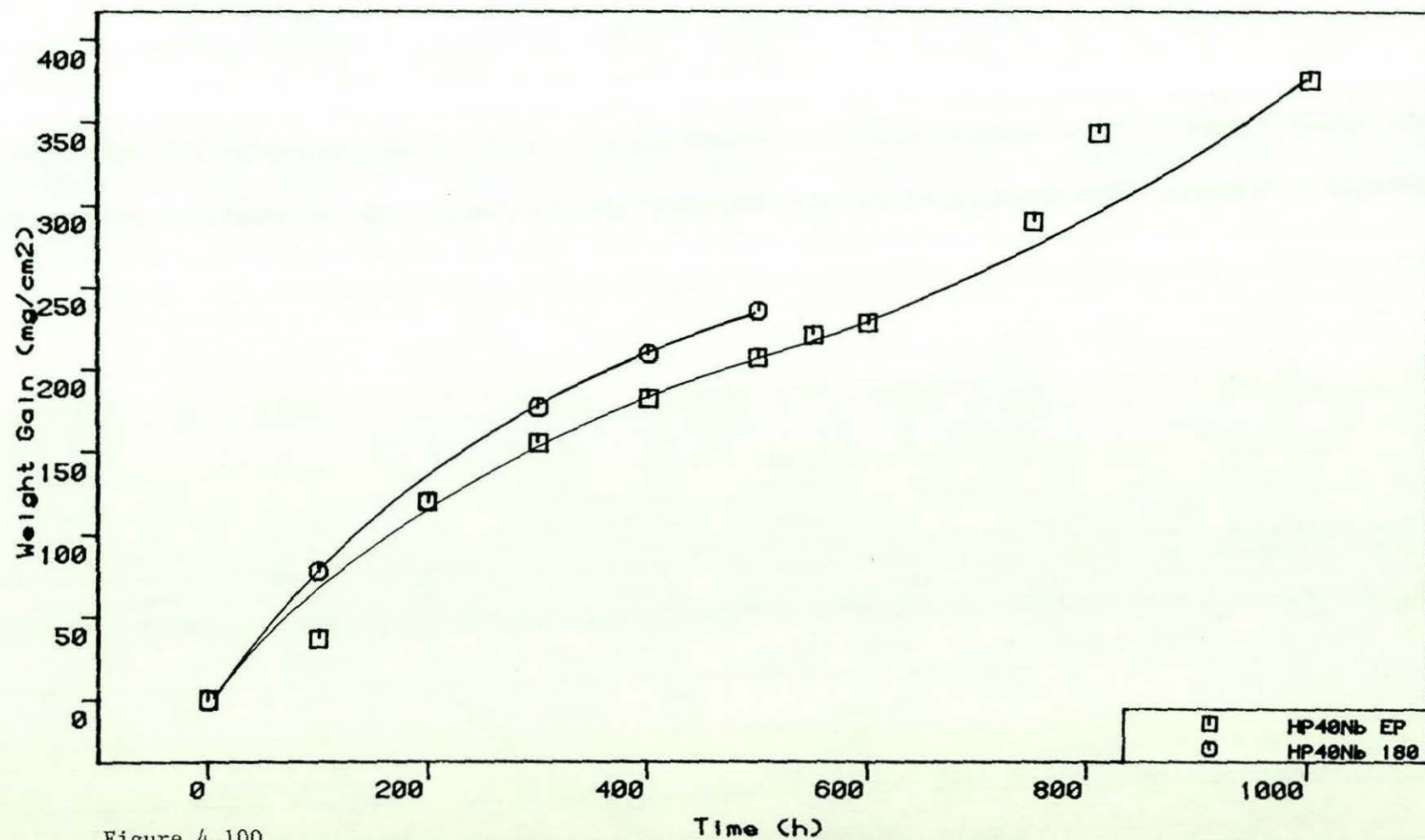
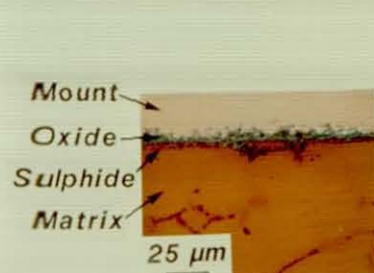


Figure 4.100
Corrosion kinetics for HP40Nb in the 0.6 % H₂S gas at 800°C.

Figure 4.101

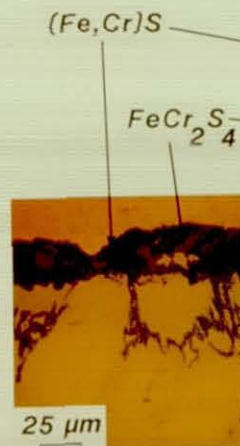
Cross-sectional examination using the Pepperhoff technique for HP40Nb exposed to the 0.6% H₂S gas at 800°C.



a) 5 minutes



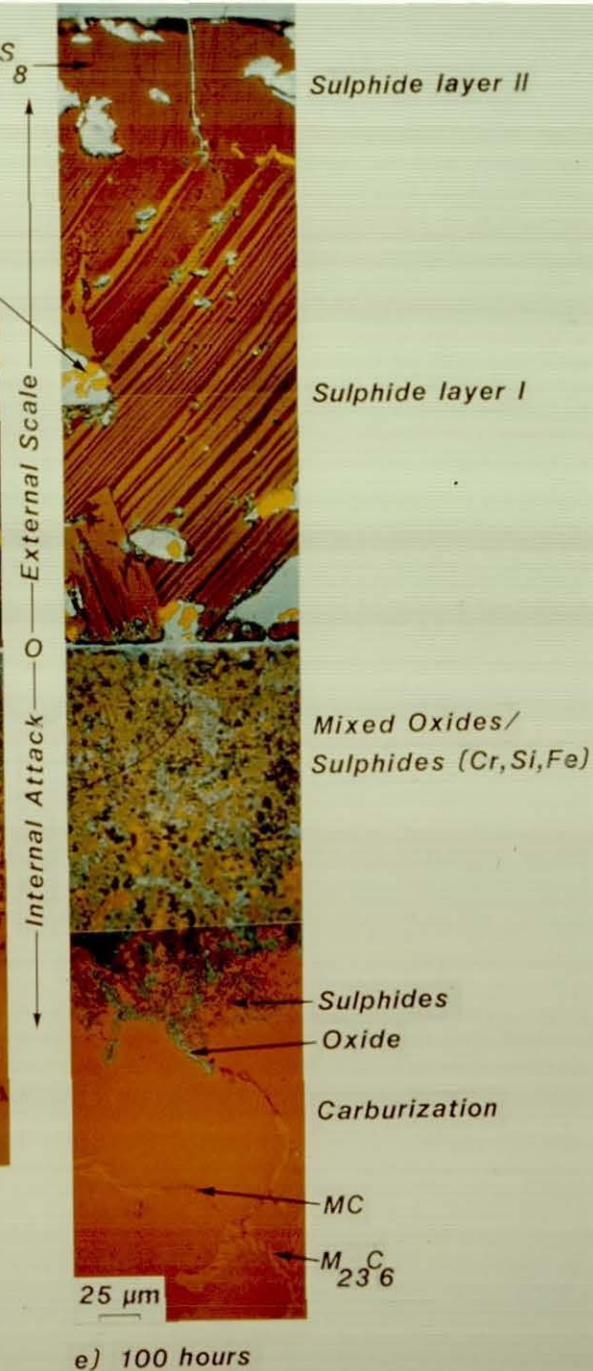
b) 1 hour



c) 5 hours



d) 25 hours



e) 100 hours

HP40Nb 0.6% H₂S 800°C

Fe_{4,5} Ni_{4,5} S₈

Ni₂ Fe

Sulphide layer II

Sulphide layer I

Mixed Oxides/
Sulphides (Cr, Si, Fe)

Sulphides

Oxide

Carburization

MC

M₂₃C₆

External Scale
O
Internal Attack

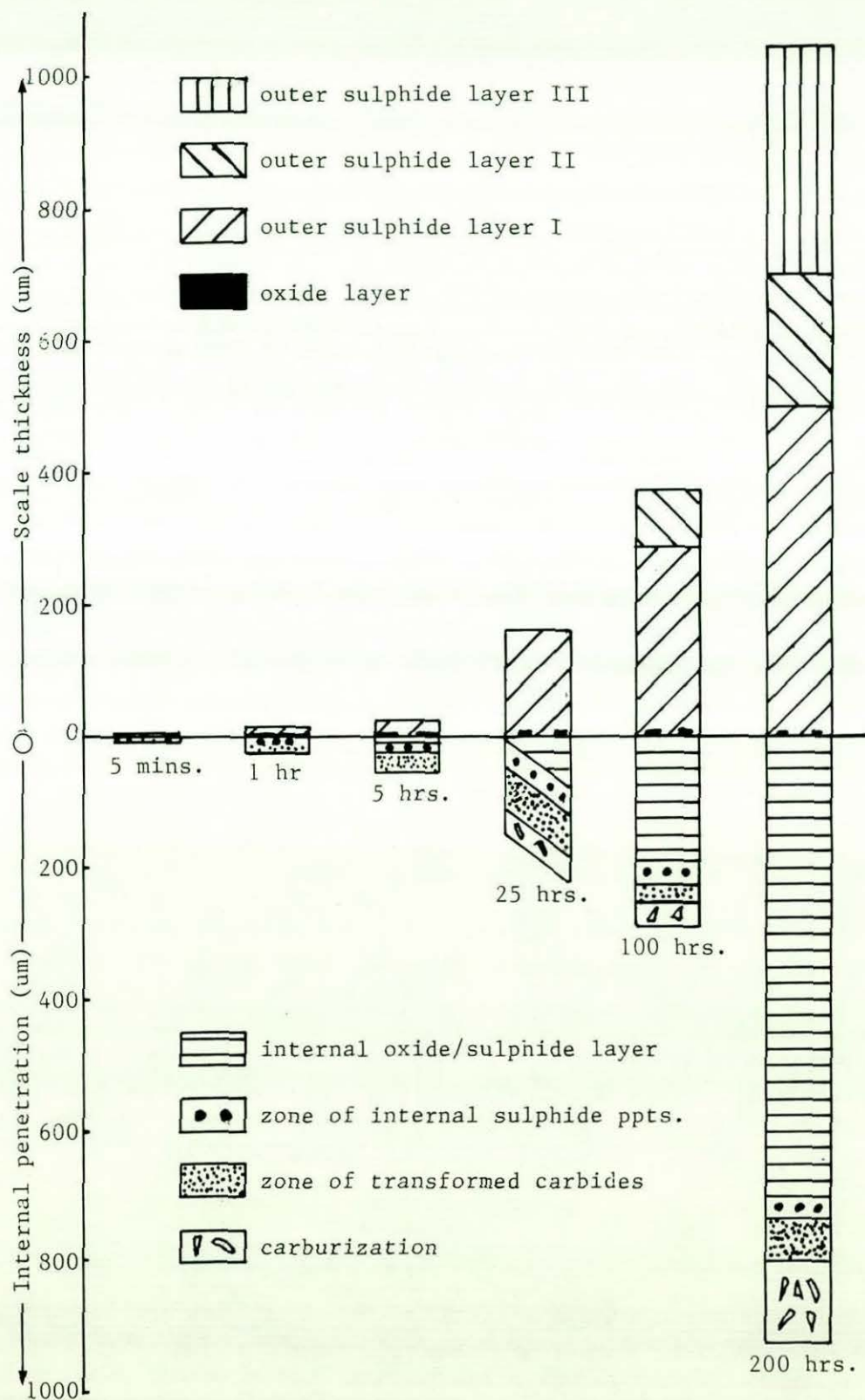


Figure 4.102

Diagram depicting the thickness of the various corrosion layers formed on the HP40Nb during exposure to the 0.6 % H₂S gas at 800°C.

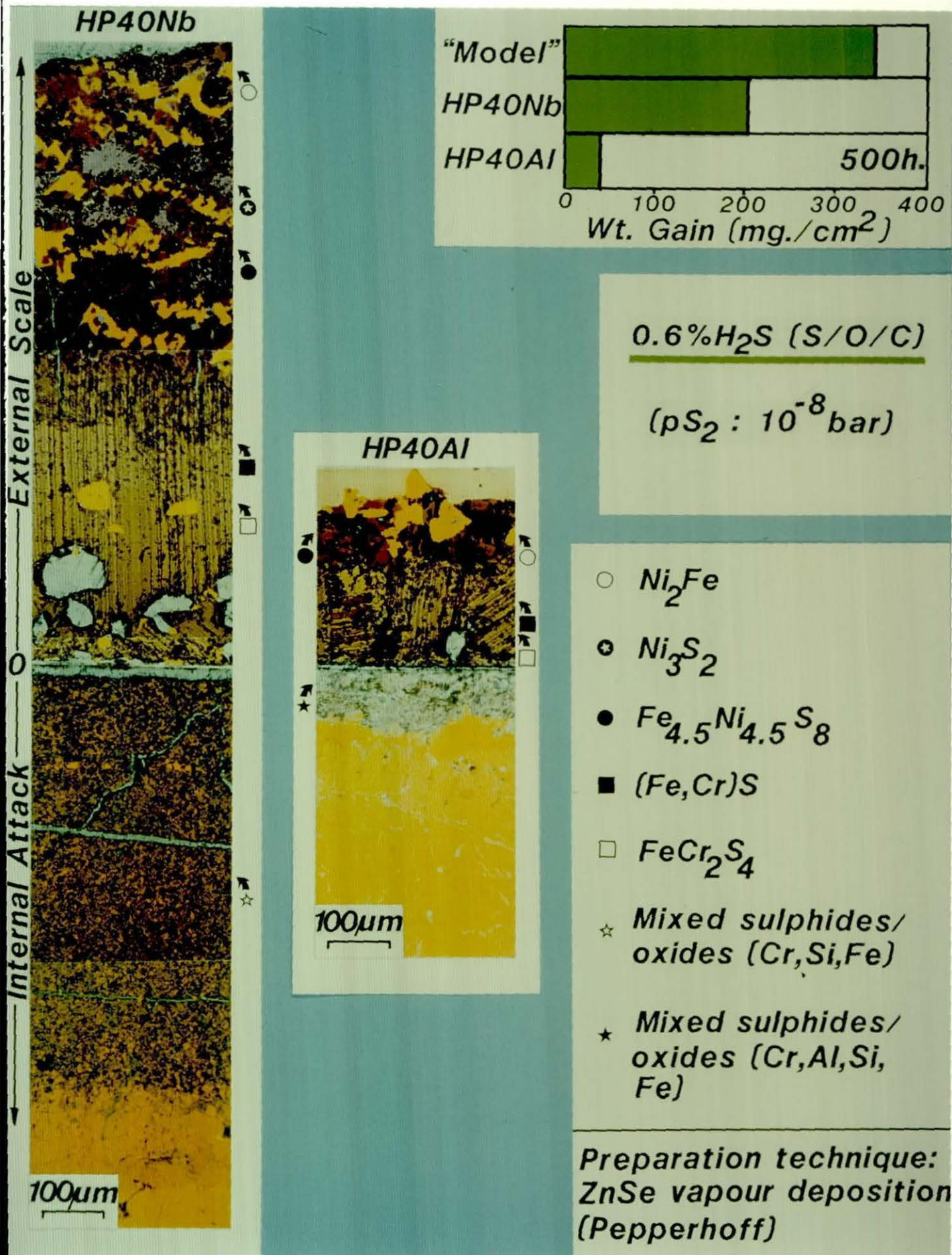


Figure 4.103

Cross-sectional examination using the Pepperhoff technique to compare the corrosion behaviour of the HP40Nb and HP40Al alloys after exposure to the 0.6 % H₂S gas for 500 hours.

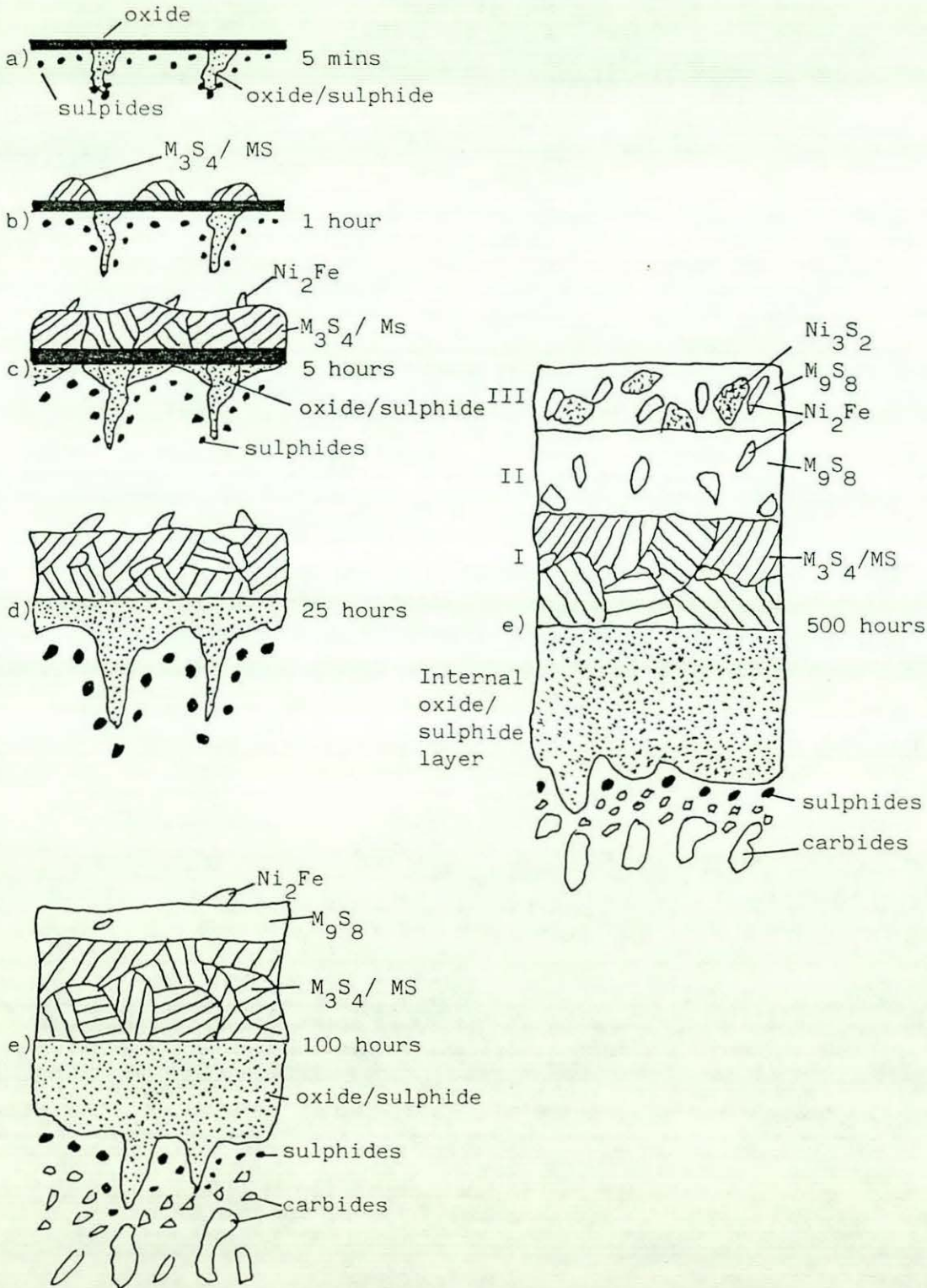


Figure 4.104

Summary figure showing the corrosion behaviour of HP40Nb in the 0.6% H_2S gas at 800° C .

4.2.3. HP40Al in the 0.6 % H₂S gas

The corrosion kinetics are presented in figure 4.105. This figure shows that the weight uptake in the early stages was low, but as time progressed the corrosion rate accelerated. Weight gains of 120 mg/cm² were obtained in 1000 hours exposure. There was little difference between the electropolished (EP) and 180 grit specimens. Although the weight uptake was considerable it was much less than the Model 25Cr-35Ni-Fe and HP40Nb alloys.

Examinations were carried out after 5 mins, 1 hour, 5 hours, 25 hours, 100 hours, 500 hours and 1000 hours.

5 mins
.....

Cross-sectional examination using the Pepperhoff technique revealed that the corrosion morphology consisted of 3 regions : an external oxide scale, a zone of internal sulphide precipitates and some localized sulphidation of the M₆C carbides, figure 4.106a.

The oxide scale (8 μm thick) contained a number of sulphide particles. X-ray diffraction using surface reflection confirmed that the scale was predominantly a mixture of FeCr₂O₄ and Cr₂O₃, table 4.25.

The zone of internal sulphide precipitates was approximately (2-3 μm) deep. The sulphide precipitates were small and the different colours indicated that they contained varying amounts of Mn and Cr.

Some localised sulphidation of the M₆C carbides had taken place (depth 17 μm). There was no sign of any localized attack of the MC and M₂₃C₆ carbides or carburization due to carbon injection from the gas at this stage.

1 hour
.....

Cross-sectional examination using the Pepperhoff technique showed that the corrosion morphology now contained 5 regions : a new discontinuous outer sulphide layer I, the oxide scale, the zone of internal sulphide

precipitates, some localized sulphidation of the M_6C carbides and now some localized oxidation of the $M_{23}C_6$ carbides, figure 4.106b.

The discontinuous sulphide layer I (upto 9 μm thick) contained two types of lamellae, the lighter $FeCr_2S_4$ and the darker coloured $(Fe_xCr_y)_7S_8$. X-ray diffraction using surface reflection confirmed the presence of M_3S_4 and M_7S_8 .

The oxide layer (8 μm thick) had not changed and still contained a number of sulphide particles. X-ray diffraction using surface reflection confirmed that this layer was still a mixture of $FeCr_2O_4$ and Cr_2O_3 , table 4.24.

The zone of internal sulphide precipitates had not changed (4 μm thick).

The M_6C carbides had continued to sulphidize (depth 15 μm). A significant amount of localized oxidation of the $M_{23}C_6$ carbides was now commencing (depth 10 μm). The major proportion of these carbides had transformed to oxide with some small sulphide particles also present. The MC carbides had not been attacked.

5 hours
.....

Cross-sectional examination using the Pepperhoff technique showed that the corrosion morphology consisted of the same 5 regions: the discontinuous outer sulphide layer I, the oxide scale, a zone of internal sulphide precipitates, some localized sulphidation of the M_6C carbides and some localized oxidation of the $M_{23}C_6$ carbides, figure 4.106c.

The discontinuous outer sulphide layer I was now upto 20 μm thick and contained some Ni_2Fe particles in addition to the $FeCr_2S_4$ and $(Fe_xCr_y)_7S_8$ sulphide lamellae. X-ray diffraction using surface reflection confirmed the presence these phases, table 4.24.

The (7 μm thick) oxide layer still contained a number of sulphide particles. X-ray diffraction using surface reflection confirmed that

this layer contained M_3O_4 and Cr_2O_3 . The lattice parameter of the oxide spinel had increased slightly indicating that it now contained Mn in addition to Fe and Cr.

The sulphides in the zone of internal precipitates had become larger and tended to be concentrated in localized areas.

The M_6C carbides had continued to be converted to sulphides (depth 18 μm) and the $M_{23}C_6$ carbides predominantly to oxides and a few sulphides particles (depth 57 μm). The MC carbides had not been attacked.

25 hours
.....

Cross-sectional examination using the Pepperhoff technique now showed that the corrosion morphology consisted of 6 regions : the now continuous outer sulphide layer I, the oxide layer at the original alloy surface, a new discontinuous internal mixed oxide/sulphide layer, a zone of internal sulphide precipitates, localized sulphidation of the M_6C carbides and localized oxidation of the $M_{23}C_6$ carbides, figure 4.106d.

The outer sulphide layer was now continuous (32 μm thick), figure 4.107. This layer still consisted of $FeCr_2S_4$ and the more iron rich sulphide lamellae which now had the composition $(Fe_xCr_y)S$ instead of $(Fe_xCr_y)_7S_8$. The metallic Ni_2Fe particles were still present and tended to be situated either on the outer surface of the scale or in cracks and pores within the scale. X-ray diffraction using surface reflection confirmed the presence of M_3S_4 , MS and Ni_2Fe and also detected a few traces of M_9S_8 .

The oxide scale at the original alloy surface had not changed and still contained a number of sulphide particles.

A new discontinuous internal mixed oxide/sulphide layer had now formed. This layer which was very uneven (upto 42 μm depth) appeared to consist of a mixture of the sulphides formally present in the zone of internal sulphide precipitates, sulphides formally present in the transformed M_6C carbides and the oxides and sulphides from the transformed $M_{23}C_6$

carbides. The very fine porous structure of this layer made it difficult to analyse but X-ray powder diffraction detected Cr_2O_3 , M_3O_4 and M_3S_4 , table 4.26.

Internal sulphide precipitates were present in the alloy substrate beneath the discontinuous internal oxide/sulphide layer. Some localized sulphidation of the M_6C and oxidation of the M_{23}C_6 carbide precipitates had continued to take place deeper in the alloy.

100 hours
.....

Cross-sectional examination using the Pepperhoff technique revealed that the corrosion morphology still consisted of the same 6 regions : the outer sulphide layer I, the oxide layer at the original alloy surface, a now continuous internal mixed oxide/sulphide layer, a zone of internal sulphide precipitates, localized sulphidation of the M_6C carbides and localized oxidation of the M_{23}C_6 carbides, figure 4.108.

The outer sulphide layer was now 60 μm thick (figure 4.107) and still contained the light coloured FeCr_2S_4 , the dark coloured $(\text{Fe}_x\text{Cr}_y)\text{S}$ sulphide lamellae and the metallic Ni_2Fe particles. X-ray diffraction using surface reflection confirmed the presence of these phases and again detected traces M_9S_8 .

The oxide layer at the original alloy surface was unchanged and still contained a number of sulphide particles.

The internal mixed oxide/sulphide layer had now become continuous but was still very uneven (upto 50 μm deep). X-ray powder diffraction again indicated that this layer was a mixture of M_3S_4 , M_3O_4 and Cr_2O_3 , table 4.26. The fine porous nature of this layer made it difficult to analyse by EPMA. X-ray mapping however indicated that the layer was rich in Al, Si and Cr, figure 4.109.

A few sulphide precipitates were still present in the depleted alloy substrate beneath the internal oxide/sulphide layer. The localized attack of the M_6C and M_{23}C_6 carbides was the same as before.

500 hours
.....

Cross-sectional examination using the Pepperhoff technique showed that the corrosion morphology now consisted of 7 regions : a new outer sulphide layer II, the outer sulphide layer I, the oxide at the original alloy interface, the internal mixed oxide/sulphide layer, a zone of internal sulphide precipitates, localized sulphidation of the M_6C carbides, and localized oxidation of the $M_{23}C_6$ carbides, figure 4.108.

The new outer sulphide layer (upto 110 μm thick) contained the dark purple sulphide phase $Fe_{4,5}Ni_{4,5}S_8$ and yellow Ni_2Fe particles. The composition of these phases was confirmed by EPMA point analysis, figure 4.110, and X-ray diffraction using surface reflection, table 4.24.

Outer sulphide layer I (190 μm thick) still contained the 2 types of sulphide lamellae. EPMA point analysis showed that the lighter (brown coloured) lamellae were still $FeCr_2S_4$ but that the darker (purple) lamellae were $Fe_{4,5}Ni_{4,5}S_8$ and contained virtually no chromium. This rather surprising observation was also confirmed by X-ray diffraction using surface reflection which detected only M_3S_4 and M_9S_8 and no MS or M_7S_8 . The presence of M_9S_8 in this layer instead of MS or M_7S_8 was an exception to an otherwise consistent trend so perhaps too much significance should be attached to this result.

The oxide layer at the original alloy surface was now discontinuous and contained a number of sulphide particles.

The internal mixed oxide/sulphide layer had only thickened slightly. EMPA area analysis again showed that this layer was rich in Cr, Al and Si, figure 4.110. X-ray powder diffraction indicated the presence of Cr_2O_3 , M_3O_4 and M_3S_4 , table 4.26.

The matrix beneath the internal mixed oxide/sulphide layer was almost totally depleted in Cr and contained only about 25 % Fe. This resulted in the matrix containing a relatively high proportion of Ni. As in the case of shorter term exposures a small amount of internal sulphide

precipitates were present in this zone. Again localized sulphidation of the M_6C carbides had taken place and the $M_{23}C_6$ carbides transformed to oxides with some sulphide particles also present.

1000 hours

.....

Cross-sectional examination using the Pepperhoff technique revealed that the corrosion morphology now consisted of 8 regions : a new outer sulphide layer III, outer sulphide layer II, outer sulphide layer I, remains of the oxide layer at the original alloy surface, the internal mixed oxide/sulphide layer, a zone of internal sulphide precipitates, localized sulphidation of the M_6C carbides and localized oxidation of the $M_{23}C_6$ carbides, figure 4.108.

Outer sulphide layer III (330 μm thick) which appeared to have been molten at the test temperature consisted of Ni_3S_2 (pink), $Fe_{4,5}Ni_{4,5}S_8$ (dark purple) and Ni_2Fe particles (yellow). The composition of these phases was confirmed by EPMA point analysis, figure 100. The Ni_3S_2 phase was not present in sufficient quantities to be detected by X-ray diffraction using surface reflection. This technique however did confirm the presence of M_9S_8 and Ni_2Fe , table 4.25.

Outer sulphide layer II had thickened considerably (240 μm) and contained $Fe_{4,5}Ni_{4,5}S_8$ and Ni_2Fe particles. The composition of these phases was confirmed by EPMA point analysis, figure 4.111.

Outer sulphide layer I (250 μm thick) still contained the two types of sulphide lamellae and the metallic particles. EPMA analysis showed that the lighter coloured (M_3S_4) lamellae now contained a considerably amount of Ni in addition to Fe and Cr. The darker coloured (MS) lamellae contained considerable quantities of Fe and Ni and less Cr.

Small amounts of the oxide layer were still visible at the original alloy surface. X-ray diffraction using surface reflection identified this as a mixture of Cr_2O_3 and M_3O_4 , table 4.25.

The internal mixed oxide/sulphide layer (240 μm thick) had not thickened to the same extent as the outer sulphide layers. EPMA analysis showed that this layer was still rich in Cr, Al and Si but now also contained an appreciable quantity of Fe.

Surprisingly the matrix beneath the internal oxide/sulphide layer did not appear to be depleted in Cr and only slightly depleted in Fe. As before a small amount of sulphide precipitates were present in the alloy substrate. Localized sulphidation of the M_6C carbides had taken place, the M_{23}C_6 carbides had transformed to oxides and some sulphide particles.

Summary

The corrosion behaviour of HP40Al alloy in the 0.6 % H_2S gas can be summarised in a number of stages, figure 4.112.

- Stage 1 (5 mins)

Initially a mixed Cr_2O_3 and FeCr_2O_4 oxide layer formed which contained a number of sulphide particles. Simultaneously a number of small sulphide precipitates formed in the alloy substrate and some localized sulphidation of the primary M_6C carbides took place, figure 4.112a.

- Stage 2 (1 hour)

A discontinuous outer sulphide layer I, containing FeCr_2S_4 and the more iron rich $(\text{Fe}_x\text{Cr}_y)_7\text{S}_8$ lamellae, formed on top of the original predominantly oxide layer. The oxide layer, the zone of internal sulphide precipitates and the localized sulphidation of the M_6C remained the same. Some localized attack of the primary M_{23}C_6 carbides took place. These carbides transformed predominantly to oxides which also contained some sulphides, figure 4.112b.

- Stage 3 (5 hours)

The discontinuous outer sulphide layer I now contained metallic Ni_2Fe particles in addition to the two types of sulphide lamellae. The rest of the corrosion morphology was the same as before, figure 4.112c.

- Stage 4 (25 hours)

The outer sulphide layer was now complete and the oxide layer at the original surface unchanged. A new discontinuous internal mixed oxide/sulphide layer started to form. This layer appeared to consist of a mixture of sulphides and oxides formally present in the zone of internal sulphide precipitates and the transformed carbides. The zone of internal sulphide precipitates and the localized sulphidation of the M_6C and oxidation/sulphidation of the $M_{23}C_6$ carbides continued to take place beneath the internal oxide/sulphide layer, figure 4.112d.

- Stage 5 (100 hours)

The internal mixed oxide/sulphide layer became continuous. This layer which contained M_3S_4 , M_3O_4 and Cr_2O_3 was rich in Al, Si and Cr. It would appear that the presence of this layer accounted for the considerably lower weight gains of this alloy. The rest of the corrosion morphology had advanced but structurally was the same as before, figure 4.112e.

- Stage 6 (500 hours)

A new outer sulphide layer II formed which contained $Fe_{4,5}Ni_{4,5}S_8$ and Ni_2Fe metallic particles. The outer sulphide layer I consisted of $FeCr_2S_4$ lamellae and Ni_2Fe metallic particles. The more iron rich lamellae at this particular time were $Fe_{4,5}Ni_{4,5}S_8$. The oxide layer at the original alloy surface was now discontinuous and contained a number of sulphide particles. The internal mixed oxide/sulphide layer which was rich in Cr, Al and Si had not thickened significantly. A small amount of internal sulphide precipitates were present beneath the internal mixed oxide/sulphide layer. The localized attack of the carbides continued as before, figure 4.112f.

- Stage 7 (1000 hours)

A new outer sulphide layer III formed which contained Ni_3S_2 , $Fe_{4,5}Ni_{4,5}S_8$ and metallic Ni_2Fe particles. This layer appeared to have been molten at the test temperature. Outer sulphide layer II had thickened but still contained $Fe_{4,5}Ni_{4,5}S_8$ and Ni_2Fe . Outer sulphide layer I had thickened slightly. Both the M_3S_4 and MS sulphide lamellae in this layer contained appreciable amounts of Ni in addition to Cr

and Fe. Small amounts of $\text{Cr}_2\text{O}_3/\text{M}_3\text{O}_4$ oxide were still present at the original alloy interface. The Cr, Al, Si rich internal mixed oxide/sulphide layer had not thickened to the same extent as the outer sulphide layers. This layer now also contained an appreciable amount of Fe. The zone of internal sulphide precipitates and the localized sulphidation of the M_6C and oxidation/sulphidation of the M_{23}C_6 carbides continued to precede the internal mixed oxide/sulphide scale, figure 4.112g.

Thus it was concluded that the 3.5 % Al addition to this alloy led to the formation of an internal Al rich mixed oxide/sulphide layer which inhibited the inward diffusion of sulphur and slowed down the outward diffusion of Cr, Fe and Ni. Corrosion was still very severe and followed the same sequence of events as the HP40Nb alloy, but at a slower rate, figure 4.103.

Exposure Time	Phase Identified (Intensity/Parameter Å)								
	Austenite	Ni ₂ Fe	Cr ₂ O ₃	M ₃ O ₄	M ₇ S ₈	MS	M ₃ S ₄	M ₉ S ₈	Ni ₃ S ₂
5 mins	197/3.578	-	2/4.961-13.465	6/8.389	-	-	-	-	-
1 hr	65/3.579	-	-	8/8.397	10/3.44-5.72	-	8/10.002	-	-
5 hrs	91/3.569	-	3/4.96-13.55	7/8.411	16/3.44-5.68	-	9/10.002	-	-
25 hrs	-	47/3.566	-	-	-	traces	17/10.020	traces	-
100 hrs	-	15/3.562	5/4.96-13.57	15/8.404	-	I = 10	33/10.001	traces	-
500 hrs	-	-	12/4.96-13.59	20/8.367	-	-	38/10.007	25/10.137	-
1000 hrs	-	-	21/4.96-13.57	29/8.377	-	-	7/10.002	32/10.118	-

Table 4.25

X-ray diffraction data HP40A1 exposed to the 0.6 % H₂S gas at 800°C.

Exposure Time	Phase Identified (Intensity/Parameter Å)								
	Austenite	Ni ₂ Fe	Cr ₂ O ₃	M ₃ O ₄	M ₇ S ₈	MS	M ₃ S ₄	M ₉ S ₈	Ni ₃ S ₂
25 hrs	-	-	5/-	10/-	-	-	10/-	-	-
100 hrs	-	-	18/4.959-13.569	12/8.440	-	-	60/10.018	-	-
500 hrs	-	-	19/4.953-13.576	10/8.388	15/3.443-5.772	-	14/ 9.987	-	-

Table 4.26

X-ray powder diffraction data for the internal mixed oxide/sulphide layer formed on HP40Al during exposure to the 0.6 % H₂S gas at 800°C.

PS2=10-8 bar, PO2=10-21 bar, aC=0.3, 800degC

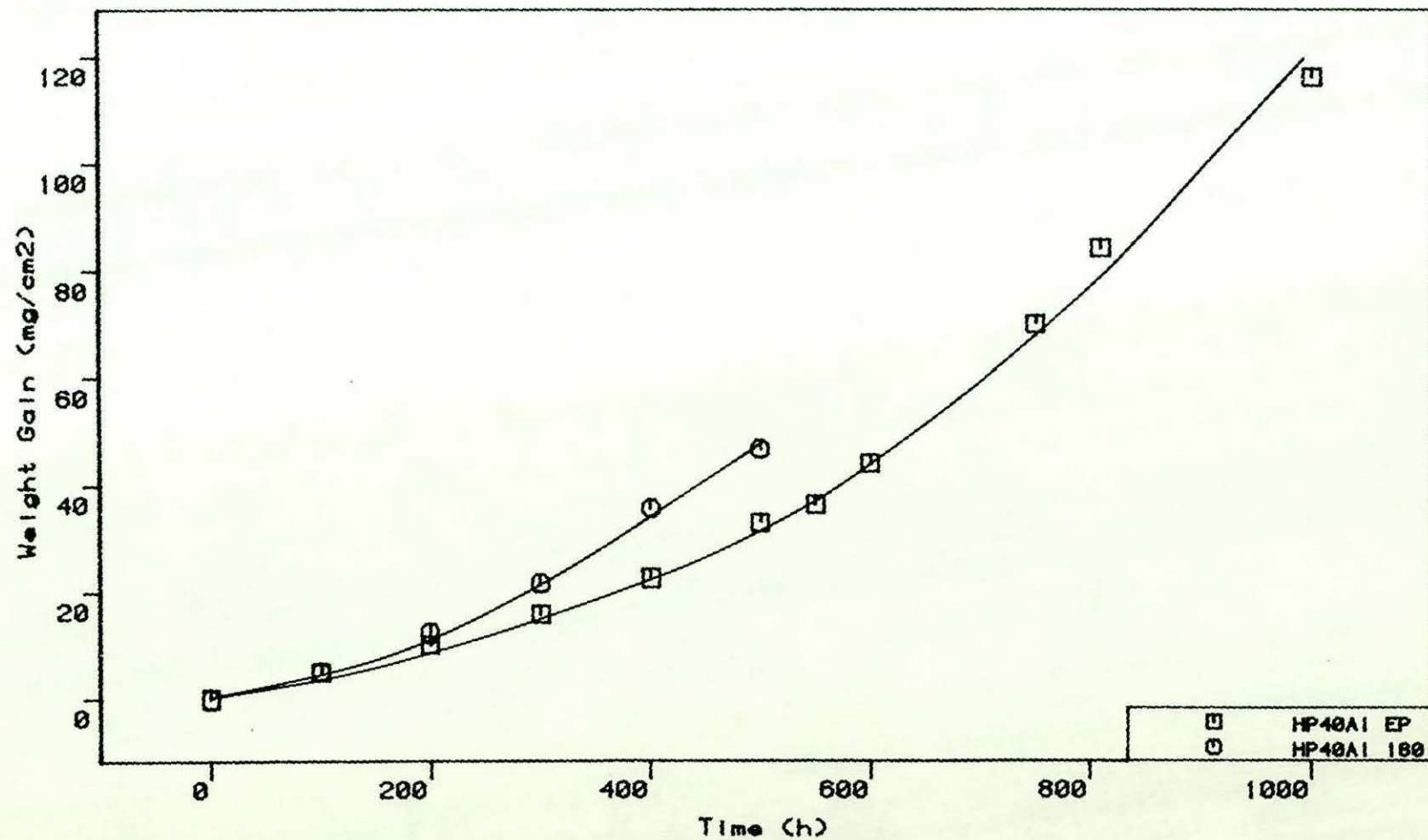


Figure 4.105

Corrosion kinetics for HP40Al in the 0.6 % H₂S gas at 800°C.

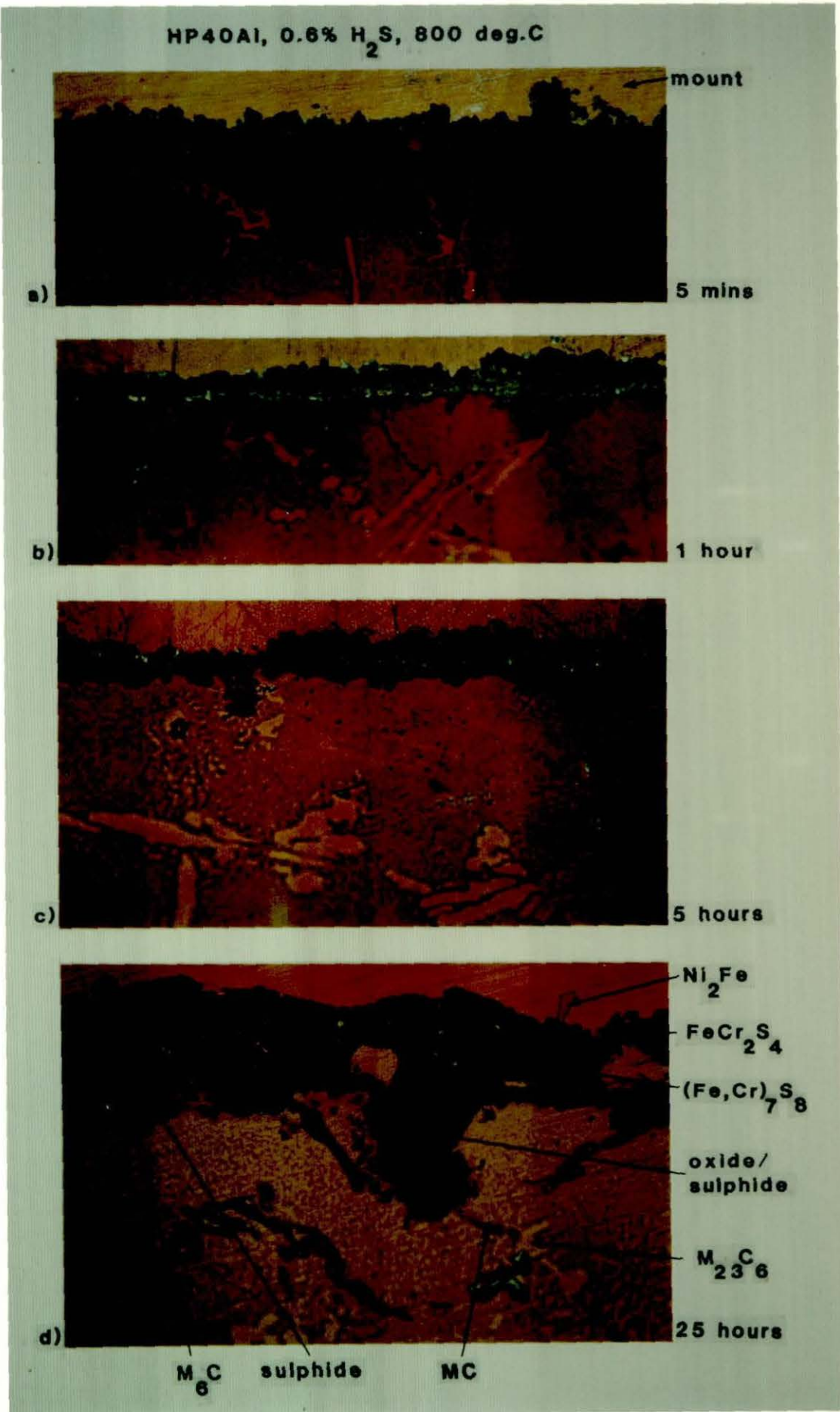


Figure 4.106

Cross-sectional examination using the Pepperhoff technique for HP40Al exposed to the 0.6 % H₂S gas at 800°C.

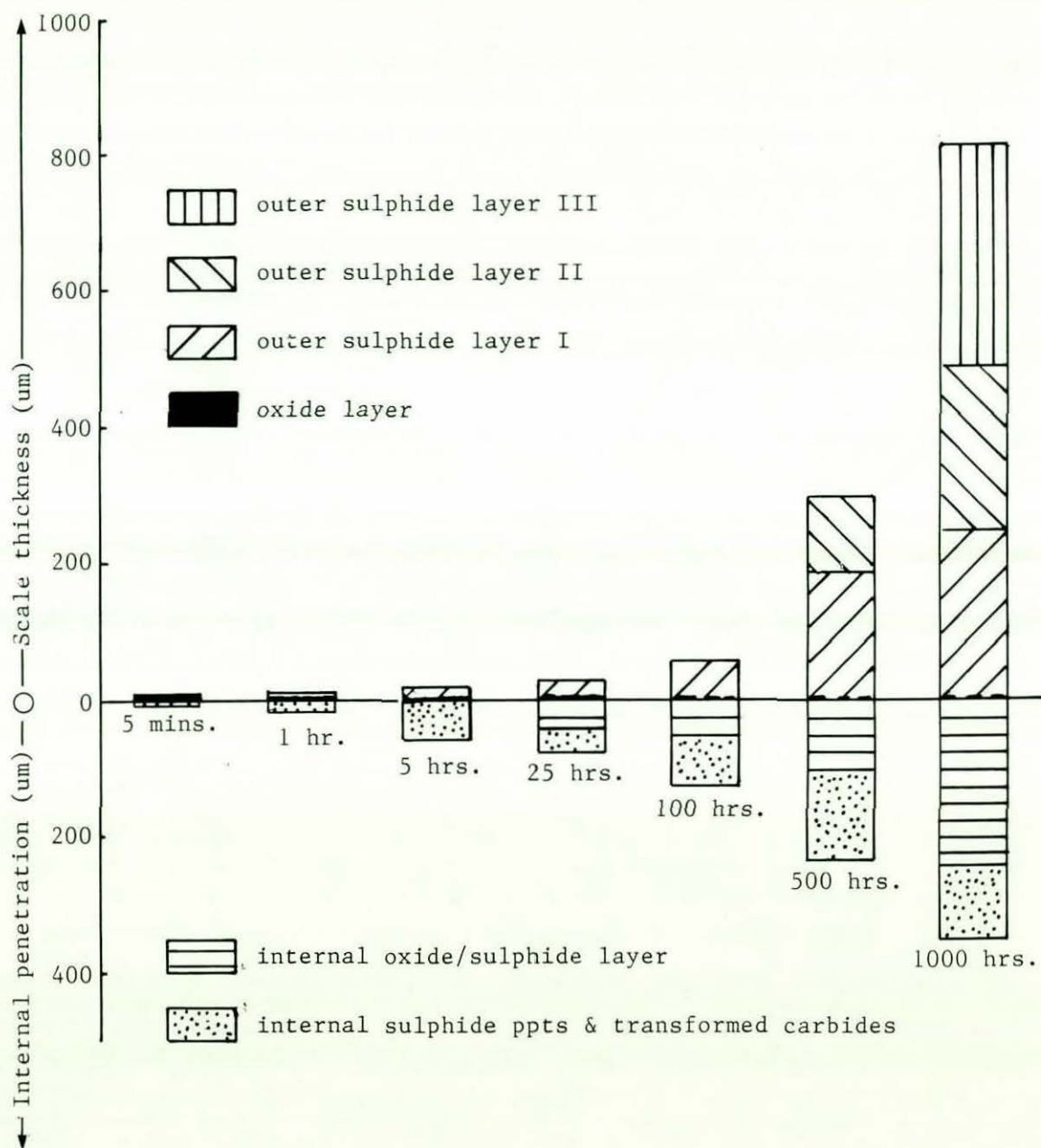


Figure 4.107

Diagram depicting the thickness of the various corrosion layers formed on the HP40Al alloy during exposure to the 0.6 % H_2S gas at $800^\circ C$.

INFLUENCE OF EXPOSURE PERIOD UPON CORROSION OF HP40Al.

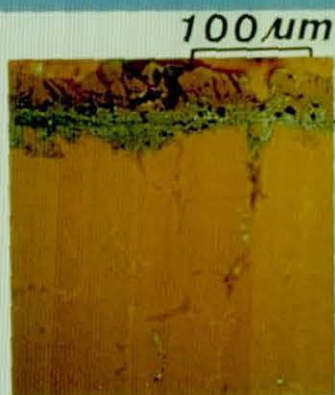
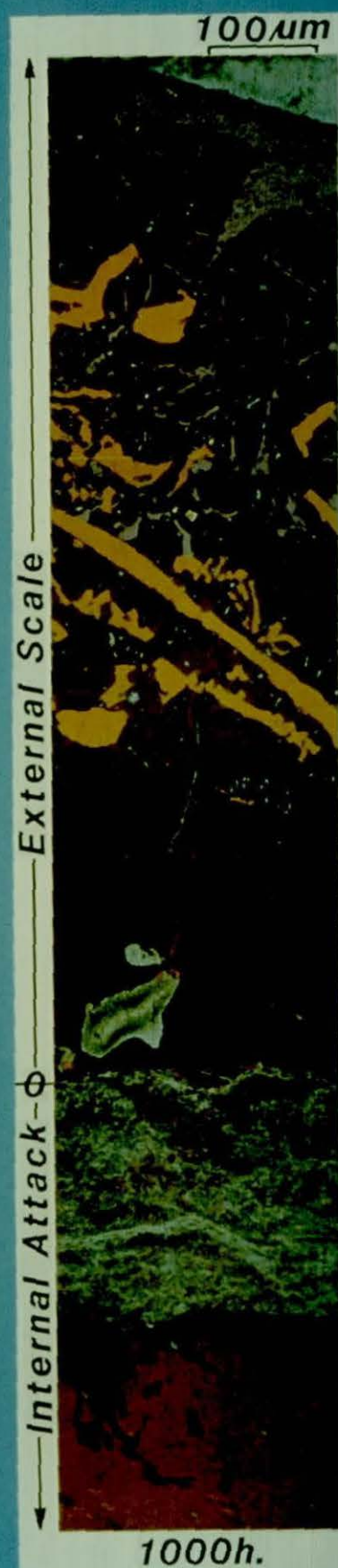
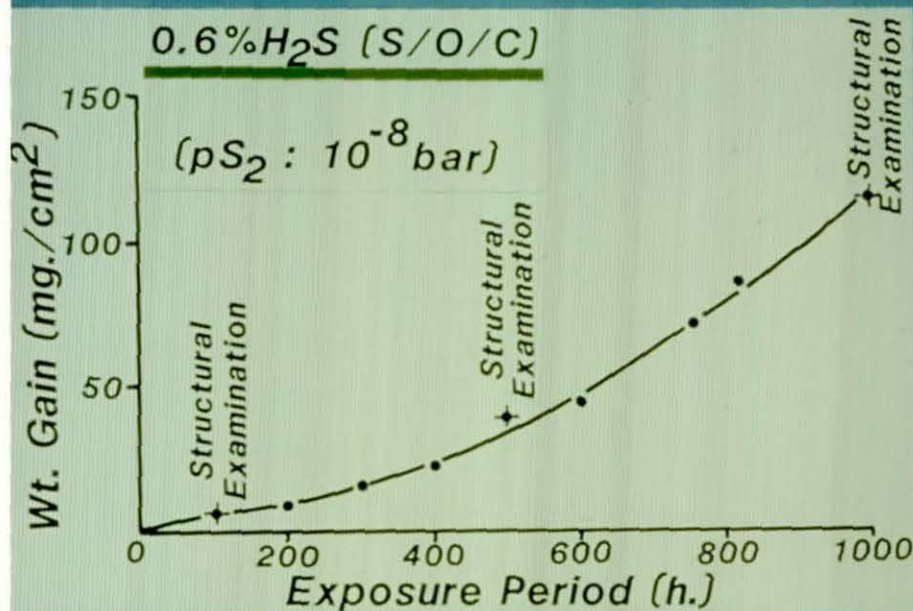
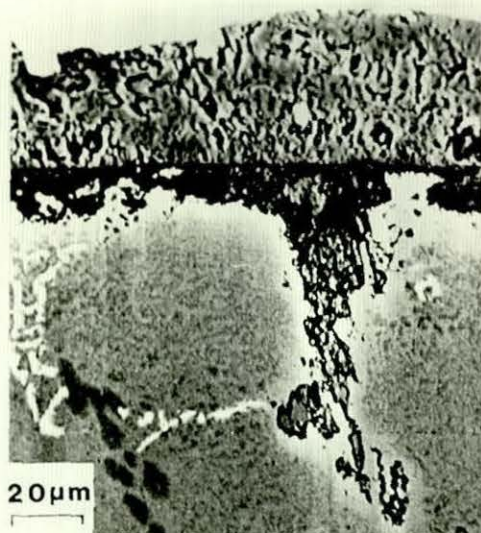
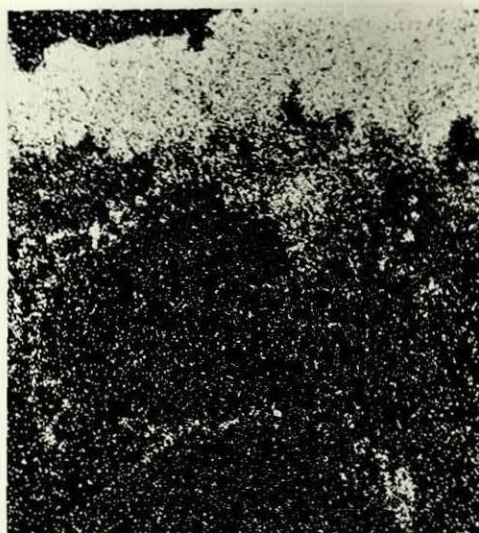


Figure 4.108

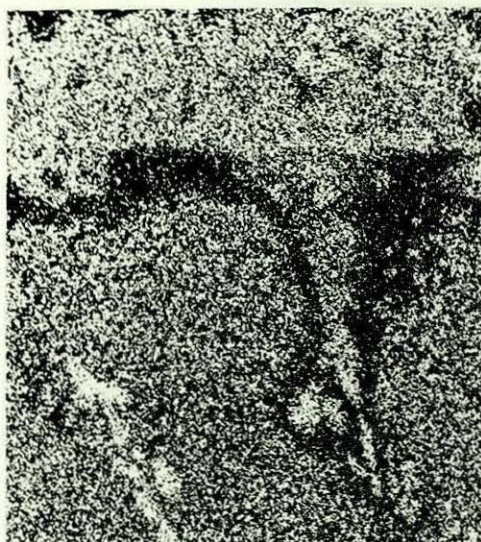
Cross-sectional examination using the Pepperhoff technique for HP40Al exposed to the 0.6 % H₂S gas at 800°C.



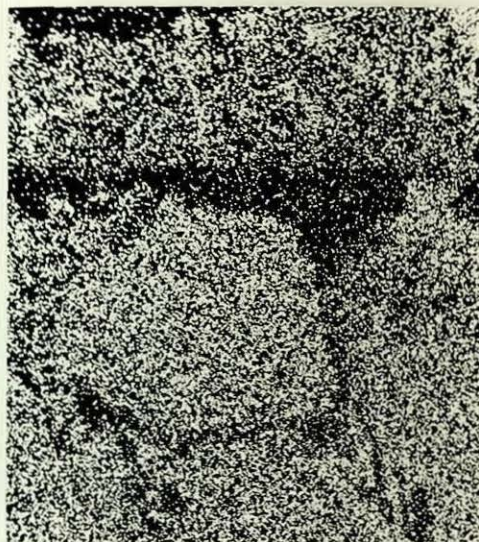
Image



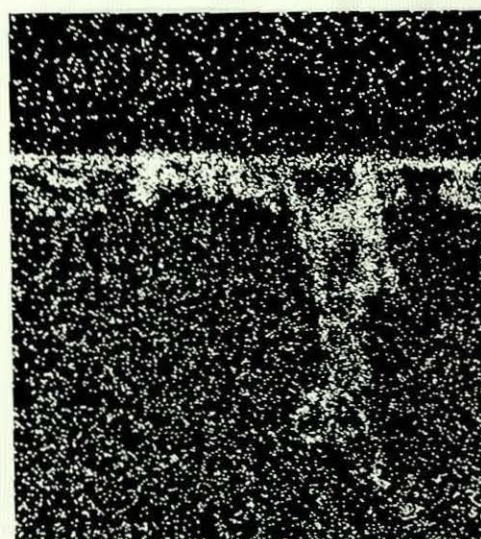
S



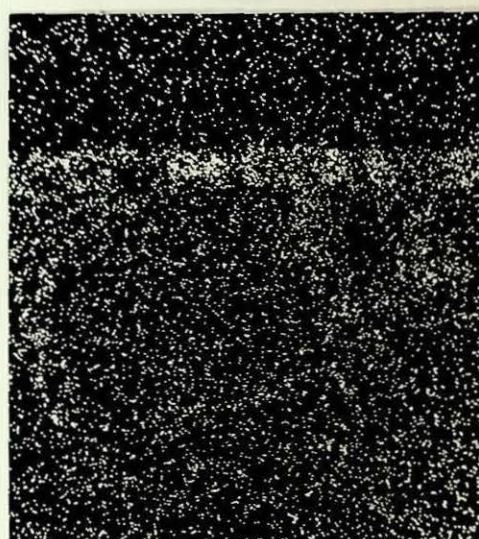
Cr



Fe



Al



Si

Figure 4.109
X-ray mapping of HP40Al exposed to the 0.6 % H_2S gas at 800°C for 100 hours.

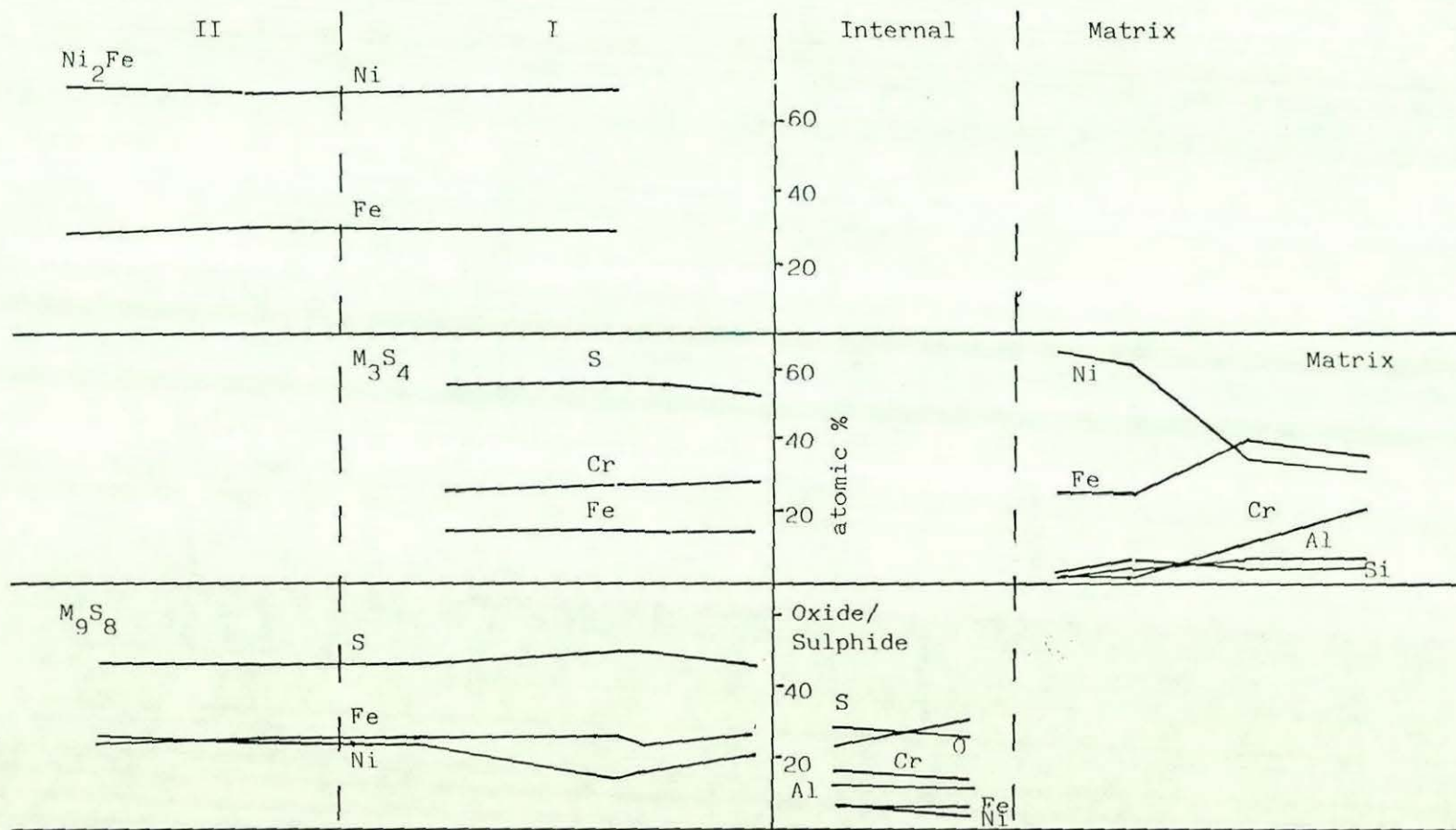


Figure 4.110

EPMA analysis on HP40Al exposed to the 0.6% H₂S gas at 800°C for 500 hours.

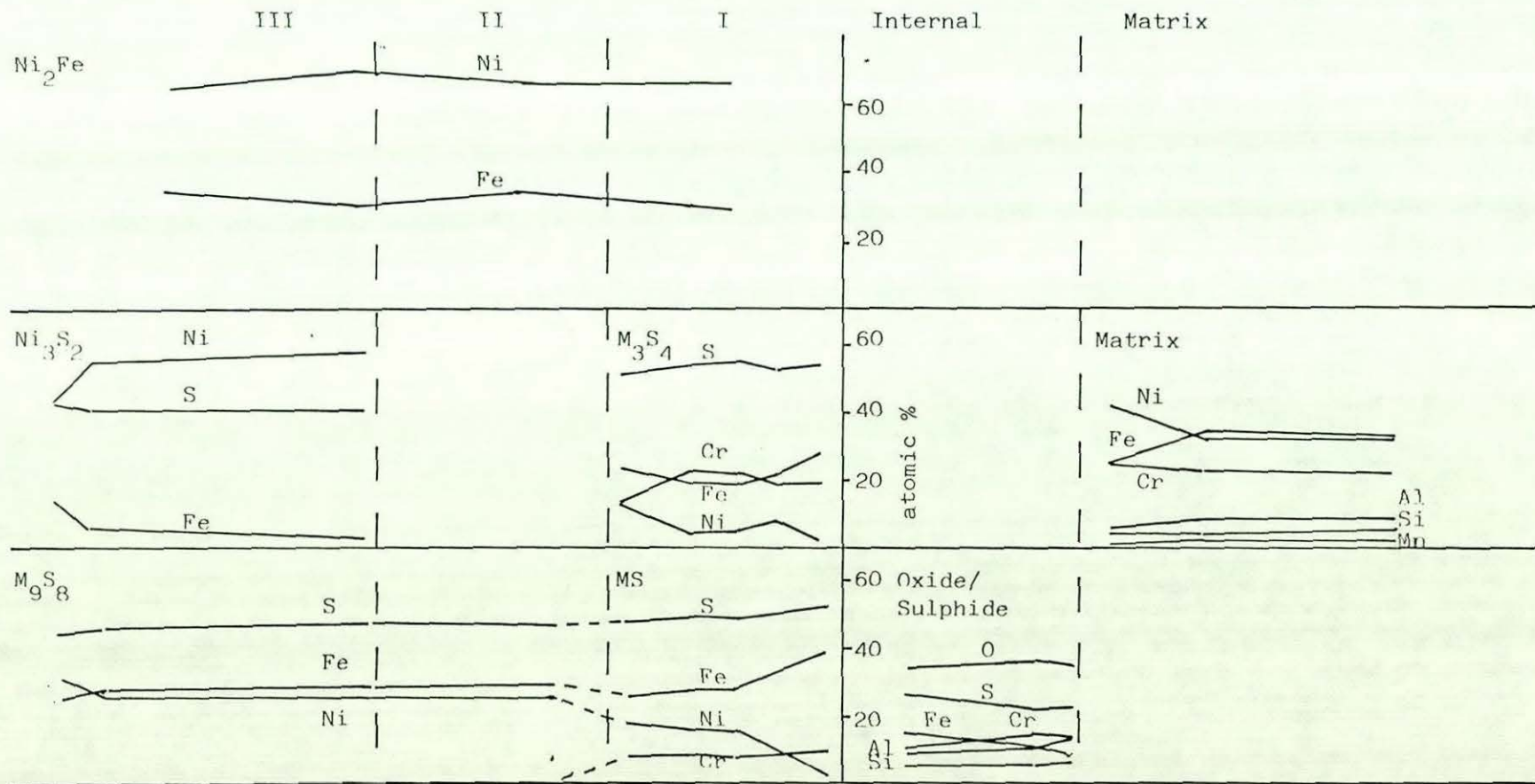


Figure 4.111

EPMA analysis on HP40Al exposed to the 0.6% H_2S gas at 800°C for 1000 hours.

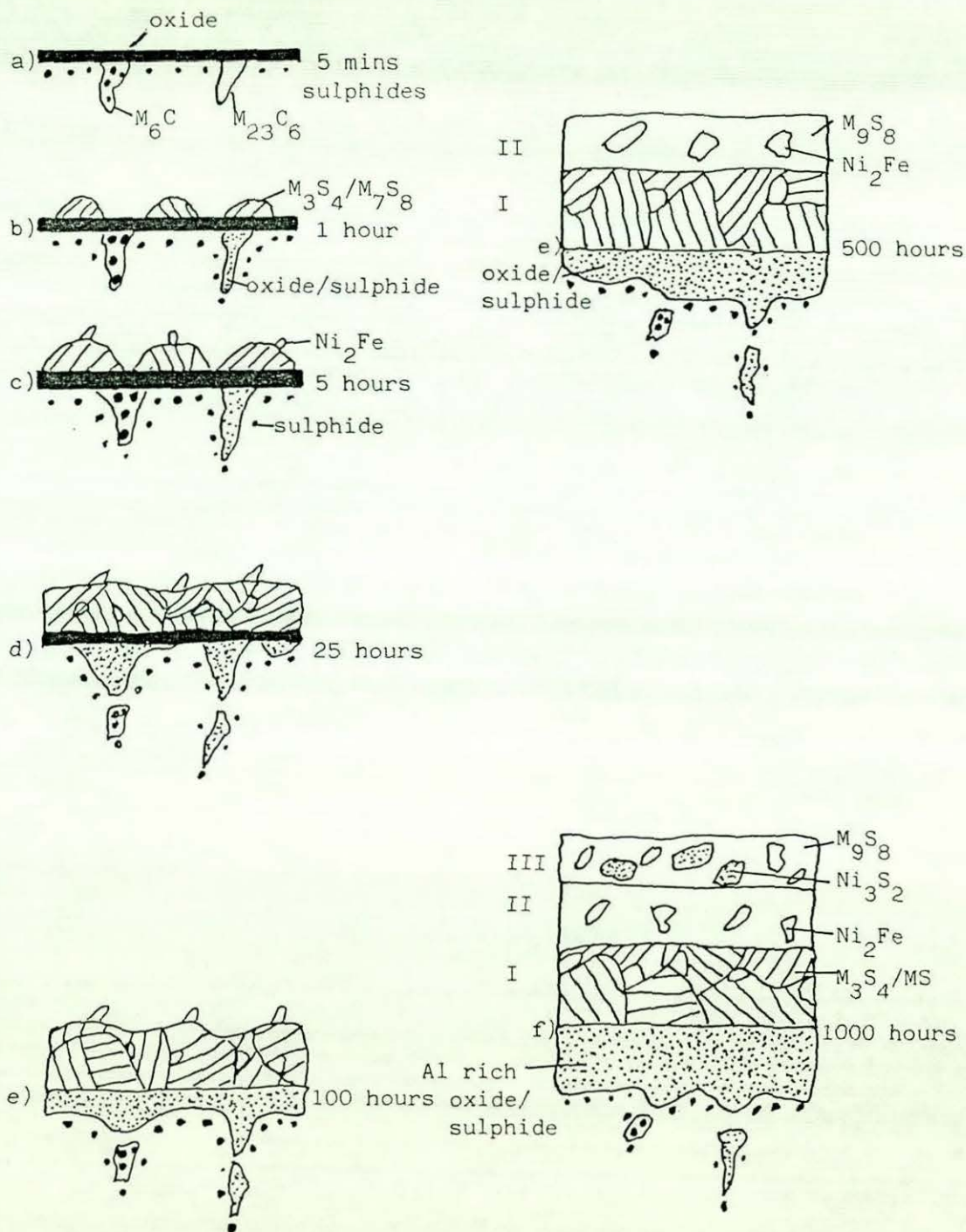


Figure 4.112

Summary figure showing the corrosion behaviour of HP40Al in the 0.6% H_2S gas at $800^\circ C$.

4.3. A PRELIMINARY INVESTIGATION ON ALLOY 800H

A preliminary investigation was carried out on Alloy 800H which has very good mechanical properties and often used in many high temperature applications. This alloy is a 20Cr-33Ni-Fe alloy with minor additions of 0.37 % Si, 0.66 % Mn, 0.48 % Ti, 0.28 % Al and 0.06 % C. The material was supplied as wrought bar which was subsequently solution treated at 1150°C for 1 hour followed by water quenching. It had an equiaxed structure with a grain size varying from 100-300 μm .

a) Sulphur-free gas

Kinetic data for the electropolished (EP) and 180 grit specimens are presented in figure 4.113. The weight uptake of the electropolished material (1 mg/cm² in 4000 hours) was slightly higher than the 180 grit material (0.7 mg/cm² in 4000 hours).

Electropolished (EP) condition

Replotting the kinetic data as weight gain squared against time (figure 4.114) showed that the corrosion rate progressively slowed down, but was never parabolic. Structural analysis examinations were carried out after 1 hour, 5 hours, 100 hours and 2000 hours.

1 hour
.....

X-ray diffraction using surface reflection detected M_{23}C_6 carbides and MnCr_2O_4 particles on the alloy surface, table 4.27 and figure 4.115. The presence of the carbides was confirmed by surface SEM.

5 hours
.....

X-ray diffraction using surface reflection again detected M_{23}C_6 and MnCr_2O_4 on the alloy surface, table 4.27 and figure 4.115.

100 hours
.....

X-ray diffraction using surface reflection now detected MnCr_2O_4 and Cr_2O_3 with no trace of M_{23}C_6 , table 4.27. The lattice parameter of the

spinel corresponded to MnCr_2O_4 , figure 4.115 and that of Cr_2O_3 to pure Cr_2O_3 , figure 4.116.

2000 hours
.....

Cross-sectional examination showed that the corrosion morphology consisted of 4 regions : an oxide scale on the alloy surface, a zone of internal oxidation, a zone of carburization and localized oxidation at the grain boundaries, figure 4.117a.

The oxide scale was approximately 5 μm thick. An EPMA line scan indicated that the scale consisted of 3 layers : an outer MnCr_2O_4 layer, an intermediate Cr_2O_3 layer and an inner layer rich in Si and Cr, figure 4.118. X-ray diffraction using surface reflection confirmed the presence of MnCr_2O_4 and Cr_2O_3 , table 4.27. The alloy substrate immediately below the oxide scale contained only 14 % Cr, figure 4.118.

The zone of internal oxidation contained a few isolated lenticular oxide particles. X-ray mapping indicated that these were rich in Al, figure 4.118.

A zone of M_{23}C_6 carbide precipitates (50 μm deep) was present beneath the zone of internal oxidation.

Some localized oxidation (depth 70 μm) of the grain boundary carbides had taken place. The EPMA line scan showed that these oxides contained Si, Ti and Al, figure 4.118. X-ray mapping indicated that these oxides were rich in Si, Ti and Al near the surface, Ti and Al deeper in the alloy and only Al at the deepest point. In other words as the oxygen activity decreased fewer oxides were thermodynamically stable. Carbides were present at grain boundaries throughout the alloy, presumably formed due to aging processes.

180 grit condition

The weight uptake was slightly lower than the electropolished specimens, figure 4.113. The kinetic rate gradually decreased but never became

parabolic, figure 4.119. Examinations were carried out after 100 hours and 5000 hours.

100 hours
.....

Cross-sectional examination showed that the corrosion morphology consisted of an oxide scale and a zone of internal oxidation.

The oxide scale was relatively uniform (approximately 2 μm thick). X-ray diffraction using surface reflection indicated that this layer contained MnCr_2O_4 and Cr_2O_3 , table 4.28. The Cr_2O_3 lattice parameter value was slightly higher than would be expected for pure Cr_2O_3 . The lattice parameter of the oxide spinel was quite large indicating a high concentration of Mn, figure 4.115.

The internal oxidation zone ($\sim 5 \mu\text{m}$ deep) contained a few isolated lenticular looking oxide particles. There was no sign of carburization at the result of carbon injection from the gas.

At this stage the grain boundaries in the alloy contained some carbide precipitates formed as the result of aging processes. There was no sign of any localized internal oxidation at the grain boundaries.

5000 hours
.....

Cross-sectional examination showed that the corrosion morphology now consisted of 3 regions : the oxide scale, the internal oxidation zone and some localized oxidation of the grain boundary carbides, figure 4.117b.

The oxide scale was rather uneven (approximately 5-7 μm thick). X-ray diffraction analysis using surface reflection confirmed that this scale still contained Cr_2O_3 and MnCr_2O_4 , table 4.28. The Cr_2O_3 lattice parameter value had increased slightly, figure 4.116, but the M_3O_4 lattice parameter value was unchanged (figure 4.115). It was strongly suspected that the oxide scale also contained an inner Si rich layer, as seen in the case of the electropolished specimens. No EPMA analysis was carried out to confirm this.

The zone of internal lenticular oxide particles was now 10 μm deep. Although not identified specifically these particles had the same morphology as the Al_2O_3 particles identified in the HP40A1 alloy.

Localized internal oxidation of the grain boundary carbides had occurred to depths of up to 80 μm . Apart from the carbides at the grain boundaries which were presumably present due to aging processes, no carburization had occurred due to carbon injection from the gas.

Summary

The corrosion behaviour of Alloy 800H in the sulphur-free gas is summarized in figure 4.120.

In the case of the electropolished material M_{23}C_6 and MnCr_2O_4 nucleated on the alloy surface in the initial stages, figure 4.120a. These subsequently grew to form a complete surface layer, figure 4.120b. The surface carbides were then converted to oxides, with the carbon released diffusing into the alloy substrate. The surface layer at this stage consisted of a mixture of MnCr_2O_4 and Cr_2O_3 , figure 4.120c. After long term exposures this surface scale separated into an outer MnCr_2O_4 layer and an inner Cr_2O_3 layer, figure 4.120d. An internal SiO_2 layer tried to form, but the alloy contained insufficient Si for this layer to be complete. The internal layer which did form therefore consisted of a mixture of SiO_2 and Cr_2O_3 formed from the transformed carbides. This allowed a small amount of carbon ingress from the gas to take place. The most significant feature was, however, the localized oxidation of the grain boundary carbides. These oxides were rich in Al, Ti and Si near the surface, Al and Ti deeper in the alloy and only Al at the deepest point of attack. In other words as the oxygen activity decreased fewer oxides were thermodynamically stable. A few lenticular Al_2O_3 particles also formed in the alloy substrate.

The corrosion process was similar for the 180 grit material, figure 102e and f. In this case surface working assisted the formation of the inner SiO_2 layer which slightly reduced the outward cationic diffusion and ingress of carbon into the alloy substrate.

b) 0.2 % H₂S gas

Kinetic data for the electropolished and 180 grit specimens are presented in figure 4.121. In the first 1500 hours there was little difference between the weight uptake of the two surface finishes (0.8 mg/cm² in 1500 hours). After this time the kinetics of the 180 grit material increased rapidly. Only a slight upturn occurred with the electropolished material.

Electropolished (EP) condition

Replotting the kinetic data as weight gain squared against time (figure 4.122) showed that initially the corrosion rate was quite high and then progressively slowed down. Between 600 and 1500 hours the rate was fairly constant but not parabolic and after 1500 hours a significant increase in the corrosion kinetics occurred. Examinations were carried out after 5 minutes and 5000 hours.

5 minutes
.....

X-ray diffraction using surface reflection detected Cr₂O₃ and MnCr₂O₄ on the surface of the alloy, table 4.29.

5000 hours
.....

Cross-sectional examination revealed that the corrosion morphology consisted of 3 regions : an outer scale, a zone of internal sulphide precipitates and localized attack at the grain boundaries, figure 4.123a.

The outer oxide scale in general was fairly even (5-7 µm thick) but in areas above grain boundaries the oxide was much thicker (15-30 µm) and contained a number of small sulphide particles. An EPMA line scan taken through the scale in one of these areas indicated that the oxide scale consisted of an outer (Mn,Fe)Cr₂O₄ layer and an inner Cr₂O₃ layer, figure 4.124. X-ray diffraction using surface reflection confirmed the presence of MnCr₂O₄, FeCr₂O₄ and Cr₂O₃, table 4.29. There was no

evidence of an inner Si rich layer. A few internal chromium sulphide precipitates were present in the alloy substrate. The depleted alloy substrate contained only 9 % Cr.

The major feature was however the massive amount of localized internal attack at the grain boundaries (up to 300 μm deep). This localized attack consisted of a mixture of oxides and sulphides. Near the alloy surface the attack consisted of a mixture of oxides and sulphides with a large number of the plate like particles in the alloy substrate. An EPMA line scan taken through one of these areas indicated that the plate like particles were rich in Al, figure 4.125. The localized attack contained Ti, Cr and Si and Al rich oxides at the edges and chromium sulphides in the middle, figure 4.123. Deeper into the alloy the Al rich plate like oxide particles were not visible, but the internal attack still consisted of mixed oxides and sulphides. Even further into the alloy only sulphide particles were present. These appeared to be advancing by attacking the grain boundary carbides. There appeared to be a small amount of carburization of the alloy substrate due to carbon injection from the gas.

180 grit condition

Replotting the kinetic data as weight gain squared against time (figure 4.122) showed that the initial corrosion rate was quite high, but then progressively slowed down. Between 500 and 2500 hours the rate was constant, but after 2500 hours a significant upturn in the kinetics occurred.

Examinations were carried out after 5 minutes, 1 hour, 5 hours, 100 hours and 2000 hours.

5 minutes
.....

X-ray diffraction using surface reflection detected Cr_2O_3 and M_3O_4 on the surface of the alloy, table 4.30. The Cr_2O_3 lattice parameter value corresponded to that of pure Cr_2O_3 , figure 4.116, and the M_3O_4 lattice parameter value indicated that the oxide spinel was MnCr_2O_4 , figure 4.115.

1 hour
.....

X-ray diffraction using surface reflection again detected Cr_2O_3 and M_3O_4 on the alloy surface, table 4.30.

5 hours
.....

X-ray diffraction using surface reflection now detected M_3S_4 in addition to Cr_2O_3 and M_3O_4 , table 4.30.

100 hours
.....

Cross-sectional examination showed that the corrosion morphology consisted of 3 regions : an oxide scale, a zone of internal sulphidation and some localized attack at the grain boundaries, figure 4.126.

The oxide scale was rather uneven ($\sim 7 \mu\text{m}$ thick) and contained a number of sulphide particles. An EPMA line scan taken through the scale showed that it was starting to consist of 3 layers : an outer $(\text{Mn,Fe})\text{Cr}_2\text{O}_4$ layer, an intermediate Cr_2O_3 layer and an inner layer rich in Cr, Si and Al, figure 4.118. The intermediate Cr_2O_3 layer contained a number of chromium sulphide particles.

The EPMA line scan and X-ray mapping confirmed that the internal sulphide precipitates were chromium sulphides. The alloy substrate immediately beneath the oxide scale contained only 10 % Cr, figure 4.127.

Some localized attack of the grain boundaries was starting to take place. At this stage this consisted of the grain boundary carbides transforming to sulphides. There was no sign of any localized internal oxidation. Deeper in the alloy the grain boundaries had carburized. This was mainly attributed to aging processes in the alloy.

500 hours
.....

Cross-sectional examination showed that the corrosion morphology consisted of an oxide scale, a zone of internal sulphide precipitates and some localized attack at the grain boundaries, figure 4.126.

The oxide layer and zone of internal attack were similar to the specimen exposed for 100 hours. The major change was however the increase in the depth of localized attack. At the deepest point of attack the sulphur appeared to be attacking the grain boundary carbides to form predominantly chromium sulphide precipitates. Nearer the surface these sulphides were themselves starting to transform to oxides. Semi-quantitative EDAX analysis indicated that some of these oxides were rich in Ti, figure 4.128.

2000 hours
.....

Cross-sectional analysis showed that the corrosion morphology still consisted of the oxide scale, the zone of internal sulphide precipitates localized attack at the grain boundaries and a zone of internal carburization, figure 4.123b.

In general the oxide scale was $\sim 6-7 \mu\text{m}$ thick. However localized thickening of the oxide had occurred above the grain boundary areas. In these places the oxide was up to $30 \mu\text{m}$ thick. An EPMA line scan taken through one of these areas showed that the oxide scale was a mixture of Cr_2O_3 and $(\text{Fe,Mn})\text{Cr}_2\text{O}_4$, figure 4.129. X-ray diffraction analysis using surface reflection confirmed the presence of Cr_2O_3 and M_3O_4 , table 4.30. The lattice parameter of the M_3O_4 spinel indicated that it had the composition FeCr_2O_4 , figure 4.115. The Cr_2O_3 lattice parameter corresponded to that of pure Cr_2O_3 , figure 4.116. Some sulphides were still present in the oxide scale. There appeared to be some evidence from the EPMA line scan for an inner Si rich layer in the scale but unfortunately an artifact obscured this area. X-ray mapping (not shown) also indicated the presence of Si in this region but showed that the layer was certainly not complete.

A number of internal sulphide precipitates were still present in the alloy substrate beneath the oxide scale. The Cr level in this region was only 8 %.

The major feature was however the amount of localized internal attack at the grain boundaries (up to $200 \mu\text{m}$ deep). Near the surface the attack consisted of a mixture of oxides and sulphides with a large number of

plate like particles in the alloy substrate. An EPMA line scan taken through one of these areas indicated that the localized attack contained Ti, Cr, Si rich oxides at the edges and chromium sulphides in the middle, figure 4.130. The plate like particles were rich in Al. Deeper in the alloy the internal attack consisted of mixed oxides and sulphides but the plate like precipitates were not visible. Even deeper in the alloy only sulphide precipitates were present. These appeared to be advancing by attacking the grain boundary carbides. There also appeared to be a significant amount of internal carburization taking place deeper in the alloy.

Summary

The corrosion behaviour of Alloy 800H in the 0.2 % H₂S gas is summarized in figure 4.131. The sequence of events for the 180 grit material can be divided into a number of stages.

- Stage 1 (5 mins)

Cr₂O₃ and MnCr₂O₄ nucleated on the alloy surface, figure 4.131a.

- Stage 2 (1 hour)

The Cr₂O₃ and MnCr₂O₄ grew to form a complete surface layer, figure 4.131b.

- Stage 3 (5 hours)

Sulphides formed on top of this layer and in the alloy substrate, figure 4.131c.

- Stage 4 (100 hours)

The oxides overgrew the sulphides to form a scale consisting of an outer (Mn,Fe)Cr₂O₄ layer and an inner Cr₂O₃ layer which contained the former sulphide growths, figure 4.131d. Internal sulphide precipitates prevented an internal SiO₂ layer from forming. Instead a discontinuous layer containing SiO₂, Cr₂O₃ and Cr-rich sulphides formed. The grain boundary carbides started to transform to sulphides.

- Stage 5 (500 hours)

A significant increase in the amount of localized attack of the grain boundaries took place. The grain boundary carbides transformed to sulphides which subsequently transformed to oxides.

- Stage 6 (2000 hours)

After approximately 1500 hours a significant increase in the corrosion rate occurred. This corresponded to a dramatic increase in the amount of localized internal attack of the grain boundaries, figure 4.131e. It appeared that this was associated with localized Cr-depletion of the alloy substrate and the stabilizing effect of Ti and Al on oxides in the transformed carbides. Localized thickening of the scale above these areas occurred due to the release of excess metal from the transformed carbides. Some isolated Al_2O_3 and M_{23}C_6 particles also formed in the alloy substrate.

The corrosion process was similar for the electropolished material, figure 4.131f and g. In this case fewer sulphides formed which placed less demand on the chromium reservoir in the alloy. This delayed the onset of breakaway corrosion.

It was concluded that the low Cr-content of this alloy led to the amount of Cr in the depleted substrate reaching a critical level after shorter exposure times than for other alloys. This led to a considerable amount of localized attack of the grain boundary carbides, initially by sulphur and then by oxygen. The process was assisted by the stabilizing effect of Ti and Al on the internal oxides.

c) 0.6 % H_2S gas

The corrosion kinetics are presented in figure 4.131. This figure shows that the weight gains were very high (350 mg/cm^2 in 1000 hours) and that there was no significant difference between the electropolished and 180 grit specimens.

Examinations were carried out after 5 mins, 1 hour, 5 hours, 25 hours, 100 hours, 500 hours and 1000 hours.

5 mins
.....

Cross-sectional examination using the Pepperhoff technique revealed that the corrosion morphology consisted of 3 regions : a discontinuous outer sulphide layer I, an oxide layer at the original alloy surface and a zone of internal sulphide precipitates, figure 4.133.

The discontinuous sulphide layer I (up to 5 μm thick) contained the FeCr_2S_4 and $(\text{Fe}_x\text{Cr}_y)_7\text{S}_8$ lamellae. X-ray diffraction using surface reflection confirmed the presence of M_3S_4 , table 4.31.

The oxide scale (4 μm thick), at the original alloy surface, contained a number of sulphides particles. X-ray diffraction using surface reflection confirmed that the oxide was a mixture of Cr_2O_3 and FeCr_2O_4 .

The zone of internal sulphide precipitates in the alloy substrate was approximately 3 μm deep. The different blue and brown colours indicated that the precipitates were mixture of Mn and Cr sulphides.

1 hour
.....

Cross-sectional examination using the Pepperhoff technique showed that the corrosion morphology still consisted of 3 regions : a discontinuous outer sulphide layer I, an oxide layer at the original alloy surface and a zone of internal sulphide precipitates, figure 4.133.

The discontinuous sulphide layer I (up to 5 μm thick) still contained the FeCr_2S_4 and $(\text{Fe}_x\text{Cr}_y)_7\text{S}_8$ lamellae. The presence of these phases was confirmed by X-ray diffraction using surface reflection, table 4.31.

The oxide layer (5 μm thick) was similar to before and still contained a number of sulphide particles. X-ray diffraction using surface reflection now detected only FeCr_2O_4 and no Cr_2O_3 , table 4.31.

The internal sulphide precipitates had advanced deeper (10 μm thick) into the alloy substrate.

5 hours
.....

Cross-sectional examination using the Pepperhoff technique showed that the corrosion morphology now consisted of 3 regions : a discontinuous outer sulphide layer I, an oxide layer at the original alloy surface and a zone of internal mixed oxidation/sulphidation in the depleted alloy substrate, figure 4.133.

The discontinuous outer sulphide layer I (up to 55 μm thick) now contained Ni_2Fe metallic particles in addition to the FeCr_2S_4 and $(\text{Fe}_{\text{x}}\text{Cr}_{\text{y}})_7\text{S}_8$ lamellae. X-ray diffraction using surface reflection confirmed the presence of M_7S_8 and M_3S_4 .

The oxide layer (5 μm thick) was similar to before and still contained a number of sulphide particles.

The internal Cr rich sulphide precipitates had advanced deeper into the alloy and a substantial amount of internal oxidation had also taken place. This zone (50 μm deep) containing the sulphide and oxide precipitates formed a mirror image of the discontinuous outer sulphide layer I.

There was no sign of any internal carburization at this stage.

25 hours
.....

Cross-sectional examination using the Pepperhoff technique showed that the corrosion morphology now consisted of 5 regions. The now continuous outer sulphide layer I, the remains of the oxide layer at the original alloy surface, a new internal predominantly sulphide layer, the zone of internal mixed oxidation/sulphidation in a depleted alloy substrate and a zone of carburization, figure 4.133.

The outer sulphide layer I which was now continuous and 155 μm thick, still consisted of the two types of sulphide lamellae and the metallic Ni_2Fe particles. X-ray diffraction using surface reflection confirmed the presence of M_3S_4 and Ni_2Fe but indicated that the other lamellae

were now M_9S_8 instead of M_7S_8 . The oxide layer at the original alloy surface had now started to break up.

The sulphide precipitates just beneath the oxide layer had grown at coalesced together to form a continuous internal predominantly sulphide layer (40 μm thick). This layer appeared to contain the same two types of sulphide present in outer sulphide layer I and the oxides which were formerly present in zone of internal mixed sulphidation/oxidation. There were only a few very small isolated patches of depleted alloy substrate in this layer.

The zone of internal mixed oxidation/sulphidation had advanced deeper into the alloy and was now 115 μm thick. The oxidation/sulphidation front appeared to be advancing into the alloy by firstly attacking grain boundary carbides and twin boundaries followed by more generalized attack of the alloy substrate.

A zone of carburization containing small $M_{23}C_6$ carbide precipitates was visible beneath the zone of internal mixed oxidation/sulphidation.

100 hours
.....

Cross-section examination using the Pepperhoff technique now showed that the corrosion morphology consisting of 6 regions. A discontinuous outer sulphide layer III, outer sulphide layer I, the remains of the oxide at the original alloy surface, the internal predominantly sulphide layer, the zone of internal mixed oxidation/sulphidation in a depleted alloy substrate and the zone of carburization, figure 4.133.

In some places blisters of outer sulphide layer III had started to form (up to 650 μm thick). These consisted of $Fe_{4,5}Ni_{4,5}S_8$, Ni_2Fe and Ni_3S_2 . The presence of these phases was confirmed by X-ray powder diffraction, table 4.31. There appeared to be no sign of an outer sulphide layer II at this stage.

Outer sulphide layer I (now 335 μm thick) still consisted of the two types of sulphide lamellae and the metallic Ni_2Fe particles. X-ray powder diffraction confirmed the presence of M_3S_4 and MS in this layer.

Semi-quantative EDAX analysis confirmed that the lamellae were still FeCr_2S_4 and $(\text{Fe}_x\text{Cr}_y)\text{S}$ and the metallic particles Ni_2Fe .

A few traces of the oxide layer were still visible at the original alloy surface.

The internal predominately sulphide layer (155 μm thick) still consisted of the same two types of sulphide present in outer layer I some oxide particles and a few metallic particles. Semi-quantative EDAX analysis confirmed that the sulphides in this layer were rich in Cr and Fe.

The zone of internal mixed oxidation/sulphidation had advanced deeper into the alloy and was now 180 μm thick. This zone contained the same oxide and sulphide phases as before. Semi quantative EDAX analysis indicated that the sulphides were rich in Cr and Fe and the oxides rich in Cr, Al, Si and Ti. The zone of carburization was now 50 μm deep and contained a higher density of M_{23}C_6 precipitates.

500 hours
.....

Cross-sectional examination using the Pepperhoff technique revealed that the corrosion morphology now consisted of 7 regions : outer sulphide layer III, outer sulphide layer II, outer sulphide layer I, the remains of the oxide layer, the internal predominantly sulphide layer, the zone of internal mixed oxidation/sulphidation in a depleted alloy substrate and a zone of carburization, figure 4.133.

Outer sulphide layer III still consisted of $\text{Fe}_{4,5}\text{Ni}_{4,5}\text{S}_8$, Ni_3S_2 and Ni_2Fe . This layer was complete but had variable thickness and appeared to have been molten at the test temperature.

Outer sulphide layer II was now clearly visible (535 μm thick) and contained $\text{Fe}_{4,5}\text{Ni}_{4,5}\text{S}_8$ and Ni_2Fe .

Outer sulphide layer I (625 μm thick) contained the two types of sulphide lamellae and the metallic Ni_2Fe particles. Semi-quantative EDAX analysis indicated that both these lamellae now contained significant amounts of Ni in addition to Cr and Fe.

A few traces of the oxide layer were still present at the original alloy surface.

The internal predominantly sulphide layer (1000 μm thick) as before contained a mixture of the same two types of FeCr rich sulphides, some oxide particles and a few metallic particles.

The zone of internal mixed oxidation/sulphidation had advanced deeper into the alloy and was now 250 μm thick. This zone contained the same oxide and sulphide phases as before.

The zone of carburization was now 150 μm deep and contained an even higher density of M_{23}C_6 precipitates.

1000 hours
.....

Cross-sectional examination showed that the same 7 regions were present but that only a small amount of the alloy remained unattacked. It was concluded that this specimen did not give a true picture of the corrosion process and that the examination after 500 hours was representative of the final microstructure in the sequence.

Summary

The corrosion behaviour of Alloy 800H in the 0.6 % H_2S gas can be summarized in a number of stages, figure 4.134.

- Stage 1 (5 mins)

Initially a $\text{FeCr}_2\text{O}_4/\text{Cr}_2\text{O}_3$ oxide layer formed on the alloy surface. This oxide layer contained a number of sulphide particles. Simultaneously a number of small Cr and Mn rich sulphide precipitates formed in the alloy substrate. In some places a discontinuous outer sulphide layer I started to form on top of the oxide. This sulphide layer consisted of FeCr_2S_4 and $(\text{Fe}_x\text{Cr}_y)_7\text{S}_8$ lamellae, figure 4.134a.

- Stage 2 (5 hours)

The discontinuous outer sulphide layer I grew quickly and started to contain metallic Ni_2Fe particles in addition to the FeCr_2S_4 and

$(\text{Fe}_{\text{x}}\text{Cr}_{\text{y}})_7\text{S}_8$ sulphide lamellae. A zone of internal mixed oxidation/sulphidation formed. This zone contained the former sulphide precipitates in addition to a significant amount of internal oxide particles. The oxide layer containing a number of sulphide particles at the original alloy surface was relatively unchanged, figure 4.134b.

- State 3 (25 hours)

The outer sulphide layer I continued to thicken. The oxide layer at the original alloy surface started to break up. An internal predominantly sulphide layer started to form. This layer contained enlarged FeCr rich sulphides and some oxide particles. The zone of internal mixed oxidation/sulphidation was now present deeper in the alloy. Below this some carburization of the substrate was starting to take place, figure 4.134c.

- Stage 4 (100 hours)

Blisters of outer sulphide layer III containing $\text{Fe}_{4,5}\text{Ni}_{4,5}\text{S}_8$, Ni_3S_2 and Ni_2Fe started to form. Outer sulphide layer I still contained FeCr_2S_4 , $(\text{Fe}_{\text{x}}\text{Cr}_{\text{y}})_7\text{S}_8$ and Ni_2Fe . The original scale layer had completely broken up. The internal predominantly sulphide layer had advanced deeper into the alloy but still consisted of FeCr rich sulphides and oxides rich in Cr, Al, Si and Ti. The zone of mixed oxidation/sulphidation in a depleted alloy substrate had advanced deeper into the alloy. The sulphide precipitates in this zone were rich in Cr and Fe and the oxide particles rich in Cr, Al, Si and Ti. The density of M_{23}C_6 precipitates in the carburization zone had increased, figure 4.134d.

- Stage 5 (500 hours)

The external sulphide scale now consisted of 3 layers : outer sulphide layer III containing $\text{Fe}_{4,5}\text{Ni}_{4,5}\text{S}_8$, Ni_3S_2 and Ni_2Fe , outer sulphide layer II containing $\text{Fe}_{4,5}\text{Ni}_{4,5}\text{S}_8$ and Ni_2Fe , and outer sulphide layer I containing the two types of sulphide lamellae now both rich in Ni and well as Fe and Cr. The metallic Ni_2Fe particles were also present in outer sulphide layer I. Only traces of the original oxide layer remained. The internal predominantly sulphide layer had increased dramatically but still consisted of the FeCr rich

sulphides with some Cr, Al, Si, Ti rich oxides also present. The zone of mixed oxidation/ sulphidation in the depleted alloy substrate was similar to before. The $M_{23}C_6$ carbide density in the carburization zone had continued to increase, figure 4.134e.

Thus in summary the corrosion sequence was very similar to the Model 25Cr-35Ni-Fe alloy. The low Cr level of this alloy led to blistering after slightly shorter exposure times. The presence of Al, Si and Ti in this alloy promoted the formation of oxides in the internal layers of the corrosion attack. This slightly reduced the corrosion rate.

d) 2.0 % H_2S

The corrosion kinetics are presented in figure 4.135. This figure shows that the increasing the sulphur level in the gas from 0.6 % to 2.0 % H_2S (i.e. the pS_2 by one order of magnitude) increased the weight uptake by about a factor of four for a given exposure time.

Cross-sectional examination using EDAX semi-quantitative analysis on a specimen exposed for 22.5 hours showed that the corrosion morphology consisted of 4 layers : outer sulphide layer II, outer sulphide layer I, an internal sulphide/oxide layer and a zone of internal carburization, figure 4.136.

Outer sulphide layer II consisted of a mixture of $Fe_{4,5}Ni_{4,5}S_8$ and Ni_2Fe metallic particles. Outer sulphide layer I contained $(Fe_xCr_y)S$ sulphide lamellae and the Ni_2Fe metallic particles. The internal sulphide layer contained Fe, Cr rich sulphides and a few oxide particles. A few $M_{23}C_6$ carbides were present in the alloy substrate.

It was therefore concluded that the corrosion process proceeded in a similar manner but at a faster rate than in the 0.6 % H_2S gas.

Exposure time	Phases Identified (Intensity/Parameter A)					
	Austenite	Cr_2O_3	M_3O_4	M_3S_4	M_{23}C_6	MC
5 mins	-	-	-	-	-	-
1 hour	110/3.602	-	4/8.435	-	13/10.580	-
5 hours	113/3.591	-	12/8.458	-	6/10.595	-
100 hours	337/3.583	10/4.948-13.654	21/8.432	-	-	-
2000 hours	60/3.580	12/4.984-13.640	30/8.455	-	-	-

Table 4.27

X-ray diffraction analysis for Alloy 800H exposed to the sulphur-free gas at 800°C. Electropolished condition.

Exposure time	Phases Identified (Intensity/Parameter A)					
	Austenite	Cr_2O_3	M_3O_4	M_3S_4	M_{23}C_6	MC
100 hours	148/3.584	19/4.973-13.682	15/8.480	-	-	-
2000 hours	-	-	-	-	-	-
5000 hours	61/3.583	17/4.983-13.638	26/8.482	-	-	-

Table 4.28

X-ray diffraction analysis for Alloy 800H exposed to the sulphur-free gas at 800°C. 180 grit condition.

Exposure time	Phases Identified (Intensity/Parameter A)					
	Austenite	Cr_2O_3	M_3O_4	M_3S_4	M_{23}C_6	MC
5 mins	310/3.587	2/4.967-13.512	2/8.424	-	-	-
1 hour	-	-	-	-	-	-
5 hours	-	-	-	-	-	-
100 hours	-	-	-	-	-	-
2000 hours	-	-	-	-	-	-
5000 hours	27/3.586	17/4.987-13.638	25/8.485 and 21/8.426	-	-	-

Table 4.29

X-ray diffraction analysis for Alloy 800H exposed to the 0.2 % H_2S gas at 800°C. Electropolished condition.

Exposure time	Phases Identified (Intensity/Parameter A)					
	Austenite	Cr ₂ O ₃	M ₃ O ₄	M ₃ S ₄	M ₂₃ C ₆	MC
5 mins	204/3.587	6/4.951-13.597	6/8.419	-	-	-
1 hour	104/3.590	3/4.950-13.601	11/8.401	-	-	-
5 hours	100/3.593	6/4.954-13.601	5/8.419	4/9.974	-	-
100 hours	-	-	-	-	-	-
2000 hours	51/3.592	14/4.961-13.619	24/8.398	-	-	-
5000 hours	-	-	-	-	-	-

Table 4.30

X-ray diffraction analysis for Alloy 800H exposed to the 0.2 % H₂S gas at 800°C. 180 grit condition.

Exposure Time	Phase Identified (Intensity/Parameter Å)								
	Austenite	Ni ₂ Fe	Cr ₂ O ₃	M ₃ O ₄	M ₇ S ₈	MS	M ₃ S ₄	M ₉ S ₈	Ni ₃ S ₂
5 mins	110/3.586	-	3/4.939-13.633	10/8.398	-	-	7/9.975	-	-
1 hour	58/3.592	-	-	4/8.409	29/3.45-5.76	-	3/9.914	-	-
5 hours	25/3.570	-	-	-	34/3.46-5.81	-	18/10.005	-	-
25 hours	-	40/3.566	-	-	-	-	15/9.984	12/10.145	-
100 hours	-	-	-	-	-	I = 10	17/10.005	70/10.121	-
1000 hours	-	-	-	-	-	-	20/9.991	43/10.104	-

Table 4.31

X-ray diffraction analysis for Alloy 800H exposed to the 0.6% H₂S gas at 800°C.

Alloy 800H, $P_{O_2}=10^{-21}$ bar, $a_C=0.3$, 800°C .

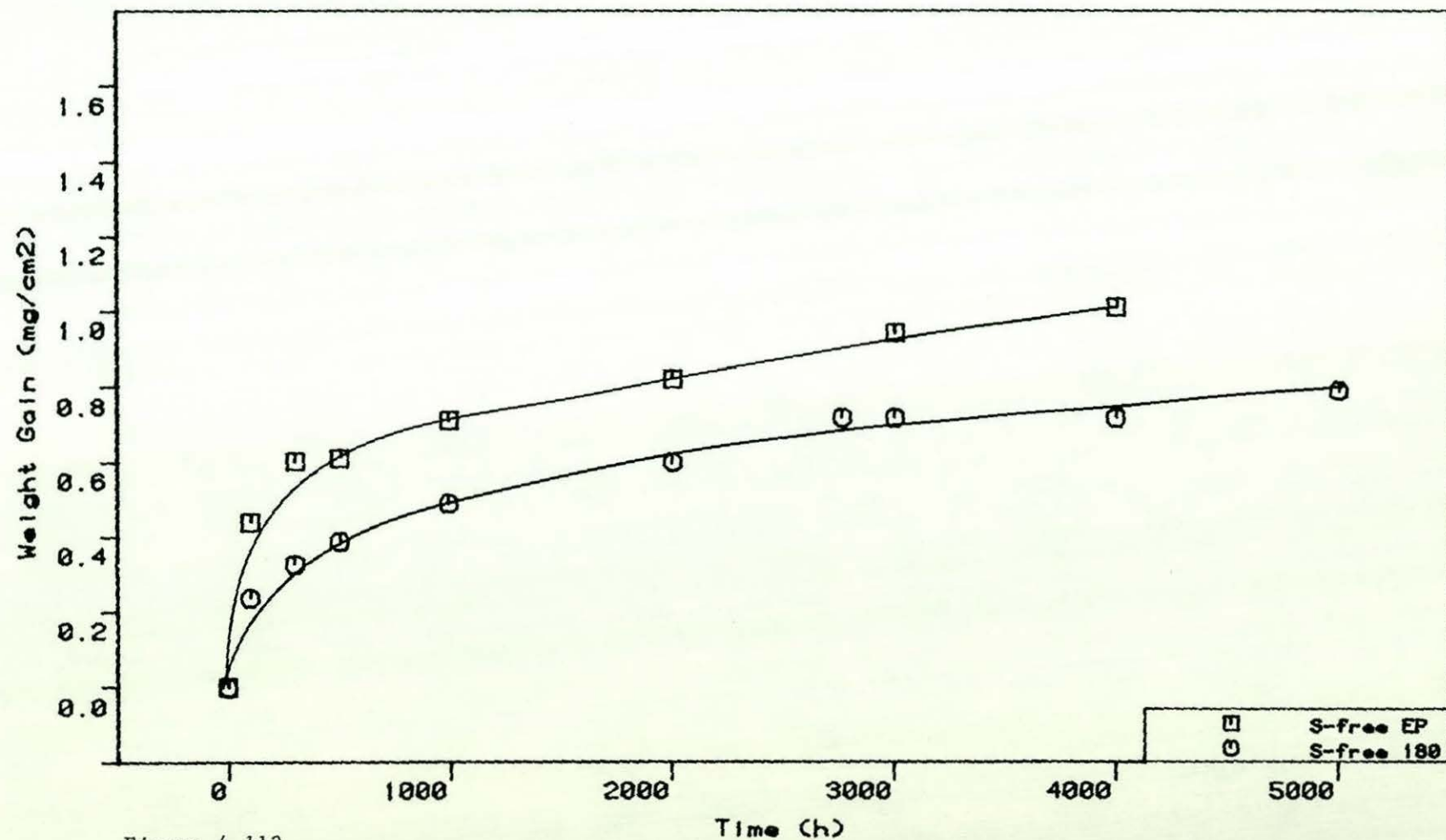


Figure 4.113

Kinetic data for Alloy 800H exposed to the sulphur-free gas at 800°C .

S-free gas, $P_{O_2}=10^{-21}$ bar, $a_C=0.3$, 800°C

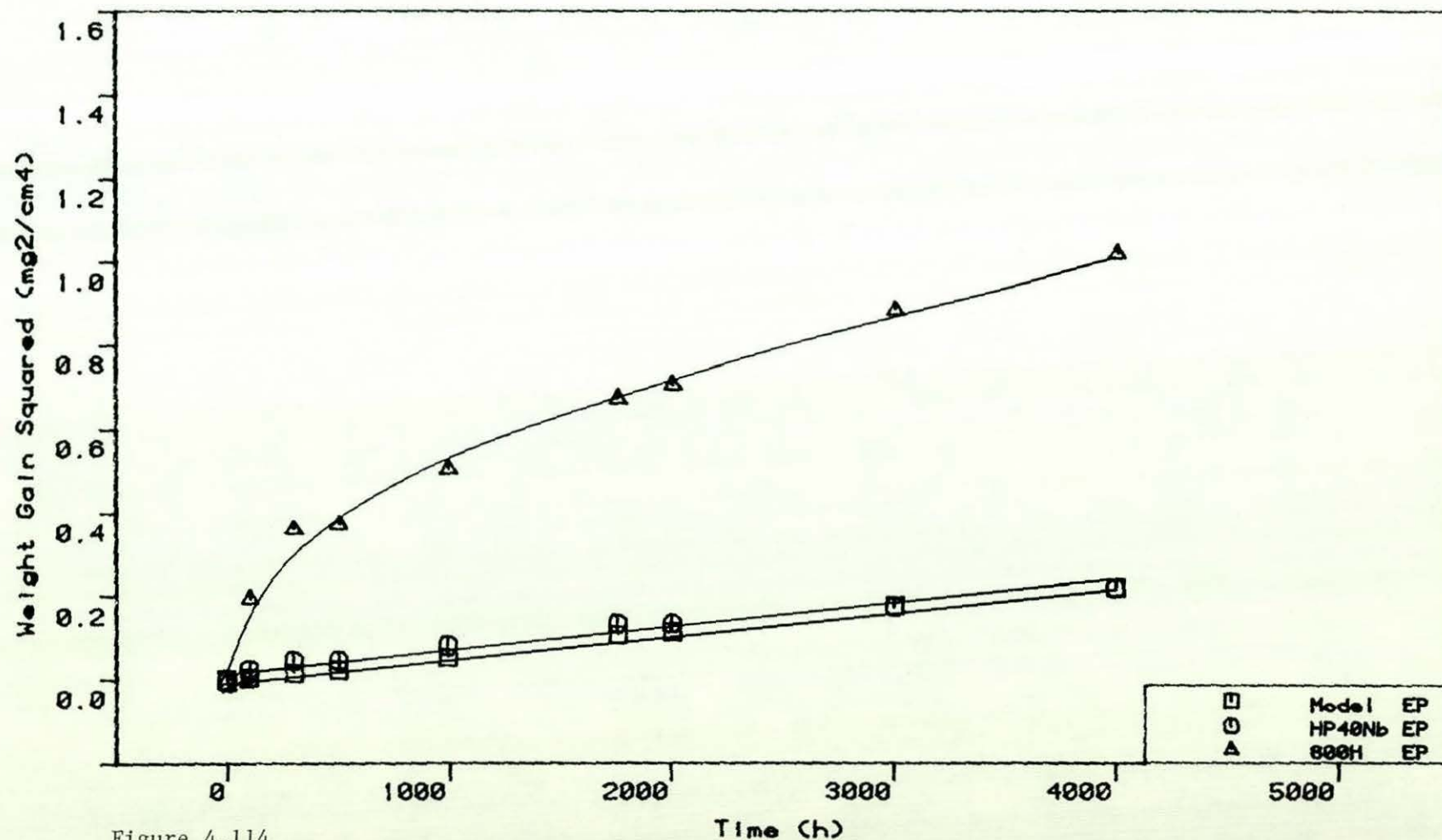


Figure 4.114

Plots of weight gain squared against time for the Alloy 800H and the Model 25Cr-35Ni-Fe alloy in the sulphur-free gas at 800°C , electropolished condition.

Alloy 800H, Oxide Spinel Lattice Parameters

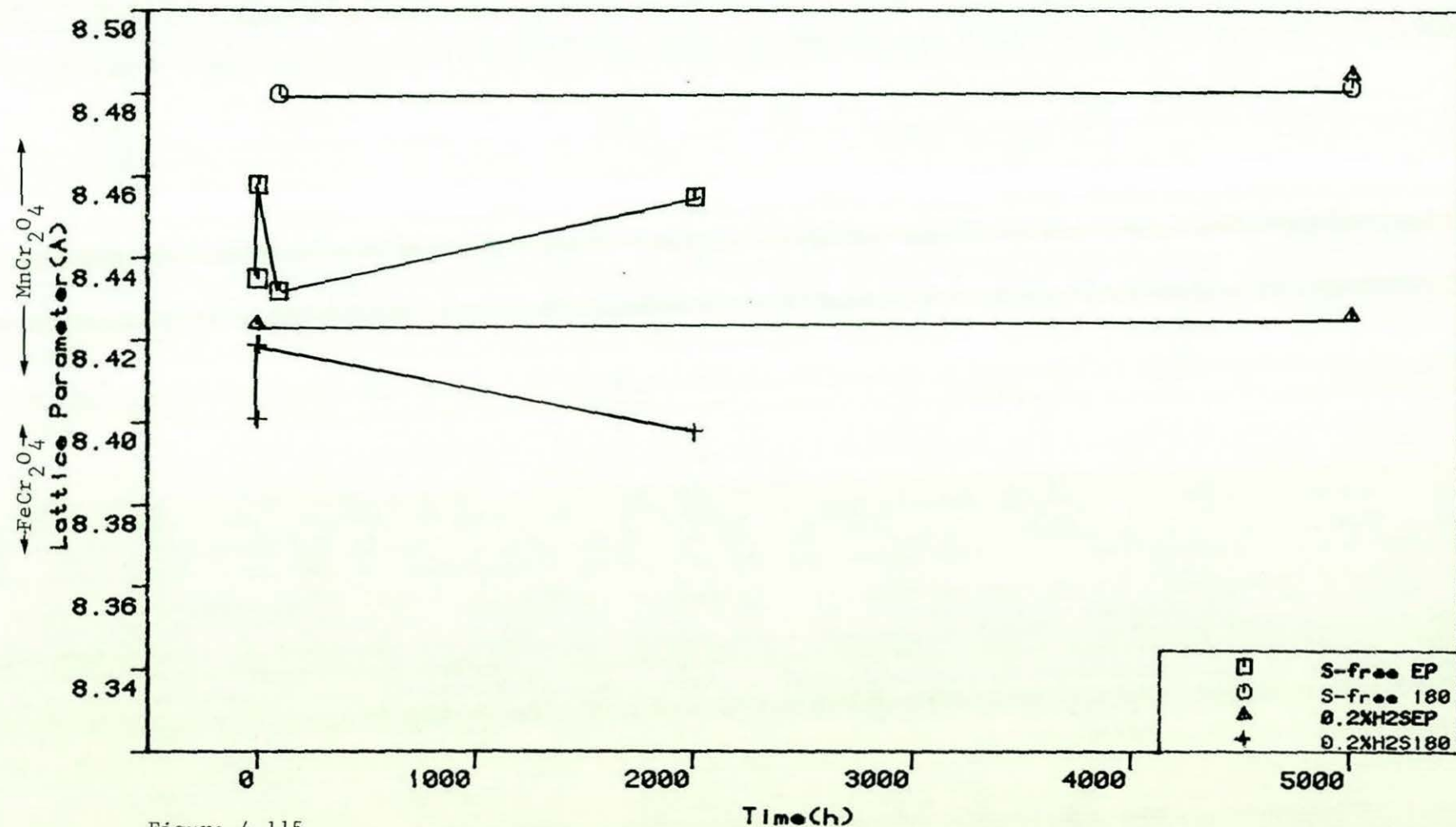


Figure 4.115

Plots of oxide spinel lattice parameter against time for Alloy 800H exposed to the sulphur-free and 0.2% H₂S gases at 800°C.

Alloy 800H, Chromia Lattice Parameters

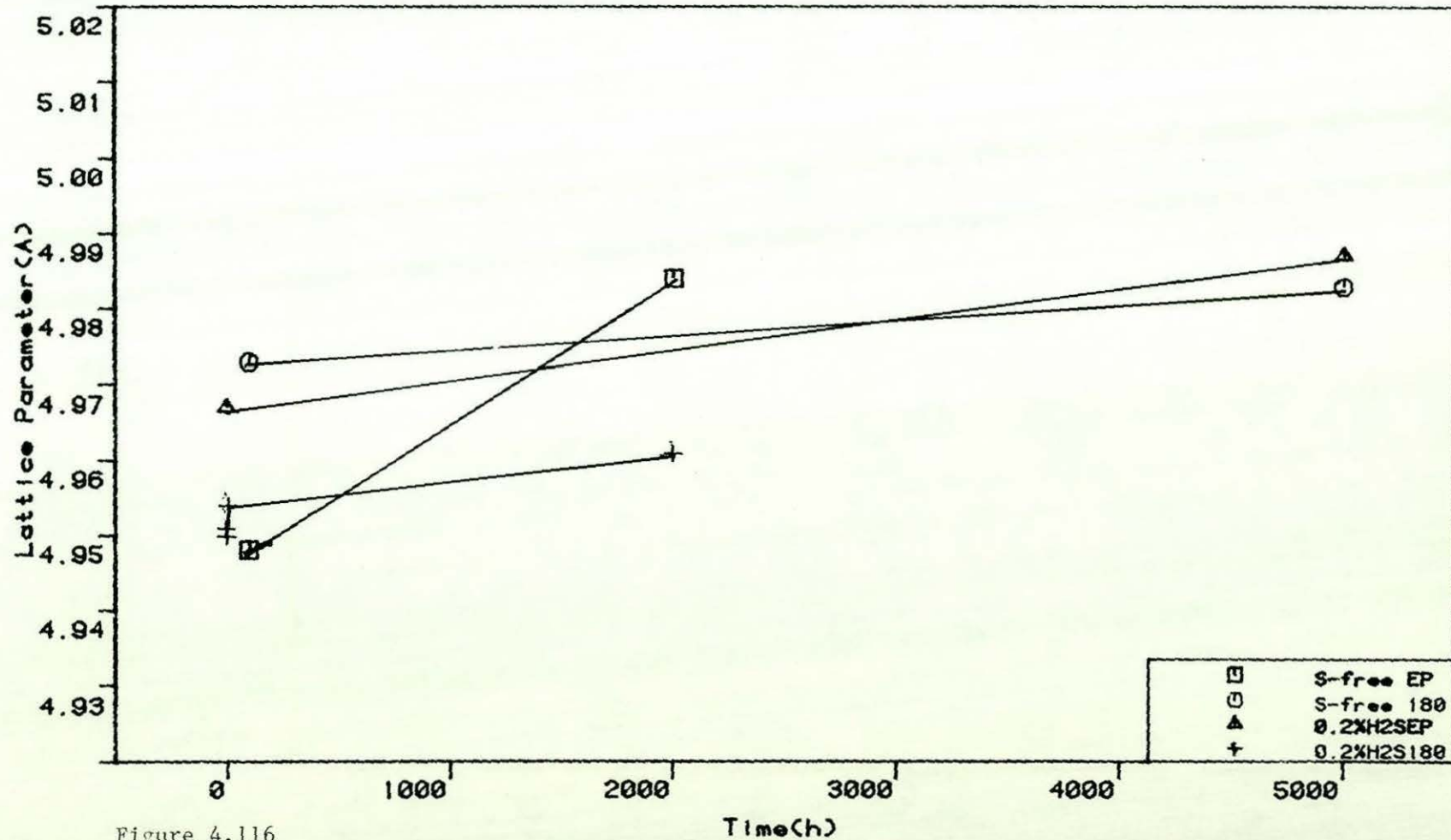


Figure 4.116

Plots of Cr_2O_3 lattice parameter against time for Alloy 800H exposed to the sulphur-free and 0.2% H_2S gases at 800°C.

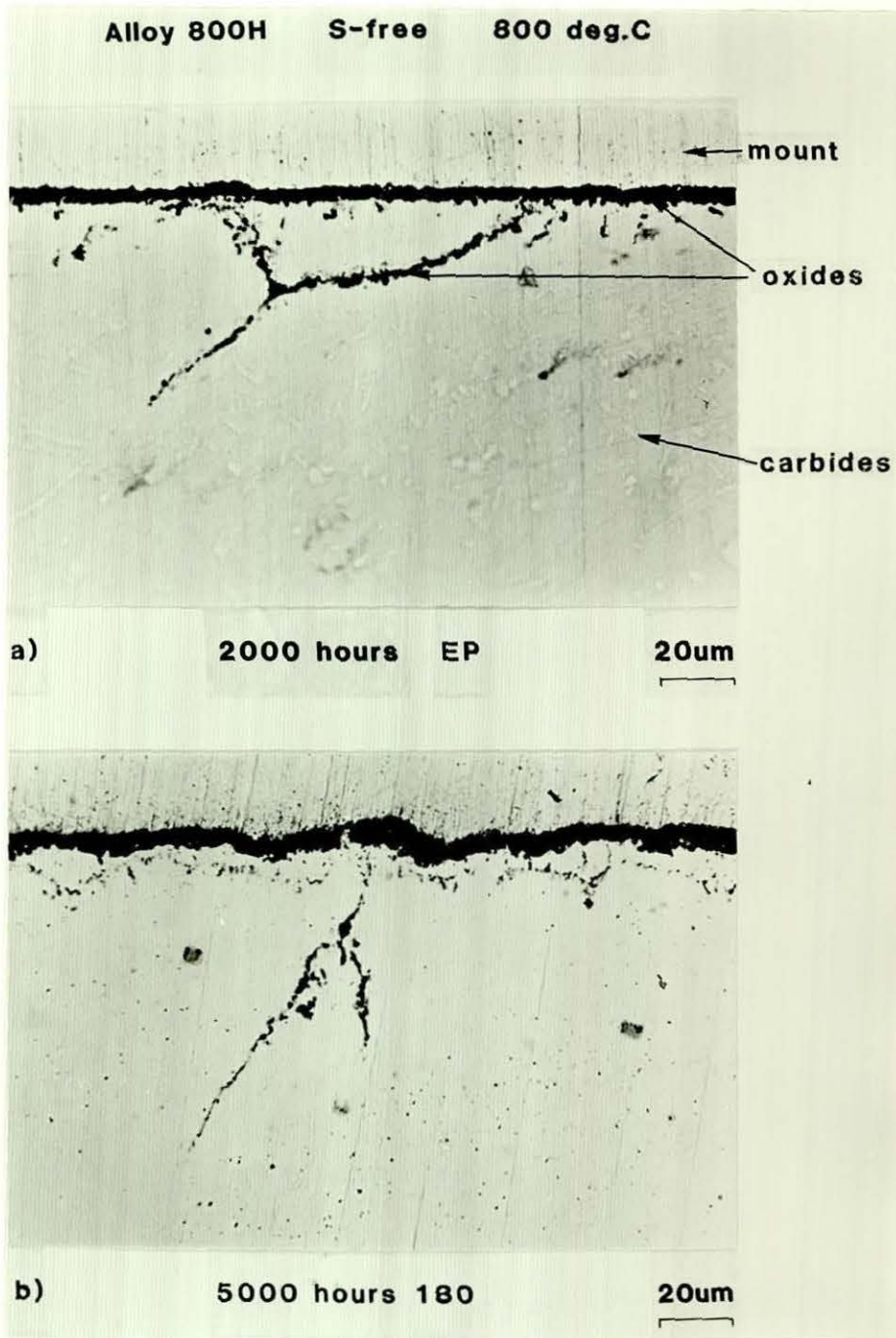


Figure 4.117

Cross-sectional metallographic examination of Alloy 800H exposed to the sulphur-free gas at 800°C.

a) Electropolished condition 2000 hours

b) 180 grit condition 5000 hours

S-free gas, $P_{O_2}=10^{-21}$ bar, $a_C=0.3$, 800°C

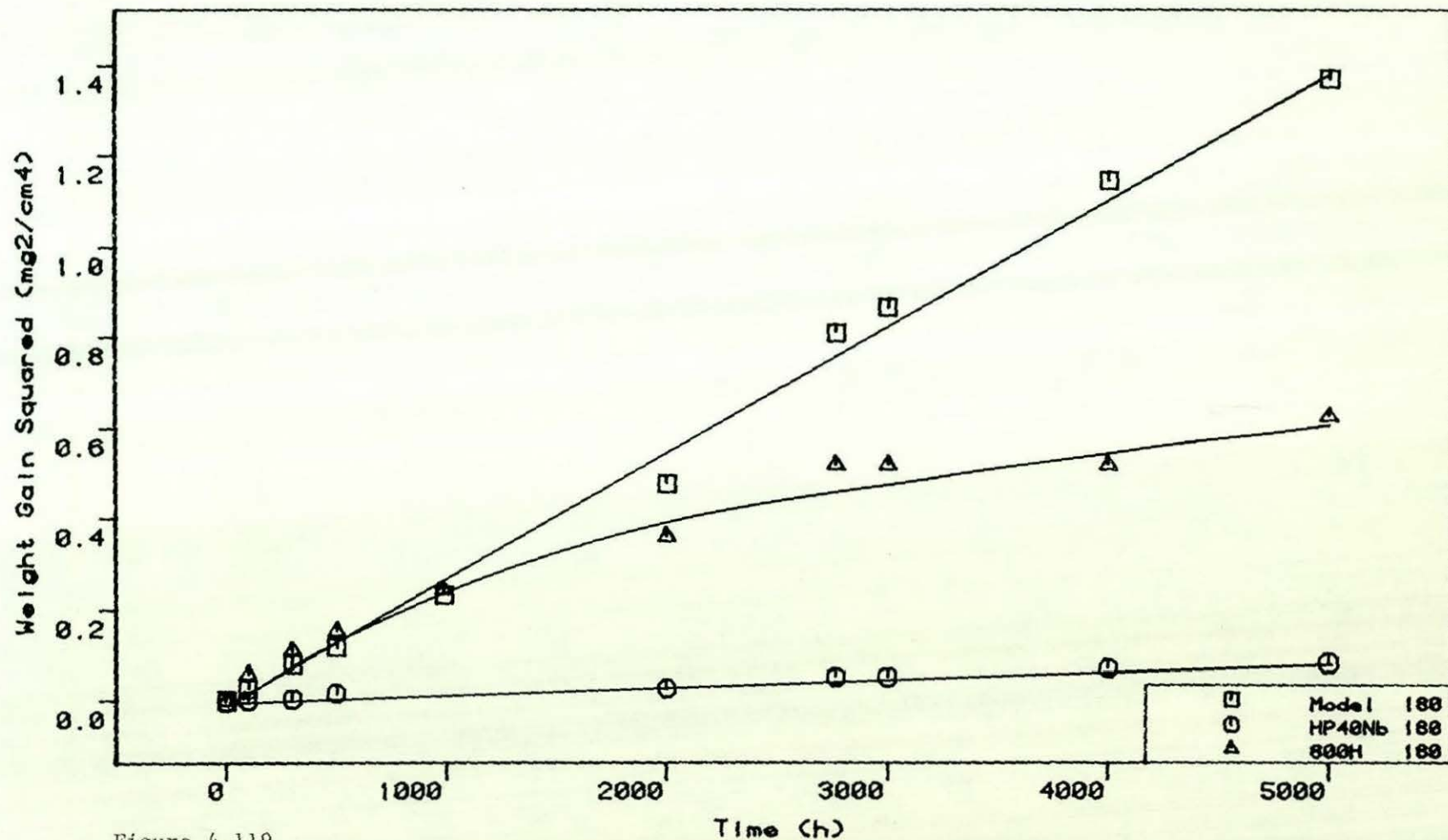


Figure 4.119

Plots of weight gain squared against time for Alloy 800H, Model 25Cr-35Ni-Fe and HP40Nb exposed to the sulphur-free gas at 800°C , 180 grit condition.

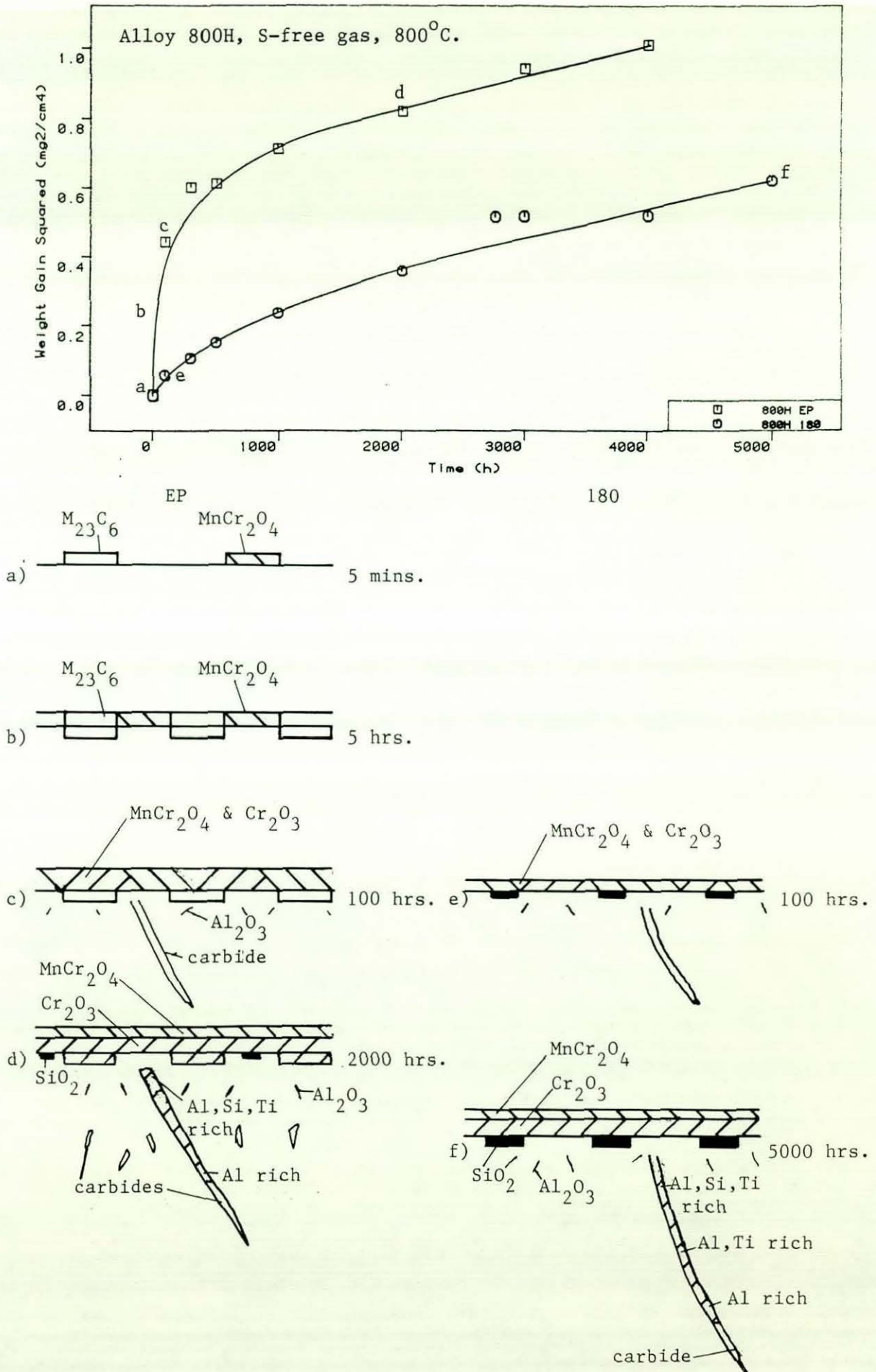


Figure 4.120

Summary figure for the corrosion behaviour of Alloy 800H in the sulphur-free gas at 800°C.

Alloy 800H, PO₂=10-21bar, aC=0.3, 800degC.

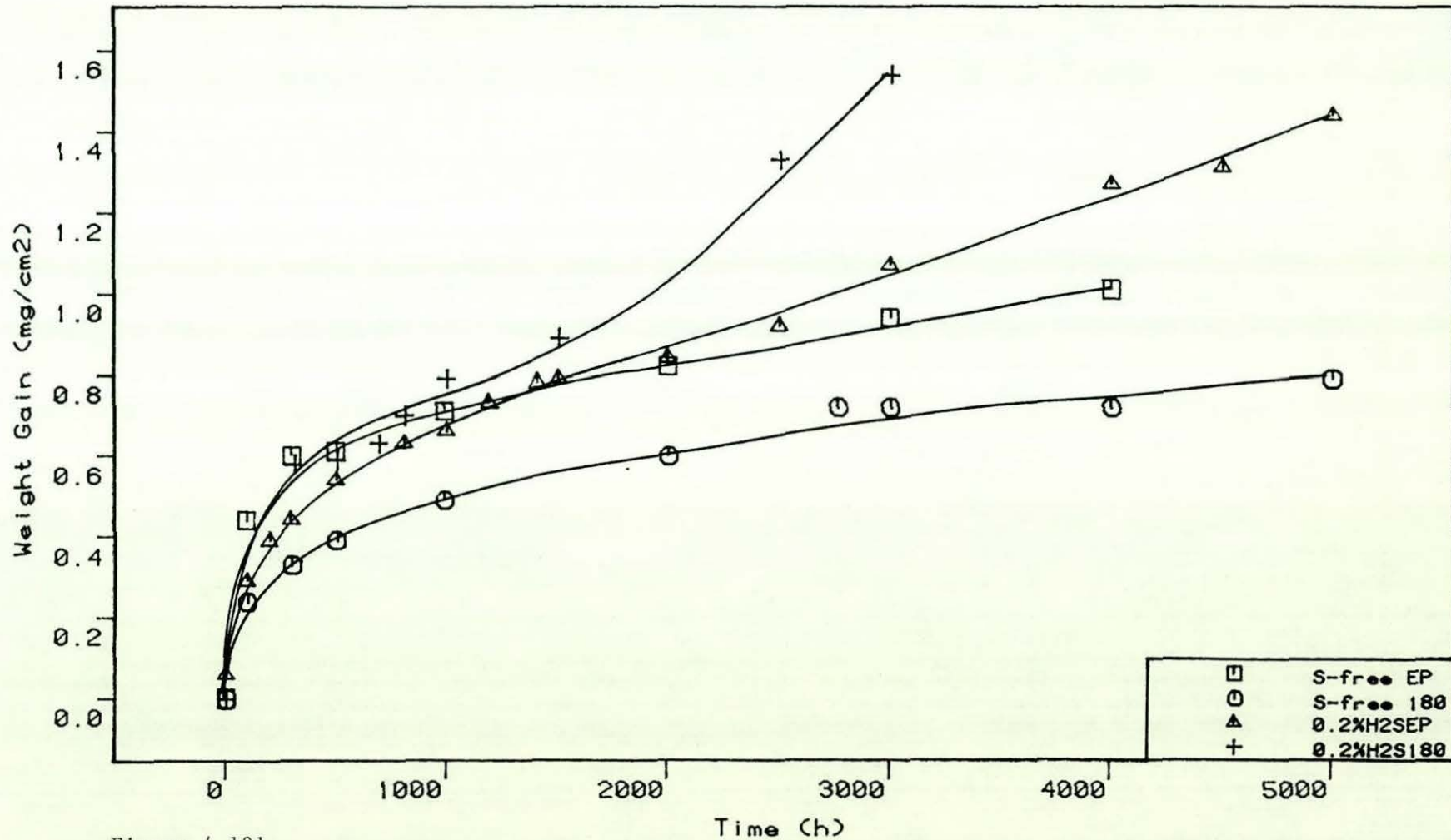


Figure 4.121

Kinetic data for Alloy 800H exposed to the sulphur-free and 0.2% H₂S gases at 800°C.

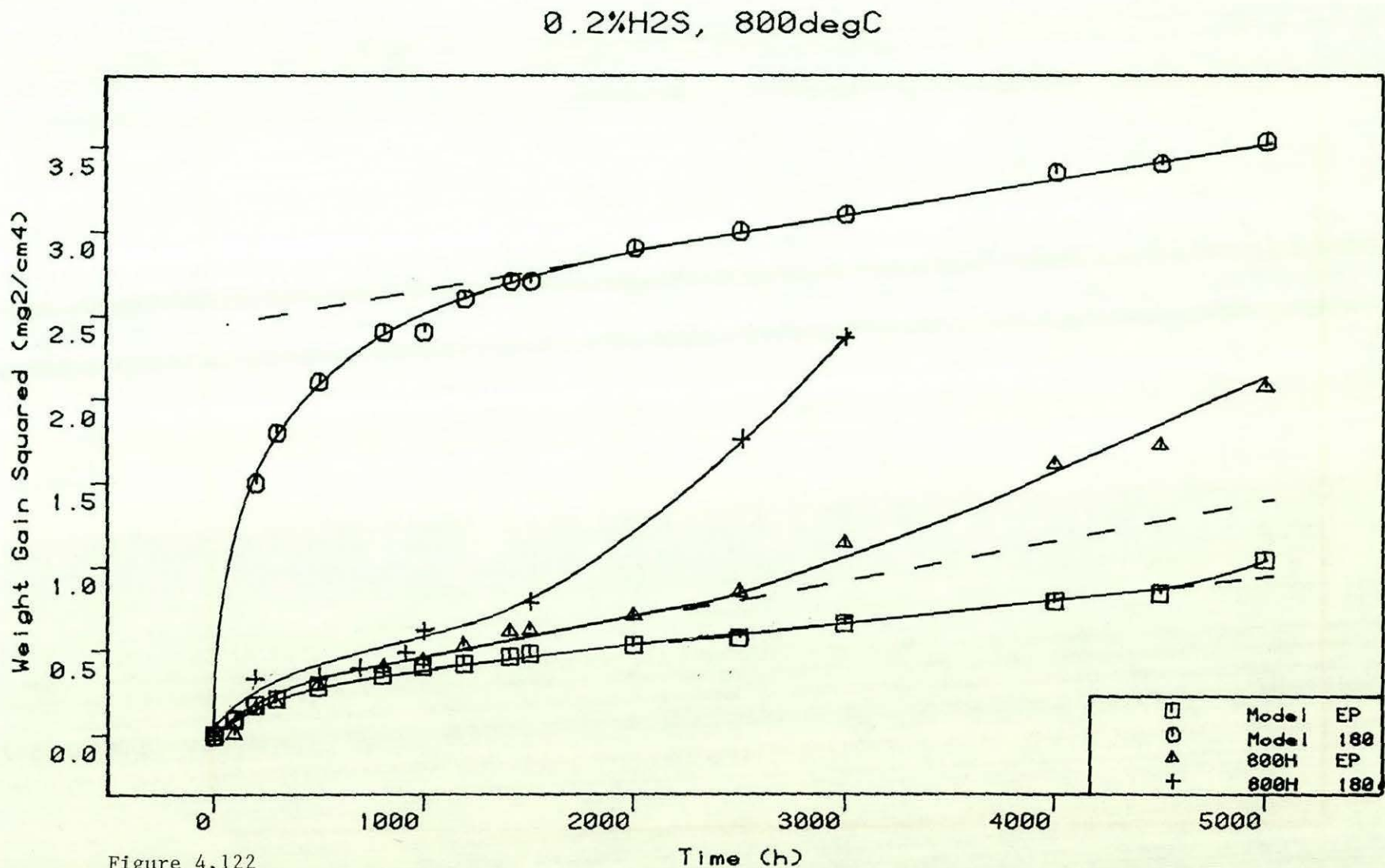


Figure 4.122

Plots of weight gain squared against time for Alloy 800H and the Model 25Cr-35Ni-Fe alloy exposed to the 0.2% H₂S gas at 800°C.

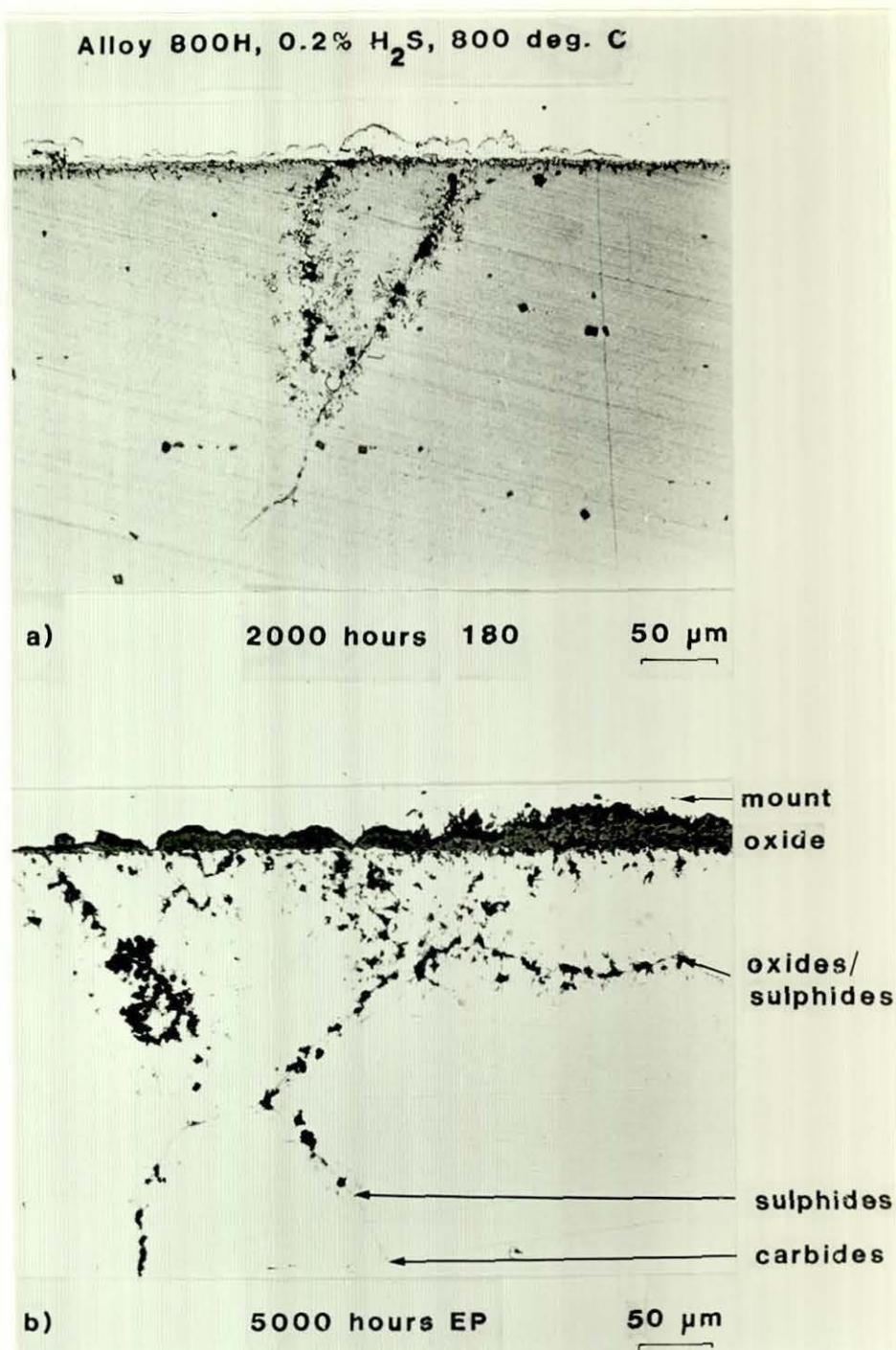


Figure 4.123

Cross-sectional metallographic examination of Alloy 800H exposed to the 0.2% H_2S gas at 800°C.

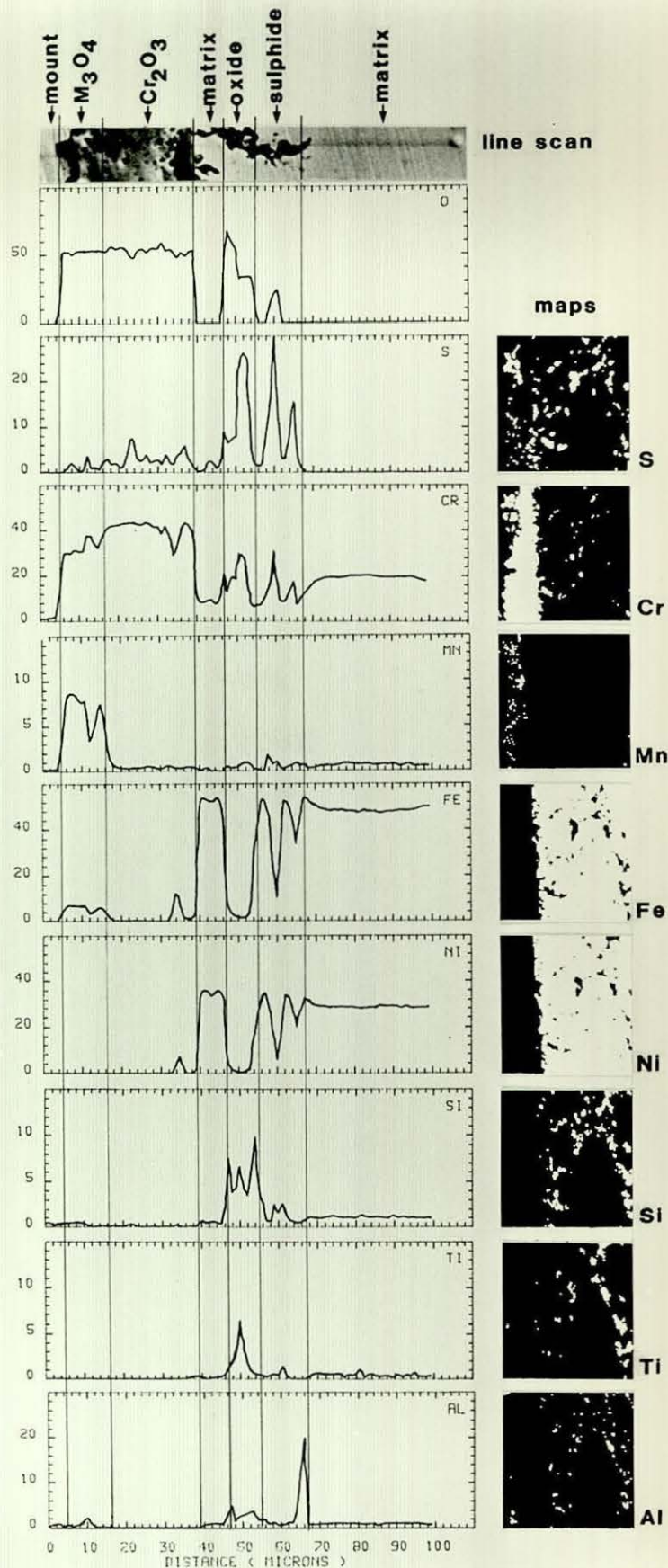


Figure 4.124

EPMA line scan on Alloy 800H exposed to the 0.2 % H₂S gas at 800°C for 5000 hours, electropolished (EP) condition.

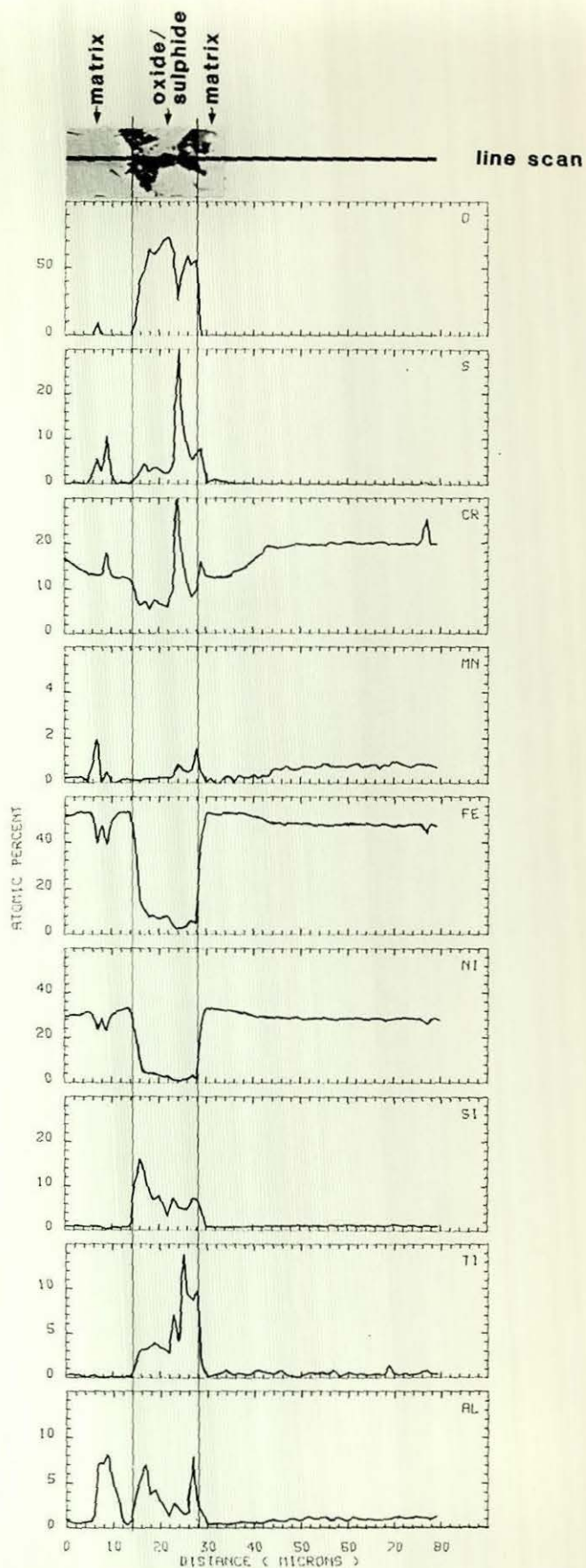


Figure 4.125

EPMA line scan on an area of localized attack in Alloy 800H exposed to the 0.2 % H_2S gas at 800°C for 5000 hours, electropolished (EP) condition.

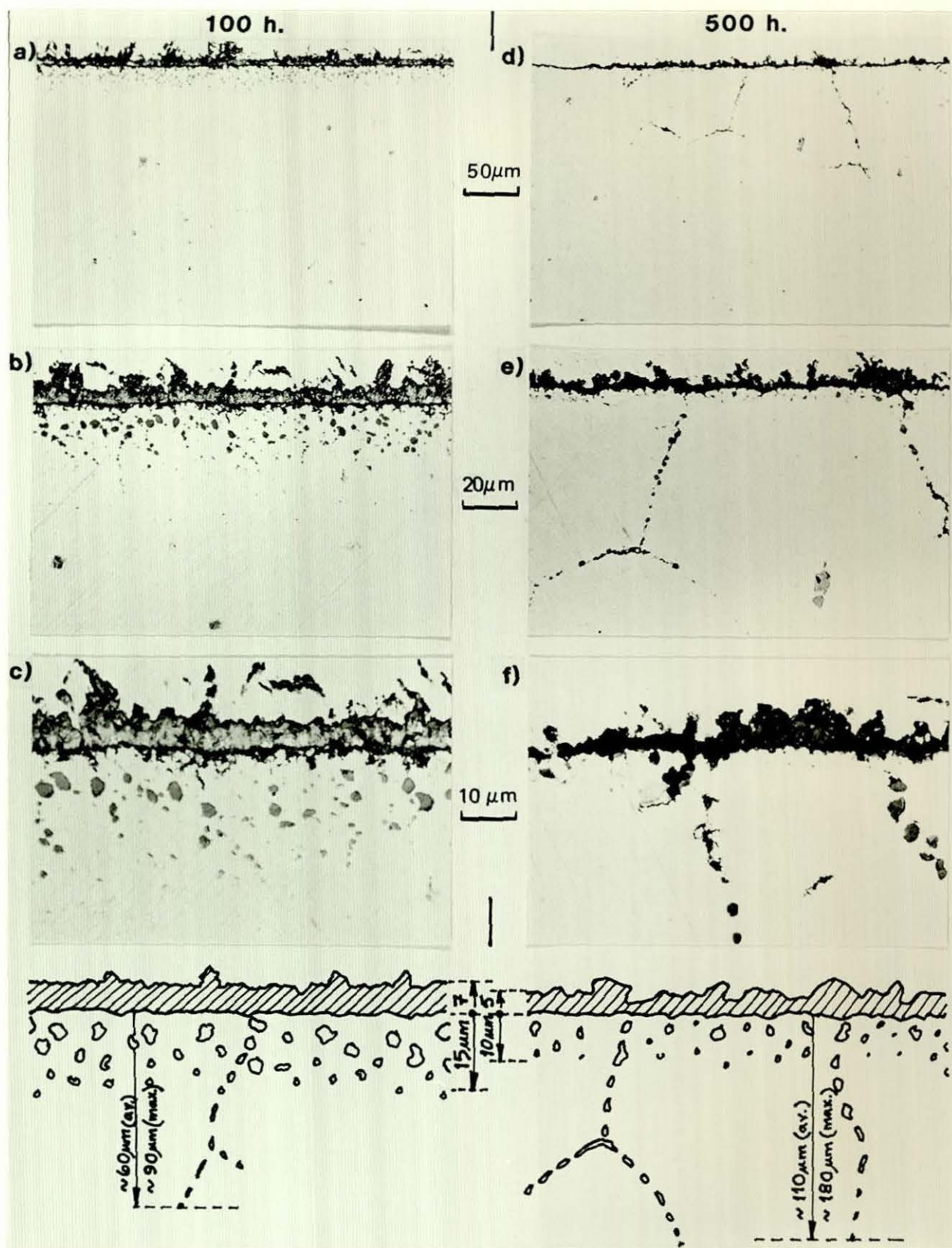


Figure 4.126

Cross-sectional metallographic examination of Alloy 800H exposed to the 0.2 % H_2S gas at 800°C, 180 grit condition.

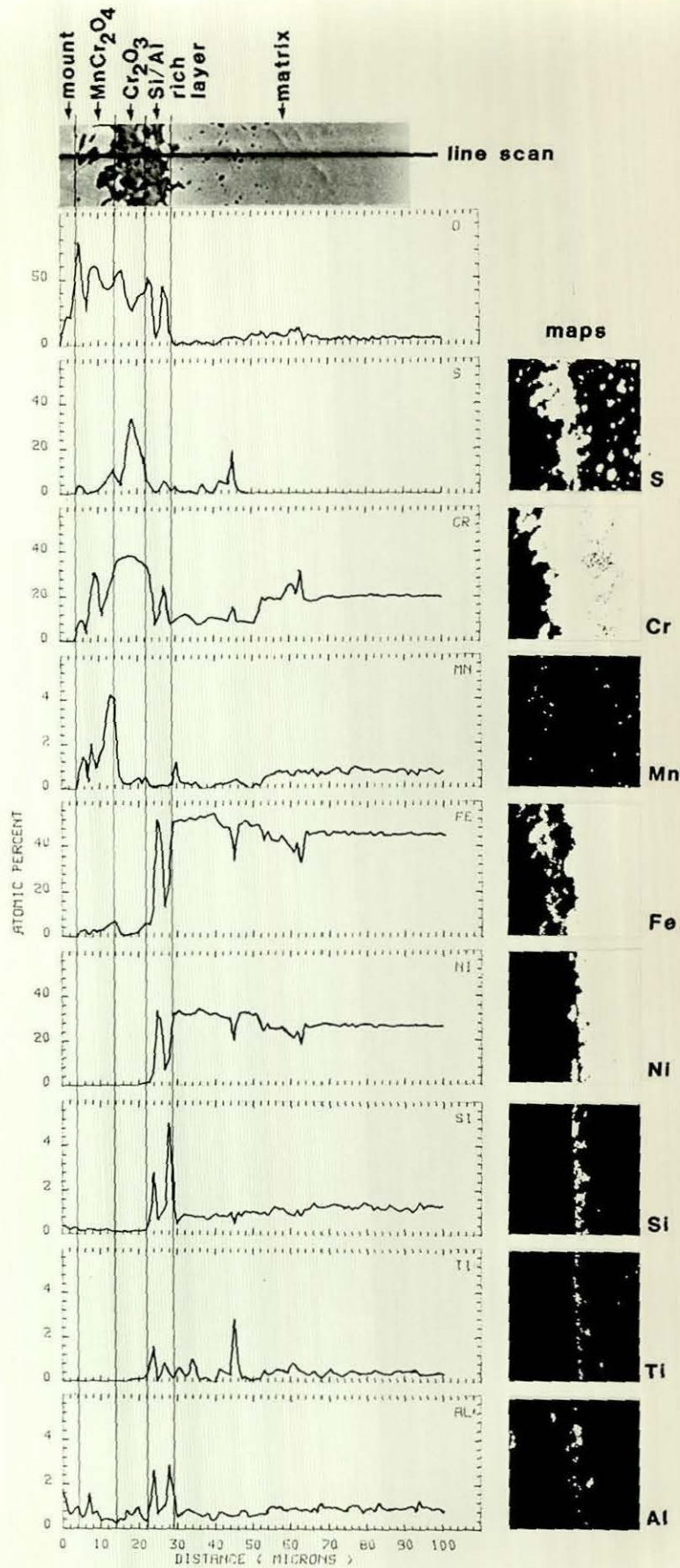


Figure 4.127

EPMA line scan and elemental concentration maps for Alloy 800H exposed to the 0.2 % H₂S gas at 800°C for 100 hours, 180 grit condition.

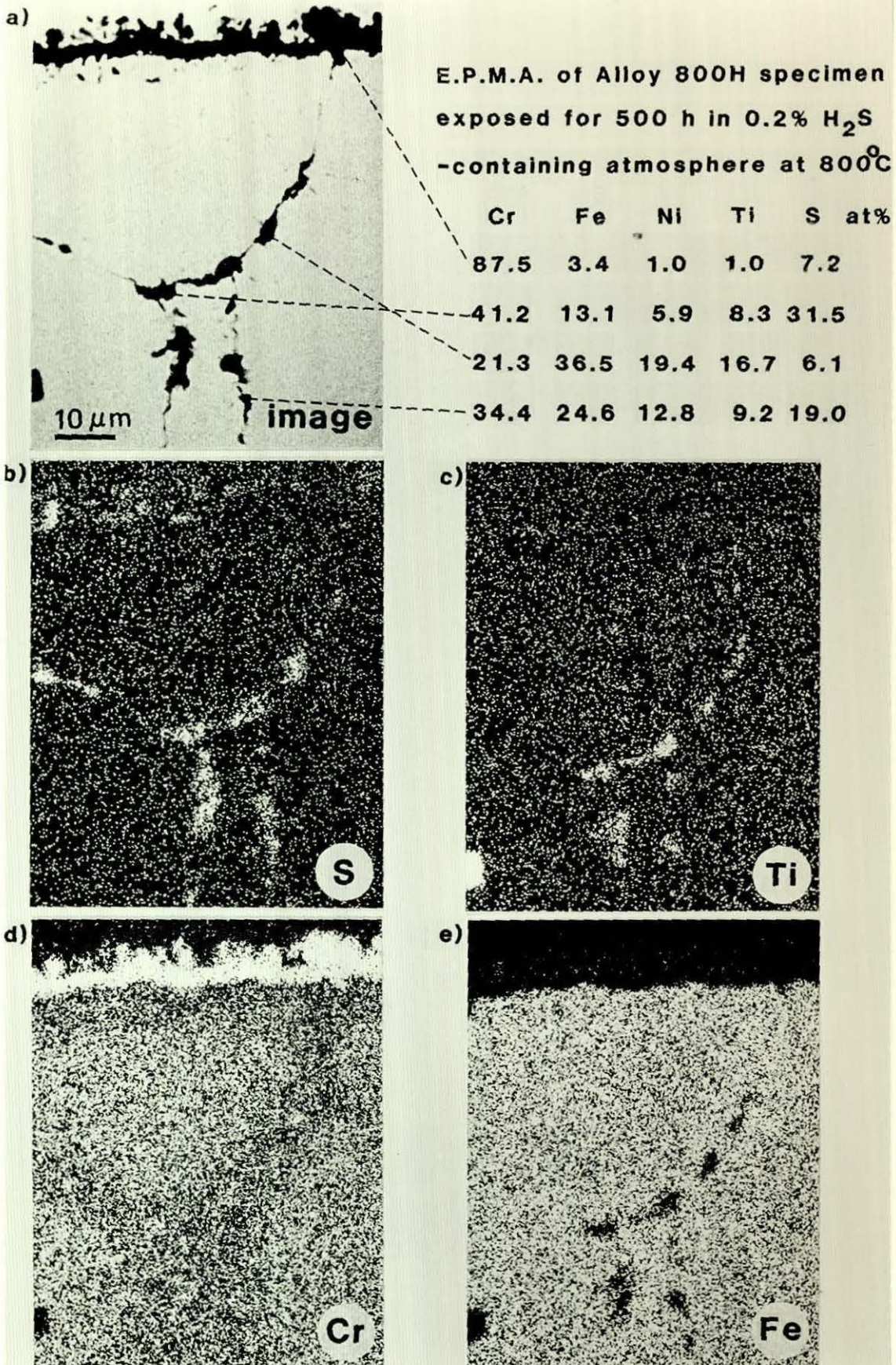


Figure 4.128

EDAX analysis on Alloy 800H exposed to the 0.2 % H₂S gas at 800°C for 500 hours, 180 grit condition.

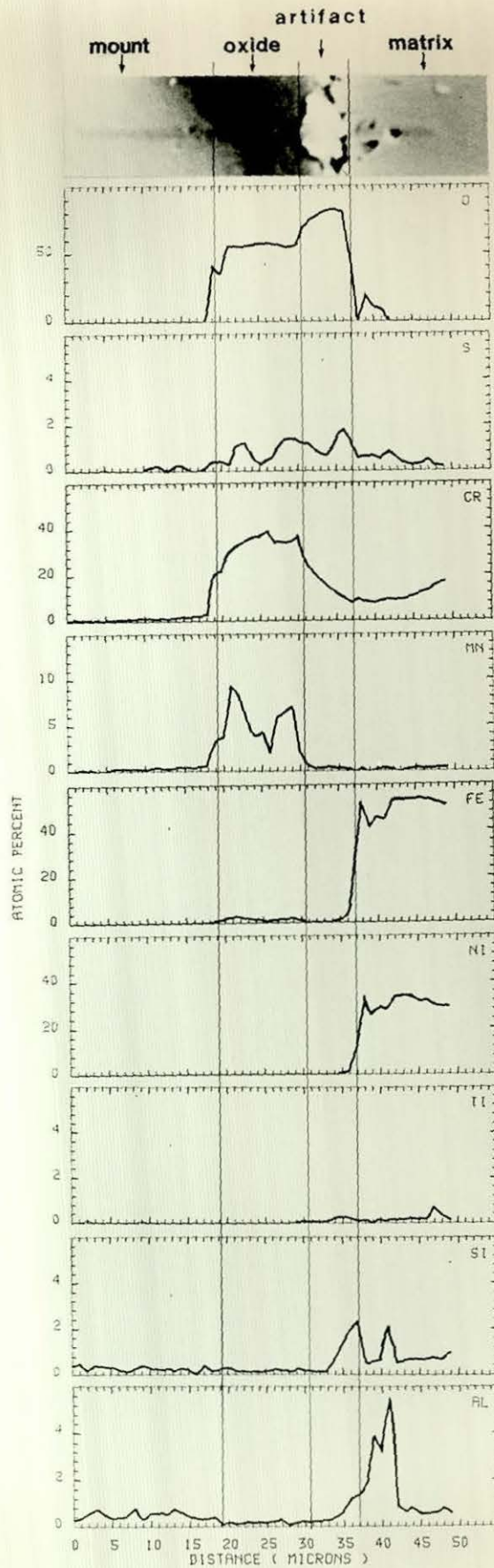


Figure 4.129

EPMA line scan on Alloy 800H exposed to the 0.2 % H_2S gas at 800°C for 2000 hours, 180 grit condition.

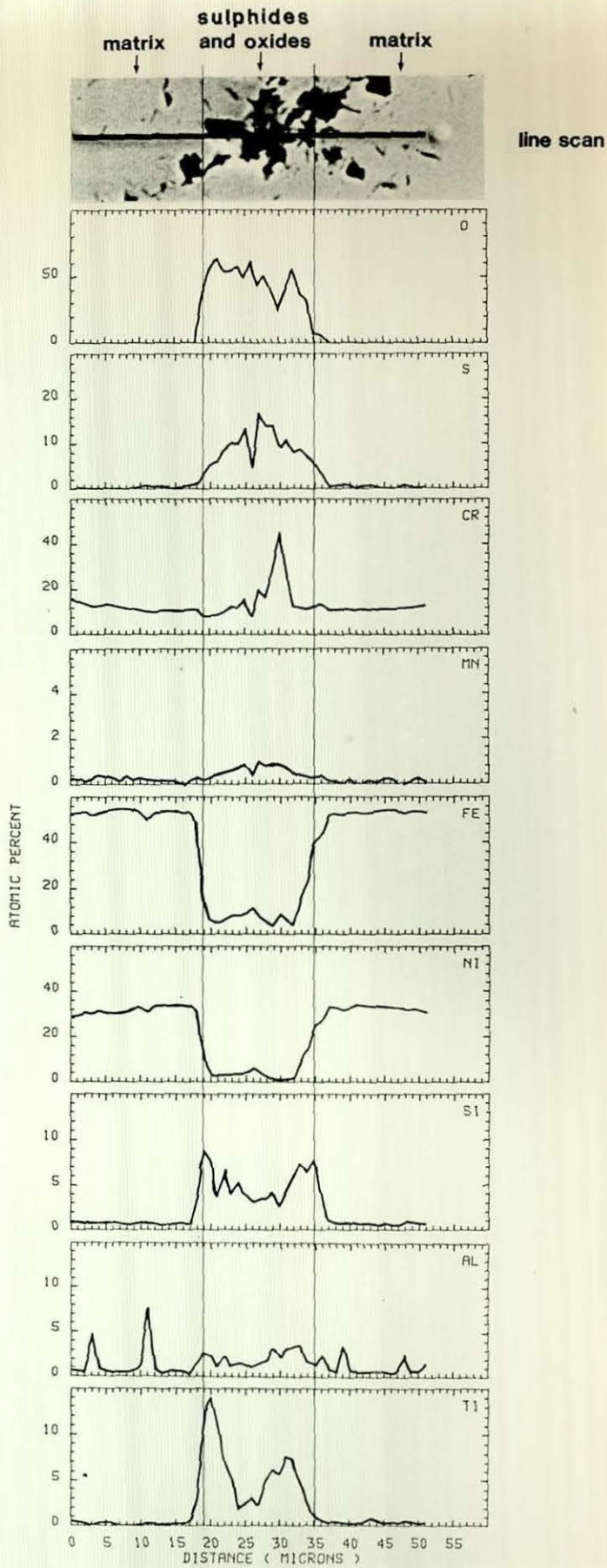


Figure 4.130

EPMA line scan on an area of localized attack in Alloy 800H exposed to the 0.2 % H_2S gas at 800°C for 2000 hours, 180 grit condition.

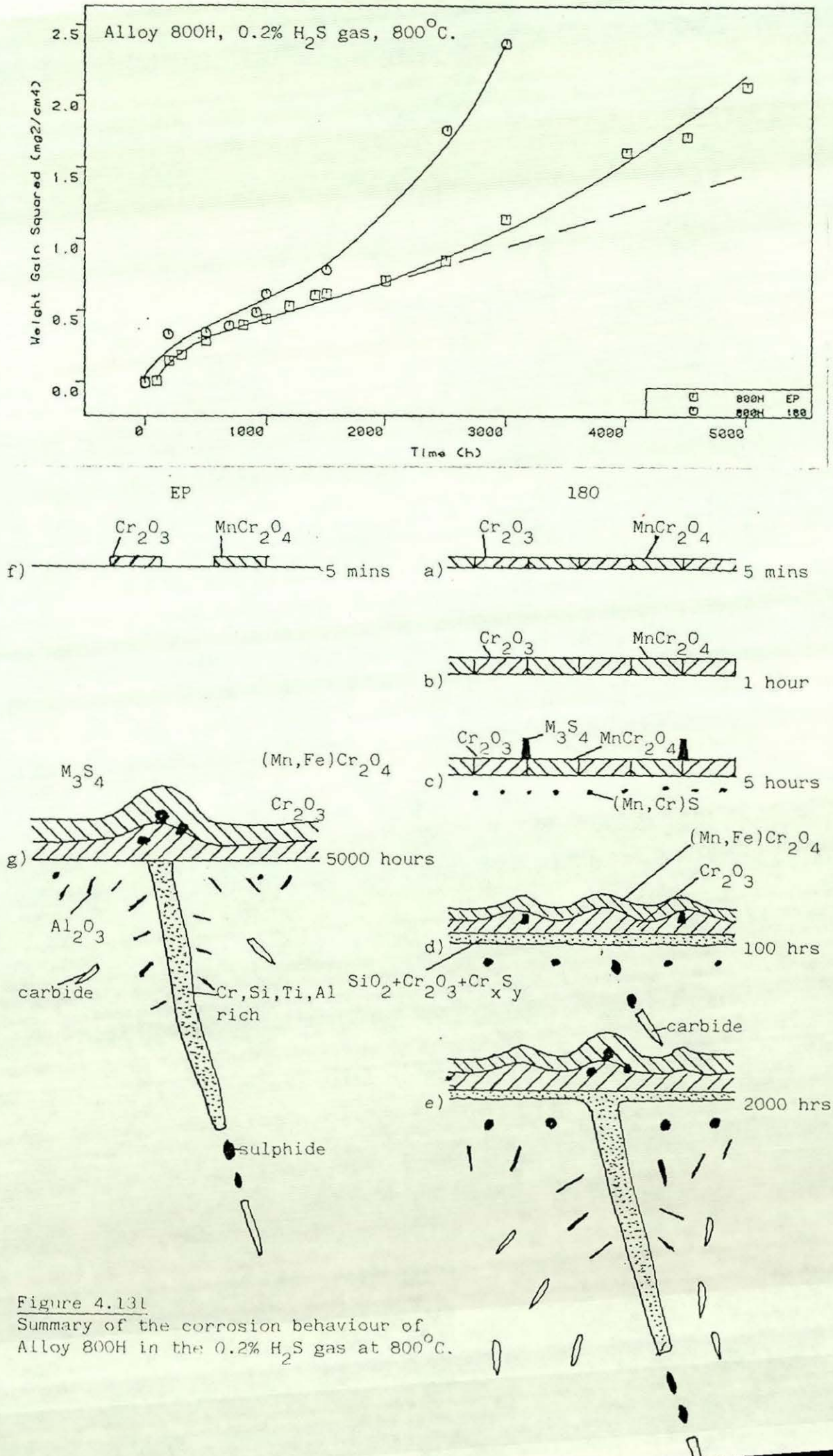


Figure 4.131
Summary of the corrosion behaviour of
Alloy 800H in the 0.2% H₂S gas at 800°C.

PS₂=10⁻⁸ bar, P_{O2}=10⁻²¹ bar, a_C=0.3, 800degC

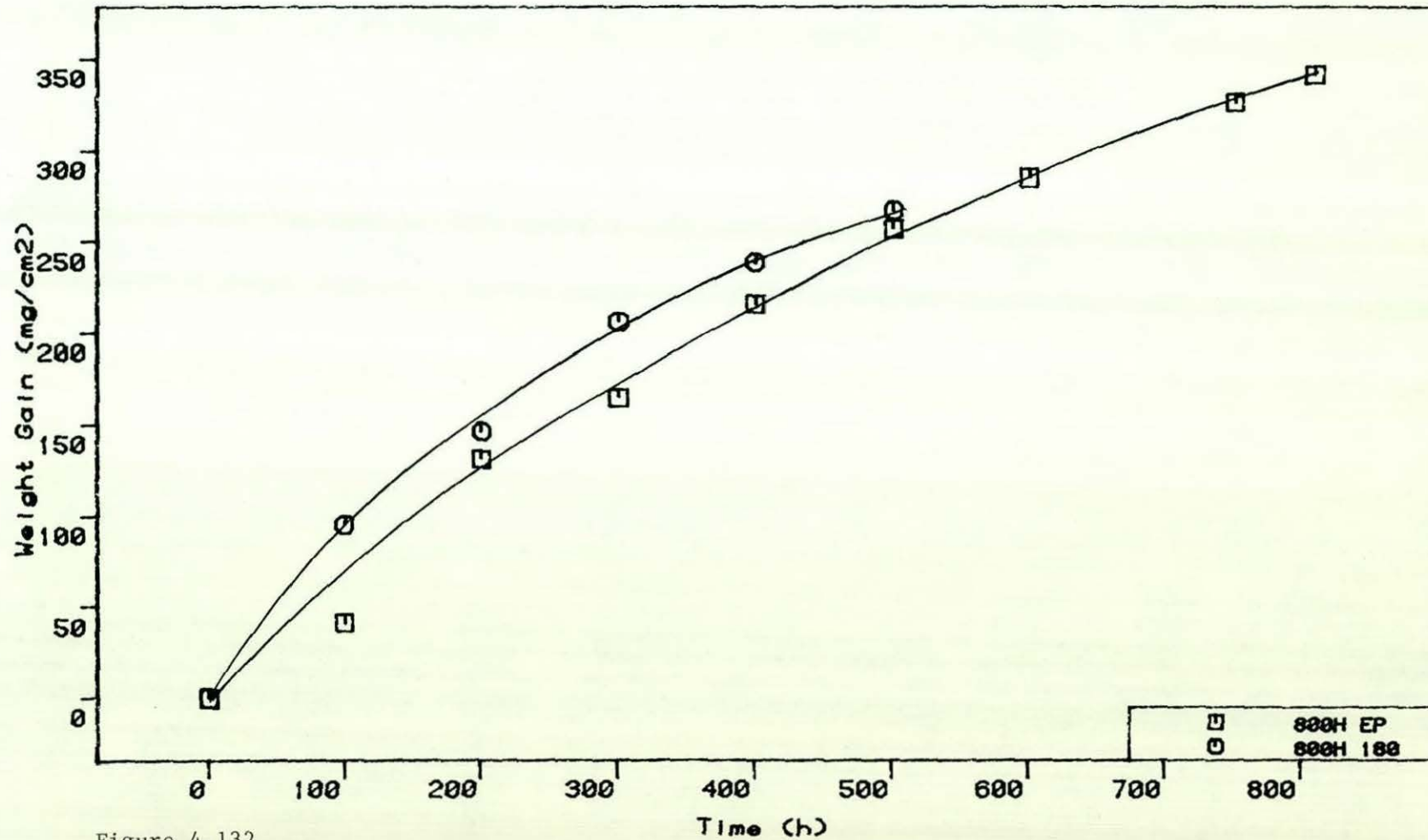


Figure 4.132
Corrosion kinetics for Alloy 800H in the 0.6% H₂S gas at 800°C.

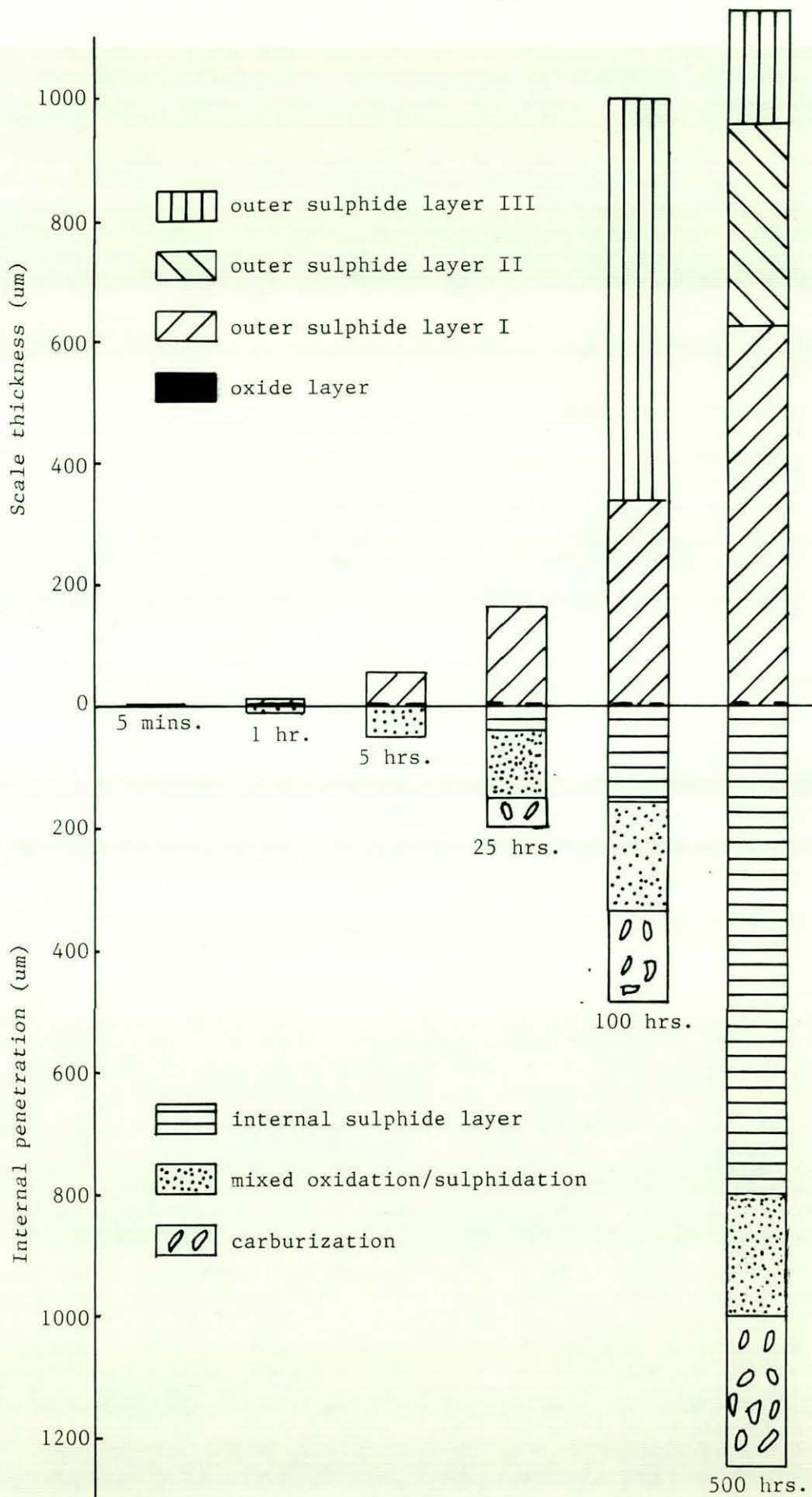


Figure 4.133

Diagram depicting the thickness of the various corrosion layers formed on Alloy 800H during exposure to the 0.6 % H_2S gas at $800^{\circ}C$.

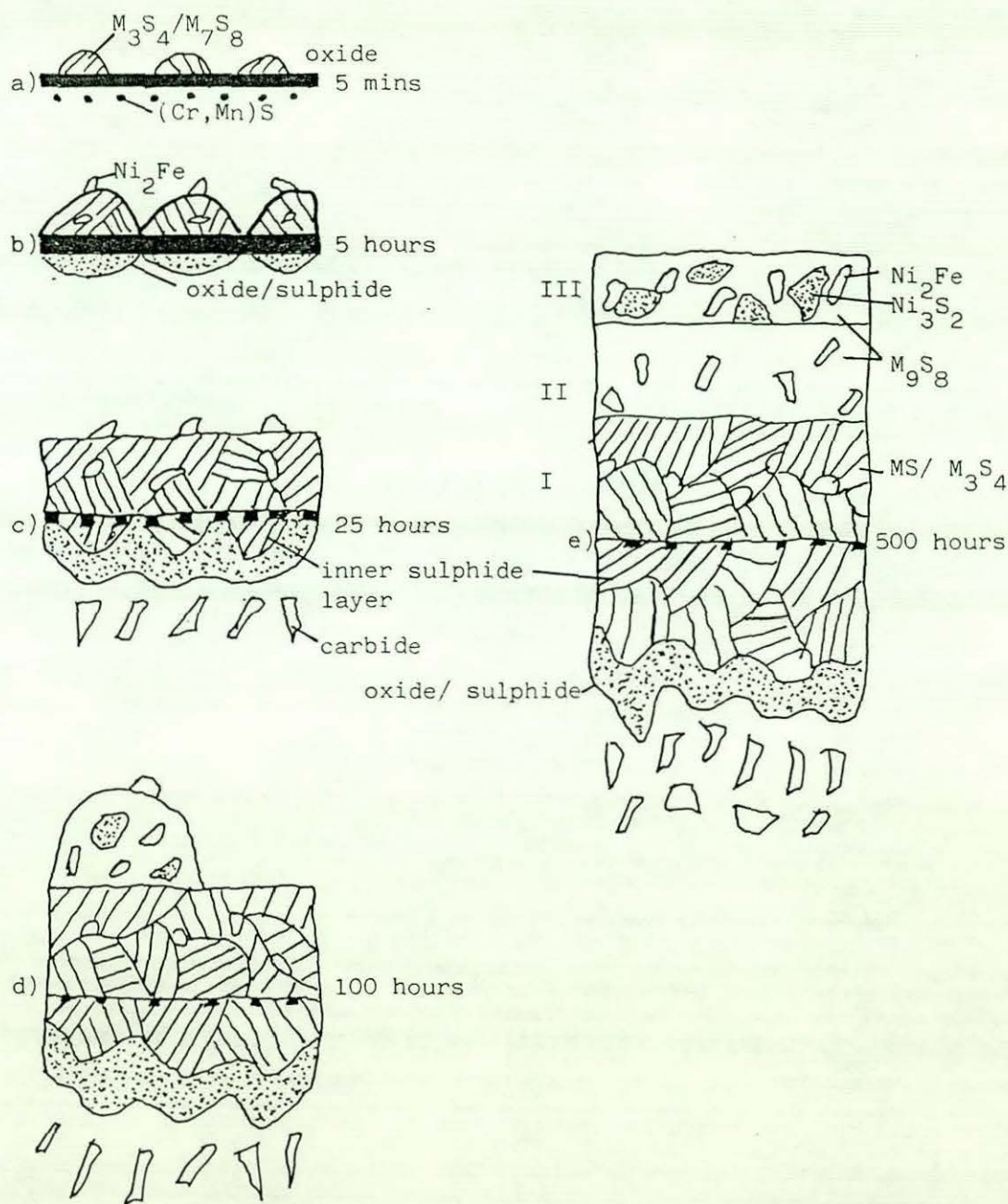


Figure 4.134

Summary figure showing the corrosion morphology of Alloy 800H in the 0.6% H_2S gas at $800^\circ C$.

800H, $P_{O_2}=10E-21$ bar, $a_C=0.3$, 800 deg.C

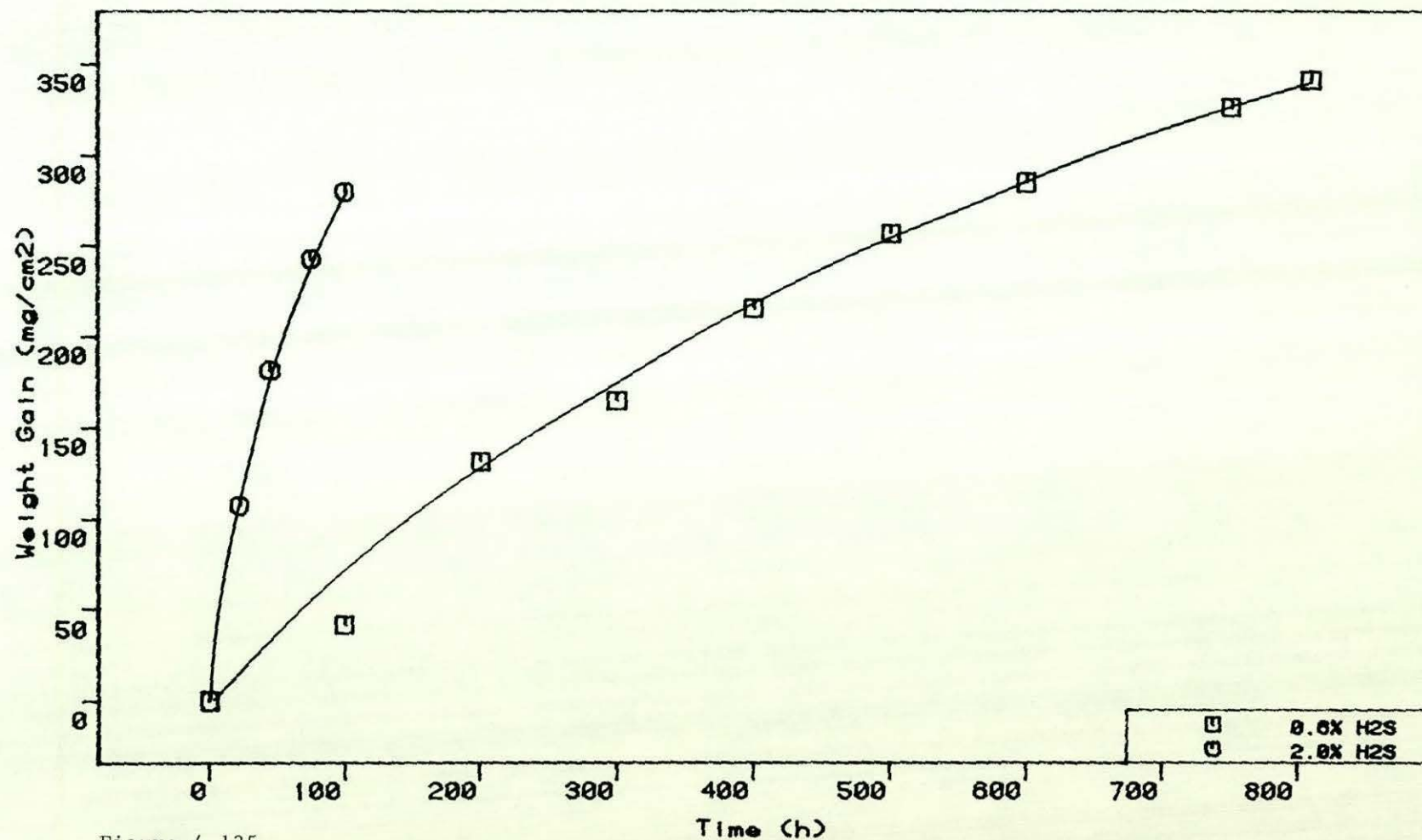
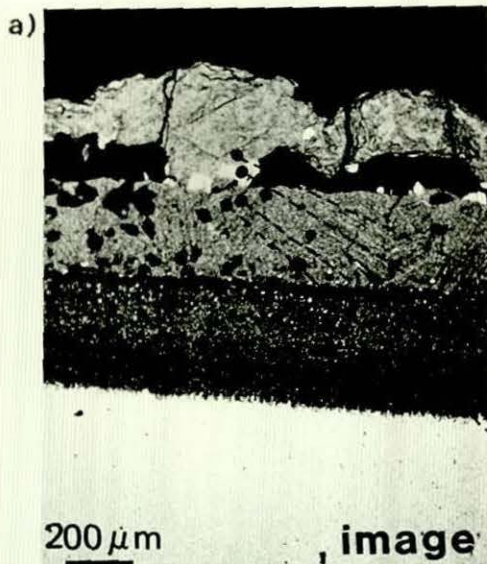


Figure 4.135

Corrosion kinetics for Alloy 800H in the 0.6% and 2.0% H_2S gases at 800°C.



E.P.M.A. of Alloy 800H specimen
exposed for 22.5 h in 2.0% H_2S
- containing atmosphere at 800°C

Cr	Fe	Ni	S at%
0.4	30.5	30.0	39.2
-	29.8	70.2	-
32.2	18.8	-	49.0
10.0	32.5	17.4	40.1

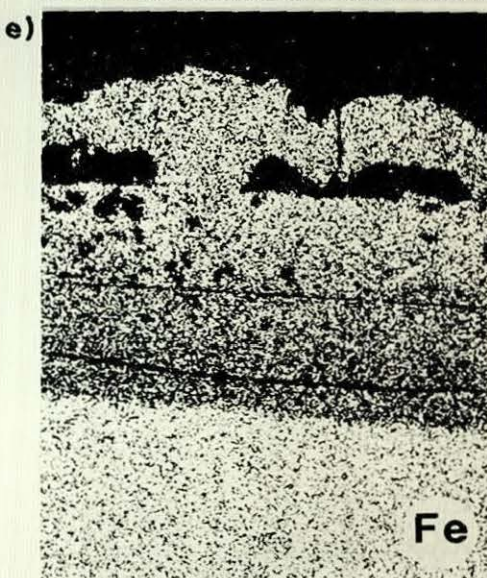
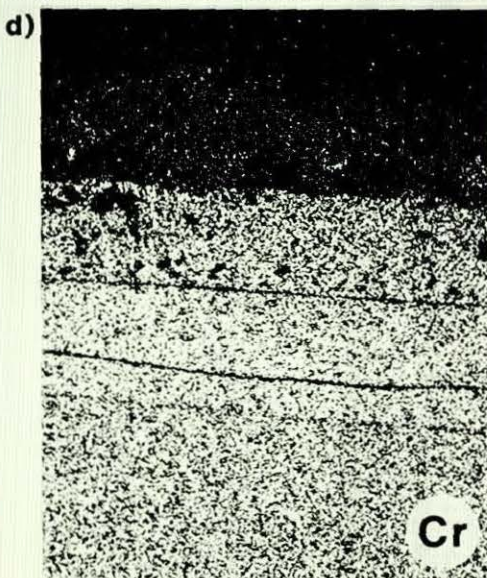
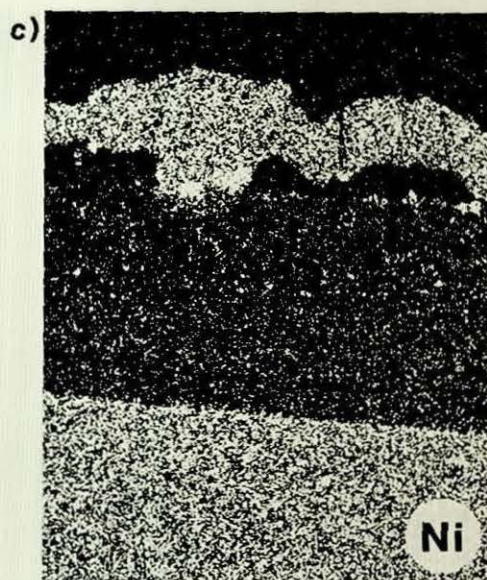
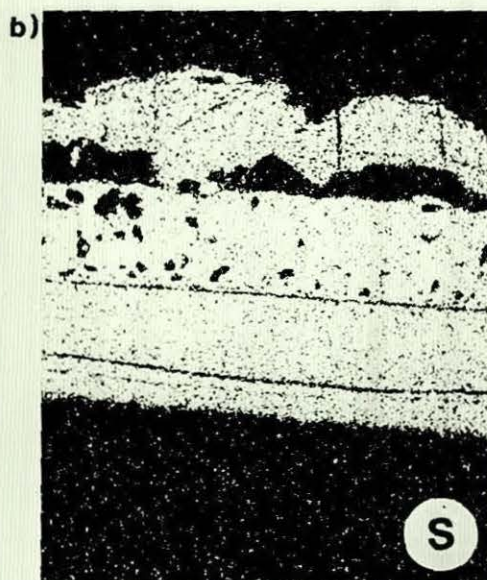


Figure 4.136

E.D.A.X analysis of Alloy 800H exposed to the 2.0% H_2S gas for 22.5 hours at 800°C.

5. DISCUSSION

The results and their interpretation were summarised at the end of each section in the previous chapter. In this chapter the various points emerging from the results will be discussed and the findings of this study compared with present knowledge. The first three sections of the discussion deal with the corrosion mechanism in:

- (i) The sulphur-free gas
- (ii) The low-sulphur containing gas (0.2% H_2S)
- (iii) The high-sulphur containing gas (0.6% H_2S)

In each section the corrosion mechanism of the simple Model 25Cr-35Ni-Fe alloy will be considered first, followed by an examination of the effect of minor alloying additions on this mechanism. The fourth and final section recommends the best alloys and surface finishes for the appropriate industrial operating conditions.

5.1. SULPHUR-FREE GAS

Chromia nucleation and growth

The Cr_2O_3 scale formed on the Model 25Cr-35Ni-Fe alloy grew at the rate of $5.6 \times 10^{-5} \text{ mg}^2 \text{ cm}^{-4} \text{ h}^{-1}$ ($1.6 \times 10^{-14} \text{ g}^2 \text{ cm}^{-4} \text{ sec}^{-1}$) for the electro-polished material and $2.8 \times 10^{-4} \text{ mg}^2 \text{ cm}^{-4} \text{ h}^{-1}$ ($7.8 \times 10^{-14} \text{ g}^2 \text{ cm}^{-4} \text{ sec}^{-1}$) for the 180 grit material. Both these rates are slightly lower than published data (10^{-11} to $10^{-13} \text{ g}^2 \text{ cm}^{-4} \text{ sec}^{-1}$) for binary Cr-containing alloys under purely oxidising conditions, reviewed by Hindam and Whittle (45), figure 2.30b. This is not really surprising in view of the fact that this study was concerned with a gas having a low partial pressure of oxygen ($pO_2 = 10^{-21}$ bar) and long term exposures (up to 5000 hours). Much of the published data was obtained at much higher pO_2 's, where oxides of Fe and Ni are thermodynamically stable, and for short exposure periods, of a few minutes to a few hours, where the corrosion rate is often at its maximum value.

Perhaps the most important point, however, to explain the difference in

parabolic rate constants obtained in this study and those in the published data is that Cr_2O_3 formed in low $p\text{O}_2$ environments is an n-type semiconductor with the majority defects chromium interstitials, whereas Cr_2O_3 formed in high $p\text{O}_2$ environments is a p-type semiconductor with the majority defects chromium vacancies (29, 43-46). Inspection of figure 2.22 clearly shows that theoretical parabolic rate constants (at 1000°C) for the Cr interstitial model (low $p\text{O}_2$ environments) are considerably lower than for the Cr vacancy model (high $p\text{O}_2$ environments). The reader is referred back to section 2.2.1 for a full description of these models.

In this study the parabolic rate constants was approximately one order of magnitude higher for the 180 grit material than for the electropolished material. This was because grinding the material on 180 grit SiC paper produced:

- (i) A much rougher uneven surface which increased the surface area of the alloy in contact with the gas.
- (ii) A high concentration of defects in the surface which provided many more nucleation sites for oxide particles.
- (iii) A worked layer (2-4 μm deep) which recrystallised on heating to the test temperature creating a very fine grain structure in the surface regions of the alloy. This produced a high concentration of grain boundaries which provided high diffusivity paths for chromium to the surface.

Most of the published work on surface finish effects has been carried out on commercial alloys and will be dealt with later.

The role of carbon

The partial pressure of oxygen ($p\text{O}_2 = 10^{-21}$ bar) and carbon activity ($a_c = 0.3$) used in this study were sufficient to allow the formation of oxides and carbides on the alloy surface in the initial stages. Thus the nucleation of Cr_2O_3 , FeCr_2O_4 and M_{23}C_6 on the electropolished material

was as expected. The fact that only Cr_2O_3 nucleated on the 180 grit material can probably be attributed to surface working homogenising the surface structure of the alloy and providing many more nucleation sites for oxide particles during the heating cycle, when the gas was not in equilibrium. These findings were very similar to those of Smith et al. (103) for alloys in a $\text{H}_2 - \text{CH}_4$ gas mixture ($p\text{O}_2 = 10^{-30}$ bar and $a_c = 0,8$ at 825°C). In the case of Smith et al's work the conditions (very low $p\text{O}_2$, high a_c) were such that the oxides were subsequently converted to carbides. In this study the conditions (higher $p\text{O}_2$, lower a_c) were such that once the surface layer became complete the carbides were initially overgrown and subsequently converted to oxides. Further work to fully investigate the heating cycle, perhaps using a hot stage microscope could be helpful to clarify the temperature and conditions at which the oxides and carbides start to form. It should be pointed out, however, that although this initial 'transient' behaviour is interesting it has little effect on the overall corrosion mechanism.

Much more important findings were that the thin uniform non-porous Cr_2O_3 scale formed on the electropolished material provided a very good barrier to carbon ingress from the gas, whereas the thick, cracked, porous and faster growing Cr_2O_3 scale on the 180 grit material allowed a significant amount of carbon ingress to take place. These observations confirm the definitive study by Wolf and Grabke (137, 145) that carbon penetrates oxide scales by the diffusion of carbon containing gaseous species through cracks and pores and not by solid state lattice or grain boundary diffusion.

A final point of interest was the absence of internal carbide precipitates in the chromium depleted zone of the alloy substrate immediately beneath the oxide scale. This was due to the lower chromium activity in the alloy (a_{cr}) in effect shifting the $\text{Cr}/\text{Cr}_{23}\text{C}_6$ thermodynamic boundary to higher values of carbon activity a_c . Thus for a fixed carbon activity in the alloy (point A on figure 5.1) the carbides are stable in the undepleted alloy (with a high a_{cr}), but not stable in the Cr-depleted region (with a low a_{cr}).

The role of silicon

The high Si content (2.04%) of the AISI314 material promoted the formation of a complete inner SiO_2 layer which reduced the kinetic rate by forming a very effective barrier to the outward diffusion of Cr, Fe and Mn and inward diffusion of C. A complete SiO_2 layer also formed on the lower (1.2%) Si containing alloy HP40Nb in the 180 grit condition. The SiO_2 layer was not complete on the HP40Nb alloy in the electro-polished condition or in the low (0.7%) Si containing alloy 800H.

These findings are in line with several other workers (97, 201 - 204) who have established that significant Si alloying additions reduce kinetic rates. Just how much Si is required to form a complete layer depends to some extent on the exposure conditions, alloy structure, temperature and amount of surface work. As far as the types of alloys and exposure conditions used in this study are concerned it can be concluded that an Si level of at least 1.2% for surface worked materials and 2% for electropolished materials are required to ensure a complete SiO_2 layer. Surface working assists the establishment of this layer by providing more defects to act as nucleation points and more grain boundaries to assist the supply of Si to the scale/alloy interface.

The critical question of why a complete SiO_2 layer forms such an effective barrier to the outward diffusion of cations and inward diffusion of carbon appears to have been ignored by many previous investigators. This could be due to the layer often being so thin that it is difficult to analyse in cross-section. The author of this study proposes that the following three reasons account for an SiO_2 layer acting as an effective barrier to ionic transport.

- (i) The solubility of most elements in SiO_2 is virtually zero. Thus it is very difficult for movement of other cations to take place via solid state lattice diffusion.
- (ii) SiO_2 can exist as an amorphous or crystalline structure. If as is the case in this study the SiO_2 is amorphous it is unlikely that any grain boundaries are present in the oxide (205). Thus ionic

diffusion via grain boundaries is not possible.

- (iii) As already discussed carbon penetration through Cr_2O_3 scales occurs via the diffusion of carbon containing gaseous species through cracks and pores. It is therefore reasonable to assume that the same mechanism applies to SiO_2 . However, as the SiO_2 layer is an inward slow growing layer it is unlikely to contain many cracks and pores and therefore provides a much more effective barrier to the ingress of carbon than an outward fast growing layer.

It could be argued that the SiO_2 layer could have become complete on the HP40Nb electropolished material if it had been exposed for very long exposure times. This was not possible due to a number of surface carbides nucleating on and below the alloy surface in the initial stages and the presence of the indigenous carbides at the alloy surface. As the surface scale became complete these carbides were converted to chromium rich oxides which provided diffusion paths for cations through the incomplete SiO_2 layer.

Another issue concerning the addition of Si to alloys is how it affects spallation/keying on of outer oxide layers. Some researches (203, 206, 207) claim that Si can key on outer oxide layers whilst others (201, 202, 208, 209) claim that it induces spallation of these layers. As far as this study is concerned the complete SiO_2 layer provided such an effective barrier to outward cationic diffusion that there was little external scale formed either to key on or spall off. This issue will be discussed further when sulphur is introduced into the gas and the situation is considerably different.

Before leaving the subject of Si it is worthwhile pointing out that whilst Si additions can be extremely beneficial for improving corrosion resistance they can be detrimental to an alloy's creep strength and weldability. High levels of Si in the alloy can also make the alloy prone to formation of the brittle σ phase (210, 211) as demonstrated in the AISI314 material.

The role of manganese

It is difficult to isolate the role of manganese in the corrosion process due to all the commercial alloys containing alloying additions of both Si and Mn. However, by making the assumption that Si had no effect when a complete SiO_2 layer did not form, it is possible to make a reasonable assessment of the role played by manganese. In such cases illustrated by HP40Nb (electropolished condition) and Alloy 800H (both surface finishes), Cr_2O_3 and MnCr_2O_4 spinel nucleated on the alloy surface in the initial stages. These nuclei grew to form a scale containing a mixture of these phases. After extended exposure periods the scale separated into an outer $(\text{Mn,Fe})\text{Cr}_2\text{O}_4$ spinel layer and an inner Cr_2O_3 layer. Two questions obviously emerge from this.

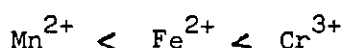
- (i) Why does MnCr_2O_4 tend to nucleate in preference to FeCr_2O_4 ?
- (ii) Why does the scale separate into an outer $(\text{Mn,Fe})\text{Cr}_2\text{O}_4$ layer and an inner Cr_2O_3 layer?

As expected oxides of all components which were thermodynamically stable formed in the initial stage. The apparent abundance of MnCr_2O_4 is due firstly to this phase having a greater affinity for oxygen than Cr_2O_3 and FeCr_2O_4 and secondly to Mn diffusing faster to the alloy surface than Cr and Fe.

Just why the scale separates into two distinct layers after longer exposure times is more difficult to explain. MnCr_2O_4 is stable at lower oxygen activities than Cr_2O_3 , which in turn is more stable than FeCr_2O_4 . Thus from a thermodynamic point of view a MnCr_2O_4 layer would form beneath a Cr_2O_3 layer, i.e. where the oxygen activity is lower. However the presence of small amounts of Fe in the spinel, as detected in this study, could be sufficient to enable the Cr_2O_3 to exist at lower oxygen activities than a $(\text{Mn,Fe})\text{Cr}_2\text{O}_4$ layer, thus allowing the formation of the outer $(\text{Mn,Fe})\text{Cr}_2\text{O}_4$ layer and inner Cr_2O_3 layer.

A much more likely reason for the development of the outer $(\text{Mn,Fe})\text{Cr}_2\text{O}_4$ layer and inner Cr_2O_3 layer is the high diffusion rate of Mn in the

spinel. Cox et al ⁽²¹²⁾ have developed a mechanism to explain different diffusion rates of different cations in oxide spinels. These authors argue that according to Azaroff ⁽²¹³⁾ cations diffuse through a close-packed anion lattice via alternate adjacent octahedral and tetrahedral positions. (Diffusion via similar interstitials, i.e. tetrahedral to tetrahedral or octahedral to octahedral positions is prohibited by the severe lattice distortions that would be required for this to take place). The amount of energy required for a cation to diffuse from one site to another is given by its crystal field preference energy. These values determined by Dunitz and Orgel ⁽²¹⁴⁾ from spectroscopic data can be ranked in terms of increasing energy as



i.e. Much less energy is required for Mn^{2+} to diffuse through the lattice than Cr^{3+} . Thus as the exposure time increases Mn diffuses rapidly through the spinel and concentrates at the scale/gas interface, leaving the spinel lattice nearer the scale/alloy interface deficient in Mn^{2+} cations. These positions were filled up again as long as new Mn^{2+} ions were available from the alloy substrate. However, as the alloys used in this study contained only 0.6 to 1.2% Mn the alloy substrate beneath the oxide scale soon became depleted in Mn, which in turn reduced the rate of supply of Mn^{2+} to the oxide. Thus the Mn^{2+} ions in the spinel at the scale/alloy interface were not replaced and transformation to Cr_2O_3 took place. The newly formed Cr_2O_3 then combined with the initial Cr_2O_3 nuclei to form the inner Cr_2O_3 layer.

This leaves the question of whether Mn can continue to diffuse through the inner Cr_2O_3 layer once it is complete. As far as the author of this thesis is aware there is a dearth of published information on the transport of Mn through Cr_2O_3 layers. Wild ⁽²¹⁵⁾ claims to have formed a thin (few atoms thick) Cr_2O_3 layer on an unstabilized austenitic stainless steel En58A under ultra-high vacuum conditions at 770 - 1070 K. Mn subsequently diffused through this layer at a rate of 2 orders of magnitude faster than Cr. No explanation is given as to how this happens. One must also remain sceptical about Wild's study as it should be impossible to form Cr_2O_3 without forming some of the Mn containing

spinel.

Clearly the fact that Mn, Cr and O form a compound demonstrates that there is some mutual solubility of Mn in Cr_2O_3 , therefore lattice diffusion of Mn through Cr_2O_3 is possible. A further piece of rather surprising evidence to support this argument can be gleaned from the examination of the Model 25Cr-35Ni-Fe alloy. Small amounts of Mn were detected in the outer regions of the Cr_2O_3 scale after long exposure times indicating that some of the very small amount (0.01%) of Mn present in this alloy had managed to diffuse through the Cr_2O_3 layer.

The observed build up of small amounts of Mn in the outer regions of the Cr_2O_3 layer formed on the Model alloy appeared to be associated with an increase in the Cr_2O_3 lattice parameter. Cox et al ⁽²¹⁶⁾ have attributed such a phenomenon to the doping of Cr_2O_3 with Fe. However according to Cox et al ⁽²¹⁶⁾ the values of lattice parameter found in this study after long exposure times would have corresponded to 10-20% Fe becoming incorporated into the Cr_2O_3 lattice. Both ESCA-AUGER and EPMA analysis on several specimens found no sign of Fe in the Cr_2O_3 layer, but did detect small quantities of Mn at the scale/gas interface. X-ray diffraction analysis using surface reflection detected no MnCr_2O_4 . It is therefore postulated that the increased lattice parameter values in this study were due to doping of the Cr_2O_3 scale with Mn and not Fe. As the atomic radius of Mn is greater than Fe the same increase in lattice parameter could be caused by a much lower quantity of Mn than Fe. This increased lattice parameter effect (with possible exception of Alloy 800H) did not occur on the commercial alloys as they contained sufficient Mn to form the MnCr_2O_4 .

Whilst dealing with the subject of lattice parameters it is worth while pointing out that increasing the amount of Mn in the $\text{Mn}_{1-x}\text{Cr}_{2-x}\text{O}_4$ layer on the alloys which formed a complete SiO_2 layer (AISI 314 both surface finishes and HP40Nb 180 grit condition) corresponded to an increase in the spinel lattice parameter. Further information concerning the effect of different components in oxide spinels is given by Francis ⁽²¹⁷⁾.

Having established that Mn can diffuse through Cr_2O_3 layers it is worth

while examining whether Mn diffuses through SiO_2 layers. As far as this study is concerned a complete SiO_2 layer formed a very effective barrier to the outward diffusion of Mn. This is contrary to the postulations of Yurek et al (203) who speculated that Mn can diffuse through an SiO_2 layer.

The role of Aluminium

The 3.5% Al addition to the HP40 type alloy (HP40Al) resulted in the formation of a number of internal lenticular shaped Al_2O_3 particles. These did not form a complete layer and therefore had no obvious effect on the corrosion mechanism. Similar findings to these were observed by Belan et al (218) for the same alloy exposed to pure oxygen at 1000°C .

Just how much Al is required to form a complete Al_2O_3 layer is a matter of considerable debate and depends on many factors such as temperature, exposure conditions, surface condition and other alloying additions. A considerable amount of work (219) has been published concerning Al_2O_3 formation and growth, but unfortunately much of this is not directly comparable with this study. Perhaps the most direct comparison can be made with the findings of Tomaszewicz and Wallwork (220) who determined an oxide map for ferritic Fe-Cr-Al alloy exposed to pure oxygen at 800°C , figure 5.2. This gives a good overall picture of the types of corrosion morphology which are possible for alloys containing both Cr and Al. The map is divided into four regions.

- (i) Type I alloys containing less than 2.5 wt% Al and < 13 wt% Cr. These formed a scale which consisted of 3 layers:- an outer Fe_2O_3 layer, and intermediate FeCr_2O_4 layer and an inner layer containing a mixture of FeAl_2O_4 and needle-like Al_2O_3 particles.
- (ii) Type II alloys with less than 2.5% Al and greater than 13% Cr. These formed a scale which consisted of a discontinuous outer Fe_2O_3 layer, an intermediate Cr_2O_3 layer and an inner discontinuous layer containing needle-like Al_2O_3 particles.
- (iii) Type III alloys containing between 2.5 and 7% Al and less than

5% Cr. In this case the scale formed consisted of a mixture of Al_2O_3 and Fe_2O_3 and was not protective.

- (iv) Type IV alloys with greater than 5% Cr and greater than 2.5% Al. In this case a protective Al_2O_3 scale formed, but at very high Al levels it tended to be susceptible to spallation.

Thus it could have been expected that the HP40Al alloy (containing 3.5% Al) would have behaved as a type IV alloy and formed a complete Al_2O_3 layer. Instead it formed an outer $(\text{Mn,Fe})\text{Cr}_2\text{O}_4$ layer, and intermediate Cr_2O_3 layer and a discontinuous layer containing needle-like Al_2O_3 particles, i.e. it behaved like a type II alloy. There are probably many reasons for this which are impossible to isolate due to the complex structure of the HP40Al alloy. These include:

- (i) Some of the Al being tied up in the intermetallic NiAl phase.
- (ii) The presence of Si forming some SiO_2 particles in the inner oxide layer.
- (iii) The presence of large amounts of primary and secondary carbides interfering with the inner oxide layer.
- (iv) The alloy having an austenitic structure which makes comparisons with the map for the ferritic alloy difficult.

It can be concluded that the 3.5% Al addition to the HP40 type alloy was not sufficient to form a complete Al_2O_3 layer and therefore offered no additional corrosion protection. In theory higher levels of Al should allow the formation of a complete Al_2O_3 layer which could be beneficial. Further work is needed to establish if this is true in these low oxygen partial pressure environments.

The role of Niobium

Niobium was present in the HP40Nb and HP40Al alloys. It had no effect on the corrosion mechanism due to most of it being tied up in the MC

carbides which remained stable throughout the exposure period. A small amount of Nb was detected at the scale/gas interface but this was insufficient to have any influence on the corrosion process. Hemptenmacher et al (221) have claimed that the presence of Nb can assist the formation of an internal (Al,Nb) rich layer on alloys containing low carbon levels, but as no meaningful explanation is offered for this one must remain sceptical about their claim.

Localised grain boundary attack in Alloy 800H and the role of titanium

A significant amount of localised internal oxidation occurred at grain boundaries in Alloy 800H. These oxides tended to be rich in Si, Ti and Al near the scale/alloy interface, Ti and Al deeper in the alloy and only Al at the deepest point of attack. It is difficult to determine the cause of this due to this alloy containing small amounts of many elements such as Ti, Al, Si and Mn. It is also difficult to compare this alloy with others in the study due to its having a much lower Cr content (approximately 20%). However as Alloy 800H was the only alloy to contain Ti and be subject to a significant amount of localised oxidation it is likely that these are linked. This is emphasised by the fact that HP40Al only containing Al, Si and Mn formed a general region of internal Al_2O_3 particles, but showed no obvious sign of any localised attack of the carbides.

It is well known that Alloy 800H is susceptible to the formation of Cr rich M_{23}C_6 carbides at grain boundaries (222). The extent of this carbide precipitation is reduced by adding Ti to the alloy to react with dissolved carbon in the alloy to form intragranular TiC precipitates. However as was observed in this study some M_{23}C_6 carbide precipitation at grain boundaries still takes place. The following hypothesis is proposed to try to explain how these Cr-rich M_{23}C_6 grain boundary carbides are eventually replaced by Si, Ti and Al rich oxides during the corrosion process.

As the alloy contained a relatively low level of Cr in the first place, the formation of the Cr rich surface scale produced a large zone in which the chromium activity (a_{Cr}) was too low for Cr rich carbides to

be stable. The grain boundary carbides therefore transformed to metal and carbon. The metal ions diffused rapidly to the surface to be incorporated into the surface scale. The carbon combined with Ti to form TiC which is a more stable carbide. As 6 carbon atoms combined with only 6 Ti atoms instead of 23 Cr atoms this created a large number of vacancies to form pores which provided an easy passage for oxygen to diffuse inwards. The local oxygen activity thus steadily increased until Al_2O_3 formed. As time progressed the local oxygen activity continued to increase and oxides first of Ti and then Si also became stable, thus explaining the ordering of these elements in the internal oxides.

It should be emphasised that this is just a hypothesis. Further experimental work of model alloys for 800H containing Si and Al with no Ti and Si and Ti with no Al is needed to prove or disprove this. If the hypothesis is true, localised attack at temperatures below 750°C should not occur due to the kinetics of TiC formation being very slow^(222, 223). Initial results within the Petten laboratories appear to confirm this (224, 225).

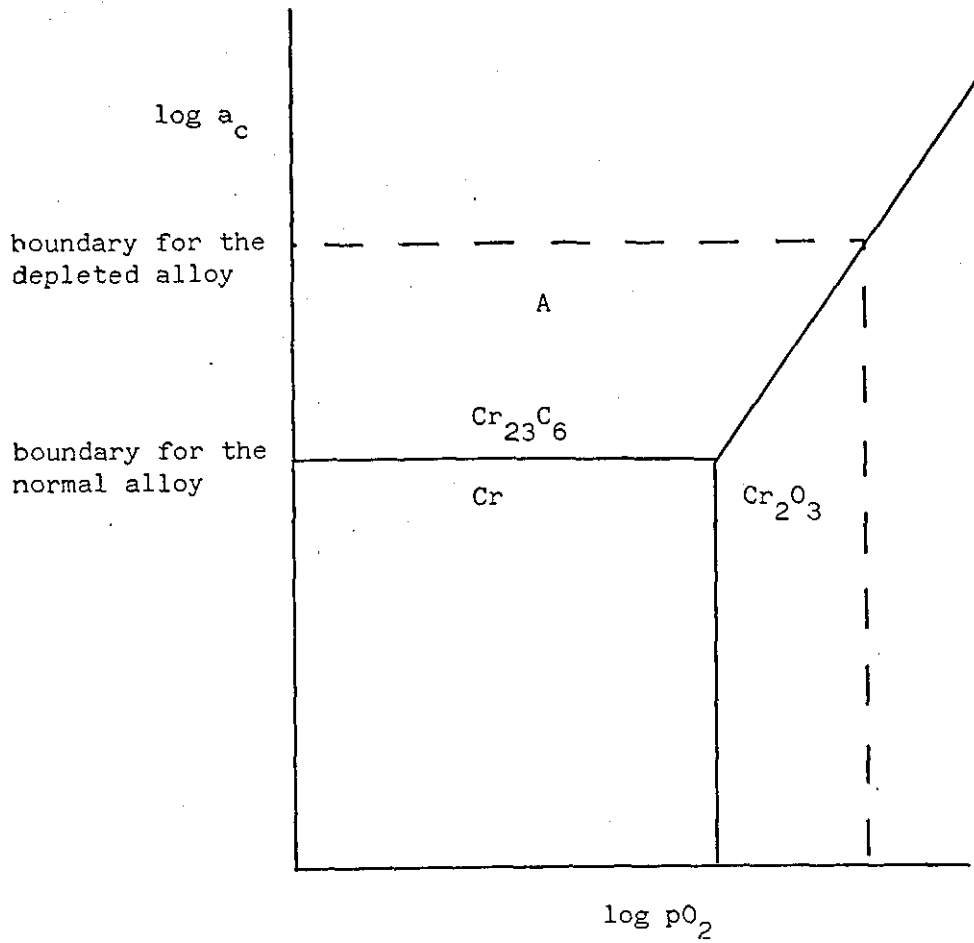


Figure 5.1
Schematic diagram showing the effect of Cr depletion of the alloy substrate on carbide stability.

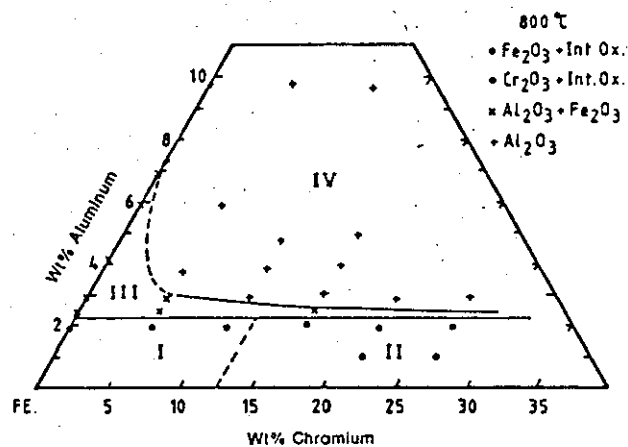


Figure 5.2
Oxide map for the oxidation of ferritic
Fe - Cr - Al alloys in pure oxygen at
800°C (220).

5.2 THE LOW SULPHUR 0.2% H₂S CONTAINING GAS

The general corrosion mechanism for the Model 25Cr-35Ni-Fe alloy

A detailed account of the corrosion behaviour of the Model Alloy in the 0.2% H₂S gas was given in section 4.1.1.b. In very general terms the whole corrosion process can be broken down into four stages.

- (i) Nucleation of oxides and sulphides on the alloy surface in the initial stages.
 - (ii) Simultaneous growth of oxides and sulphides.
 - (iii) Overgrowth of the sulphides by the oxides to form an oxide layer containing sulphide particles, which shut off any further ingress of sulphur from the gas.
 - (iv) Redistribution of the sulphur from the sulphide particles in the oxide layer to sulphide precipitates in the alloy.
- (i) Nucleation
.....

The oxygen partial pressure ($pO_2 = 10^{-21}$ bar), sulphur partial pressure ($pS_2 = 10^{-9}$ bar) and carbon activity ($a_c = 0.3$) in theory were sufficient for oxides, sulphides and carbides to form on the alloy in the initial stages. Although oxides and sulphides nucleated carbides did not form. This was attributed to an adsorbed layer of sulphur inhibiting the adsorption of carbon on the alloy surface, as seen previously in carburizing/sulphidizing environments ^(125, 146, 148), section 2.2.3.

Yurek and La Branche ⁽¹⁶¹⁾ have established that the relative proportions of a metal surface covered with sulphides and oxides in the initial stages are determined by the ratios of sulphur and oxygen containing species in the gas. A detailed description of the reasoning behind this was given earlier in section 2.3.4. At this stage it is reasonable to assume that the growth rate was determined by the rate of supply of gaseous species to the alloy surface and by phase boundary

transport.

Whilst dealing with the subject of nucleation it is worth while pointing out that a large number of internal sulphide precipitates formed in the 180 grit material, but hardly any in the electroplated material. This was due to surface working creating a large number of defects in the surface regions of the alloy which provided a large number of nucleation sites for the internal sulphide precipitates.

(ii) Simultaneous growth of oxides and sulphides
.....

After nucleating the oxides and sulphides grew side by side to form a surface layer. Once this became complete the growth rate started to be controlled by the rate of chromium diffusion through the surface layer. As sulphides have much greater deviations from stoichiometry and therefore a high concentration of defects they grew much quicker than the oxides, thus explaining the presence of the large sulphide filaments and the high kinetic rate in the first 1000 to 2000 hours.

(iii) Overgrowth of sulphides by oxides
.....

Once the corrosion rate was controlled by solid state diffusion, thermodynamic considerations determined that only one phase could come to stable equilibrium with the gas. In the case of this 0.2% H_2S gas the partial pressure of sulphur ($pS_2 = 10^{-9}$ bar) was low enough and partial pressure of oxygen ($pO_2 = 10^{-21}$ bar) high enough to fall to the right of the kinetic or threshold boundary determined by Natesan and Delaplane (149) and Perkins (151, 152), described in section 2.3.4. Thus the oxides overgrew the sulphides to form a Cr_2O_3 layer containing chromium sulphide particles. This complete oxide layer shut off any further ingress of sulphur from the gas. The reasons for this will be discussed later. The sulphide particles in the oxides acted as short circuit diffusion paths for the outward diffusion Cr ions which led to localised thickening of the scale.

(iv) Sulphur redistribution
.....

Perhaps the most significant observation was, however, the eventual

redistribution of the sulphur from sulphides contained in the oxide scale to internal sulphide precipitates in the alloy substrate. This was particularly evident in the 180 grit material. Surface working created a large number of defects in the worked layer which provided a large number of nucleation sites for internal sulphide precipitates in the early stages. The worked layer once recrystallized also provided many grain boundaries which acted as short circuit diffusion paths and therefore increased the rate of supply of Cr to the surface. This caused the oxides and sulphides in the scale to grow rapidly to form a fast growing but porous defective scale. The pores allowed carbon containing gaseous species to penetrate the scale to form internal carbide precipitates beneath the internal sulphide precipitates. The carbides then assisted the inward advancement of the sulphides. This was due to the chromium activity in the depleted alloy substrate dropping to below the point where the carbides were thermodynamically stable. As the local sulphur activity was high enough for sulphides to be stable the carbides transformed to sulphides instead of metal, with the carbon released diffusing deeper into the alloy. The outward diffusion of chromium into the scale and the inward diffusion of carbon deeper into the alloy created voids into which the sulphide precipitates could grow. The internal sulphide precipitates became larger and fewer in number as time progressed due to ostwald ripening processes.

The redistribution of the sulphur was not as obvious in the case of the electropolished material with internal sulphides only forming at grain boundaries. Elsewhere the sulphides remained at the scale/alloy interface with ripening processes causing the sulphur to regroup from an almost continuous inner chromium sulphide layer into large chromium sulphide particles. The redistribution into the alloy tended not to occur due to a number of factors. Firstly the clean smooth electropolished surface did not contain many defects to act as nucleation sites for internal sulphide precipitation. The alloy had a large grain size and therefore there were very few grain boundaries to act as short circuit diffusion paths for Cr to the surface with the result that the scale grew at a much lower rate than the 180 grit material. As the scale grew more slowly it was compact and did not contain many pores and therefore acted as an effective barrier to any carbon ingress from the gas.

Also chromium was able to diffuse from the bulk of the alloy to replace that removed from the depleted zone to form the scale preventing voids forming into which sulphide precipitates could grow. Thus it can be concluded that the lack of grain boundaries, defects, carbides and voids prevented internal sulphide precipitates from forming except at the isolated grain boundaries where carbides were present and the material behaved like the 180 grit material.

Internal sulphidation beneath oxide scales

Two mechanisms are often proposed in the published literature to explain the formation of internal sulphide precipitates beneath oxide scales.

- (i) Lattice and/or grain boundary diffusion of sulphur ions through the oxide.
- (ii) The diffusion of sulphur containing gaseous species through physical defects in the oxide.

This study clearly shows that there is a third possibility that has been overlooked, namely that most, if not all, of the sulphur was incorporated into either sulphide particles in the scale or sulphide precipitates in the alloy before the outer Cr_2O_3 layer completely overgrew the sulphides. Once the outer oxide layer was complete further ingress of sulphur from the gas ceased. The sulphur present as sulphide particles in the scale then redistributed into sulphide precipitates in the alloy. Thus although the volume of internal sulphide precipitates increased the total volume of sulphur in the scale and alloy together remained the same.

These observations have important implications as internal sulphidation could certainly be reduced and probably eliminated if the oxide scale was established in a sulphur-free gas prior to exposure in a low sulphur containing environment which fell to the right of the kinetic or threshold boundary. Although no experimental work was carried out in this study to establish if this is true, other workers have preoxidized metals and alloys prior to exposure to similar types of sulphur contain-

ing environments. Perkins (152) for example found that sulphur did not penetrate a preformed Cr_2O_3 layer on a Ni-46Cr alloy exposed to a medium B.T.U. gas containing 1% H_2S for 1500 hours at 871° and 982°C. Natesan (182) also found that sulphur did not penetrate a preformed Cr_2O_3 layer on pure Cr exposed CO_2 -CO- CH_4 - H_2 - H_2O gas mixtures to the right of the kinetic boundary at 875°C. On the other hand he found internal sulphide precipitates in preoxidised Incoloy 800 specimens exposed under the same conditions as the chromium. Obviously it is impossible from other people's work to assess the quality and composition of the performed oxide scales, but examination of the two established mechanisms of sulphur transport through oxide scales sheds some light on the discrepancy in Natesan's results.

For the first mechanism of sulphur transport via lattice or grain boundary diffusion to operate there must be some solid solubility of sulphur in oxides. Birks (226) has carried out a survey of existing data which showed that values of 0.1 - 0.01% are typical in the temperature range 600 - 1000°C. There is however a considerable amount of scatter in these results and one cannot help feeling that perhaps some of the oxides contained actual sulphide particles distorting the figures. However it would appear certainly in the case of NiO, the system on which most of the work has been carried out that sulphur is soluble in the oxide.

Wagner and co-workers (227-229) and Suntsov and Antonenko (230) have established that:

- (i) NiO is a p-type semiconductor with the majority defects cation vacancies and associated electron holes.
- (ii) Sulphur replaces oxygen in the anion sub-lattice as S^{2-} .
- (iii) Sulphur acts as an electron donor reducing the concentration of electron holes and conductivity of the oxide.
- (iv) Sulphur diffuses through NiO at a faster rate than oxygen but at a slower rate than nickel.

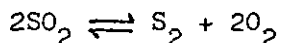
- (v) Doping the oxide with Cr^{3+} decreased the diffusivity of sulphur.
- (vi) The rate of diffusion of sulphur in polycrystalline NiO than single crystal NiO indicating that some grain boundary diffusion takes place.

From these findings Suntsov and Antonenko ⁽²³⁰⁾ developed a 3 stage mechanism to explain the diffusion of sulphur through NiO. In the first stage the sulphur ion moves into the cation vacancy with the capture of electron holes. In stage 2 the oxygen moves to the position vacated by the sulphur. Finally in stage 3 the sulphur moves to the original position of the oxygen. The net result is the change of places between oxygen and sulphur atoms. The sulphur diffuses faster apparently because more favourable thermal vibrations enable it to capture the electron holes associated with the cation vacancies. Thus it is the concentration of electron holes and not the cation vacancies which is the important factor. This hypothesis was confirmed by doping NiO with Chromium. Cr^{3+} acts as an electron donor reducing the number of electron holes and increasing the number of cation vacancies (due to the need to maintain electrical neutrality). Thus although the Cr doped NiO contained more cation vacancies, sulphur diffusion was slower than in pure NiO due to the lower concentration of electron holes. The authors also showed that the mechanism also applied to Co_3O_4 which has a p-type spinel structure.

It is important to emphasise that both NiO and M_3O_4 are p-type semiconductors in which the majority defects are cation vacancies with associated electron holes. Kofstad and Lillerad ⁽²⁹⁾, Hindam and Whittle ^(45, 46), Young et al ⁽⁴³⁾ and Matsui and Naito ⁽⁴⁴⁾ have all shown that although Cr_2O_3 formed in high $p\text{O}_2$ environments is a p-type semiconductor, in the case of low $p\text{O}_2$ environments, such as this study and those of Perkins ⁽¹⁵²⁾ and Natesan ⁽¹⁸²⁾, Cr_2O_3 is an n-type semiconductor with the majority defects Cr interstitials with excess electrons. It is therefore highly unlikely that sulphur penetrates n-type Cr_2O_3 , thus accounting for the shut off of the ingress of sulphur from the gas once the Cr_2O_3 layer became complete on the model 25Cr-35Ni-Fe in this study. This also appears to explain the apparent discrepancy between Natesan's findings for pure Cr and Alloy 800. In the case of

pure (n-type) Cr_2O_3 formed on Cr no sulphur penetration occurred, whereas in the case of the alloy sulphur was able to penetrate the oxide scale via cation defects in the (p-type) spinel.

The mechanism of diffusion of sulphur-containing gaseous species has been proposed by Birks and co-workers (226, 231-233) and applies to SO_2 containing environments. In this case SO_2 can diffuse through cracks and pores and dissociate according to the reaction



at the scale/alloy interface. It is therefore possible for a very high local sulphur activity to exist beneath the scale even when the sulphur partial pressure in the gaseous atmosphere is well below the M/MS thermodynamic boundary. Singh and Birks (231) have conclusively proved that this mechanism operates in SO_2 containing environments. There is no apparent reason why the mechanism cannot operate in H_2S containing environments. However, it was found in this study in the case of the 180 grit material that once the oxide layer was complete no ingress of sulphur occurred via physical defects even though carbon containing molecules continued to penetrate the scale via this route. Presumably the size of the gaseous molecules, size of physical defects and ease of decomposition of the gaseous species all could have something to do with this. Certainly the scale did appear to become much less porous as the exposure time increased. Otherwise the author is unable to offer any further explanation.

It can be concluded that H_2S does not penetrate Cr_2O_3 via cracks and pores. However it is extremely important to realise that if the gaseous environment contains appreciable amounts of SO_2 the mechanism of gaseous transport through cracks and pores must be taken into account.

General corrosion mechanism for HP40Nb and AISI314

A detailed account of the corrosion behaviour of HP40Nb and AISI314 in the 0.2% H_2S was given in sections 4.1.2 and 4.1.3 respectively. In very general terms the corrosion process for these alloys can be broken down

into 7 stages.

- (i) Nucleation of Cr_2O_3 , M_3O_4 and M_3S_4 on the alloy surface and internal Cr/Mn rich sulphide precipitates in the alloy.
- (ii) Simultaneous growth of Cr_2O_3 , M_3O_4 and M_3S_4 on the alloy surface.
- (iii) Overgrowth of the sulphides by oxides to form a porous uneven external scale containing Cr_2O_3 , M_3O_4 and M_3S_4 sulphide particles.
- (iv) Formation of an inner layer consisting of SiO_2 , the former internal sulphide precipitates, Cr-rich oxides and metallic particles.
- (v) Separation of the external scale into an outer M_3O_4 layer and an inner Cr_2O_3 layer both of which contained sulphide particles.
- (vi) An increase in the corrosion rate after several thousand hours which coincided with a substantial amount of localised internal attack of the carbide precipitates in the alloy (break-away corrosion).
- (vii) Formation of external Fe, Cr-rich sulphides instead of oxides at the scale/gas interface (AISI314 only).

Instead of discussing this complex mechanism stage by stage a clear understanding of the corrosion process can be obtained by grouping some of the stages together and considering:

- a) The effect of sulphur on SiO_2 formation and growth (stage iv).
- b) The combined effect of sulphur and manganese (stages i-iii and v).
- c) Factors causing internal attack which lead to break-away corrosion (stages vi and vii).

a) The effect of sulphur on SiO_2 formation and growth
.....2.....

In the sulphur-free gas a complete inner SiO_2 layer formed on AISI314 (both surface conditions) and HP40Nb (180 grit condition). This layer proved to be a very effective barrier to the outward diffusion of cations and inward diffusion of carbon. In the 0.2% H_2S gas, however, internal sulphide precipitates also formed. The inner layer therefore consisted of a mixture of SiO_2 and Cr/Mn-rich sulphide precipitates. As time progressed some of the sulphide precipitates transformed to Cr-rich oxides and metallic particles, so that the inner layer then consisted of a mixture of SiO_2 , Cr-rich oxides, Cr-rich sulphides and metallic particles. Cr, Mn and Fe were therefore able to diffuse through the Cr-rich oxides, sulphides and metallic particles to form thick external oxide layers.

Internal sulphidation was possible in AISI314 due to its having a small grain size. The high concentration of grain boundaries even in the electropolished material acted as nucleation points for the internal sulphide precipitates. The grain boundaries also provided easy diffusion paths for the inward diffusion of sulphur and outward diffusion of cations. Surface working produced even more defects and grain boundaries which further assisted the formation of internal sulphide precipitates and outward diffusion of cations, which in turn increased the corrosion rate and thickness of the corrosion layers.

The mechanism was exactly the same for the HP40Nb alloy in the 180 grit condition.

It can therefore be concluded that Si alloying additions had no benefit in the 0.2% H_2S environment. In fact they tended to be detrimental due to the SiO_2 reducing the adherence between the inner oxide layer and the external scale, which led to a considerable amount of spallation of the external scale.

b) The combined effect of sulphur and manganese
.....

In the case of HP40Nb in the electropolished condition the clean smooth

surface and large grain size provided very few nucleation sites for sulphide particles either on the alloy surface or within the alloy. MnCr_2O_4 spinel and Cr_2O_3 therefore nucleated on the alloy surface in the initial stages. The spinel grew faster than the Cr_2O_3 and eventually the scale separated into an outer spinel layer and an inner Cr_2O_3 layer. Thus the corrosion process was the same as in the sulphur-free gas for the same alloy in the same surface finish. The corrosion rate was slightly higher in the presence of sulphur. To understand the reasons for this it is necessary to consider the behaviour of the HP40Nb alloy with the 180 grit surface finish and AISI314 (both surface finishes) in which this feature was far more exaggerated.

In the case of HP40Nb in the 180 grit condition and AISI314, electropolished and 180 grit conditions, the high concentration of defects and grain boundaries in surface regions of the alloy provided many nucleation sites for sulphides both on the alloy surface and in the alloy substrate. The internal sulphide precipitates formed in the alloy substrate tied up some of the manganese and therefore reduced the amount of manganese available to form MnCr_2O_4 in the external scale. This allowed Fe to become incorporated in the M_3O_4 spinel in place of some of the Mn. The increased activity of Fe in the scale then allowed Fe,Cr-rich sulphides to form in the scale instead of just Cr sulphides which formed in the Model alloy. One would have expected manganese sulphides, which are much more thermodynamically stable than sulphides of iron and chromium to form in the scale. This was found not to be the case. Instead all the Mn in the scale was concentrated in the oxide spinel.

As the scale grew it separated into the outer M_3O_4 layer and inner Cr_2O_3 layer in a similar manner to the HP40Nb electropolished material. In this case (HP40Nb 180 grit condition and AISI314 both surface finishes), however, the Cr_2O_3 layer was much thicker than the equivalent layer formed on both the HP40Nb electropolished material and the Model 25Cr-35Ni-Fe alloy. This appeared to be related to the presence of a considerable amount of sulphur in both the M_3O_4 spinel and Cr_2O_3 oxides. Unlike the Model 25Cr-35Ni-Fe the shut off of sulphur ingress from the gas did not occur. To understand the reasons for the sulphur ingress not

shutting off, the presence of sulphur in the oxides and the much thicker Cr_2O_3 layer, it is necessary to examine again just how the Cr_2O_3 layer forms on the two commercial alloys (HP40Nb and AISI314) and the Model alloy.

In the case of the Model alloy the n-type Cr_2O_3 layer, with Cr interstitials as the predominant defect, formed mainly from the outward diffusion of Cr via these defects. In the case of HP40Nb and AISI314 the inner Cr_2O_3 layer formed predominantly from the p-type M_3O_4 outer layer. It could therefore be possible that this inner Cr_2O_3 layer could be p-type with Cr vacancies as the predominant defects. If this hypothesis is true, sulphur would be able to take the place of some of the oxygen in the anion lattice and diffuse through the scale via cation vacancies according to the mechanism discussed earlier for NiO, thus explaining the presence of sulphur in the Cr_2O_3 oxide and that the ingress of sulphur did not shut off.

The presence of sulphur in the Cr_2O_3 lattice also explains why the Cr_2O_3 was much thicker. According to Romeo et al (234) sulphur can act as an electron donor which in p-type Cr_2O_3 reduces the concentration of electron holes and increases the concentration of cation vacancies, thus allowing the outward diffusion of Cr, Mn and Fe to occur more rapidly, increasing the kinetic rate and in turn producing a thicker scale.

A final piece of evidence which could support the p-type structure of Cr_2O_3 on the HP40Nb and AISI314 alloys is that the Cr_2O_3 lattice parameter did not increase with time, whereas the n-type Cr_2O_3 lattice parameter on the Model 25Cr-25Ni-Fe alloy increased with exposure time due to Mn doping.

c) Factors causing internal attack leading to breakaway corrosion

After several thousand hours exposure the alloy substrate became severely depleted in Cr. This was due to:

- i) The incomplete inner SiO_2 layer failing to cut off the outward diffusion of Cr into the external scale.

- ii) The combined effect of Mn and S increasing the growth rate of the Cr_2O_3 layer and M_3O_4 layer in the external scale.
- iii) The formation of Cr containing sulphide particles in the oxide layers and the alloy substrate.
- iv) The formation of Cr-containing carbides and the σ -phase due to aging processes.

The Cr depletion caused a massive amount of internal attack to take place. This coincided with an upturn in the corrosion rate (breakaway corrosion). The reasons for this are as follows:

Cr depletion of the alloy substrate lowered the chromium activity in the alloy beneath the scale to a level where the Cr-rich M_{23}C_6 carbides became unstable. These carbides therefore converted to metal and carbon. The metal rapidly diffused outwards to form oxides in the scale increasing the corrosion rate. The carbon diffused deeper into the alloy to reform carbides where the chromium activity was higher. The outward diffusion of metal and inward diffusion of carbon created voids into which sulphur diffused to form sulphide precipitates. As these sulphides were predominantly Cr-rich this caused more Cr depletion and thus accelerated the whole process. As more voids formed oxygen diffused in behind the sulphur to form internal oxides. As the local oxygen activity increased some of the sulphides transformed to oxides releasing sulphur to diffuse deeper into the alloy to recommence the whole process again.

In the case of AISI314 the σ -phase also became unstable as the Cr activity dropped, releasing Cr and Fe into the alloy. The chromium rapidly diffused outwards into the scale leaving voids into which initially the sulphur and subsequently the oxygen diffused to form sulphides and oxides.

Further evidence to support the fact that Cr-depletion of the substrate was the cause of the internal attack and breakaway corrosion is that

- i) The NiNbSi-rich MC carbides remained stable in the Cr-depleted

zone. A few sulphides formed around these carbides due to the formation of voids in the surrounding Cr-depleted substrate. The free surface of the carbides provided good nucleation sites for the sulphides.

- ii) Alloy 800H with a lower 20% Cr content than the other 25% Cr containing alloys went into breakaway after shorter exposure times (1500 - 2000 hours) than the other alloys (~ 3000 hours). As the grain boundary carbides in this alloy formed a very fine continuous structure, internal attack proceeded on a very narrow front leading to very deep localized penetration even though the total volume of sulphides and oxides formed was relatively small.

The considerable thickness of the external M_3O_4/Cr_2O_3 scale and the presence of Si in the inner oxide layer made the external scale very susceptible to spallation. If this occurred (as was the case at corners of the AISI314 material) Cr_2O_3/M_3O_4 and M_3S_4 again nucleated on the alloy surface. However the alloy now contained insufficient Cr for the oxides to overgrow the sulphides with the result that the Fe,Cr-rich M_3S_4 sulphides kept growing to form an external sulphide scale. As these sulphides are very defective they grow very quickly and as seen in the 0.6% H_2S lead to catastrophic failure of the alloys in a very short time.

The effect of other alloying additions Al, Nb and Ti

The HP40Al alloy containing 3.5% Al failed to form a complete Al_2O_3 layer in the 0.2% H_2S gas which is not surprising in view of the fact that it failed to do this in the sulphur-free gas. Internal Al_2O_3 particles formed but these had little influence on the breakaway process.

Nb contained in the HP40 type alloys had no influence on the corrosion process as most of this remained tied up in the MC carbides.

In the case of the sulphur-free gas Cr-depletion of the alloy substrate in Alloy 800H caused the grain boundary carbides to transform to metal

and carbon with the metal diffusing outwards and the carbon being tied up with the Ti in situ to form TiC carbides. In the 0.2% H₂S gas the Cr depletion was much greater with the result that the localized internal attack was much deeper. It can be concluded that the Ti effect is very secondary to that of Cr depletion.

5.3 THE HIGH SULPHUR 0.6% H₂S CONTAINING GAS

The general corrosion mechanism for the Model 25Cr-35Ni-Fe alloy

A detailed account of the corrosion behaviour of the Model alloy in the 0.6% H₂S gas was given in section 4.2.1. In very general terms the whole corrosion process can be broken down into 6 stages.

- (i) Nucleation of oxide and sulphide particles on the alloy surface and internal sulphide precipitates in the alloy substrate in the initial stages.
- (ii) Simultaneous growth of oxides and sulphides on the alloy surface.
- (iii) Overgrowth of the oxides by the sulphides to form outer sulphide layer I, containing Fe,Cr-rich sulphides.
- (iv) Coalescence of the internal sulphide precipitates to form an internal Fe,Cr-rich sulphide layer.
- (v) Development of outer sulphide layer II, containing Fe,Ni-rich sulphides.
- (vi) Development of outer sulphide layer III, containing nickel sulphides in addition to the Fe,Ni-rich sulphides.

The corrosion rate in this sulphidation governed regime was very high making this type of alloy unusable under these conditions. The discussion of the corrosion mechanism will therefore be restricted to the main issue of why in this 0.6% H₂S gas the sulphides overgrew the oxides to form a sulphide scale whereas in the 0.2% H₂S gas (discussed in section 5.2) the oxides overgrew the sulphides to form an oxide scale. In both cases thermodynamic considerations should have determined that an oxide scale should have formed, figure 3.6.

Yurek and La Branche (161) have established that the relative proportions of a metal surface covered with sulphides and oxides in the

in the initial stages are determined by the ratios of sulphur and oxygen containing species in the gas. A detailed description of the reasoning behind this was given earlier in section 2.3.4. If the number of gaseous oxygen containing species was kept constant and the number of gaseous sulphur containing species increased, the proportion of the alloy surface covered with sulphides increased. Thus in the 0.6% H_2S gas a higher proportion of sulphides nucleated than in the 0.2% H_2S gas.

The 0.6% H_2S gas corresponded to a partial pressure of sulphur ($pS_2 = 10^{-8}$ bar) well in excess of the Fe/FeS thermodynamic boundary and thus it was much more thermodynamically favourable for Fe,Cr-rich sulphides to form as opposed to just Cr-rich sulphides in the 0.2% H_2S gas. As the Fe/Cr-rich sulphides contained a greater concentration of defects than the Cr-rich sulphides, and as more sulphur was also available from the gas, the sulphides grew at a very fast rate, overwhelming the very slow growing oxides, to form the outer Fe,Cr-rich sulphide layer I.

Thus although thermodynamic factors predicted that an oxide layer should come to equilibrium with the gas, the high proportion of sulphides which nucleated and the subsequent high growth rates of these sulphides dominated the process resulting in the formation of the sulphide scale instead of an oxide scale. This accounts for the kinetic or threshold boundary determined by other workers (149, 151, 152, 161), described in section 2.3.4.

The rapid outward diffusion of Cr and Fe to form the outer layer created voids into which the sulphur could diffuse to form the internal sulphide layer. As time progressed, the alloy substrate became very depleted in Cr and Fe with the result that more Ni was taken into the scale. Initially this existed in solid solution but after reaching a certain level it exceeded its solubility limits and led to the formation of the outer Fe,Ni-rich sulphide layer II. This layer formed at the scale/gas interface as Fe,Ni sulphides could not exist at the scale/alloy interface where the sulphur partial pressure was much lower. Eventually the Ni activity in the scale increased to the point where Ni_3S_2 precipitated out to form outer sulphide layer III.

Work by Rao and co-workers (172-174) has shown that the lamellar structure and the metallic Ni_2Fe phase which also were present in some of these sulphide layers were formed on cooling to room temperature. Hot-stage microscopic and D.T.A. analysis in this study certainly proved that the Ni_2Fe particles were rejected on cooling. Many phase changes were detected but it was not possible to tie down which phase was forming at a specific temperature due to the complex structure of the scale.

Again it should be pointed out that although the formation of all the sulphides is interesting, the severe corrosion rates make them irrelevant to practical application and will therefore not be discussed further.

The general mechanism for HP40Nb and HP40Al

The mechanism was essentially the same as for the Model alloy except that the presence of elements such as Si in HP40Nb and Si and Al in HP40Al led to the formation of an internal oxide/sulphide layer which tended to slow down the outward diffusion of cations and inward diffusion of sulphur. In spite of this, even in the case of the HP40Al alloy, the corrosion rate was still very severe.

5.4 RECOMMENDATIONS FOR TECHNOLOGICAL APPLICATIONS

The following recommendations are made which, if adhered to, should from a corrosion point of view enable Fe-Cr-Ni alloys to operate in service at 800°C for many thousands of hours in gaseous environments containing the reactants oxygen, sulphur and carbon.

The environment

- (i) The oxygen partial pressure must be in excess of the threshold or kinetic boundary (3 orders of magnitude in excess of the $\text{Cr}_2\text{O}_3/\text{CrS}$ boundary at this temperature) to ensure that an oxide scale and not a sulphide scale forms, figure 5.3.
- (ii) The sulphur partial pressure must be below the Fe/FeS thermodynamic boundary to prevent the formation of Fe-rich sulphides if the oxide scale is disrupted in any way during service, figure 5.3.
- (iii) The carbon activity should not exceed unity to avoid carbon deposition which could destroy the oxide scale and lead to metal dusting attack.

Start up procedure

It is advantageous to start up in a gas containing no sulphur or as low a level of sulphur as possible to prevent or at least reduce the formation of sulphide particles in the scale and internal sulphide precipitates in the alloy during the initial stages, figure 5.3. The oxygen partial pressure should be kept low to allow an n-type Cr_2O_3 layer to form which should resist penetration of sulphur during normal operating conditions and avoid the formation of Fe-rich oxide spinels. Once the scale has been established the level of sulphur could be increased to the levels stated.

Alloys

- (i) The Cr content of the alloy should be as high as possible,

certainly in excess of 25% Cr, to minimise the possibility of the Cr level in the depleted substrate reaching levels where break-away corrosion can occur.

- (ii) The alloy should contain no manganese to prevent the formation of the outer MnCr_2O_4 spinel layer.
- (iii) The alloy should have a low carbon content to prevent the formation of a large number of carbide precipitates which tie up considerable quantities of Cr and promote localized internal attack if the alloy becomes severely depleted in Cr.
- (iv) Nb should be used as a carbide stabilising element in preference to Ti as it does not promote localized attack.
- (v) Low levels of Si are acceptable but these should not reach levels which could promote σ -phase formation or spallation of the oxide scale.
- (vi) The inclusion of a rare earth element would be advantageous to key on the oxide and reduce spallation. Although no work was carried out in this study to investigate this, the literature appears to indicate that Ce is the most promising rare earth alloying addition.
- (vii) A small grain size is desirable to provide diffusion paths into the alloy for any sulphur that became trapped at the scale/alloy interface. A small number of internal sulphides is acceptable but large sulphide particles growing at the scale/alloy interface could cause the oxide scale to be disrupted and therefore cannot be tolerated.

Surface preparation

The alloy should have a clean smooth work-free surface to promote a slow growing oxide scale and minimise the formation of cracks and pores in the oxide which can allow the inward penetration of carbon containing

gaseous species and SO_2 which could result in excessive internal carburization and sulphidation.

Environments containing no sulphur

The above recommendations can be modified for gases containing low partial pressures of oxygen and a significant carbon activity but no sulphur.

- (i) In this case the alloy should have a high Si content ($>1.2\%$ for worked surfaces and $>2.0\%$ for work-free surfaces) to enable a complete inner SiO_2 layer to form a barrier to the outward diffusion of cations and inward diffusion of carbon.
- (ii) The surface should be worked to assist the formation of the complete SiO_2 layer.
- (iii) Mn additions are quite acceptable in this case.

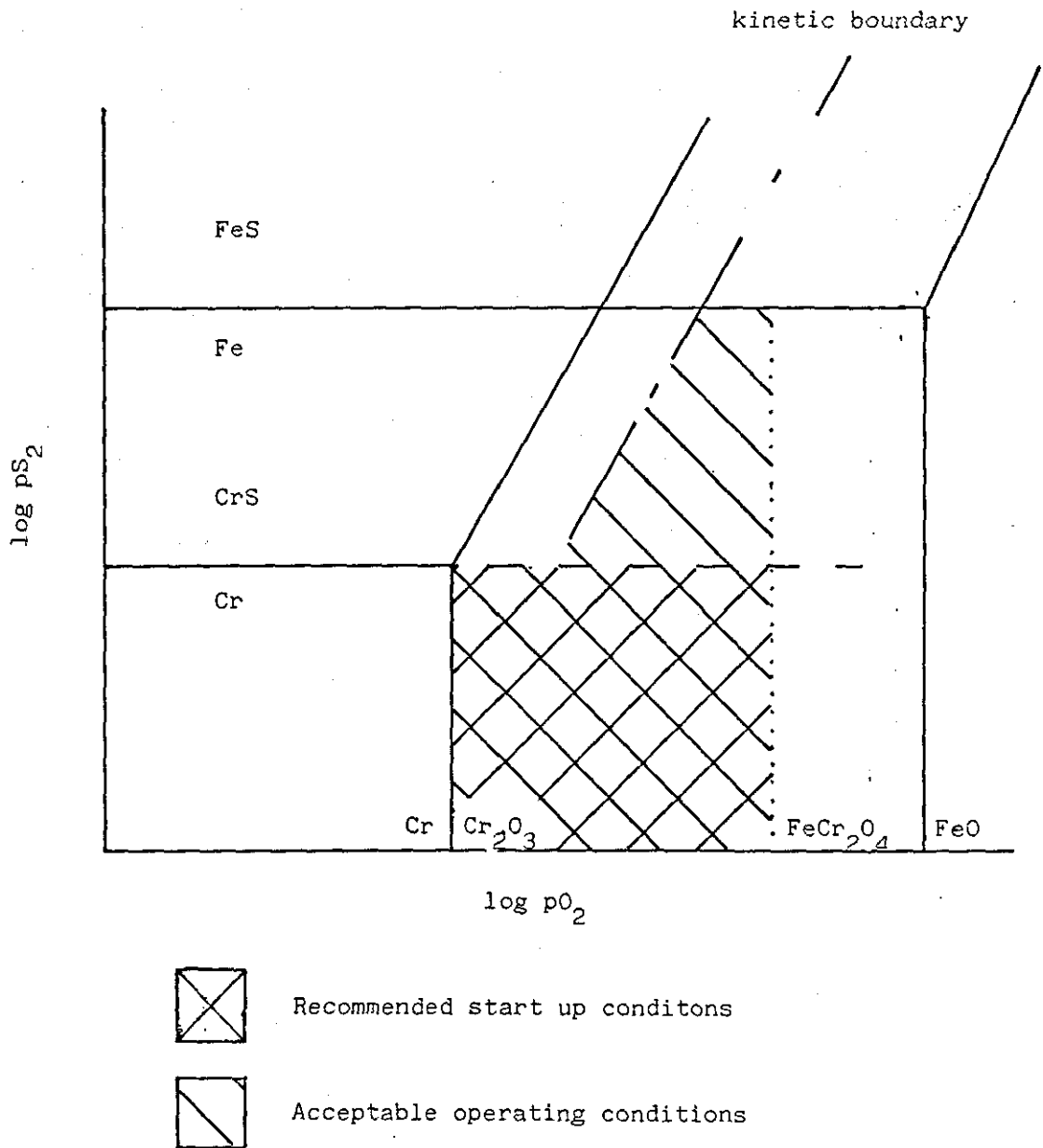


Figure 5.3

Schematic metal stability diagram indicating acceptable start up and operating conditions for technological processes.

6. CONCLUSIONS

=====

1. The Model 25Cr-35Ni-Fe alloy formed a thin uniform Cr_2O_3 layer in the sulphur-free gas, which grew at a constant parabolic rate throughout the exposure period. Surface working increased the growth rate and thickness of the Cr_2O_3 layer, but created a large number of cracks and pores which allowed carbon containing gaseous species to diffuse through the oxide to form carbide precipitates in the alloy substrate.
2. Adding a low level of sulphur (0.2% H_2S) to the gas increased the corrosion rate of the Model alloy in the initial stages. This rate gradually slowed down before becoming parabolic after 1000 - 2000 hours. This was due to the nucleation of sulphides in addition to oxides. The oxides and sulphides subsequently grew side by side until the oxides overgrew the sulphides to form a complete Cr_2O_3 layer which cut off further ingress of sulphur from the gas. The entrapped sulphides promoted localized thickening of the oxide layer. Eventually the sulphur redistributed from the sulphides in the scale to internal sulphide precipitates in the alloy, with the corrosion rate returning to that of the sulphur-free gas. These trends were more pronounced in the 180 grit condition than in the electropolished condition.
3. A silicon alloying addition of 2.0% Si in AISI314 was very beneficial in the sulphur-free gas as it promoted the formation of a complete inner SiO_2 layer which reduced the corrosion rate by blocking the outward diffusion of Cr, Mn and Fe. Surface working assisted the formation of a complete SiO_2 layer on the borderline 1.2% Si containing alloy HP40Nb.
4. The beneficial effect of Si was lost in the 0.2% H_2S gas due to the formation of internal sulphide precipitates in the alloy which prevented the inner SiO_2 layer from becoming complete and this allowed Cr, Mn and Fe to diffuse outwards to form a thick external scale. If anything the presence of SiO_2 was now detrimental as it promoted spallation of the thick external scale.

5. Mn alloying additions promoted the formation of an additional $(\text{Mn,Fe})\text{Cr}_2\text{O}_4$ outer layer on the commercial alloys which did not form a complete inner SiO_2 layer in the sulphur-free gas. The intermediate Cr_2O_3 layer grew from the $(\text{Mn,Fe})\text{Cr}_2\text{O}_4$ layer and therefore had a different defect structure to the Cr_2O_3 layer formed on the Model alloy.
6. Mn alloying additions were very detrimental in the 0.2% H_2S gas. The sulphur doped the $(\text{Mn,Fe})\text{Cr}_2\text{O}_4$ spinel and the Cr_2O_3 increasing concentration of cation vacancies which increased the corrosion rate. Some of the sulphur remained in the external scale and sulphur shut off did not occur.
7. The incomplete SiO_2 layer, the fast growing $(\text{Mn,Fe})\text{Cr}_2\text{O}_4/\text{Cr}_2\text{O}_3$ scale, formation of sulphides in the scale and alloy during the initial stages and carbide precipitation due to aging processes all contributed to a severe Cr depletion of the alloy substrate of the commercial alloys in the 0.2% H_2S gas. This caused the internal carbide precipitates to become unstable which led to a massive amount of internal attack and a dramatic increase in the corrosion rate (breakaway). The thickness of the external scale and presence of SiO_2 in the inner layer made the external scale susceptible to spallation. When this occurred the oxides and sulphides nucleated on the surface again but insufficient Cr was available to allow the oxides to overgrow the sulphides. The sulphides therefore grew to form a non-protective fast growing sulphide scale which soon leads to catastrophic failures of the alloy.
8. The 3.5% Al content of the HP40Al alloy was insufficient to form a complete Al_2O_3 layer both in the sulphur-free and 0.2% H_2S gases. Isolated internal Al_2O_3 particles formed but these has no effect on the corrosion mechanism.
9. The 0.8% Nb content of the HP40Nb and HP40Al alloys had no effect on the corrosion process in the sulphur-free and 0.2% H_2S gases as most of this element was contained in the very stable MC carbides.

10. The low Cr content of Alloy 800H made it very susceptible to localized internal attack in the sulphur-free gas and especially in the 0.2% H_2S gas where breakaway occurred after shorter times than on the other commercial alloys.
11. Increasing the level of H_2S in the gas to 0.6% crossed the threshold or kinetic boundary with the sulphides overgrowing the oxides to form thick fast growing non-protective sulphide scales on all the alloys.
12. The 3.5% Al content of HP40Al promoted the formation of an internal Al rich sulphide/oxide layer in the 0.6% H_2S gas which reduced the corrosion rate. Corrosion was however still extremely severe.

7. SUGGESTIONS FOR FURTHER WORK

1. Having established the corrosion mechanisms at 800°C it is important to determine whether the same mechanisms operate at other lower temperatures which are more representative of metal temperatures in use at present in industrial and pilot plant. A very valuable experiment would be a long-term (1 year) exposure in a H_2 -7%CO-1.5% H_2O -0.05% H_2S gas at 600°C which corresponds to the same relative position on a thermodynamic metal stability diagram as the 0.2% H_2S at 800°C.
2. To establish the effect of applied stress on oxide scales in the 0.2% H_2S gas at 800°C to assess how this influences the breakaway process.
3. To investigate corrosion process that could take place due to condensation at low temperatures when process plant in shut down. Chlorine could be a very important factor in this process.
4. This study showed that external oxide scales were rather prone to spallation after long exposure times. It would be valuable to assess the effect of rare earth elements such as Ce at keying on the oxide scale in the 0.2% H_2S gas and sulphur-free environment at 800°C.
5. It was impossible in this study to determine the exact reasons for the localized attack of grain boundaries in Alloy 800H due to this alloy containing small quantities of several minor alloying elements. To establish this a study is required on different batches of this alloy containing only Al and no Ti and an alloy containing Ti and no Al.
6. Most important of all however is to work on simpler alloys, e.g. Model alloy, Model alloy plus 2% Si, Model alloy plus 1% Mn, Model alloy plus 2% Si and 1% Mn, and to reduce the amount of work by studying fewer alloys and standardising on one surface finish.

REFERENCES

1. Gray, J.A. and Starr, F.
In "The behaviour of high temperature alloys in aggressive environments".
Eds. Kirman, I., Marriott, J.B., Merz, M., Sahm, P.R. and Whittle, D.P., Metals Soc. 1980, 3 - 27
2. Anon
New Scientist, 22nd May 1986, 22
3. Mac Nab, A.J., Schulz, C.A. and Black, H.L.
In "The properties and performance of materials in coal gasification environments".
Eds. Hill, V.L. and Black, H.L.
American Society of Metals, 1981, 7-24
4. Stringer, J.
High Temperature Technology 3, 1985, 119 - 141
5. Meadowcroft, D.B.
Paper presented at Symposium on "High temperature materials for coal conversion and utilization", SCK/CEN, Mol, Belgium
(Nov. 1983), 127 - 142
6. Holmes, D.R. and Stringer, J.
In "Materials to supply the energy demand"
Eds. Hawbolt, E.B. and Mitchell, A.
American Society of Metals, 1981, 165 - 204
7. Anon
EPRI Journal, April 1979, 6-13
8. Natesan, K.
Proceedings of Conference on "Corrosion - erosion - wear of materials in emerging fossil energy systems". Berkeley, California.
Ed. Levy A.V., National Association of Corrosion Engineers, 1982, 100 - 136
9. Hoy, H.R.
In "Corrosion resistant materials for coal conversion systems".
Eds. Meadowcroft, D.B. and Manning, M.I.
Applied Science Publishers, 1983, 275 - 279.
10. Nagarajan, V., Rocazella, M.A., Wright, I.G. and Smith, R.D.
In "Corrosion resistant materials for coal conversion systems".
Eds. Meadowcroft, D.B. and Manning, M.I.
Applied Science Publishers, 1983, 371 - 388.
11. Minchener, A.J., Lloyd, D.M. and Cooke, M.J.
Proceedings of conference on "Corrosion - erosion - wear of materials in emerging fossil energy systems".
Berkeley, California.
Ed. Levy, A.V., National Association of Corrosion Engineers 1982, 511 - 547.

12. Rademakers, P.L.F.
Private communication.
13. Rademakers, P.L.F. and Kolster, B.H.
Procestechniek 38, 1983, 1 - 6
14. Minchener, A.J., Lloyd, D.M. and Stringer, J.
In "Corrosion resistant materials for coal conversion systems".
Eds., Meadowcroft, D.B. and Manning, M.I.
Applied Science Publishers 1983, 371 - 388
15. Saunders, S.R.J. and Spencer, S.J.
Proceedings of conference "International symposium on high
temperature corrosion"
Marseille 7 - 12th July 1986.
16. Barton, K.J., Hill, V.L. and Yurkewycz.
In "The properties and performance of materials in coal gasifi-
cation environments".
Eds. Hill, V.L. and Black, H.L.
American Society of Metals, 1981, 65 - 95
17. Danyluk, S. and Diercks, D.R.
In "The properties and performance of materials in coal gasifi-
cation environments".
Eds. Hill, V.L. and Black, H.L.
American Society of Metals, 1981, 155 - 178
18. Ellingham, H.J.T.
J. Soc. Chemical Industry 63, 1944, 125.
19. Richardson, F.D. and Jeffes, J.H.E.
J. Iron and Steel Inst., 171, 1952, 165.
20. Kofstad, P.
High-Temperature Oxidation of Metals,
Wiley, New York, 1966.
21. Kubaschewski, O. and Hopkins, B.E.
Oxidation of Metals and Alloys
Butterworth, London, 1967.
22. Evans, U.R.
The Corrosion and Oxidation of Metals
Arnold, London, 1960, 1968 and 1977.
23. Bénard, J.
L'Oxidation des Métaux, Vols. 1 and 2
Gauthier-Villars, Paris, 1963 and 1964.
24. Birks, N. and Meier, G.H.
Introduction to High Temperature Oxidation of Metals
Edward Arnold, London, 1983.

25. Kofstad, P.
In "High Temperature Corrosion"
NACE 6, Ed. R.A. Rapp, 1983, 123-138.
26. Hauffe, K.
Oxidation of Metals
Plenum Press, New York, 1965.
27. Kofstad, P.
Nonstoichiometry, Diffusion and Electrical Conductivity in Binary
Metal Oxides
Wiley, New York, 1972.
28. Lillerud, K.P. and Kofstad, P.
J. Electrochemical Soc., 127, 1980, 2397-2410.
29. Kofstad, P. and Lillerud, K.P.
J. Electrochemical Soc., 127, 1980, 2410-2419.
30. Lillerud, K.P. and Kofstad, P.
Oxidation of Metals, 17, 1982, 127-139.
31. Kofstad, P. and Lillerud, K.P.
Oxidation of Metals, 17, 1982, 177-194.
32. Lillerud, K.P. and Kofstad, P.
Oxidation of Metals, 17, 1982, 195-203.
33. Wyckoff, R.W.G.
Crystal Structures
Interscience Publishers Inc. New York 1960.
34. Hatfield, W.H.
J. Iron Steel Inst., 115, 1927, 483.
35. Phalnikar C.A., Evans, E.B. and Baldwin, W.M.
J. Iron Steel Inst., 103, 1956, 429.
36. Hagel, W.C.
Trans. Am. Soc. Met., 56, 1963, 583.
37. Cadiou, L. and Paidassi, J.
Mem. Sci. Rev. Metall., 66, 1969, 217.
38. Caplan, D. and Cohen, M.
J. Electrochemical Soc., 112, 1965, 471-477.
39. Caplan, D. and Sproule, G.I.
Oxidation of Metals, 9, 1975, 459-472.
40. Gulbransen, E.A. and Andrew, K.F.
J. Electrochemical Soc., 99, 1952, 402.
41. Gulbransen, E.A. and Andrew, K.F.
J. Electrochemical Soc., 104, 1957, 334.
42. Young, D.J. and Cohen, M.
J. Electrochemical Soc., 124, 1977, 775-779.

43. Young, E.W.A., Gerretsen, J.H. and de Wit, J.H.W.
Submitted to J. Electrochemical Soc.
44. Matsui, T. and Naito, K.
J. Nucl. Mat., 120, 1984, 115-119.
45. Hindam, H. and Whittle, D.P.
Oxidation of Metals, 18, 1982, 245-284.
46. Hindam, H. and Whittle, D.P.
J. Electrochemical Soc., 130, 1983, 1519-1523.
47. Caplan, D., Harvey, A. and Cohen, M.
Corrosion Science, 3, 1961, 161.
48. Atkinson, H.V.
Oxidation of Metals, 24, 1985, 177-147.
49. Hughes, A.E., Atkinson, A. and Chadwick, A.T.
In "Materials Research Society Symposia Proceedings"
Elsevier, New York, 24, 1984, 27.
50. Volpe, M.L. and Reddy, J.
J. Chem. Phys., 53, 1970, 1117.
51. Atkinson, A. and Taylor, R.J.
J. Materials Science, 13, 1978, 427.
52. Atkinson, A., Taylor, R.I.
AERE - R11314 (1984)
53. Rhines, F.N. and Wolf, J.S.
Metallurgical Transactions, 1, 1970, 1701.
54. Brückman, A.
Corrosion Science, 7, 1967, 51-59.
55. Mrowec, S.
Corrosion Science, 7, 1967, 563-577.
56. Kofstad, P.
Oxidation of Metals, 24, 1985, 265-276.
57. Lillerud, K.P. and Kofstad, P.
In "High Temperature Corrosion", NACE 6, Ed. R.A. Rapp., 1983,
155-161.
58. Kofstad, P.
High Temperature Corrosion (to be published)
59. Whittle, D.P.
In "High Temperature Corrosion", NACE 6, Ed. R.A. Rapp. 1983,
171-183.
60. Chattopadhyay, B. and Wood, G.C.
Oxidation of Metals, 2, 1970, 373-399.

61. Wood, G.C.
Oxidation of Metals, 2, 1970, 11-57.
62. Giggins, C.S. and Pettit, F.S.
Trans. Metall. Soc. AIME, 245, 1969, 2495.
63. Whittle, D.P. and Wood, G.C.
J. Electrochemical Soc. 114, 1967, 986; 115, 1968, 133.
64. Wood, G.C. and Whittle, D.P.
Corrosion Science 7, 1967, 763.
65. Douglass, D.L.
In "Oxidation of Metals and Alloys"
Ed. Douglass, D.L., A.S.M. Metals Park, Ohio, 1971.
66. Stringer, J.
Corrosion Science, 10, 1970, 513.
67. Hancock, P. and Hurst, R.C.
In "Advances in Corrosion Science and Technology"
Eds. Staehle, R.W. and Fontana, M.G.
Fontana, Plenum Press, New York, 1974.
68. Baxter, D.J. and Natesan, K.
Reviews on High Temperature Materials, 5, 1983, 149-250.
69. Pilling, N.B. and Bedworth, R.E.
J. Inst. Met., 29, 1923, 529.
70. Jaenicke, W., Leistikow, S., and Stadler, A.J.
J. Electrochem. Soc., 111, 1964, 1031.
71. Horibe, S. and Nakayama
Corrosion Science, 15, 1975, 589-590.
72. Shatynski, S.R.
Oxidation of Metals 11, 1977, 307.
73. Strafford, K.N.
Met. Rev. 138, 1969, 153.
74. Mrowec, S. and Przybylski, K.
High Temperature Materials and Processes, 6, 1984, 1-79.
75. Mrowec, S.
Werkstoffe und Korrosion, 31, 1980, 371-386.
76. Mrowec, S. and Przybylski, K.
Oxidation of Metals 23, 1985, 107-139.
77. Wagner, C.
Z. Physik.Chem. 21, 1933, 25.
78. Strafford, K.N.
In Proc. Conf. on "Environmental Degradation of High Temperature Materials" Isle of Man. UK. 1980.

79. Strafford, K.N.
High Temperature Technology 1, 1983, 307-318.
80. Geld, P.V. and Krasovskaya, A.K.
Zh. Fiz. Khim. 34, 1960, 1585.
81. Geld, P.V. and Krasovskaya, A.K.
Ibid 34, 1960, 1721.
82. Pfeiffer H. and Ilschener, B.
Z. Electrochem 60, 1956, 424.
83. Arkharov, V.I. and Blankova, E.B.
Fiz. Met. Metalloid 8, 1959, 452.
84. Jesin, O.A. and Geld, P.V.
Zh. Prikl. Khim. 19, 1946, 678.
85. Bruckman, A. and Romanski, J.
Corrosion Science 5, 1965, 185.
86. Mrowec, S.
Corrosion Science 7, 1967, 563-578.
87. Strafford, K.N.
In "Course on High Temperature Corrosion" organised by J.R.C.
Petten 1978, 49-78 - private communication.
88. Bastow, B.D. and Wood, G.C.
Oxidation of Metals 9, 1975, 473-496.
89. Narita, R., Smeltzern W.W. and Nishida, K.
Oxidation of Metals, 17, 1982, 299.
90. Chan, W.Y., Strafford, K.N. and Norton, J.F.
Proceedings of 8th International Congress on Metallic Corrosion,
Mainz, 1981, 1575-1587.
91. Chan, W.Y., Strafford, K.N. and Norton, J.F.
In "Corrosion Resistant Materials for Coal Conversion Systems"
Eds. Meadowcroft D.B. and Manning, M.I.
Applied Science Publishers, 1983, 517-549.
92. Davies, D.P.
Metals and Materials 2, 1986, 342-348.
93. Hochman, R.F.
Proc. of Symposium on Properties of High Temperature Alloys
Eds. Foroulis, Z.A. and Pettit, F.S.
Electrochemical Soc. 1976, 715-732.
94. Perkins, R.A., Coons, W.C. and Radd, F.J.
Ibid. 733-754.
95. Koszman, I.
In "High Temperature Gas-Metal Reactions in Mixed Environments"
Eds. Jansson, S.A. and Foroulis Z.A., Boston, 1972.

96. Barnes, J.J.
Ph.D. Thesis, National University of Ireland, 1983.
97. Smith, P.J.
Ph.D. Thesis, National University of Ireland, 1984.
98. Perkins, R.A.
In "The Behaviour of High Temperature Alloys in Aggressive Environments"
Eds. Kirman, I., Marriott, J.B., Merz, M., Sahm, P.R. and Whittle, D.P.
Metals Soc., 1980, 617-647.
99. Schnaas, A. and Grabke, H.J.
Oxidation of Metals 12, 1978, 387-404.
100. Harrison, J.M., Norton, J.F., Derricott, R.T. and Marriott, J.B.
Werkstoffe und Korrosion 30, 1979, 785.
101. Norton, J.F., Blidegn, L., Canetoli, S. and Frampton, P.D.
Werkstoffe und Korrosion 32, 1981, 467-478.
102. Norton, J.F.
Private Communication.
103. Smith, P.J., Van der Biest, O. and Corish, J.
Oxidation of Metals 24, 1985, 47-83.
104. Grabke, H.J.
Materials Science and Engineering 42, 1980, 91-99.
105. Grabke, H.J.
Ber. Bunsenges. Phys. Chem. 69, 1965, 409.
106. Shatynski, S.R.
Oxidation of Metals 13, 1979, 105-118.
107. Bresseleers, C., Gavison, R., Harrison, J., Kemeny, G., Norton, J., Rother, H., Van de Voorde, M., Whittle, D.
Euroreport No.6203, 1978.
108. Grabke, H.J. and Schnaas, A.
In "Proc. Petten Int. Conf. on Alloy 800".
Eds. Betteridge, W., Krefeld, R., Kröckel, H., Lloyd, S.J., Van de Voorde, M., Vivante, C.
North Holland Publishing Company, Amsterdam, 1978, 195-211.
109. Wang, D. and Douglass, D.L.
Oxidation of Metals 20, 1983, 111-146.
110. Norton, J.F. and Barnes, J.J.
In "Corrosion in Fossil Fuel Systems"
Ed. Wright I.G. Electrochemical Soc. 1982, 277-304.
111. Bose, S.K. and Grabke, H.J.
Z. Metallkde 69, 1978, 8.

112. Wada, T., Wada, H., Elliott, J.F. and Chipman, J.
Metallurgical Transactions 2, 1971, 2199-2208.
113. Van der Biest, O., Harrison, J.M. and Norton, J.F.
In "The Behaviour of High Temperature Alloys in Aggressive Environments"
Eds. Kirman, I., Marriott, J.B., Merz, M., Sham, P.R. and Whittle, D.P.
Metals Soc. 1980, 681-701.
114. Demel, O. and Degischer, H.P.
Ibid., 649-659.
115. Gravenhorst, U. and Steinkusch, W.
Arch. Eisenhüttenwas 46, 1975, 397.
116. Grabke, H.J., Gravenhorst, U. and Steinkusch, W.
Werkstoffe und Korrosion 32, 1981, 467-478.
117. Roy, S.K., Grabke, H.J. and Wepner, W.
Arch. Eisenhüttenwas 51, 1980, 91.
118. Smith, R.P.
J. Amer. Chem. Soc. 70, 1948, 2724.
119. Smith, G.M., Young, D.J. and Trimm, D.L.
Oxidation of Metals 18, 1982, 229.
120. Perkins, J. and Goldberg, A.
Oxidation of Metals 11, 1977, 23-56.
121. Swales, G.L.
Rev. Int. Hautes Temp. Réfract. 13, 1976, 146.
122. Hemmings, P.L. and Perkins, R.A.
Intrim report on EPRI contract 716-1, 1977.
123. Natesan, K.
Proceedings of Conf. on Corrosion/Erosion of Coal Conversion System Materials, Berkeley, 1979, 223-270.
124. Gulbransen, E.A. and Jansson, S.A.
In "High Temperature Metallic Corrosion of Sulphur and its Compounds"
Ed. Foroulis Z.A., Electrochem. Soc., New York 1970, 3-51.
125. Barnes, J., Corish, J., Franck, F., Norton, J.F.
Oxidation of Metals 24, 1985, 85-87.
126. Grabke, H.J.
In "High Temperature Materials Corrosion in Coal Gasification Atmospheres"
Ed. Norton J.F., Elsevier Applied Science Publishers, 1984, 59-82.
127. Stringer, J. and Whittle, D.P.
Rev. Int. Htes Temp. et Réfract. 14, 1977, 6-20.

128. Mazandarany, F.N. and Pehlke, R.D.
Metallurgical Transactions 4, 1973, 2067-2076.
129. Giggins, C.S. and Pettit, F.S.
Oxidation of Metals 14, 1980, 363-413.
130. Kirkaldy, J.S., Bolze, G.M., McCutcheon, D. and Young, D.J.
Metallurgical Trans. 4, 1973, 1519-1526.
131. Tellez, A.V.
Ph.D. Thesis
Rheinisch-Westfälischen Technischen Hochschule, Aachen, 1984.
132. Kane, R.H.
Corrosion 37, 1981, 187-199.
133. Ramanarayanan, T.A. and Petkovic-Luton, R.
Corrosion 37, 1981, 713-721.
134. Tomas, P., Young, D.J. and Trimm, D.L.
International Congress on Metallic Corrosion, Toronto, 1, 1984,
58-65.
135. Meier, G.K., Coons, W.C. and Perkins, R.A.
Oxidation of Metals 17, 1982, 235-262.
136. Guttman, V., Hurst, R.C., Norton, J.F., Van der Biest, O. and
Van de Voorde, M.
In "Corrosion in Fossil Fuel Systems"
Ed. : Wright I.G. Electrochemical Soc. 1982, 147-171.
137. Wolf, I. and Grabke, H.J.
8^e Congrès Européen de Corrosion 1, 1986, paper 46.
138. Waher, S.
Werkstoffe und Korrosion 26, 1975, 936-942.
139. Schütze, M. and Rahmel, A.
Proc. Conf. "Corrosion in Coal Conversion Systems" London, 1982.
140. Guttman, v. and Beck, K.
In "High Temperature Corrosion in Energy Systems", Ed.
Rothman, M.F., Met. Soc. of A.I.M.E. 1985, 611-623.
141. Ledjeff, K., Rahmel, A. and Schorr, M.
Werkstoffe und Korrosion 30, 1979, 767-784.
142. Ledjeff, K., Rahmel, A. and Schorr, M.
Werkstoffe und Korrosion 31, 1980, 83-97.
143. Gibbs, G.B.
Oxidation of Metals 7, 1973, 7.
144. Rowlands, P.C. et al.
In "Metal-Slag-Gas Reactions and Processes",
Electrochem. Soc. Toronto 1975.

145. Wolf, I. and Grabke, H.J.
Solid State Comm. 54, 1985, 5-10.
146. Grabke, H.J., Möller, R. and Schnaas, A.
In "Behaviour of High Temperature Alloys in Aggressive Environments"
Eds. Kirman, I., Marriott, J.B., Merz, M., Sahm, P.R. and Whittle, D.P.
Metals Society, 1980, 759-768.
147. Fruehan, R.J.
Metallurgical Transactions, 4, 1973, 2129-2132.
148. Barnes, J., Corish, J. and Norton, J.F.
Oxidation of Metals 26, 1986, 333-350.
149. Natesan, K. and Delaplane, M.B.
In "Proc. Conf. on Corrosion-Erosion Behaviour of Materials"
Ed. Natesan, K., TMS-AIME, Warrendale, Pennsylvania 1978, 1-29.
150. Tiearney, T.C. and Natesan, K.
J. Materials for Energy Systems, 1, 1980, 13-29.
151. Perkins, R.A.
Conf. on the Environmental Degradation of High Temperature Materials.
Institute of Metallurgists, Series 3, No.13, Vol. 2, London, 1980.
152. Perkins, R.A.
In "High Temperature Corrosion" NACEG
Ed. Rapp, R.A., 1983, 345-353
153. Rahmel, A.
Corrosion Science 13, 1973, 125.
154. Rahmel, A.
Oxidation of Metals, 9, 1975, 401-
155. Flatley, T. and Birks, N.
J. Iron Steel Inst. 209, 1971, 523.
156. Luthra, K.L. and Worrell, W.L.
Metallurgical Trans 9A, 1978, 1055.
157. Luthra, K.L. and Worrell, W.L.
Metallurgical Trans 10A, 1979, 621.
158. Gesmundo, F.
Oxidation of Metals, 13, 1979, 237-244.
159. Gesmundo, F., de Asmundis, C. and Nanni, P.
Oxidation of Metals, 20, 1983, 217.
160. Stroosnijder, M.F. and Quadackers, W.J.
High Temperature Technology, 4, 1986, 83-96.

161. Yurek, G.J. and La Branche, M.H.
In Proc. of Conf. on "Corrosion-Erosion-Wear of Materials in Emergency Fossil Energy Systems".
Berkeley California.
Engineers 1982, 933-958.
162. La Branche, M., Garrott-Reed, A. and Yurek, G.J.
J. Electrochemical Soc., 130, 1983, 2405-2413.
163. Birks N.
Proc. Conf. on Corrosion-Erosion Behaviour of Materials"
Ed. Natesan, K., TMS-AIME, Warrendale, Pennsylvania 1978, 1-29.
164. Yurek, G.J., La Branche, M.H. and Kim, Y.K.
In "High Temperature Corrosion in Energy Systems".
Ed. Rothman, M.F. Metallurgical Soc. of AIME 1985, 195-307.
165. Hussey, R., Papaioannou, P. and Grabke, H.J.
Proc. 8e Congrès Européen Corrosion, Nice, 1985, Paper 51.
166. Rao, D.B., Jacob, K.T. and Nelson, H.G.
Metallurgical Transactions 14A, 1983, 295-305.
167. Cooper and Strafford.
Private communication.
168. Hill, V.L. and Meyer, H.S.
In "High Temperature Corrosion in Energy Systems"
Ed. Rothman, M.F.
Metallurgical Soc. of AIME 1985, 29-52.
169. Humphreys, B.A., Hill, V.L. and Blough, J.L.
In Proc. of 1983 Gas Research Conf., Chicago, Illinois, 1983,
423-433.
170. Hill, V.L. and Humphreys, B.A.
In "The Properties and Performance of Materials in Coal
Gasification Environment"
American Society of Metals, 1981, 257-288.
171. Tiearney, T.C. and Natesan, K.
Oxidation of Metals, 17, 1982, 1-26.
172. Rao, D.B. and Nelson, H.G.
Oxidation of Metals, 12, 1978, 111-138.
173. Jacob, K.T., Rao, D.B. and Nelson, H.G.
Oxidation of Metals 13, 1979, 25-55.
174. Rao, D.B. and Nelson, H.G.
In "Properties of High Temperature Alloys"
Eds. Foroulis Z.A. and Pettit, F.S.
Electrochemical Soc. 1977, 464-492.
175. Chu, W.F. and Rahmel, A.
Oxidation of Metals 16, 1981, 175-191.

176. Hindam, H. and Whittle, D.P.
Corrosion 38, 1982, 32-39.
177. Nagarajan, V., Miner, R.G. and Levy, A.V.
J. Electrochemical Soc., 129, 1982, 782-788.
178. Danielewski, M. and Natesan, K.
Oxidation of Metals, 12, 1977, 227-245.
179. Nagarajan, V., Miner, R.G. and Levy, A.V.
J. Electrochemical Soc., 129, 1982, 789-795.
180. Perkins, R.A. and Bhat, M.S.
Lockhead Research Laboratory Report, Palo Alto, CA, 1977.
181. Williams, D.S., Moller, R. and Grabke, H.J.
Oxidation of Metals, 16, 1981, 253-266.
182. Natesan, K.
Corrosion 41, 1985, 646-655.
183. Stott, F.M., Chong, F.M.F. and Stirling, C.A.
In "High Temperature Corrosion in Energy Systems"
Ed. Rothman, M.F., Metallurgical Soc. of AIME 1985, 253-263.
184. Stott, F.M., Chong, F.M.F. and Stirling, C.A.
Proc. Int. Conf. on Metallic Corrosion, 2, Toronto, 1984, 1-16.
185. Stott, F.M. and Chong, F.M.F.
In "Corrosion Resistant Materials for Coal Conversion Systems"
Ed. Meadowcroft, D.B. and Manning, M.I., Applied Science Publishers,
1983, 491-516.
186. Croll, J.E. and Wallwork, G.R.
Oxidation of Metals 4, 1972, 121.
187. Allan, S.J. and Dean, M.J.
Proc. Int. Conf. on the Behaviour of High Temperature Alloys in
Aggressive Environments, Petten 1979, 319.
188. Schreiner, W.N., Surdukowski, C. and Jenkins, R.
J. Appl. Crys. 15, 1982, 512.
189. International Centre for Diffraction Data (Joint Committee on
Powder Diffraction Standards)
Swarthmore, PA, USA.
190. Burley, N.A. and Dale, J.J.
Metallurgia 1962, 203.
191. Bühler, H.E., Hougardy, H.P.
Atlas der Interferenzschichten, Metallographie, Deutsche
Gesellschaft für Metallkunde, 1979.

192. Quested, P.N. and Raine, K.N.
Metals and Materials, Oct. 1981.
193. Wu, T.W., Buhler, H.E. and Rahmel, A.
Practical Metallography, 20, 1983, 479-494.
194. Buhler, H.E., Kossel, D.
Practical Metallography, 18, 1981, 384-391.
195. Schroer, B., Hougady, H.P.
Practical Metallography, 22, 1985, 587-596.
196. Aydin, I., Buhler, H.E.
Practical Metallography, 17, 1980, 441-446.
197. Aydin, I., Buhler, H.E. and Rahmel, A.
Microstructural Science, 9, 1981, 55-63.
198. Wu, W.I., Aydin, I. and Buhler, H.E.
Practical Metallography, 19, 1982, 322-346.
199. Andersen, C.A.
Microprobe Analysis, Wiley, New York, 1973.
200. Reed, S.J.B.
Analysis of High Temperature Materials
Ed. O. Van der Biest, Applied Science Publishers, 1983, 91.
201. Douglass, D.C., and Armijo, J.S.
Oxidation of Metals 2, 1970, 207-231.
202. Gildegorn, I.S., and Rogelberg, I.L.
Fiz. Metal, Metalloved 18, 1964, 935-938.
203. Yurek, G.J., Eisen, D. and Garratt-Reed, A.
Metallurgical Transactions 13A, 1982, 473-485.
204. Evans, H.E., Hilton, D.A., Holm, R.A. and Webster, S.J.
Oxidation of Metals 19, 1983, 1-18.
205. Rahmel, A., Wood, G.C., Kofstad, P., Douglass, D.L.
Oxidation of Metals 21, 1985, 251-337.
206. Allan, S.J., Norton, J.F. and Popple, L.A.
Int. Conf. of the British Nuclear Energy Society on Effects
of Environment on Materials Properties in Nuclear Systems,
1974, 294.
207. Wood, G.C., Hobby, M.G. and Vaszko, B.
J. Iron and Steel Institute 202, 1964, 685.
208. Baxter, D.J.
Ph.D. Thesis, Wolverhampton Polytechnic 1981.
209. Francis, J.M. and Jutson, J.A.
Materials Science and Engineering 4, 1969, 84.
210. Hall, E.O. and Algie, S.H.
Metallurgical Reviews 11, 1966, 61-88.
211. Ansara, I., Chart, T.G., Chevalier, P.Y., Hack, K., McHugh, G.,
Rand, M.H. and Spencer, P.J.
Eur. Report 9657/1/EN.
212. Cox, M.G.C., McEnaney, B. and Scott, V.D.
Phil. Mag. 26, 1972, 839-851.

213. Anzaroff, L.V.
J. Appl. Phys. 32, 1961, 1638.
214. Dunitz, J.B. and Orgel, L.E.
J. Phys. Chem. Solids 3, 1957, 20 and 318.
215. Wild, R.K.
Corrosion Science 17, 1977, 87-104.
216. Cox, D.E., Takei, W.J. and Shirane, G.
J. Phys. Chem. Solids 24, 1963, 405-423.
217. Francis, J.M.
J. Appl. Chem. 16, 1966, 264-265.
218. Belan, N., Tomaszewick, P. and Young, D.J.
Oxidation of Metals 22, 1984, 227-245.
219. Wood, G.C. and Stott, F.H.
In NACE 6, 1983, 227-250.
220. Tomaszewicz, P. and Wallwork, G.R.
Corrosion 40, 1984, 152-157.
221. Hemptenmacher, J., Onel, K. and Grabke, H.J.
Proc. 8th Int. Conf. on Metallis Corrosion, Mainz 1981, 742-747.
222. Orr, J.
In "Proc. Petten Int. Conf. on Alloy 800".
Eds Betteridge, W., Krefeld, R., Krockel, H., Lloyd, S.J.,
Van de Voorde, M. and Vivante, C.
North Holland Publishing Company, Amsterdam, 1978, 25
223. McAllister, A.S.
Ph.D. Thesis, Loughborough University, 1986.
224. Gandrey, F.
Private communication.
225. Guttman, V.
Private communication.
226. Birks, N.
In "Properties of High Temperature Alloys".
Eds Fouroulis, Z.A. and Pettit, F.S.
Electrochemical Soc. 1976, 215-260.
227. Wagner, J.B.
In "Defects and Transport in Oxides".
Eds Seltzer M. and Jaffee, R.I.
Plenum, 1974, 283-301.
228. Chung, D.R., Nemeto and Wagner, J.B.
Metallurgical Transactions 7A, 1976, 803-806.
229. Howng, W.Y. and Wagner, J.B.
J. Phys. Chem. Solids 39, 1978, 1019.
230. Suntsov, N.V. and Antonenko, V.M.
Zashchita Metallov II, 1975, 361-363.
231. Singh, P. and Birks, N.
Werkstoffe und Corrosion 31, 1980, 682-688.

- 232. Singh, P. and Birks, N.
Oxidation of Metals 19, 1983, 37-52.
- 233. Pope, M.C. and Birks, N.
Oxidation of Metals 12, 1978, 191-204.
- 234. Romeo, G., Spacil, H.S. and Pasko, W.J.
J. Electrochem. Soc. 122, 1975, 1329-1333.

APPENDIX 1

Gas characterisation

A gaseous atmosphere relevant to this study containing the reactants C, H, O and S could consist of upto nine gaseous species (H_2 , H_2S , H_2O , CH_4 , CO , CO_2 , COS , SO_2 and SO_3). A method of characterising these complex atmospheres in terms of partial pressures of oxygen (pO_2), sulphur (pS_2) and carbon activity (a_c) has been devised by Kemeny and Whittle⁽¹⁾.

The total number of atoms of C, H, O and S, n_C , n_H , n_O and n_S respectively can be given by

$$n_C = n_{CO} + n_{CO_2} + n_{CH_4} + n_{COS} \quad (1)$$

$$n_H = 2n_{H_2} + 2n_{H_2O} + 4n_{CH_4} + 2n_{H_2S} \quad (2)$$

$$n_O = n_{H_2O} + n_{CO} + 2n_{CO_2} + n_{COS} + 2n_{SO_2} + 3n_{SO_3} \quad (3)$$

$$n_S = n_{COS} + n_{SO_2} + n_{SO_3} + n_{H_2S} \quad (4)$$

where n_i is the number of moles of component i .

These can be conveniently expressed as fractions N_C , N_H , N_O and N_S such that

$$N_C = \frac{n_C}{n_C + n_H + n_O + n_S} \quad (5)$$

$$N_H = \frac{n_H}{n_C + n_H + n_O + n_S} \quad (6)$$

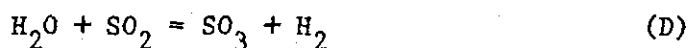
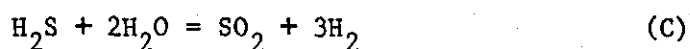
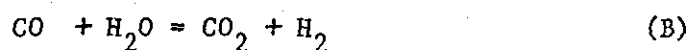
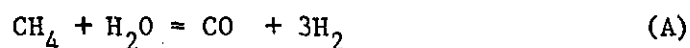
$$N_O = \frac{n_O}{n_C + n_H + n_O + n_S} \quad (7)$$

$$N_S = \frac{n_S}{n_C + n_H + n_O + n_S} \quad (8)$$

and thus

$$N_C + N_H + N_O + N_S = 1 \quad (9)$$

There are five independent equilibria possible between the various species viz. :



The law of mass action states that for a given reaction the equilibrium constant (K) is given by

$$K = \frac{\text{activity of the products}}{\text{activity of the reactants}}$$

The equilibrium constant for the reaction is related to the standard free energy (ΔG°) by the Vant Hoff Isotherm :

$$\Delta G^\circ = -RT \ln K$$

where R = gas constant.

Thus for the reaction (A-E) the equilibrium constants are given by

$$K_A = \frac{p_{\text{CO}} \cdot (p_{\text{H}_2})^3}{p_{\text{CH}_4} \cdot p_{\text{H}_2\text{O}}} = \exp. \frac{-\Delta G_A^\circ}{RT} \quad (10)$$

$$K_B = \frac{p_{\text{CO}_2} \cdot p_{\text{H}_2}}{p_{\text{CO}} \cdot p_{\text{H}_2\text{O}}} = \exp. \frac{-\Delta G_B^\circ}{RT} \quad (11)$$

$$K_C = \frac{p_{SO_2} \cdot (p_{H_2})^3}{p_{H_2S} \cdot (p_{H_2O})^2} = \exp. \frac{-\Delta G_C^\circ}{RT} \quad (12)$$

$$K_D = \frac{p_{SO_3} \cdot p_{H_2}}{p_{H_2O} \cdot p_{SO_2}} = \exp. \frac{-\Delta G_D^\circ}{RT} \quad (13)$$

$$K_E = \frac{p_{COS} \cdot p_{H_2}}{p_{H_2S} \cdot p_{CO}} = \exp. \frac{-\Delta G_E^\circ}{RT} \quad (14)$$

where p_i is the partial pressure of component i (atm.).

Assuming ideal behaviour the mole fractions of the gaseous species (x_i) can be introduced.

$$x_i = \frac{n_i}{n_{H_2} + n_{H_2O} + n_{CO} + n_{CO_2} + n_{CH_4} + n_{H_2S} + n_{COS} + n_{SO_2} + n_{SO_3}} = \frac{P_i}{P} \quad (15)$$

where P is the total pressure.

Thus substituting equation (15) into equations (10-14) gives :

$$K_A = \frac{x_{CO} \cdot (x_{H_2})^3}{x_{CH_4} \cdot x_{H_2O}} p^2 \quad (16)$$

$$K_B = \frac{x_{CO_2} \cdot x_{H_2}}{x_{H_2O} \cdot x_{CO}} \quad (17)$$

$$K_C = \frac{x_{SO_2} \cdot (x_{H_2})^3}{x_{H_2S} \cdot (x_{H_2O})^2} p^2 \quad (18)$$

$$K_D = \frac{x_{SO_3} \cdot x_{H_2}}{x_{H_2O} \cdot x_{SO_2}} \quad (19)$$

$$K_E = \frac{x_{COS} \cdot x_{H_2}}{x_{H_2S} \cdot x_{CO}} \quad (20)$$

By using equations (1-4) and substituting equation (15) into equations (5), (7) and (8) gives

$$N_C = \frac{1}{\Omega} (x_{CO} + x_{CO_2} + x_{CH_4} + x_{COS}) \quad (21)$$

$$N_O = \frac{1}{\Omega} (x_{H_2O} + x_{CO} + 2x_{CO_2} + x_{COS} + 2x_{SO_2} + 3x_{SO_3}) \quad (22)$$

$$N_S = \frac{1}{\Omega} (x_{COS} + x_{SO_2} + x_{SO_3} + x_{H_2S}) \quad (23)$$

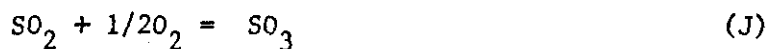
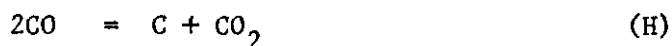
$$\text{where } \Omega = 2x_{CO} + 3x_{CO_2} + 5x_{CH_4} + 3x_{COS} + 2x_{H_2} + 3x_{H_2O} + 3x_{H_2S} + 3x_{SO_2} + 4x_{SO_3}$$

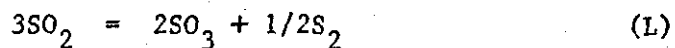
$$x_{CO} + x_{CO_2} + x_{CH_4} + x_{COS} + x_{H_2} + x_{H_2O} + x_{H_2S} + x_{SO_2} + x_{SO_3} = 1 \quad (24)$$

Thus given the free energy data⁽²⁾ in table 1 it is possible to calculate K_A , K_B , K_C , K_D , K_E from equations (10-14).

The nine equations (16) to (24) are sufficient to solve for the nine unknowns (x_{H_2} , x_{H_2S} , H_2O , CH_4 , CO , CO_2 , COS , SO_2 and SO_3) for given conditions of temperature total pressure and overall gas composition in terms of N_O , N_C and N_S with the assistance of a computer programme⁽³⁾.

Finally the carbon, oxygen and sulphur potentials can be calculated using the following reactions (F-L) for which the free energy data are given in table 1.





Thus using the law of mass action the partial pressures of oxygen and sulphur and the carbon activity can be calculated from

$$pO_2 = \left[\frac{x_{H_2O}}{x_{H_2}} \cdot \frac{1}{K_F} \right]^2 = \left[\frac{x_{CO_2}}{x_{CO}} \cdot \frac{1}{K_G} \right]^2 \quad (25)$$

$$a_c = \frac{p (x_{CO})^2 K_H}{x_{CO_2}} = \frac{x_{CH_4}}{p (x_{H_2})^2 K_I} \quad (26)$$

$$pS_2 = \left[\frac{x_{H_2S}}{x_{H_2}} \cdot \frac{1}{K_K} \right]^2 = \left[\frac{p (x_{SO_2})^3}{(x_{SO_3})^2} \right]^2 K_L \quad (27)$$

Since the atmosphere is at equilibrium the two expressions in equations (25), (26) and (27) should be identical and thus provides an internal check to the calculation.

<u>Reaction</u>	<u>ΔG° (cal)</u>	<u>Temp. Range (K)</u>
$2C + H_2 = C_2H_2$	52940 - 12.32 T	800 - 2000
$C + 2H_2 = CH_4$	-21470 + 26.1 T	800 - 2000
$C + \frac{1}{2} O_2 = CO$	-26700 - 20.95 T	298 - 2500
$C + O_2 = CO_2$	-94200 - 0.2 T	298 - 2000
$H_2 + \frac{1}{2} O_2 = H_2O$	-58900 + 13.1 T	298 - 2500
$H_2 + \frac{1}{2} S_2 = H_2S$	-21580 + 11.81 T	298 - 1800
$\frac{1}{2} S_2 + O_2 = SO_2$	-86620 + 17.31 T	298 - 2000
$\frac{1}{2} S_2 + \frac{1}{2} O_2 = SO_3$	-109220 + 38.62 T	318 - 1800
$CO + \frac{1}{2} S_2 = COS$	-22860 + 18.7 T	298 - 1500
$\frac{1}{2} O_2 = O$	60130 - 15.69 T	800 - 2000
$\frac{1}{2} H_2 = H$	53360 - 13.85 T	800 - 2000
$\frac{1}{2} H_2 + \frac{1}{2} O_2 = OH$	9820 - 3.46 T	800 - 2000

Table 1

Free energy of formation of gaseous species (2).

Compound / species	β_i at 800°C. (from Barlin & Knacke (1))
Cr	+ 2.008
O ₂	+ 11.620
Cr ₂ O ₃	+ 62.716
CrS	+ 12.480
S ₂	+ 6.653

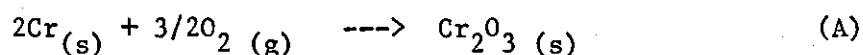
Table 2

APPENDIX 2

Construction of Metal Stability Diagrams

Figure 1 shows a schematic metal stability diagram for the M-O-S system. The procedure for calculating the position of the lines on the diagram is as follows, using the Cr system as an example.

The vertical line gives the partial pressure of oxygen (pO_2) above which it is thermodynamically favourable for chromium to react with oxygen to form chromia, i.e.



Vant Hoff isotherm states that

$$\Delta G^\circ = -RT \ln K \quad (1)$$

ΔG° = free energy of formation

R = gas constant

T = temperature

K = equilibrium constant

For any reaction

$$\Delta G^\circ = \sum G \text{ products} - \sum G \text{ reactants}$$

Thus equation (1) can be written

$$\log K_{(T)} = \frac{- \sum_i \nu_i G_i^\circ}{RT \ln 10} \quad (2)$$

$$\text{or } \log K_{(T)} = \sum_i \nu_i \beta_i(T) \quad (3)$$

where

$$\beta_i = \frac{-G_T^\circ}{RT \ln 10}$$

and

$$v_i = \text{stoichiometric numbers.}$$

Thus using the values of β_i given in Barlin and Knacke (1,2) table 1 it is possible to calculate the values of K_T for reaction (A)

$$\begin{aligned} \log K_T &= -2 (\beta_{Cr}) - 3/2 (\beta_{O_2}) + 1 (\beta_{Cr_2O_3}) \\ &= -2 (2,008) - 3/2 (11,620) + 1 (61,716) \end{aligned}$$

$$\underline{\log K_T = + 41,270}$$

The law of mass actions states

$$K_{(T)} = \frac{\text{activities of products}}{\text{activities of reactants}} \quad (4)$$

i.e.

$$K_{(T)} = \frac{a_{Cr_2O_3}}{a_{Cr}^2 p_{O_2}^{3/2}} \quad (5)$$

$$\log K_{(T)} = \log a_{Cr_2O_3} - 2 \log a_{Cr} - 3/2 \log p_{O_2} \quad (6)$$

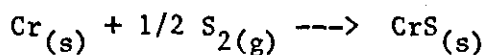
If $a_{Cr_2O_3}$ and a_{Cr} are assumed to be unity

$$\log K = -3/2 \log p_{O_2}$$

$$\log p_{O_2} = -2/3 \times 41,270$$

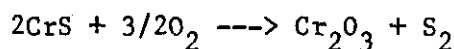
$$\underline{\log p_{O_2} = -27.513 \text{ atm.}}$$

The same procedure can be used to calculate the position of the horizontal Cr/CrS boundary by considering the reaction :



$$(\log p\text{S}_2 = -14,292 \text{ atm.})$$

To calculate the sloping line (CrS/Cr₂O₃ boundary) on the metal stability diagram the reaction



must be considered.

$$\log K_T = -2 (\Delta \text{CrS}) - 3/2 (\Delta \text{O}_2) + 1 (\Delta \text{Cr}_2\text{O}_3) + 1 (\Delta \text{S}_2)$$

Using the values from table.

$$\log K_T = -2 (12,480) - 3/2 (11,620) + 62,716 + 6,653$$

$$\underline{\log K_T = 26,979}$$

Thermodynamic equation.

$$K = \frac{a_{\text{Cr}_2\text{O}_3} p\text{S}_2}{a_{\text{CrS}}^2 p\text{O}_2^{3/2}}$$

$$\log K = \log a_{\text{Cr}_2\text{O}_3} + \log p\text{S}_2 - 2 \log a_{\text{CrS}} - 3/2 \log p\text{O}_2$$

If $a_{\text{Cr}_2\text{O}_3}$ and a_{CrS} are unity.

$$\log p\text{S}_2 = 3/2 \log p\text{O}_2 + 26,979.$$

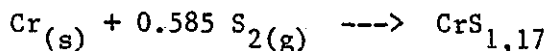
This gives the slope and intersect of the line and thus the 2-dimensional metal stability diagram can be constructed, figure 2a.

The same procedure can be used for calculating the positions of the lines for

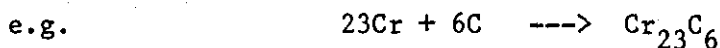
- (i) The equilibrium of different sulphides/oxides of the same system

e.g. $\text{CrS}/\text{CrS}_{1,17}$

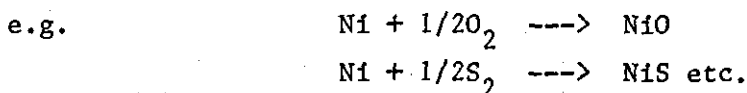
by considering the reaction



- (ii) Cr-C-O and Cr-S-C systems (figure 2b and c)



- (iii) Other metallic systems



- (iv) When the activity of the metal is not unity.

For example considering reaction (A) again

$$\log K_T = \log a_{\text{Cr}_2\text{O}_3} - 2 \log a_{\text{Cr}} - 3/2 \log p\text{O}_2 \quad (6)$$

If the Cr activity in an alloy was 0,1

$$\log K_T = -3/2 \log p\text{O}_2 - 2 \log (0,1)$$

$$\underline{\log p\text{O}_2 = - 26,18 \text{ atm.}}$$

i.e. reducing the Cr activity from unity moves the boundaries between Cr and Cr_2O_3 by 1,3 orders of magnitude.

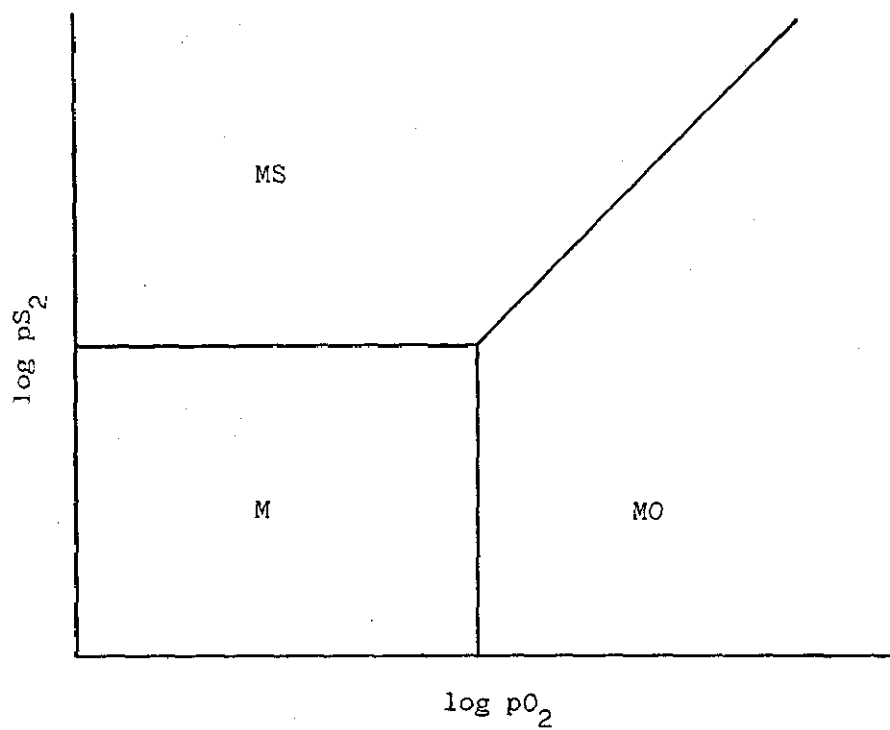


Figure 1
Schematic metal stability diagram for the M-O-S system.

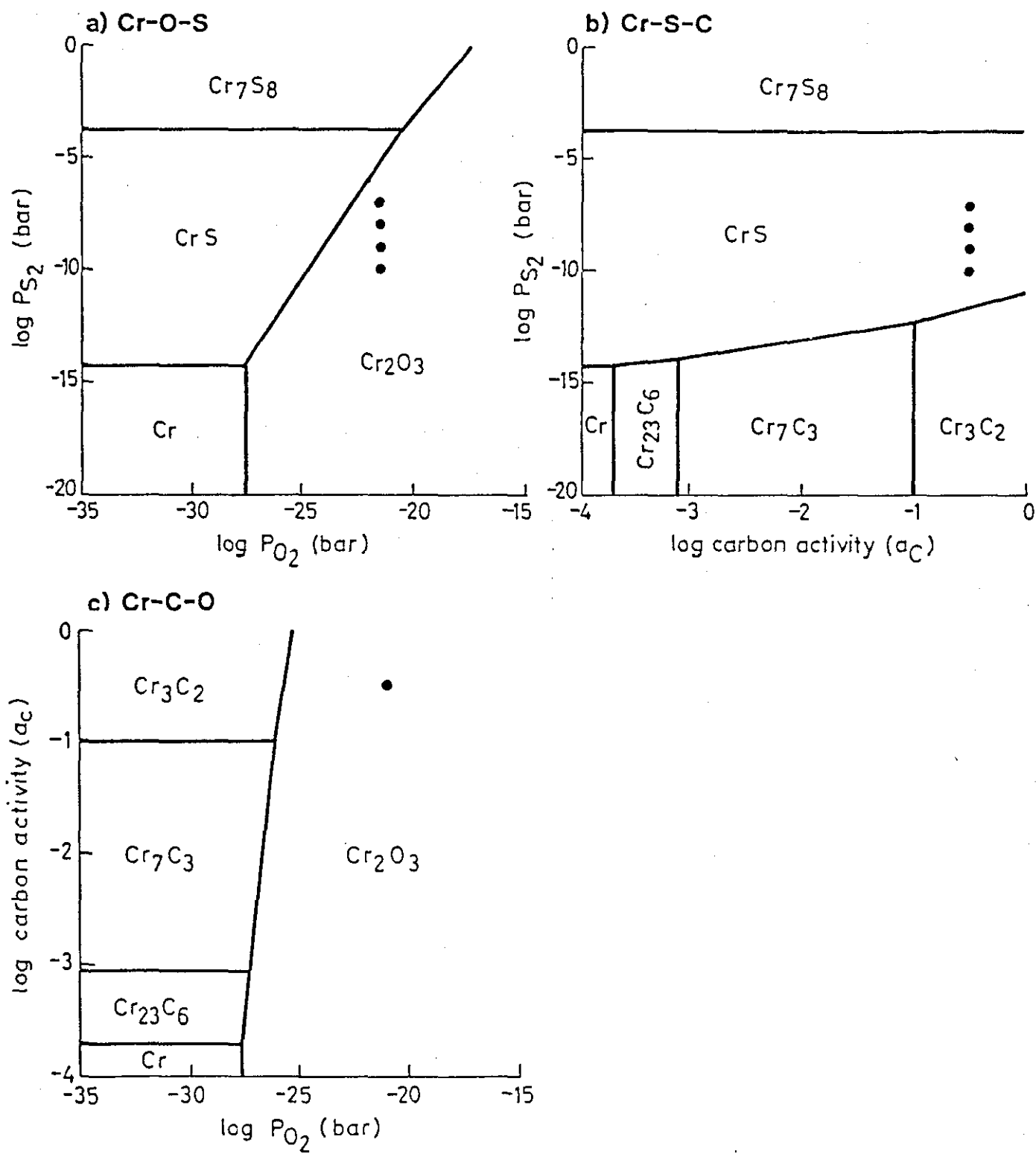


Figure 2
Phase stability diagrams for Cr-O-S-C at 800°C.

